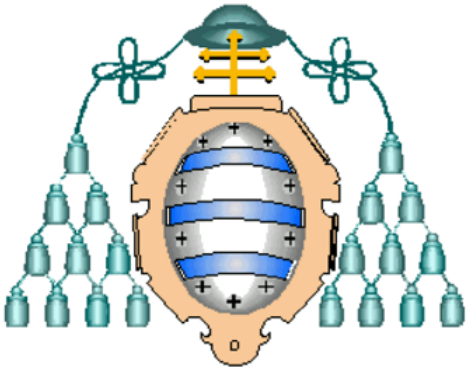

Universidad de Oviedo

PhD Thesis

Advanced techniques for the analysis and synthesis of reflectarray antennas with applications in near and far fields

Daniel Rodríguez Prado

October, 2016

Programa de Doctorado en Tecnologías de la Información y Comunicaciones en Redes Móviles

PhD Thesis

Advanced techniques for the analysis and synthesis of reflectarray antennas with applications in near and far fields

Author

Daniel Rodríguez Prado

Ingeniero de Telecomunicación

Supervisors

Dr. Manuel Arrebola Baena

Dr. Marcos Rodríguez Pino

October, 2016

Programa de Doctorado en Tecnologías de la Información y Comunicaciones en Redes Móviles

A mis padres
y mi hermano.

Acknowledgments

I wish to express my gratitude to the staff of the Área de Teoría de la Señal y Comunicaciones of Universidad de Oviedo. The discussions on technical and non technical topics with the professors and students from this department have been a fruitful experience and even a pleasure. In particular, I am grateful to Dr. Manuel Arrebola Baena and Dr. Marcos Rodríguez Pino, supervisors of this work, for their patience, expertise and continuous support which has made this thesis possible. I would also like to thank them for giving me the opportunity to work on many research projects.

Also, I would like to mention Dr. Óscar Quevedo-Teruel, for taking me under his supervision during a short stay at KTH Royal Institute of Technology, in Stockholm, Sweden, where we worked together in Transformation Optics applied to dielectric lenses. His enthusiasm, knowledge and persistance made the experience an unforgettable one.

Finally, I would also like to thank several institutions for supporting projects related to the scope of this thesis and providing the grant which made it possible: Ministerio de Economía y Competitividad, Gobierno de España; European Space Agency (ESA); Principado de Asturias, España; and Fundación para el Fomento en Asturias de la Investigación Científica Aplicada y la Tecnología (FICYT).

Resumen

Introducción

El constante desarrollo de los sistemas de comunicaciones ha propiciado la necesidad de disponer de sistemas que cumplan las cada vez más estrictas especificaciones impuestas para mejorar la calidad de los mismos. En particular, las antenas son un componente muy importante de los sistemas de comunicación pues permiten las comunicaciones móviles a grandes distancias. Según la aplicación, se intentan optimizar distintos parámetros de la antena, como puedan ser su eficiencia, tamaño, adaptación, diagrama, etc. Las aplicaciones de radiodifusión directa por satélite (Direct Broadcast Satellite, DBS por sus siglas en inglés) son particularmente desafiantes ya que requieren del conformado del diagrama de radiación para cumplir con una determinada huella sobre la superficie terrestre, a la vez que se consigue una alta pureza de polarización, todo ello trabajando con antenas de considerable tamaño. Tradicionalmente, las antenas basadas en reflectores parabólicos conformados han sido la solución adoptada para este tipo de aplicación. Sin embargo, estas antenas resultan muy grandes, pesadas y costosas. Con la popularización de la tecnología microstrip, las antenas de tipo reflectarray se han erigido como un potencial sustituto de los reflectores parabólicos, no solo para aplicaciones satelitales, sino para todo tipo de aplicaciones en las que el uso de dichos reflectores es norma común hoy en día.

Un reflectarray está compuesto de un alimentador primario, típicamente una bocina, y un array de elementos reflectantes que introducen un determinado desfase en la onda reflejada. El diseño de reflectarrays se basa en la obtención de dicho desfase en cada elemento del reflectarray de forma que se obtenga el campo radiado deseado, ya sea un haz de tipo pincel o haz conformado en campo lejano; o ciertas características en campo cercano, como enfoque, multienfoque o planitud en fase y amplitud.

Los reflectarrays poseen ciertas características que los hacen atractivos en comparación con los reflectores parabólicos y los arrays tradicionales. Primero, al ser antenas impresas son de bajo perfil, por lo que en comparación con los reflectores parabólicos son más ligeras y ocupan menos espacio volumétrico. Sin embargo, en relación a los arrays clásicos la estructura completa del reflectarray ocupa más volumen. Segundo, las pérdidas dependen de la calidad del substrato y la geometría del elemento impreso, y son significativamente más bajas que en los arrays ya que la red de alimentación no es necesaria. Además, empleando materiales de bajas pérdidas, éstas son similares a las de los reflectores parabólicos. Y tercero, la tecnología necesaria para fabricar reflectarrays es la misma que se utiliza

para producir circuitos impresos, siendo una tecnología madura: bien conocida, precisa y relativamente barata. Otra ventaja importante de los reflectarrays es que el coste de producirlo es independiente del tipo de haz. Además, los reflectarrays impresos presentan ventajas económicas respecto a reflectores parabólicos conformados utilizados en misiones espaciales, que son muy caros debido a que los moldes empleados no pueden ser reutilizados para otras misiones. Además, al ser los reflectarrays planos, pueden ser fácilmente doblados para su transporte y despliegue en aeronaves y satélites.

Sin embargo, los reflectarrays presentan algunas desventajas, principalmente dos: un ancho de banda inherentemente bajo y la escasez de técnicas adecuadas de síntesis u optimización de la componente contrapolar. En primer lugar, el bajo ancho de banda de los reflectarrays se da por dos motivos: el reducido ancho de banda de los elementos resonantes de los que está compuesto, que suelen ser del orden del 3 %-5 %; y el desfase por la diferencia de caminos espacial. El primer problema suele resolverse empleando elementos de banda ancha que introducen múltiples resonancias. El segundo problema puede ser afrontado ajustando la geometría del elemento a varias frecuencias para compensar dicho desfase, usar elementos con retardo de tiempo real, incrementando el ratio f/D, usando reflectarrays curvos o multipanel.

La otra desventaja se haya en la síntesis de reflectarrays de haz conformado para aplicaciones con requisitos de contrapolar muy estrictos, como pueden ser las misiones satelitales. La técnica predominante de síntesis de reflectarrays se conoce como síntesis solo fase, que se puede llevar a cabo con múltiples algoritmos. Está basada en un análisis simplificado del reflectarray en el que solo se trabaja con especificaciones de diagrama copolar, por lo que no hay control sobre el nivel de contrapolar durante el proceso de síntesis. Aunque se han desarrollado algunas técnicas de optimización del diagrama contrapolar, resultan ser poco flexibles o basadas en modelos simplificados.

Esta tesis está dedicada al desarrollo de nuevas técnicas de análisis y síntesis de reflectarrays. Se pretende prestar especial atención a la eficiencia de dichas técnicas. En particular, las nuevas técnicas de análisis se centran en el desarrollo de algoritmos precisos y rápidos para el cálculo de diagramas de radiación, basadas en el uso de algoritmos como la Transformada Rápida de Fourier (Fast Fourier Transform, FFT por sus siglas en inglés) y la Transformada Rápida de Fourier No Uniforme (Non-Uniform Fast Fourier Transform, NUFFT). Por otro lado, se presentarán nuevas técnicas de síntesis para la optimización del diagrama contrapolar, así como síntesis en campo cercano.

Mejoras en el análisis de antenas reflectarray

El análisis de reflectarrays puede dividirse en varios bloques, incluyendo el análisis del alimentador, de los elementos y el cálculo del campo radiado. Cada uno de estos subanálisis se puede mejorar de forma independiente, aumentando la precisión del mismo y disminuyendo los tiempos de computación. Respecto al cálculo de los diagramas de radiación, ya se disponen de técnicas precisas y eficientes para el caso de reflectarrays periódicos. La eficiencia radica en el uso de la FFT en el cálculo de las funciones espectrales, que son la transformada de Fourier del campo tangencial en la apertura; mientras que la precisión

se basa en considerar cada elemento del reflectarray como una pequeña apertura en lugar de una fuente puntual con diagrama isotrópico. Sin embargo, en el caso de reflectarrays aperiódicos, no existe actualmente una técnica que englobe ambos aspectos, por lo que cabían dos posibilidades hasta ahora. Por un lado, un análisis considerando elementos rectangulares en lugar de fuentes puntuales, pero evaluando directamente las ecuaciones sin usar algoritmos eficientes, lo que conlleva altos tiempos de computación. Por otro lado, se pueden modelar los elementos como fuentes puntuales y emplear la NUFFT, de forma que se gana eficiencia computacional a costa de perder precisión.

En esta tesis se ha desarrollado por primera vez una técnica para poder usar la NUFFT para el análisis de reflectarrays aperiódicos modelando sus elementos como aperturas rectangulares. Dicho desarrollo se basa en la descomposición de las funciones sinc en exponenciales mediante la fórmula de Euler. Tras algunas manipulaciones, se puede identificar la ecuación obtenida como una combinación lineal de cuatro NUFFT por cada función espectral. De esta forma, se consigue un cálculo eficiente de los elementos modelados como aperturas rectangulares. Más aún, como la NUFFT es una generalización de la FFT, la nueva técnica puede también ser empleada para el caso periódico, eliminando una limitación en el uso de la FFT, a saber, la imposibilidad de calcular el diagrama de radiación en toda la zona visible cuando la periodicidad del reflectarray es mayor que media longitud de onda. El algoritmo NUFFT dispone de un parámetro gracias al cual se puede ajustar la precisión deseada. A través de varios ejemplos se ha mostrado un rango de valores adecuados entre los que escoger según un compromiso entre velocidad de cálculo y precisión. Además, se ha llevado a cabo un estudio de tiempos de computación, mostrando la eficiencia del algoritmo respecto de una evaluación directa de las ecuaciones de las funciones espectrales.

Para los análisis anteriores de reflectarrays periódicos y aperiódicos se utiliza una aproximación: el campo incidente en cada elemento es constante. Esta aproximación facilita los cálculos analíticos con las ecuaciones de las funciones espectrales. Sin embargo, puede generalizarse el análisis suponiendo una variación continua del campo incidente. Éste puede considerarse de variación lenta en cada celda, por lo que su señal asociada será de banda estrecha. De esta forma, el campo incidente puede representarse mediante un desarrollo en serie de Fourier truncado a unos pocos armónicos sin cometer un error excesivo. Sustituyendo el campo incidente en cada celda por su desarrollo en serie de Fourier y operando, se llega a obtener una expresión de las funciones espectrales que nuevamente se puede calcular mediante el algoritmo FFT para el caso periódico, y mediante la NUFFT en el caso aperiódico. La diferencia radica en que ahora el número de evaluaciones de la FFT/NUFFT aumenta, aunque el análisis sigue siendo eficiente por recurrir al uso de dichos algoritmos, al mismo tiempo que se gana precisión por eliminar la aproximación de campo incidente constante en cada celda del reflectarray.

Aunque estos nuevos desarrollos en las técnicas de análisis de campo lejano se han enfocado principalmente a antenas de tipo reflectarray, se pueden aplicar al análisis de otras estructuras planas como arrays, transmitarrays o superficies selectivas en frecuencia (FFS), debido a sus similitudes con los reflectarrays (principalmente que son también

antenas de apertura).

Finalmente, los modelos de campo cercano de arrays suelen considerar los elementos como fuentes puntuales. En esta tesis se propone mejorar dicho modelo considerando cada elemento, al igual que en el caso de campo lejano, como aperturas rectangulares, de forma que se mejore la precisión de la evaluación del campo cercano. El campo cercano radiado por el reflectarray se calcula como contribución, en cada punto del espacio, de todos los campos lejanos radiados por los elementos del reflectarray. El objetivo de este análisis es calcular y optimizar el campo cercano radiado por reflectarrays para su posterior uso como sondas de medida en rangos compactos. Por ello, se ha detallado una manera de calcular el campo cercano en planos perpendiculares a la dirección de colimado de la antena. El cálculo del campo cercano es más lento que el del campo lejano ya que no se puede usar la FFT, por lo que se ha presentado una estrategia para paralelizar su computación, acelerando los cálculos de simulación aprovechando los recursos disponibles en ordenadores modernos. El modelo de campo cercano presentado en esta tesis ha sido validado mediante simulaciones con software comercial y medidas.

Nuevas técnicas de síntesis con requisitos de contrapolar

El segundo bloque de la tesis está dedicado al desarrollo de técnicas eficientes de síntesis de reflectarrays con requisitos de contrapolar. Hasta ahora, la técnica predominante de síntesis solo trabajaba con requisitos de copolar por la dificultad de incluir un análisis fidedigno del elemento del reflectarray durante el proceso de síntesis. En primer lugar, se ha descrito una implementación eficiente del algoritmo Aproximación por Intersección para síntesis de solo fase (Intersection Approach for Phase-Only Synthesis, IA-POS). Este algoritmo se ha empleado extensamente en la literatura para la síntesis de reflectarrays con éxito. Es un algoritmo muy eficiente que es capaz de trabajar con reflectarrays de gran tamaño. Su eficiencia radica en el uso de la FFT para calcular el campo lejano y para recuperar el campo tangencial en la superficie del reflectarray. La síntesis de reflectarrays de gran tamaño se aborda con una reducción ficticia del número de variables modificando el táper de iluminación que produce el alimentador y realizando la síntesis en varias etapas, de forma que se reduce en las primeras etapas el número de mínimos locales para mejorar la convergencia. Sin embargo, al tratarse de un algoritmo para POS, solo trabaja con requisitos de diagramas copolar y no se puede controlar el nivel de contrapolar durante la síntesis. Este hecho motivó la búsqueda de un algoritmo eficiente para la síntesis de la componente contrapolar en reflectarrays. Partiendo del IA-POS, su formulación se generalizó para incluir requisitos de contrapolar durante el proceso de síntesis, obteniendo el algoritmo llamado IA-XP. Para ello, en lugar de trabajar con distribuciones de fases, ahora el algoritmo trabaja con distribuciones de matrices de coeficientes de reflexión, ya que esta matriz caracteriza por completo el comportamiento del elemento y tiene en cuenta la contribución del elemento al diagrama contrapolar. Al igual que el IA-POS, el IA-XP es muy eficiente computacionalmente, ya que emplea la FFT en ambos proyectores, aunque ahora se emplean el doble de FFT (por considerar también los diagramas contrapolares). Si el IA-XP se ejecuta sin restricciones sobre los coeficientes de reflexión, convergerá rápi-

damente a la solución deseada, aunque los coeficientes de reflexión no serán realizables por reflectarrays pasivos ya que no cumplirán con el balance de potencia. Debido a ello, se desarrolló una formulación para obtener las condiciones de realizabilidad de redes de dos puertos con pérdidas, para introducir las restricciones adecuadas en el algoritmo. De esta manera, la convergencia se hace algo más difícil, pero los coeficientes de reflexión obtenidos serán realizables por redes pasivas, incluyendo reflectarrays pasivos. El algoritmo fue validado con varios ejemplos, mostrando buenos resultados.

A pesar de haber desarrollado un algoritmo eficiente para la síntesis de contrapolar junto con restricciones adecuadas para obtener coeficientes realizables por redes pasivas, el algoritmo presenta una limitación importante. Se entenderá mejor si se compara con el IA-POS. La salida del IA-POS son dos distribuciones de fases, una por cada polarización. El diseño del reflectarray se obtiene ajustando la geometría de cada elemento de forma individual de forma que genere las dos fases requeridas. Esto es fácil de conseguir debido al buen comportamiento de las fases (casi lineales en el rango de diseño), también porque solo hay dos parámetros para ajustar por cada elemento del reflectarray, y finalmente porque las dimensiones ortogonales del elemento pueden ajustar, casi de forma independiente, cada fase requerida. Sin embargo, para el IA-XP, en lugar de dos parámetros reales para ajustar, hay cuatro parámetros complejos (o equivalentemente, ocho parámetros reales). Más aún, los coeficientes cruzados tienen un comportamiento altamente no lineal, por lo que encontrar un diseño de reflectarray que sea capaz de ajustar las matrices de coeficientes de reflexión requeridas es una tarea realmente difícil.

Otra opción consiste en una optimización directa de la geometría del reflectarray usando un análisis de onda completa basado en periodicidad local, Método de los Momentos (MoM) en este caso. Debido a la nueva capa añadida en el análisis del reflectarray, el IA no podía ser usado tal y como fue formulado para el IA-POS e IA-XP. Ahora, un algoritmo de optimización más general es necesario. Se escogió el algoritmo Levenberg-Marquardt (LMA) debido a su simplicidad, capacidad de trabajar con problemas no lineales y experiencia previa. Sin embargo, en lugar de afrontar directamente la optimización de la contrapolar con el LMA, primero se desarrolla una versión POS para estudiar el algoritmo e introducir una serie de mejoras para acelerar las computaciones del mismo. Este algoritmo se conoce como LMA-POS. Las mejoras introducidas en el algoritmo fueron la paralelización de la evaluación de la matriz Jacobiana; la minimización del error en las derivadas, que se calculan mediante diferencias finitas; elección de las librerías adecuadas para realizar multiplicaciones entre matrices y matrices y vectores; simplificación de la multiplicación de la matriz, puesto que solo es necesario calcular una parte triangular de la misma por ser el resultado simétrico; y elección del método de resolución de ecuaciones óptimo, basado en la descomposición de Cholesky debido a la naturaleza del problema, siendo el método exacto más rápido que existe para estos casos. Con estas mejoras, se consiguió acelerar considerablemente el LMA. Más aún, los resultados obtenidos mejoran otros de la literatura, además de obtener un algoritmo preciso y escalable.

El LMA-POS es posteriormente modificado para incluir la herramienta de análisis de reflectarrays en campo cercano. El nuevo objetivo fue la optimización de la zona quieta

generada por el reflectarray para su uso como sonda en sistemas de medida de rango compacto. Este tipo de optimización resulta más difícil de llevar a cabo, puesto que a diferencia de la optimización en campo lejano, donde solo se trabaja con la amplitud del campo, ahora hay que optimizar tanto la amplitud como la fase, de forma que cumplan con las especificaciones requeridas. Se llevaron a cabo dos ejemplos de validación, a 20 GHz y en bandas milimétricas a 100 GHz. En ambos casos, la limitación inicial en el tamaño de la zona quieta era el táper en amplitud, causado por la iluminación de la bocina en la superficie del reflectarray. Sin embargo, tras la optimización, la amplitud del campo cercano se consiguió aplanar, mejorando también en algunos casos el rizado de la fase.

El siguiente paso consiste en extender el LMA-POS para incluir MoM como herramienta de análisis con el objetivo de optimizar el diagrama de radiación contrapolar, obteniendo el algoritmo LMA-XP. A pesar de las mejores introducidas en el LMA-POS, incluir MoM en la optimización causa que el algoritmo se vuelva extremadamente lento y no sea práctico. Por ello, se han concebido e implementado estrategias para minimizar el impacto de MoM en el algoritmo. En primer lugar, se emplea una diferencia lateral en la implementación de la derivada por diferencias finitas, reduciendo a la mitad el número de llamadas a MoM. Además, al calcular cada columna de la matriz Jacobiana, solo se modifica un elemento, por lo que no hay necesidad de recalcular el campo tangencial procesando todos los elementos del reflectarray, sino solo uno, por lo que se puede reutilizar la matriz del campo tangencial de la primera llamada a la función de coste al inicio de cada iteración del LMA. Ya que el punto de inicio es muy importante en optimizadores locales, para validar el LMA-XP primero se lleva a cabo una POS de un diagrama LMDS, y después de obtener un diseño, el diagrama contrapolar se optimiza, reduciendo su valor máximo varios dB con el LMA-XP, validando el método propuesto. Sin embargo, el LMA-XP presenta ciertos problemas de convergencia cuando trabaja con reflectarrays muy grandes debido al alto número de variables a optimizar y a que la función de coste representa un espacio de búsqueda no convexo. Por este motivo, se decidió mejorar la convergencia del algoritmo siguiendo un camino diferente.

Para mejorar la convergencia del LMA-XP se decidió volver a usar el marco de optimización propuesto por el IA, que es más flexible y genérico. En particular, trabajando con el módulo del campo al cuadrado, en lugar de con el campo, se consigue aliviar el problema de los mínimos locales ya que uno de los conjuntos con los que se trabaja se convierte en convexo. Sin embargo, esto causa una redefinición de la proyección hacia atrás, que ahora implica la minimización de una distancia, implementada con un algoritmo de optimización general. Para aprovechar todo el trabajo desarrollado con el LMA, se ha escogido el LMA como proyector hacia atrás en el IA, obteniendo el IA-LMA-XP (una versión intermedia para POS se ha desarrollado y llamado IA-LMA-POS). El nuevo algoritmo mejora sustancialmente la convergencia del LMA-XP. Ahora, el IA-LMA-XP puede manejar decenas de miles de variables a optimizar y conseguir buenos resultados. Se propusieron dos ejemplos, uno con diagrama isoflux para cobertura global de la Tierra, y otro con una cobertura europea para aplicaciones DBS. En ambos casos el diagrama contrapolar se redujo varios dB conservando la forma del diagrama copolar, y en el caso del diagrama DBS se manejaron

más de 30 mil variables a optimizar. Aún así, los tiempos de computación empleando MoM en la optimización fueron aceptables en servidores de simulación. Además, el LMA-XP y el IA-LMA-XP se han comparado para evaluar la mejora en la convergencia, mostrando que el IA-LMA-XP proporciona mejores resultados en menos iteraciones.

Organización de la tesis

La tesis está dividida en seis capítulos. En el primer capítulo se incluyen la introducción; estado del arte en reflectarrays, incluyendo una revisión de distintos elementos reflectantes, análisis de onda completa, análisis del alimentador, cálculo del campo radiado y técnicas de síntesis de diagramas; enumeración de los objetivos de la tesis y organización de la misma.

En el capítulo dos se detalla extensamente el análisis de antenas de tipo reflectarray en configuración descentrada, con el fin de obtener tanto el campo lejano como el cercano. En el mismo se aborda el cálculo del campo incidente desde la bocina, análisis de los elementos, y cálculo eficiente de los diagramas de radiación tanto para reflectarrays periódicos como aperiódicos. Asimismo, se introduce un modelo de campo cercano para el cálculo de la zona quieta radiada por reflectarrays.

En el capítulo tres se abordan dos implementaciones eficientes del algoritmo Aproximación por Intersección, basadas en el uso de la FFT en ambos proyectores. La primera implementación, IA-POS, es la más utilizada para el diseño de reflectarrays, aunque solo trabaja con especificaciones de diagrama copolar. Posteriormente, se generaliza su formulación en el IA-XP para incluir requisitos de contrapolar, trabajando con la matriz de coeficientes de reflexión en lugar de con fases.

El capítulo cuatro está dedicado al estudio del algoritmo Levenberg-Marquardt (LMA) y a su implementación para POS. Se detallan varias optimizaciones del LMA-POS para acelerar sus tiempos de computación el máximo posible, con el objetivo de usarlo posteriormente junto con un análisis de onda completa para la optimización de la contrapolar.

El capítulo cinco aprovecha el trabajo desarrollado en el capítulo previo y extiende el LMA para la optimación de la contrapolar, obteniendo el LMA-XP. A pesar de que este algoritmo consigue optimizar bien el diagrama de radiación, presenta problemas de convergencia, por lo que se implementa un nuevo algoritmo, esta vez basado en el IA y utilizando el LMA en uno de sus proyectores para mejorar la convergencia. Se consigue un algoritmo, el IA-LMA-XP, que es capaz de manejar decenas de miles de variables a optimizar, mejorando el diagrama contrapolar varios dB en reflectarrays de gran tamaño.

Finalmente, en el capítulo seis se hallan las conclusiones finales, un resumen de las contribuciones originales de la tesis, una lista de las publicaciones relacionadas con la tesis, así como proyectos relacionados y las líneas futuras de investigación abiertas a partir del trabajo realizado en la tesis.

Conclusiones

Esta tesis se ha dedicado al desarrollo de técnicas eficientes y precisas para el análisis y síntesis de antenas de tipo reflectarray para campos lejano y cercano. Con respecto a la mejora de las técnicas de análisis, la eficiencia en el cálculo de los diagramas de radiación radica en el hecho de que se emplea el algoritmo FFT para el cálculo eficiente de las funciones espectrales, que es mucho más rápido que una evaluación directa de las ecuaciones. Además, la precisión se mejora considerando cada elemento como una pequeña apertura rectangular en lugar de una fuente isotrópica puntual. Sin embargo, este análisis solo estaba disponible en la literatura para reflectarrays periódicos, por lo que se ha desarrollado una formulación equivalente para el análisis eficiente de reflectarrays aperiódicos basada en el empleo de la NUFFT. La mejora en los tiempos de computación es patente debido a la escalabilidad del algoritmo NUFFT con respecto a una evaluación directa de las ecuaciones de las funciones espectrales. Esta mejora en el análisis de reflectarrays periódicos es adecuada para su inclusión en bucles de optimización, ya que podrá ahorrar considerables cantidades de tiempo, especialmente para reflectarrays de gran tamaño.

El análisis del reflectarray considera que el campo incidente es constante en la superficie de cada elemento (modelado como una pequeña apertura). Esta suposición es conveniente ya que facilita las operaciones analíticas con las ecuaciones. En esta tesis se ha desarrollado una generalización en la que se considera un campo incidente variable en la superficie de cada elemento, tanto para reflectarrays periódicos como aperiódicos. Dicha formulación sigue siendo eficiente ya que emplea la FFT/NUFFT, además de precisa por seguir modelando los elementos como pequeñas aperturas rectangulares, y eliminando la aproximación de tener el campo constante en toda la celda. Esta nueva formulación puede usarse para calcular con mayor precisión los diagramas de radiación de los reflectarrays, si bien su uso en bucles de optimización está restringido ya que un mayor número de llamadas a la FFT/NUFFT lo hace más lento que el descrito en el párrafo anterior.

Finalmente, se ha presentado un nuevo modelo de campo cercano para el análisis de reflectarrays. De nuevo, en lugar de modelar los elementos como fuentes puntuales, se modelan como aperturas rectangulares con campo constante. Luego, el campo cercano radiado por el reflectarray se calcula como contribución, en cada punto del espacio, de todos los campos lejanos radiados por los elementos del reflectarray. El objetivo de este análisis ha sido la predicción de la zona quieta generada por el reflectarray. Por ello, se ha detallado una manera de calcular el campo cercano en planos perpendiculares a la dirección de colimado de la antena. El cálculo del campo cercano es más lento que el campo lejano

ya que no se puede usar la FFT. Se ha presentado una estrategia para paralelizar su computación, acelerando los cálculos de simulación aprovechando los recursos disponibles en ordenadores actuales. El modelo de campo cercano presentado en esta tesis ha sido validado mediante simulaciones con software comercial y medidas.

El resto de la tesis está dedicada al desarrollo de técnicas eficientes de síntesis y optimización para mejorar la componente contrapolar de los campos lejanos radiados por un reflectarray. En primer lugar, se describió una implementación eficiente del algoritmo Aproximación por Intersección para síntesis solo fase, el IA-POS. Sin embargo, al tratarse de un algoritmo para POS, solo trabaja con requisitos de diagrama copolar y no se puede controlar el nivel de contrapolar durante la síntesis. Este hecho motivó la búsqueda de un algoritmo eficiente para la síntesis de la componente contrapolar en reflectarrays. Partiendo del IA-POS, su formulación se generalizó para incluir requisitos de contrapolar durante el proceso de síntesis, obteniendo el algoritmo llamado IA-XP. El nuevo algoritmo trabaja con distribuciones de matrices de coeficientes de reflexión en lugar de fases, ya que esta matriz caracteriza por completo el comportamiento del elemento y tiene en cuenta la contribución del elemento al diagrama contrapolar. Al igual que el IA-POS, el IA-XP es muy eficiente computacionalmente, ya que emplea la FFT en ambos proyectores. Además, se ha desarrollado una formulación para obtener las condiciones de realizabilidad de redes de dos puertos con pérdidas, con el objetivo de incluir dichas restricciones en el IA-XP. El algoritmo se ha validado con varios ejemplos, mostrando buenos resultados.

Otra alternativa consiste en una optimización directa de la geometría del reflectarray usando un análisis de onda completa basado en periodicidad local. Para ello, se empleará un algoritmo de optimización más general, el Levenberg-Marquardt (LMA) en este caso. Para ello, se desarrolla una versión POS, en la que se introducen una serie de mejoras en su implementación para acelerar los cálculos del mismo. Las mejoras introducidas en el algoritmo fueron la paralelización de la evaluación de la matriz Jacobiana; la minimización del error en las derivadas, que se calculan mediante diferencias finitas; elección de las librerías adecuadas para realizar multiplicaciones entre matrices y matrices y vectores; simplificación de la multiplicación de la matriz, puesto que solo es necesario calcular una parte triangular de la misma ya que el resultado es simétrico; y elección del método de resolución de ecuaciones óptimo, basado en la descomposición de Cholesky debido a la naturaleza del problema, siendo el método exacto más rápido que existe para estos casos. Con estas mejoras, se consigue acelerar considerablemente el LMA. Más aún, los resultados obtenidos mejoran otros de la literatura, además de obtener un algoritmo preciso y escalable.

El siguiente paso consiste en extender el LMA-POS para incluir MoM como herramienta de análisis con el objetivo de optimizar el diagrama de radiación contrapolar, obteniendo el algoritmo LMA-XP. Para hacerlo práctico, se introducen más mejoras con el objetivo de minimizar el impacto de MoM en los cálculos. En particular, se usa una diferencia lateral para evaluar las derivadas, reduciendo a la mitad el número de llamadas a MoM. Además, se reduce la complejidad computacional en la evaluación de la matriz Jacobiana procesando solo un elemento con MoM en el cálculo de cada columna de la matriz,

reduciendo sustancialmente los tiempos de optimización. Como validación, se reduce el diagrama contrapolar de un reflectarray con diagrama LMDS. Sin embargo, el LMA-XP presenta ciertos problemas de convergencia, por lo que se decide mejorar este aspecto del algoritmo.

Para mejorar la convergencia del LMA-XP se decide volver a usar el marco de optimización propuesto por el IA. En particular, trabajando con el módulo del campo al cuadrado se consigue aliviar el problema de los mínimos locales ya que uno de los conjuntos con los que se trabaja se convierte en convexo. Sin embargo, la definición de la proyección hacia atrás cambia, y ahora hay que usar un algoritmo de optimización general. Para aprovechar todo el trabajo desarrollado con el LMA, se escoge el LMA como proyector hacia atrás en el IA, obteniendo el IA-LMA-XP (una versión intermedia para POS fue desarrollada y llamada IA-LMA-POS). El nuevo algoritmo mejora sustancialmente la convergencia del LMA-XP. Se propusieron dos ejemplos de validación, uno con diagrama isoflux para cobertura global de la Tierra, y otro con una cobertura europea para aplicaciones DBS. En ambos casos el diagrama contrapolar se reduce varios dB conservando la forma del diagrama copolar, y en el caso del diagrama DBS se manejan más de 30 mil variables a optimizar. Aún así, los tiempos de computación empleando MoM en la optimización son aceptables en servidores de simulación. Además, el LMA-XP y el IA-LMA-XP se comparan para evaluar la mejora en la convergencia, mostrando que el IA-LMA-XP proporcionaba mejores resultados en menos iteraciones. Este algoritmo es susceptible de mejora, optimizando el diagrama en un cierto ancho de banda, a costa de tiempos de computación más lentos y mayor uso de memoria.

Contents

List of Figures

List of Tables

List of Symbols

Equivalent parabolic reflector

C	Clearance or offset distance of the equivalent parabolic reflector system.
D	Projected aperture of the equivalent parabolic reflector system.
F	Focal distance of the equivalent parabolic reflector system.

Reflectarray and feed parameters

$(a,\, b)$	Reflectarray periodicity in $\hat{x}_r$ axis (a) and in $\hat{y}_r$ axis (b).
$(\theta_0,\, \varphi_0)$	Radiation direction of the reflectarray in spherical coordinates expressed in the reflectarray coordinate system.
N, N_x, N_y	Number of physical elements of the reflectarray. $N = N_x \cdot N_y$ is the total number of reflctarray elements, while N_x and N_y are the elements in the $\hat{x}_r$ and $\hat{y}_r$ axis, respectively.
$(x_m,\, y_n)$	Coordinates of the center of the $(m,\, n)$th reflectarray element.
R^{mn}	Matrix of reflection coefficient for the $(m,\, n)$th reflectarray element. It is a 2×2 matrix of complex numbers that fully characterizes the behavior of the element. Usually computed with a full-wave technique, such as MoM.
$\rho_{xx},\, \rho_{yy}$	Direct reflection coefficients of R^{mn} matrix that mostly conform the copolar radiation pattern and add an important contribution to the crosspolar one.
$\rho_{xy},\, \rho_{yx}$	Cross reflection coefficients of R^{mn} matrix that introduce an important contribution to the crosspolar radiation pattern, although they are negligible in the computation of the copolar one.
$q,\, q_x,\, q_y$	Parameter which provides the directivity for the feed model, employed in the analysis of the reflectarray. When the feed has an axial symmetric

pattern, $q = q_x = q_y$. Otherwise, $q_x \neq q_y$. If q_x and q_y are similar, it is common to use an averaged q value of q_x and q_y.

Fields

M, M_u, M_v Number of points in the UV grid for the computation of the radiation patterns. $M = M_u \cdot M_v$ is the total number of points, while M_u and M_v are the points in the u and v axis, respectively.

k_0 Vacuum wavenumber, which is calculated as $k_0 = 2\pi f/c$, where f is the working frequency and c the speed of light in vacuum.

$\vec{E}^{X/Y}_{\text{inc},(x|y|z)}$ Incident electric field on the reflectarray surface from the feed. The superscript indicates the polarization of the feed regarding the FCS, while the subscript indicates the component of the field with regard to the RCS, which can be x, y or z.

$\vec{E}^{X/Y}_{\text{ref},(x|y|z)}$ Reflected electric field on the reflectarray surface. It is computed from the incident field and matrix R^{mn}. For an explanations of the super and subscript, see $\vec{E}^{X/Y}_{\text{inc},(x|y|z)}$.

$\vec{H}^{X/Y}_{\text{ref},(x|y|z)}$ Reflected magnetic field on the reflectarray surface. It is computed from the reflected electric field assuming a locally incident plane wave. For an explanations of the super and subscript, see $\vec{E}^{X/Y}_{\text{inc},(x|y|z)}$.

$P^{X/Y}_{x|y}$ Spectrum function of the electric field computed as the Fourier transform of the tangential electric field on the surface of the reflectarray.

$Q^{X/Y}_{x|y}$ Spectrum function of the magnetic field computed as the Fourier transform of the tangential magnetic field on the surface of the reflectarray.

$E^{X/Y}_{\theta|\varphi}$ Components of the far field radiated by the reflectarray in spherical coordinates.

$E^{X/Y}_{\text{cp|xp}}$ Copolar and crosspolar components of the far field according to Ludwig's third definition of crosspolarization.

$G^{X/Y}_{\text{cp|xp}}$ Copolar and crosspolar gain of the reflectarray. It is computed taking into account the feed total radiated power.

$D^{X/Y}_{\text{cp|xp}}$ Copolar and crosspolar directivity of the reflectarray.

Coordinate systems

$(\hat{x}, \hat{y}, \hat{z})$ Global Coordinate System (GCS), which is used as reference in the equivalent parabolic reflector system.

$(\hat{x}_f, \hat{y}_f, \hat{z}_f)$ Feed Coordinate System (FCS), which defines the polarization of the feed. If the feed is X-polarized, the electric field will be aligned with the $\hat{x}_f$ axis. The same for Y polarization.

$(\hat{x}_r,\, \hat{y}_r,\, \hat{z}_r)$ Reflectarray Coordinate System (RCS), which is placed in the center of the reflectarray with $\hat{z}_r$ perpendicular to its surface and $\hat{y}_r$ parallel to $\hat{y}$ of the Global Coordinate System.

$(\hat{x}_a,\, \hat{y}_a,\, \hat{z}_a)$ Pointing Coordinate System (PCS), which is equivalent to the Global Coordinate System, but shifted to the center of the reflectarray.

$(x_f,\, y_f,\, z_f)$ Feed coordinates in the reflectarray coordinate system $(\hat{x}_r, \hat{y}_r, \hat{z}_r)$.

Optimization algorithms

$\mathcal{O}(\cdot)$ Big O notation to specify the asymptotic behavior when the argument tends to a particular value or infinity.

$\mathcal{R}$ In the IA framework, set of radiation patterns that can be obtained with the reflectarray.

$\mathcal{M}$ In the IA framework, set of radiation patterns that comply with the requirements.

$\mathcal{F}$ In the IA framework, forward projection that projects a far field belonging to $\mathcal{R}$ onto the set $\mathcal{M}$.

$\mathcal{B}$ In the IA framework, backward projection that projects a far field belonging to $\mathcal{M}$ onto the set $\mathcal{R}$.

T Template which can be either expressed in field or gain in natural units. It gives the minimum and maximum specifications for the copolar and/or crosspolar pattern.

C_n In the IA framework, a constant to normalize the templates to the current field/gain value in an specified UV direction.

$F_t^{X/Y}$ In the LMA, residuals which are minimized by the algorithm.

$F^{X/Y}$ In the LMA, cost function which provides the total error.

J In the LMA, Jacobian matrix which is computed by means of finite differences using the residuals.

α In the LMA, array with the optimizing variables.

μ In the LMA, real positive number which controls the convergence of the algorithm.

s In the LMA, number of variables per element of the reflectarray which are being optimized.

L Total number available processors.

List of Abbreviations

CP *Copolar radiation pattern*, which is the desired far field component, being the non-desired one the crosspolar.

DFT *Discrete Fourier Transform*, is the transformation that converts a finite sequence of function samples into a list of coefficients finite combination of complex sinusoids. It can be efficiently computed by the FFT algorithm.

FCS *Feed Coordinate System*, defined by $(\hat{x}_f, \hat{y}_f, \hat{z}_f)$.

FF *Far Field*, field radiated by the reflectarray antenna in the region where it can be described in terms of a radial distance and azimuthal and polar angles, according to the *IEEE Standard Definitions of Terms for Radio Wave Propagation*.

FFT *Fast Fourier Transform*, is an algorithm used to efficiently compute the Fourier transform in a regular grid, which reduces the time complexity of this computation from $\mathcal{O}\left(M^{2d}\right)$ to $\mathcal{O}\left(M^d \log M\right)$, where M is the size of the problem and d its dimensionality.

GCS *Global Coordinate System*, defined by $(\hat{x}, \hat{y}, \hat{z})$.

IA *Intersection Approach*, an algorithm for the synthesis of antennas.

IA-LMA-XP *Intersection Approach using the LMA as backward projection for XP optimization*, and algorithm based on a general IA framework for the direct optimization of reflectarray antennas.

IA-POS *Intersection Approach for Phase-Only Synthesis*, a version of the IA algorithm adapted to perform phase-only synthesis.

IA-XP *Intersection Approach with XP requirements*, an efficient version of the IA algorithm to include crosspolar requirements, obtaining a distribution of reflection coefficient matrices.

LMA *Levenberg-Marquardt Algorithm*, used to solve non-linear least squares problems.

LMA-NF *Levenberg-Marquardt Algorithm for NF optimization*, a version of the LMA adapted to perform near field optimization.

LMA-XP *Levenberg-Marquardt Algorithm for XP optimization*, an extension of the LMA which optimizes the crosspolar component of the far field.

MoM *Method of Moments*, is a numerical computational method of solving linear partial differential equations which have been formulated as integral equations. It is used to analyze the reflectarray element in order to characterize its behavior by means of the reflection coefficients matrix.

NF *Near Field*, field radiated by the reflectarray antennas which cannot be considered at far field distance of the antenna.

NUFFT *Non-Uniform Fast Fourier Transform*, is an algorithm used to efficiently compute the Fourier transform in a non-uniform grid. It reduces the time complexity of this computation from $\mathcal{O}\left(M^{2d}\right)$ to $\mathcal{O}\left(M^d \log M + M^d \log^d 1/\xi\right)$, where M is the size of the problem, d its dimensionality and ξ the desired accuracy.

RCS *Reflectarray Coordinate System*, defined by ($\hat{x}_r$, $\hat{y}_r$, $\hat{z}_r$).

PCS *Pointing Coordinate System*, defined by ($\hat{x}_a$, $\hat{y}_a$, $\hat{z}_a$).

POS *Phase-Only Synthesis*, a technique for the synthesis of reflectarray radiation patterns based on the optimization of the direct reflection coefficient phases.

XP *Crosspolar radiation pattern*, which is the non-desired far field component, being the desired one the copolar.

CHAPTER 1

Introduction

1.1. Motivation

The constant development of communication systems has resulted in the need of systems which fulfill increasing tighter requirements in order to improve their quality. In particular, antennas are a very important subsystem in communication systems since they allow wireless communications. Depending on the application, different parameters can be optimized, such as efficiency, size, matching, radiation pattern, etc. Radiation pattern synthesis is important for both terrestrial and space applications, since non-canonical beam patterns are not easy to achieve. Furthermore, within antenna pattern synthesis, copolar shaped patterns are easier to obtain compared with the crosspolar far field optimization. Some applications that require shaped beams are central stations for Local Multipoint Distribution Service (LMDS), which present a sector beam in azimuth and a squared cosecant beam in elevation; global Earth coverage applications, which require an isoflux pattern providing constant energy flux on the surface of the Earth; and Direct Broadcast Satellite (DBS) applications, which require a shaped beam to fulfill a given footprint on the Earth surface. DBS applications are particularly challenging since they also require a high polarization purity, working with very large antennas. Traditionally, shaped parabolic reflector antennas have been used for this kind of applications. However, they are bulky and expensive. With the popularization of the microstrip technology, reflectarrays have become a potential substitute to parabolic reflector dishes, not only for satellite applications, but for any kind of application in which the use of parabolic reflector is common nowadays.

A reflectarray consists of a primary feed, typically a horn antenna, and an array of radiating elements, which add a certain phase-shift on the reflected wave. In principle, the concept of reflectarray is not associated to any particular technology. In fact, the first reflectarray antenna was proposed by Berry et al. [1] and the phase-shifter elements were short-ended waveguides of different length, resulting in a bulky and heavy structure with difficult practical applications [2]. Reflectarrays became really interesting with the development of printed antenna technology. In printed reflectarrays, the reflector is a

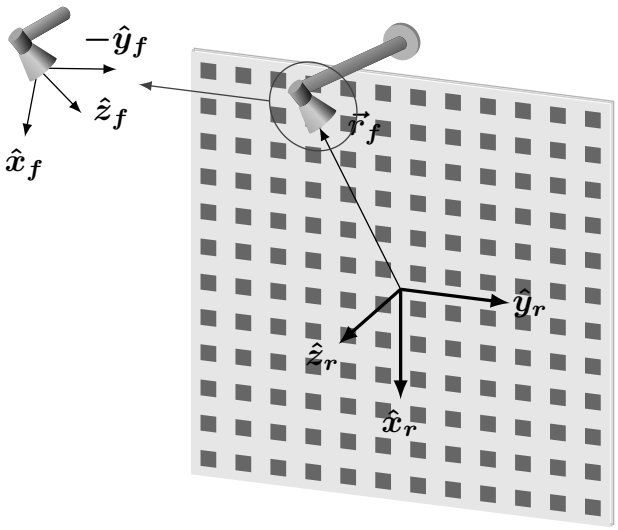

Figure 1.1: *Scheme of a general single-offset printed reflectarray.*

flat array of elements, such as printed patches, dipoles, slots rings, etc., that introduce a shift on the phase of the reflected field. By choosing the appropriate phase shift at each reflectarray element, a focused or shaped beam can be obtained.

Reflectarray antennas exhibit some characteristics that make them very interesting compared to parabolic reflectors or large phased array antennas. First, they are printed antennas and therefore they have a low profile. For this reason, reflectarrays are lighter and require less volume than parabolic reflectors. With regard to classic printed arrays, the complete reflectarray structure (reflector plus feed) certainly requires a larger volume than a planar phased array. Second, the losses depend on the quality (loss tangent) of the substrate and the geometry of the printed element, and they are significantly lower than those of a classic array, since the feeding network is not necessary. Using low-loss materials, the losses produced in a reflectarray are similar to those produced by a parabolic reflector. Third, the technology necessary to manufacture a reflectarray is the same photo-etching processes developed to produce printed circuits. This is a mature technology: well known, precise and relatively cheap.

Reflectarray antennas also have advantages in terms of costs, beam reconfigurability and mechanic characteristics. The main advantage of reflectarrays in cost terms is that the cost of producing a reflectarray is independent of the type of beam: pencil or shaped beam. Thus, reflectarray antennas present an important monetary advantage to shaped reflectors in space antennas, which are very expensive because of the cost of molds, which cannot be reused for different missions. Another important advantage in space applications is the fact that, having a flat profile, is relatively simple to fold the antenna for the transportation in the spacecraft and deployment in space [3–6]. Also, inflatable reflectarrays have been developed by printing the patches on flexible thin substrates [7], as well as transportable reflectarrays for satellite emergency communications [8].

The main drawback of printed reflectarrays is they inherent narrow bandwidth, mainly due to two factors, namely the poor bandwidth of narrowband resonant elements, which is usually around 3%-5% and the differential spatial phase delay [9, 10]. The first

issue is solved by employing wideband printed elements which introduce several resonances [11–13]. The second issue can be solved by properly adjusting the geometry of the reflectarray element at one or several frequencies [11], using true time delay reflectarray elements [14], increasing the $^{f}/_{D}$ ratio [10] or using curved [15, 16] or faceted [17, 18] reflectarrays.

Another drawback is in the synthesis of shaped-beam reflectarrays for applications with tight crosspolar requirements, such as space DBS missions. The predominant technique in reflectarray synthesis is the phase-only synthesis, which can be carried out using a number of algorithms. It is based on a simplified analysis of the reflectarray antennas which is suitable only for copolar pattern synthesis. This technique has provided very good results in the past [2, 19–22]. However, since it is aimed to copolar pattern synthesis, there is no control over the crosspolar component. Some techniques have been developed in order to reduce the crosspolar pattern but their usefulness is limited. Only recently there have been serious efforts to effectively reduce the crosspolar component during the synthesis process, and they will be reviewed in a following section.

This thesis proposes new techniques for the analysis and synthesis of reflectarray antennas. Special effort is made in the efficiency of those techniques. In particular, the analysis techniques focus on an accurate and fast method of computation of the spectrum functions, needed in the computation of the far fields. The efficiency lies on the use of fast algorithms such as the Fast Fourier Transform (FFT) and the Non-Uniform FFT (NUFFT). Also, the use of the First Principle of Equivalence and the modeling of the reflectarray dielectric frame provide further accuracy in the characterization of the copolar and crosspolar far fields. On the other hand, new techniques are proposed for the copolar and crosspolar optimization of reflectarray antennas as well as near field optimizations, which take advantage of the improvements in the reflectarray analysis.

Reflectarray antennas are subject of many research projects worldwide, which demonstrate their potential for many applications, with the powerful performances of conformal parabolic reflectors and the flexibility of microstrip technology. In particular, the research carried out during this thesis is framed within several projects ranging a number of applications. *"Innovative Reconfigurable Systems based on Liquid Crystals"*, with code 1-6419/10/NL/JK is a European Space Agency (ESA) funded project which aims to develop reconfigurable antennas based on liquid crystal technology. The Ministerio de Economía y Competitividad, belonging to the Spanish Goverment, has funded two research projects related to imaging applications, *"Técnicas de imaging mediante problema inverso de dispersión: nuevos algoritmos y técnicas de medida (iScat)"*, with code TEC2011-24492; and *"Múltiples fuentes de información para mejorar técnicas de EM inverso para aplicaciones de reflectometría e imaging (MIRIIEM)"*, with code TEC2014-54005-P; for which reflectarray antennas can be employed working within near field distances. Finally, another ESA funded project is *"Reflectarray Antennas with Improved Performances And Design Techniques (RAIPAD)"*, with code 1-7064/12/NL/MH, which aims to develop new techniques for the analysis and synthesis of reflectarray antennas, in particular, for the crosspolar optimization.

1.2. State of the art

In this section, a review of the state of the art on reflectarray antennas will be presented. There are many aspects that can be reviewed, but only those directly related with the work developed in this thesis will be mentioned. They include the elements of which the reflectarray is made up; efficient full-wave techniques to analyze those elements; some techniques to analyze the reflectarray, including the feed and ways of computing the radiation patterns; and finally, algorithms for reflectarray synthesis and crosspolar optimization.

The reflectarray antenna was first introduced in 1963 by Berry, Malech and Kennedy [1] and it consisted of an array of short-ended waveguides of variable length which reradiated the incident field. The variable length allowed to obtain different phase shifts, allowing to tilt the beam. However, this first prototype was bulky and heavy, hence not being practical. In the 1970s a reflectarray was developed consisting of four arms with spiral shape, known as spiraphase reflectarray [23]. Switching diodes were used to electronically scan the main beam. However, it was not until the 1980s, with the popularization of the microscrip technology, that the reflectarrays were investigated with more depth.

1.2.1. Reflectarray elements

The performances of printed reflectarrays, such as bandwidth, crosspolarization, dissipative losses, etc., depend strongly on the elements used to produce the phase-shift. Reflectarray elements comprise one of the most fruitful research topics and there are many proposed elements for reflectarray design, although only some of them will be mentioned. A few examples are shown in Figure 1.2. One of the classical elements used to produce the required phase-shift is microstrip patches with unequal lengths of microstrip transmission lines attached [24]. This element introduces a phase-shift proportional to the length of the stub, but two drawbacks are found. The first one is the high crosspolar radiation produced by the elements because of the spurious radiation of the bent stubs. However, it can be compensated by changing the bending direction of the stubs [25].

One of the most widely used phase-shift concepts of microstrip reflectarrays is the adjustment of resonant length in dipoles for single linear polarized reflectarrays [26, 27], crossed dipoles for dual polarization [28] or the sizes of rectangular patches [22, 29, 30]. These elements produce lower dissipative losses and crosspolarization than the patches with stubs. Other elements are apertures of different length on a metal plane [31], elements with variable rotation angles [32], spiraphase-type reflectarrays based on loaded ring slot resonators [23], and other configurations. Some of the concepts, such as spiraphase and elements with variable rotation angles are only valid for circular polarisation and a narrow frequency band operation. Actually, most of these concepts suffer from the limitation of a narrow band imposed by the bandwidth of the radiating element. Practical designs of reflectarrays need a full 360° phase cycle, which those elements are not able to provide, and along with the strongly non-linear behavior of the phase, limit the frequency band of operation.

One of the most used reflectarray elements is the rectangular patch of variable size [29].

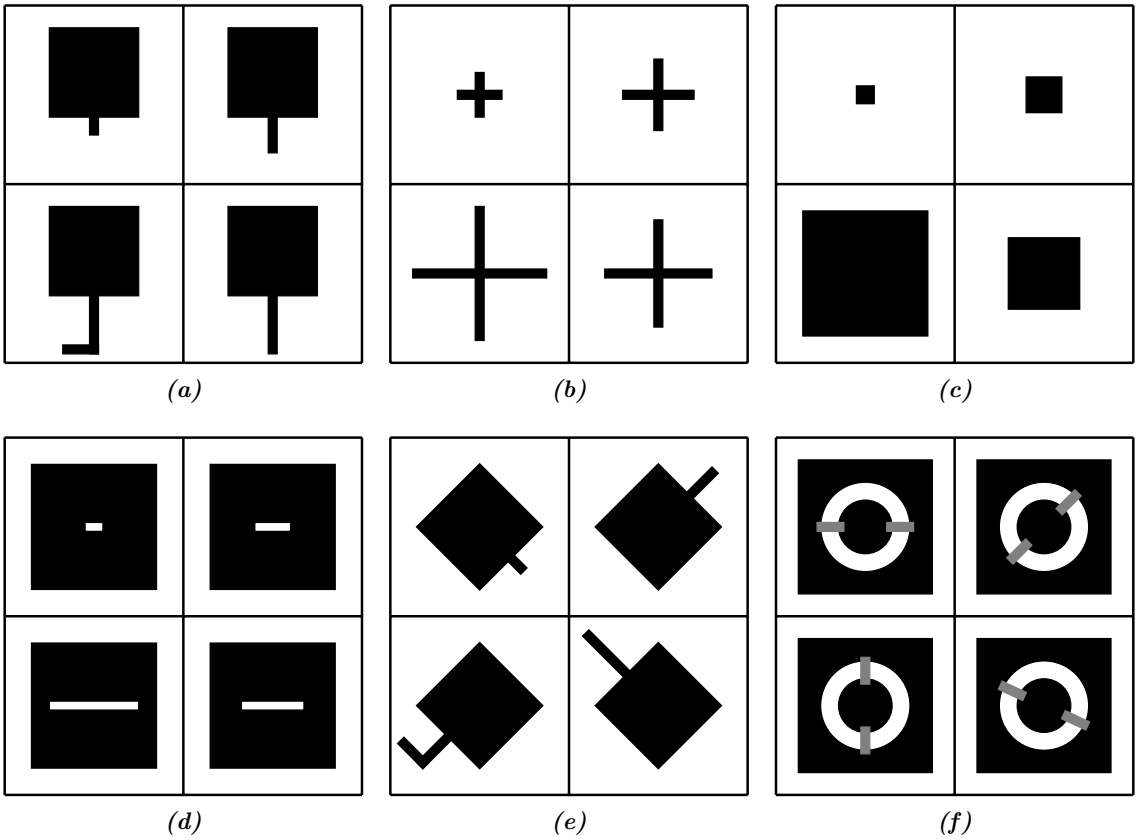

Figure 1.2: *Several phase-shift elements. (a) Squared patches loaded with stubs. (b) Crossed dipoles. (c) Patches. (d) Patches with slot. (e) Rotated patches with stubs. (f) Loaded ring slot resonators.*

It is a resonant element whose size is approximately half wavelength in the substrate. A small change in its size produces a wide phase shift. Also, the amplitude of the reflection coefficient must be nearly equal to one, provided that there is no grating lobe or surface wave generation, due to the ground plane. A small reduction in the amplitude is only produced by the dissipative losses in the dielectric substrate and on the metal patches. However, the maximum range of phase variation that can be achieved is in the order of 330° for substrates that are very thin, for thickness smaller than tenth a wavelength [2]. However, the phase variation with regard to the patch size is strongly non-linear, which can be smoothed by using thicker substrates, at the cost of reducing the total phase range. A broadband element, with smooth phase variation in ranges larger than 360° can be obtained by stacking two or three layers of rectangular patches [11, 33–35]. Four or more layers are not used because the phase curve would be too steep, and it would be too sensitive to manufacture tolerances, since a small error in the patch length would cause a very large variation in the phase-shift. For a good bandwidth of the radiating element, the phase curves at different frequencies should be parallel, so when frequency changes, only a small constant is added to the phase distribution. Dual-polarized reflectarrays are easy to design with this topology, since each polarization is controlled by one dimension of the patches [2]. However, there is certain coupling between both linear polarizations,

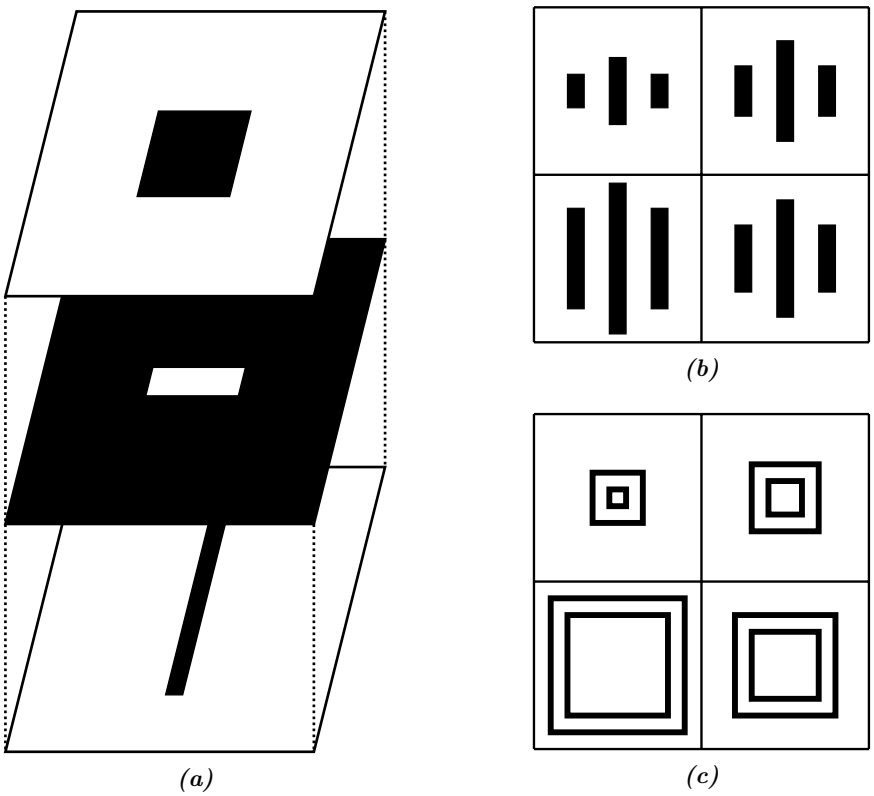

Figure 1.3: *Some broadband reflectarray elements. (a) Patch coupled to a delay line. (b) Parallel dipoles. (c) Concentric square rings.*

and the design process should take this fact into account [2, 19, 20].

Some broadband reflectarray elements are shown in Figure 1.3. The aperture coupled reflectarray element has been demonstrated to be broadband since the delay line can be very long [36–38]. However, this configuration introduce more dissipative losses because of the length of the delay line. Also, a good design is more complicated, since apart from obtaining the appropriate stub length to match the required phase-shift, the stub must be well matched to the impedance of the radiating patch to allow the transmission of the power to the delay line (stub) [2]. A variation of this topology was presented in [39] using a cut-ring patch coupled to a delay line, presenting similar performances to the coupled patch, and the same inconveniences.

More recently, modifications of the dipole element were presented, using three [40] and five [41] parallel dipoles to increase the phase shift range overcoming the bandwidth limitation. Although these elements present the advantage of having just one layer, they are only capable of working in one polarization. This issue was overcome in [42], where two orthogonal sets of three parallel dipoles were used as unit cell. It increased the complexity of the cell by adding an extra layer, but now it can work in dual-polarization. Moreover, with regard to the topology of stacked patches, the new cell improved the coupling isolation between polarizations and introduced less crosspolarization. This cell was improved in [43], where three modifications were studied, with the aim of improving the cell performance. First, the same cell as in [42] was studied but this time with five dipoles instead of three

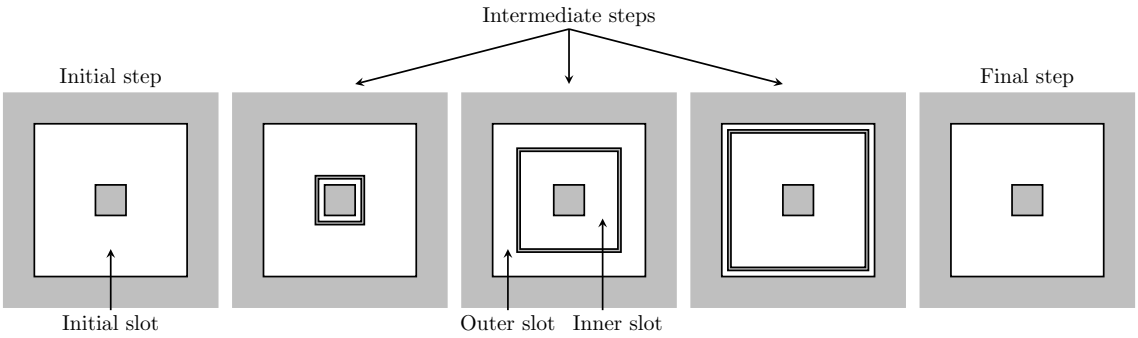

Figure 1.4: *Evolution of the original Phoenix cell geometry over a complete 360˚ cycle.*

in each layer. It turned out that this cell did not improve significantly the results over the cell with three dipoles in each set. In order to obtain more resonances to increase the phase range, a four layer reflectarray element, combining laterally coupled parallel dipoles with dipoles in stacked configuration was presented, while keeping an independent phase control for each polarization. This cell provided excellent results in phase range, polarization independence and crosspolarization level. However, due to the four levels of metallization, complexity and thus manufacturing cost increase. This last cell design was modified to reduce the number of layers from four to two by shifting half-a-period the set of dipoles associated to one polarization, and by printing on the same surface three parallel dipoles for one polarization and one dipole for the orthogonal polarization. This new cell reduces the complexity while maintaining the same performance as the four-layered cell. As a drawback, care is needed to avoid overlapping of orthogonal dipoles in the same layer when doing reflectarray design or optimization.

Other broadband elements are proposed as reflectarray unit cells with only one layer. They are based on concentric topologies that introduce several resonances increasing the phase range employing only one layer with metallizations. They present some disadvantages with the cells based on parallel coplanar dipoles. The first one is that even though the number of layers is reduced from two to one, the metallization geometry is more complex. Also, the coupling isolation between the two polarizations is not as good. One of this new cells was presented in [13] and is known as the Phoenix cell, since it presents a rebirth capability, i.e., its geometry cycle is reset after an almost 360° phase cycle has been achieved, as it can be seen in Figure 1.4. This ensures a very smooth geometrical variation in the reflectarray design. Some modifications were proposed to the Phoenix cell in order to reduce its size and improve the phase response linearity [44, 45].

Other single-layer reflectarray elements include a quasi-spiral phase delay line with the capability of operating in linear or circular polarization depending on the polarization of the incident wavefront, and able to produce around 1000° of phase delay [46]; concentric hexagonal rings [47]; double square rings and double cross loops [48]; circular patch with a curved stub which is able to provide more than 1000° linear phase range and low crosspolarization [49] using an element arrangement similar to the one shown in [25]; among others.

1.2.2. Full-wave reflectarray analysis based on local periodicity

A printed reflectarray can be analyzed through different numerical methods. However, the complexity of the problem makes the full-wave analysis of the whole structure usually unaffordable and reflectarrays are commonly analyzed by considering local periodicity [29, 50], so that the analysis is carried out element by element, each reflectarray cell being considered in a periodic environment comprised of the same cell, using the Floquet Theorem. There are commercial software packages that employ different techniques to perform the full-wave analysis of such periodic structures. In particular, the Finite Element Method (FEM) is used by HFSS [51], the Method of Moments (MoM) by FEKO [52] and the Finite-Difference Time-Domain (FDTD) method by CST [53]. However, the FDTD method might not be suitable since the reflectarray elements are usually resonant. Since these commercial software packages are aimed to serve as multipurpose software to solve electromagnetic problems, there are faster approaches to the analysis of reflectarray antennas, such as the development of homemade software specially tailored at analyzing unit cells.

An efficient, homemade implementation of MoM in spectral domain for multilayer periodic structures [54] was used for the analysis and design of reflectarrays based on two and three layers of varying-sized patches, as described in [33, 34]. This technique is very accurate, as it was demonstrated by the design, manufacture and test of several reflectarrays [2, 5, 19, 20]. The local periodicity approach provides accurate results when the variation of the patch dimensions in the reflectarray is smooth, because all mutual couplings are taken into account under the assumption that all the neighboring elements are identical.

Several full-wave techniques based on MoM have been developed and applied to the analysis of reflectarrays [55–58]. In these techniques, the complete reflectarrays is electromagnetically modeled with the real dimensions of all the elements, and therefore the mutual coupling is computed without approximations. These techniques can provide more accurate results, but they are much more time-consuming than those based on local periodicity. Hence, they cannot be implemented in design or optimization loops for reflectarray design or synthesis. However, they can be used for a more accurate analysis after the design has been completed, in order to find out whether a further refinement of the design is required.

Another common method for the reflectarray analysis used in the literature is the use of lookup tables or databases [59–62]: tables that give the phase of the reflection coefficient as a function of the element dimensions. These tables are generated using full-wave analysis tools, either commercial or handmade, and thus can be slow to generate, since many combinations of the element dimensions need to be taken into account, including combinations that might not be used in the design. However, once the table has been generated for a given frequency, substrate and element topology, the design process is very fast. In order to correctly generate a database, the angles of incidence need to be taken into account, increasing by two the number of variables (and the number of combinations grow exponentially with the number of variables), since the reflection coefficients

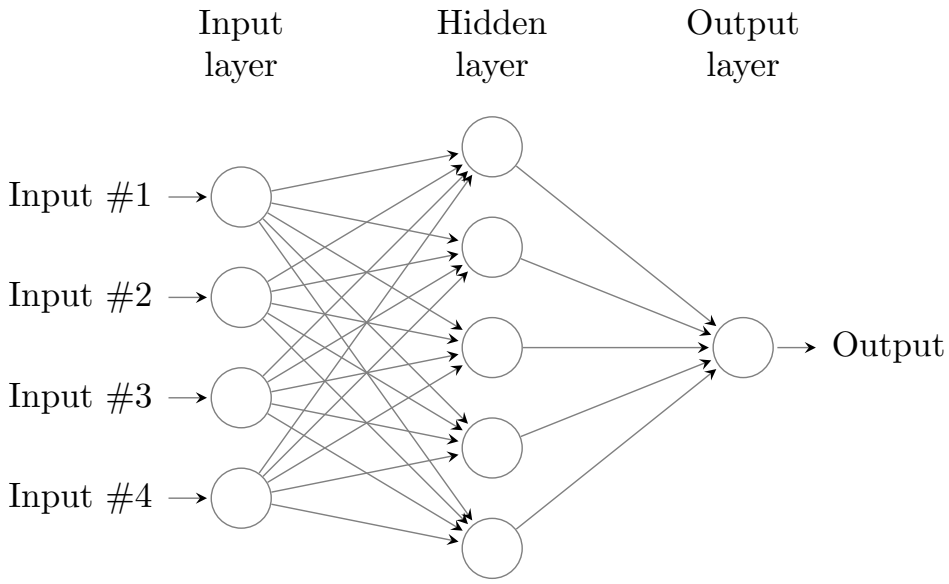

Figure 1.5: *Basic structure of an ANN for modeling reflectarray elements.*

change with the incidence angle [2]. The common practice of considering only the normal incidence might lead to inaccurate analysis and designs. As a drawback, the tables must be regenerated when the substrate, frequency and/or cell topology is changed. Also, some approximation needs to be used when accessing the tables, since not all combinations are possible to store (it would required infinite computing times and memory usage). The closest combination can be used, or some kind of interpolation, which can cause some inaccuracies.

The use of Artificial Neural Networks to analyze reflectarrays is an alternative to the use of lookup tables and databases for a fast analysis. Instead of generating a table, the ANN produces a model of the reflectarray element, which potentially can improve the results of the tables [63]. However, most works in the literature focus on the phase modeling [64–68], which is only useful for the copolar pattern prediction. A recent work [69] has proved that the ANN is able to model the full reflection coefficient matrix, although the results are still preliminary. The use of Support Vector Machines (SVM) [70] remain uncharted for the reflectarray element modeling. They have the potential to improve the ANN performances, obtaining better results with smaller training sets, overcoming some of the problems of the ANN, such as overfitting [71, 72].

The convenience of having a homemade full-wave analysis tool based on local periodicity tailored for the analysis of periodic structures has made possible to efficiently analyze, design and optimize reflectarray antennas [2]. A number of techniques for this analysis have been reported in the literature based on MoM [54, 73–77]. Some of these techniques are flexible and can be applied to a number of periodic structures with different number of layers, such as the one developed in [54]. Even though this implementation is faster than other multipurpose full-wave simulators, it can be sped up at the cost of loosing flexibility. In [76, 77] a faster technique is developed, which improves the analysis time between one and two orders of magnitude with regard to others in the literature.

1.2.3. Incident and radiated fields

For a proper analysis of reflectarray antennas, not only the elements have to be accurately characterized by means of a full-wave technique; the feed and radiation patterns computation also play a role in the correct characterization of the radiated far fields.

The feed pattern can be approximated by a far field ideal model, i.e. a $\cos^q \theta$ function or a Gaussian beam [78,79]. These models have been demonstrated to be useful for modeling the main beam of horn antennas and they are used to compute the incident field on the reflectarray surface. They are widely used since they have several parameters that permit to determine the characteristics that should be achieved by the actual feed. The calculation of the impinging wave phase from the feed is based on the concept of the antenna phase center and the distance from it to the center of the reflectarray element. Although the phase center is different for the E and H planes of the feed, an intermediate value can be taken for the analysis of the reflectarray. Thus, in many practical configurations, the focal distance is defined in the design process so that the reflectarray is in the far field zone of the feed and the ideal far field model is valid [2]. However, in some configurations, the far field approximation is inappropriate because the reflectarray elements are placed on the Fresnel zone of the primary feed, as for example, when the reflectarray is fed by a high gain feed, or in the case of dual-reflector configuration using a reflectarray as subreflector [80,81]. In those cases, the real near field of the primary feed can be used to improve the results [82]. Also, the aperture efficiency can be improved by tailoring the design of the feed antenna [83]. In [84] a semi-analytical method is proposed to compute the incident field on the entire plane that contains the reflectarray using a discrete plane-wave expansion. It can be used for any arbitrary excitation and improves the results of [82], but it is computationally more expensive.

Since the reflectarray is an aperture, its radiation patterns can be calculated using the Equivalence Principles [2]. The most time consuming operation is the computation of the spectrum functions, which are calculated as the Fourier transforms of the tangential field on the aperture [85]. For regular grids, this operation can be efficiently performed using the Fast Fourier Transform (FFT) [2], modeling each reflectarray element as a small aperture instead of a punctual source, which is more accurate. However, for the aperiodic case the element is considered a punctual isotropic source, since only the array factor is taken into account [86,87]. When the reflectarray element is modeled as a small aperture, the field at each cell is considered constant, which is convenient because it facilitates operating with the equations. Little research has been carried out considering a continuous incident field in an efficient fashion.

Finally, it is very common to compute the reflectarray far fields using the Second Principle of Equivalence [2], which only considers the electric field on the reflectarray surface. However, it has been demonstrated [43,88] that the First Principle is more suitable for both the copolar and crosspolar patterns prediction. The First Principle of Equivalence uses both the electric and magnetic fields on the reflectarray surface, and thus the number of spectrum functions to evaluate is double with regard to the Second Principle. However, all of them can be efficiently computed by means of the FFT algorithm, and the increased

computational effort is acceptable.

1.2.4. Reflectarray pattern synthesis

The antenna synthesis problem can be viewed as the inverse of the analysis problem. In the analysis problem, given the antenna full structure, the radiated field is obtained. Conversely, in the antenna synthesis, given a set of field specifications, the antenna geometry is sought so that it fulfills the specified requirements. Although in a very general case any aspect of the antenna is suitable to be optimized in the synthesis process, such as its structure, feed system, etc., and there are algorithms that are able to deal with this generalized problem [89], it is more common to work with a simplified case, in which the antenna structure and feed system are fixed and known beforehand.

The most common technique for the synthesis of shaped-beam reflectarrays is known as Phase-Only Synthesis (POS). Since the phases of the direct reflection coefficients directly control the shape of the copolar pattern, the POS only works with these phases, enormously simplifying the reflectarray analysis. Despite all the simplifications, this technique is able to provide accurate results and achieve very complex shaped-beams. The main disadvantage is that it only works with the copolar patterns, and there is no control over the crosspolar ones during the synthesis process.

In order to achieve the required specifications, a number of algorithms has been used to synthesize the radiation patterns in the POS case, for instance, analytical [90,91], steepest descent [92], conjugate gradient [93], Intersection Approach (IA) [94, 95], Levenberg-Marquardt Algorithm (LMA) [96,97], genetic algorithms [98] or particle swarm optimization [21, 99], among others. However, the analytical approaches have limitations when applied to complex shaped patterns, although they can be used to generate a starting point for a more powerful synthesis algorithm [81]. The steepest descent has a very slow convergence rate [100,101], which makes it impractical to synthesize arrays with a moderate number of elements. Conjugate gradient methods can be adapted to solve non-linear optimization problems and are faster than the steepest descent [100], but they tend to be both less efficient and less robust than quasi-Newton methods [101]. The intersection approach is very efficient when using only the FFT, but suffers from the problem of traps (i.e. local minima), due to the non-convexity of the sets dealt with [89]. One manner of dealing with the trap problem is working with the far field squared amplitude instead of just the amplitude or complex field [89, 102]. However, this approach causes that one of the projectors of the intersection approach cannot be implemented with the FFT (the projector which recovers the reflected field on the reflectarray surface), and a minimization algorithm based on optimization techniques has to be used, greatly reducing the efficiency of the intersection approach algorithm (in [102], the Broyden-Fletcher-Goldfarb-Shanno (BFGS) algorithm is used, although other algorithms are also suitable, such as the LMA). The LMA, has high memory requirements, due to the fact that it needs to store a Jacobian and Hessian approximation matrices, which can limit its usage when optimizing large antennas. Also, some expensive operations, such as a big matrix multiplication, needs to be performed, slowing the computations. This operation may be avoided by using a QR

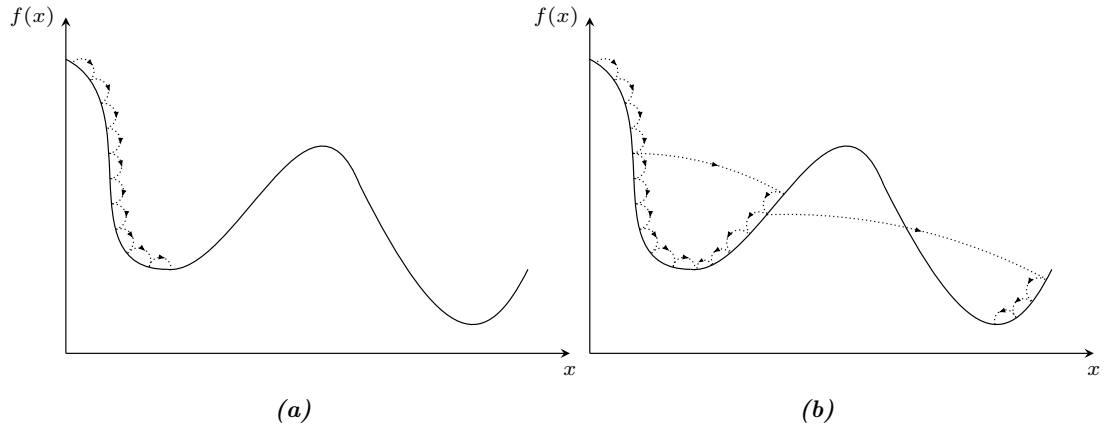

Figure 1.6: *Local vs. global search with the same starting point. (a) Local search finds a local minimum. (b) Global search finds global minimum after a more exhaustive and time consuming exploration.*

factorization, at the expense of more memory usage [100]. All these algorithms are local optimizers and depend strongly on the starting point to converge with success.

Genetic algorithms (GA) and particle swarm optimization (PSO) are global search algorithms, which in contrast with the previous local search algorithms, do not depend on the starting point. These algorithms are potentially able to find the global maximum at the expense of taking many iterations. However, as the number of variables increase, the search space size grows exponentially, making it harder for these algorithms to find a suitable solution. Another aspect of evolutionary algorithms is that due to their non-deterministic approach, two instances using the same parameters will yield different results, in contrast with the deterministic approach of the local optimizers mentioned above. GA and PSO have been demonstrated capable of synthesizing phased arrays, although at the cost of several thousand iterations [103]. Each iteration involves several evaluations of the cost function, one for each member of the population, thus making their computing times very sensitive to the to the time cost of the cost function (also known as fitness in evolutionary algorithm terms). Both algorithms seem to have similar performance with small arrays, although PSO is easier to implement [103]. Recently, the PSO has been used to synthesize several reflectarray radiation patterns [21,99]. In [21], a single-fed reflectarray of 848 elements with asymmetric multiple beams was synthesized, taking more than 70 000 iterations to converge and 44 hours. In [99], a reflectarray of 900 elements was synthesized, taking 5500 iterations to converge. Increasing the size of the antenna would dramatically increase computing times to achieve convergence with these algorithms because of their global search approach, unless a suitable starting point was used and the PSO was set up to prioritize local search.

Other global search algorithms, less common in antenna synthesis than the two algorithms mentioned above, are the differential evolution [104, 105], ant colony optimization [106, 107], firefly algorithm [108], bacterial foraging optimization [109, 110], biogeography based optimization [111] and the Taguchi method [112], among others.

Regarding memory usage, the LMA presents a disadvantage with regard to other syn-

thesis algorithms. The LMA needs to store a Jacobian matrix, which is generally bigger than the Hessian matrix (or its approximation) used by Newton and quasi-Newton methods. Additionally, the LMA also needs to store the approximation of the Hessian. In contrast, the conjugate gradient only needs to store a smaller matrix (same size as the Hessian) and a few vectors, while the steepest descent only stores vectors. The intersection approach uses one to four small matrices with dimension the number of samples of the radiation pattern. (When an optimization algorithm is introduced in the intersection approach, the storage needs would be the same as the ones of the optimization algorithm plus the needs of the intersection approach.) Evolutionary algorithms, such as GA or PSO, store one solution per member of the population. In the phase-only synthesis case, the solution is a vector or matrix with the number of elements equal to the number of unknowns. Exact storage needs for the mentioned algorithms will vary according to their implementations, although they have been roughly laid out for the main data structures. The LMA trades more memory usage for a more robust algorithm for non-linear optimization when compared with other gradient methods, and a less powerful framework when compared with the intersection approach. The LMA is also simpler and easier to implement than other quasi-Newton methods, and is faster than evolutionary algorithms due to its local search nature.

As an example, a reflectarray of $N_x \times N_y$ elements (which correspond to the unknowns of the problem) is considered, computing the radiation pattern only for one polarization in a grid with $M_u \times M_v$ points. The evolutionary algorithms are considered to have L members in their population. Note that, in general, $N_x \cdot N_y \leq M_u \cdot M_v$. In this case, the size of the Jacobian matrix is $N_x \cdot N_y \cdot M_u \cdot M_v$, the size of the Hessian or its approximation is $N_x^2 \cdot N_y^2$ and the size of a solution is $N_x \cdot N_y$. Then, the memory usage is $\mathcal{O}(N_x \cdot N_y \cdot M_u \cdot M_v + N_x^2 \cdot N_y^2)$ for the LMA, corresponding to the Jacobian and approximation of the Hessian; $\mathcal{O}(N_x^2 \cdot N_y^2)$ for quasi-Newton methods and the conjugate gradient, corresponding to the Hessian or its approximation; $\mathcal{O}(N_x \cdot N_y + M_u \cdot M_v)$ for the intersection approach, corresponding to a solution and the computed far field; and $\mathcal{O}(L \cdot N_x \cdot N_y + L \cdot M_u \cdot M_v)$ for the GA and PSO, corresponding to one solution and one computed far field per member of the population. Auxiliary vectors and matrices might be used depending on the implementation, but the main data structures shown above take up most of the memory used by the algorithm.

As stated before, the POS technique has demonstrated to be very effective in the design of reflectarrays that fulfill very stringent requirements, for instance [19,20]. However, since it is a POS, it has no control over the crosspolar far fields during the synthesis process. Some techniques for lowering the crosspolarization of reflectarrays have been described which rely on positioning the elements in certain configurations [113] or by adjusting the elements dimensions forcing a null in the amplitude and a change of sign in the phase of the crosspolar reflection coefficients [114, 115]. However, these techniques present limitations and are not flexible, since they only try to reduce the contribution of the cross-coefficients after the synthesis is done, instead of synthesizing the crosspolar pattern to a desired value. This latter approach was followed in [116–118], where the Intersection Approach is

used along with the Broyden-Fletcher-Goldfarb-Shanno (BFGS) optimization algorithm as backward projector. However, only single-polarized reflectarrays were considered with very few elements (225 in total) since the algorithm was slow. More recently, some works have appeared that deal with dual-polarized reflectarrays with crosspolar constraints. For instance, in [17], a faceted dual-polarized reflectarray with crosspolar suppression is presented, where after a POS pattern is obtained, the crosspolar component is suppressed and the currents on the surface of the reflectarray are obtained. From there, the matrix of reflection coefficients are computed, which fully characterize the reflectarray element. Finally, in [119–121] a general optimization technique for printed reflectarrays is presented and used, which employs a gradient minimax algorithm for the direct optimization of the reflectarray geometry. It allows to synthesize both copolar and crosspolar components using several degrees of freedom. Nevertheless, it uses a look-up table of scattering parameters to speed up computations during the optimization process, which needs to be generated for each substrate and unit cell. However, as the number of optimizing variables is increased, the times required to generate the table rapidly increase as well. Furthermore, to create the table some variables which are not needed during the optimization process (i.e. they are not optimized) are considered, such as the pair of incident angles, since for a given reflectarray geometry, varying the incident angle can modify the reflection coefficients. Also, because interpolation is used to calculate the scattering parameters from the look-up table, precision is lost, which is essential for the crosspolar optimization, since its behavior is highly non-linear and its absolute values are very low with regard to those of the copolar component.

1.3. Thesis goals

This thesis is devoted to the analysis and synthesis of reflectarray antennas in single-offset configurations. The goals are divided in three blocks: the development of efficient techniques for reflectarray analysis, the improvement of the synthesis of the copolar far field component, and the development of efficient algorithms for the reflectarray crosspolar optimization.

The reflectarray analysis can be divided in a number of steps, including the analysis of the feed, the reflectarray element and the computation of radiation patterns. Each one of these subanalyses can be independently improved to speed up computations and obtain higher numerical accuracy. With regard to the computation of radiation patterns, efficient and accurate techniques are available for periodic reflectarrays. The efficiency lies in the use of the FFT algorithm for the computation of the spectrum functions, and the accuracy in the consideration of the reflectarray element as a small aperture instead of a punctual source. However, for aperiodic reflectarrays there is no such technique that includes both considerations. If the NUFFT were used, the reflectarray elements can be only be analyzed as punctual sources. Conversely, if they were analyzed as small apertures, a direct evaluation of the spectrum functions would need to be implemented, since the NUFFT cannot be directly applied. Thus, the first goal of this thesis is to develop an

efficient and accurate technique for the analysis of aperiodic reflectarrays which presents the same capabilities as the analysis of periodic reflectarrays.

The reflectarray analysis usually considers the incident field from the feed to be constant at each reflectarray element. This is convenient because it facilitates the analytical operations with the equations. A generalization of the analysis considering a variable incident field at each cell will be proposed to improve the accuracy while still keeping the analysis efficiency. This generalization will be developed for both cases, periodic and aperiodic reflectarrays using the FFT and NUFFT algorithms, respectively.

The characterization of the reflectarray far fields can be improved by using the First Principle of Equivalence instead of the Second Principle, since it also takes into account the magnetic field on the reflectarray aperture. In addition, reflectarray antennas usually have a dielectric frame backed by a ground plane at the edges. This frame is a continuation of the reflectarray breadboard without metallizations and needs to be conveniently characterized to correctly predict the far fields.

Array near field models usually consider each element as punctual isotropic sources. It is proposed to improve those models by modeling the reflectarray element as a small aperture, as in the case of far field analysis. The aim of improving this model is its use within an optimization algorithm in order to be able to develop techniques for the near field synthesis of reflectarray antennas.

The second and third blocks are closely related since they both comprise the development of efficient techniques for the synthesis of reflectarray antennas. The second block is aimed to the improvement of the copolar synthesis, by including the First Principle of Equivalence in the phase-only synthesis as well as the characterization of the dielectric frame. In addition, an improved POS technique will be developed which will allow the future crosspolar optimization developed in the third block, as well as its extension to near field phase-only synthesis with the model previously improved.

The third block of the thesis is focused on the crosspolar optimization of reflectarray antennas. Typically, reflectarray synthesis techniques are based on phase-only techniques, which can only impose copolar specifications during the synthesis process and there is no control over the crosspolar component. Some techniques to improve the crosspolar far field have been devised for the case of reflectarray antennas, although they are limited. Only recently some works have addressed the crosspolar optimization of reflectarrays, relying on look-up tables for the reflection coefficient matrices. Thus, another goal of the thesis is the development of efficient algorithms for the crosspolar optimization of reflectarray antennas, that add new contributions to this recent opened research line.

1.4. Thesis outline

The present thesis has been organized in six chapters, including this one for the introduction and the last one for summarizing the main ideas and novel contributions of the thesis. The remain chapters include the analysis and synthesis techniques developed as well as examples to demonstrate and validate the presented original contributions.

Chapter 2 is devoted to the analysis of a single offset reflectarray antenna and the computation of its radiated fields. It starts with the equivalent parabolic reflector geometry and from the parabolic reflector parameters, the reflectarray is geometrically characterized. Then, the analysis to obtain the tangential field on the surface of the reflectarray from the incident field of the feed is described. The feed is usually a horn antenna, which is modeled as a mathematical function in order to simplify the analysis. The tangential field is obtained analyzing the reflectarray with a full-wave Method of Moments (MoM) based on local periodicity in order to account for substrate losses and other effects introduced by the reflectarray element. The reflected tangential magnetic field is derived from the reflected electric field from the plane wave relation at each reflectarray element. The magnetic field is necessary in order to compute the far fields using the First Principle of Equivalence, which characterizes the radiated fields better than the Second Principle. Then, an efficient technique to compute the far fields from the tangential field is described, which is based on the Fast Fourier Transform (FFT) algorithm. This technique is only suitable for periodic reflectarrays and is later extended to aperiodic reflectarrays employing the Non-Uniform FFT (NUFFT). This analysis technique is later generalized assuming a continuous variable incident field across the reflectarray surface. Numerical examples are provided to show the capabilities of the new developed techniques. Finally, a new model for the computation of the reflectarray near field is presented and validated.

Chapter 3 describes the Intersection Approach (IA) for Phase-Only Synthesis (POS), a widely used algorithm to obtain shaped-beam reflectarrays. Its formulation is presented for the Second Principle of Equivalence and is then extended to the First Principle. The success of this algorithm lies in its computational efficiency due to its use of the FFT, which is its most time consuming operation, and the ability to handle very large reflectarrays. Some techniques for the convergence improvement and design control are presented, along with an example of a reflectarray with an isoflux pattern for global Earth coverage. Since the IA-POS only deals with copolar requirements, the IA formulation is extended in an efficient fashion to include crosspolar requirements during the synthesis process. The resulting algorithm (IA-XP) is still computationally efficient since it is still based on the use of the FFT. Some examples are provided to validate the developed algorithm.

Chapter 4 is dedicated to the optimization of the Levenberg-Marquardt Algorithm (LMA) for reflectarray POS, since the formulation of the IA in Chapter 3 presents some inconveniences: it is difficult to obtain a reflectarray layout with the IA-XP and neither the IA-POS nor the IA-XP can be used for near field synthesis. The chosen algorithm is the LMA, which is extensively detailed and optimized in this chapter for POS. The two formulations of the IA presented in Chapter 3 were only suitable for far field synthesis. However, the LMA developed in this chapter is also used for near field optimization, only changing the analysis tool. The reflectarray quiet zone is optimized with the goal of obtaining reflectarrays for their use as probes for Compact Antenna Test Ranges (CATR).

Chapter 5 addresses the crosspolar optimization in reflectarrays by performing a direct optimization of the antenna geometry. For this optimization, a full-wave analysis based on local periodicity of the reflectarray element is used directly in the optimization loop,

employing the Method of Moments (MoM) in spectral domain. The techniques developed in this chapter take advantage of the work done in previous chapters. First, an extension of the LMA previously developed (LMA-POS) is realized in order to carry out crosspolar optimization of reflectarrays (LMA-XP). Although the LMA-POS was thoroughly improved, now that MoM is used in the optimization process, some further improvements are introduced to minimize the impact of MoM, by reducing the number of calls needed to the MoM routine. The LMA-XP effectively reduces the crosspolar component of the far field while preserving the copolar shape, although it presents some convergence issues for large reflectarrays. Hence, a new algorithm is developed in order to improve the convergence of the LMA-XP. This new algorithm is based on the IA framework and works with the squared field amplitude. The backward projector is modified to use the LMA and the resulting algorithm is known as IA-LMA-XP. It can handle thousands of optimizing variables and reduce the crosspolar component of very large reflectarrays, as demonstrated in the provided test cases.

Finally, Chapter 6 contains the final conclusions of the work presented in the thesis, as well as a summary of the original contributions, a number of future lines of research opened during the development of this work and a list of the published papers in international journals and conferences.

CHAPTER 2

Efficient analysis of printed reflectarrays

2.1. Introduction

A printed reflectarray consists of a planar array of printed radiating elements, such as patches with stubs, rectangular patches, parallel dipoles, rings, crosses, etc., in a single or multiple stacked layers backed by a ground plane and illuminated by a feed. Although the list of reflectarray element topologies is wide, the operating principle is always the same. The reflectarray is illuminated by a primary feed, typically a horn antenna (although other types are possible). The incident field from the feed is reflected back by the radiating elements introducing a phase-shift in the field. This phase-shift can be modified by adjusting one or several parameters of the reflectarray element geometry. Hence, the phase distribution of the tangential field can be controlled in order to collimate or shape the beam.

The analysis of the reflectarray is divided in several steps throughout this chapter. First, the geometry of the antenna is analyzed. In this work, the single-offset configuration is considered. This configuration is based on an equivalent parabolic reflector setup defined by the equivalent or projected aperture, the focal distance and the clearance. From these parameters the reflectarray parameters can be derived.

Then, the incident field on the reflectarray surface is obtained. It is usually done by modeling the feed with a far field ideal model, which only takes into account the main beam. However, side lobes of the real feed usually fall at angles outside the surface of the reflectarray, so this model provides a good enough approximation for the feed. The computation of the impinging wave phase from the feed is based on the concept of the antenna phase center and the distance from it to the center of the reflectarray element.

In order to obtain the reflected or tangential field, it is necessary to know how the reflectarray elements affect the incident field from the feed. Ideally, only a phase shift would be produced, although in reality the amplitude is slightly changed and crosspolar components are added to the field. The reflectarray element is analyzed using the Method

of Moments (MoM) in spectral domain and the Floquet theorem assuming local periodicity. This means that each element is analyzed by embedding the element in an infinite array comprised of the same element, taking into account mutual coupling between elements. Due to this fact, it is important that reflectarray designs present phase distributions that are smooth, since for similar phases, the dimensions of the elements are also similar, thus preserving the local periodicity assumption. With this analysis, the matrix of reflection coefficients is obtained. This matrix relates the incident field with the reflected field on the surface of the reflectarray and accounts for the phase shift, losses due to the substrate and crosspolarization introduced by the element.

Once the reflected field has been obtained, it is used to compute the radiated far fields. Since the reflectarray is an aperture antenna, the Equivalence Principles can be employed in the calculation of the far fields. Depending on the available knowledge on the electric and magnetic fields, the First, Second or Third Equivalence Principles may be used. In practice, it is common to only work with the electric field, so the Second Principle of Equivalence is used. In any case, all of them require the computation of the spectrum functions, which are obtained as the Fourier transform of the tangential field, and is the most time consuming operation in the calculation of the far field. For this reason, the Fast Fourier Transform (FFT) can be used in order to efficiently compute the spectrum functions for a periodic reflectarray. However, when the grid is aperiodic, the FFT can no longer be used and, in order to preserve the efficiency, the non-uniform FFT (NUFFT) must be employed.

Finally, from the tangential field the near field radiated by the reflectarray can also be obtained. A near field model is developed and validated, in which each reflectarray element is considered a radiation unit and is modeled as a small aperture. The total near field is obtained as far field contributions from all the reflectarray elements. Then, this model is validated through simulations with the commercial software GRASP and measurements from a reflectarray antenna.

2.2. Geometry of the equivalent parabolic reflector

This section is devoted to the geometrical definition of the reflectarray antenna under study. The most common configuration in the literature is the single-offset reflectarray [2] (from which the centered configuration is a particular case), although there exist others having the reflectarray as subreflector of a main parabolic reflector [80, 122] or a dual reflectarray setup [115,123]. Due to its simplicity, the single-offset configuration has been selected and a sketch is shown in Figure 2.1. This configuration is based on an equivalent parabolic reflector setup defined by the equivalent or projected aperture D, the focal distance F and the clearance C. (The centered configuration would be defined by $C = -D/2$.) From these parameters and the equation of an elliptic paraboloid, the reflectarray parameters can be derived.

The equation of the elliptic paraboloid surface (from which the parabolic reflector is a section of its surface) is

$$x^2 + y^2 = 4Fz, \tag{2.1}$$

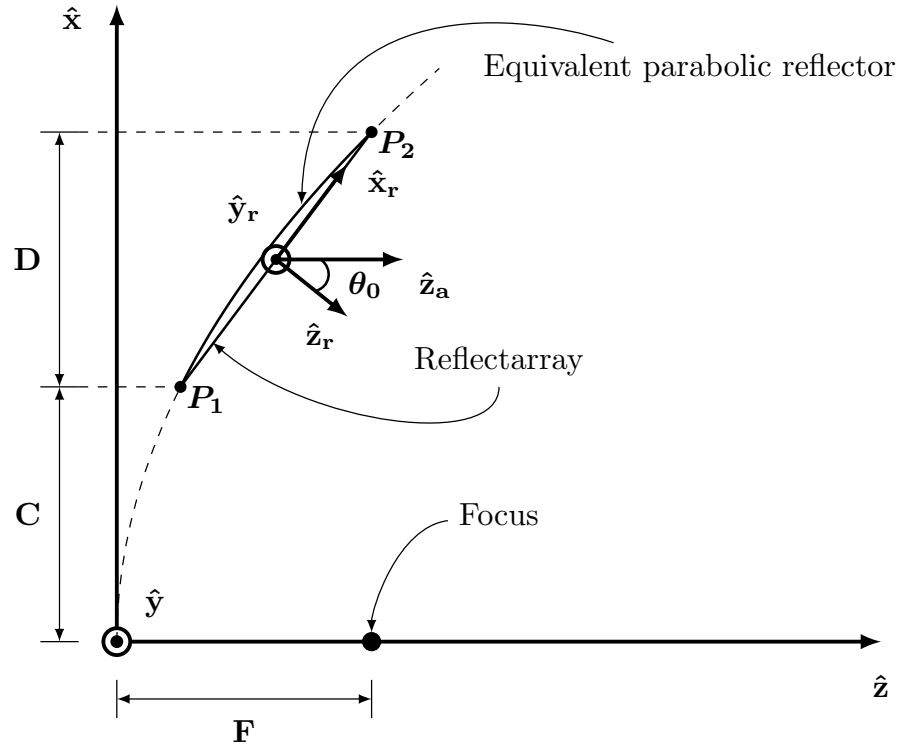

Figure 2.1: *Sketch of a single-offset reflectarray and its equivalent parabolic reflector system.*

where F is the focal distance as shown in Figure 2.1. The reflectarray is placed in the chordal plane of the parabolic reflector. In the following sections, important reflectarray parameters will be derived starting from eq. (2.1).

2.2.1. Focus in the reflectarray coordinate system

When analyzing the reflectarray, it is common to do it in its own coordinate system ($\hat{x}_r$, $\hat{y}_r$, $\hat{z}_r$), see Figure 2.1. Hence, we have to express the reflectarray parameters in that coordinate system, in particular the focus coordinates, where the feed will be placed. The focal point coordinates in the Global Coordinate System (GCS) are $(x_f,\, y_f,\, z_f)_{\mathrm{GCS}} = (0,\, 0,\, F)$. In order to obtain the coordinates in the Reflectarray Coordinate System (RCS), we need to obtain the change of basis matrix. This can be done by expressing the vectors $\hat{x}_r$, $\hat{y}_r$, $\hat{z}_r$ in the $(\hat{x},\, \hat{y},\, \hat{z})$ basis. In the XZ plane with $y = 0$, (2.1) is reduced to the parabola equation

$$x^2 = 4Fz. \tag{2.2}$$

The reflectarray is resting in the parabolic reflector at the points $P_1 = (x_1,\, z_1)$ and $P_2 = (x_2,\, z_2)$. Knowing that $x_1 = C$, $x_2 = C + D$ and using (2.2) both points are obtained as

$$P_1 = \left(C,\, \frac{C^2}{4F}\right), \tag{2.3a}$$

$$P_2 = \left(C + D,\, \frac{(C+D)^2}{4F}\right). \tag{2.3b}$$

Once P_1 and P_2 are obtained, vector $\hat{x}_r$ can be easily calculated as

$$\begin{aligned}\vec{x}_r &= (x_2 - x_1)\,\hat{x} + 0\,\hat{y} + (z_2 - z_1)\,\hat{z} = (C + D - C)\,\hat{x} + 0\,\hat{y} + \left(\frac{(C+D)^2}{4F} - \frac{C^2}{4F}\right)\hat{z} \\ &= D\,\hat{x} + 0\,\hat{y} + \frac{1}{4F}\left(C^2 + 2CD + D^2 - C^2\right)\,\hat{z} = D\,\hat{x} + 0\,\hat{y} + \frac{D(2C+D)}{4F}\,\hat{z},\end{aligned} \tag{2.4}$$

$$\|\vec{x}_r\| = \sqrt{D^2 + \frac{D^2(2C+D)^2}{16F^2}} = \frac{D}{4F}\sqrt{16F^2 + (2C+D)^2}, \tag{2.5}$$

$$\hat{x}_r = \frac{\vec{x}_r}{\|\vec{x}_r\|}. \tag{2.6}$$

Since $\hat{y}_r = \hat{y}$, only $\hat{z}_r$ is left, and can be easily calculated as the cross product of $\hat{x}_r$ and $\hat{y}_r$, $\hat{z}_r = \hat{x}_r \times \hat{y}_r$. Operating:

$$\begin{aligned}\hat{z}_r = \hat{x}_r \times \hat{y}_r &= \begin{vmatrix} \hat{x} & \hat{y} & \hat{z} \\ \frac{D}{\|\vec{x}_r\|} & 0 & \frac{D(2C+D)}{4F\|\vec{x}_r\|} \\ 0 & 1 & 0 \end{vmatrix} = \hat{x}\left(0 - \frac{D(2C+D)}{4F\|\vec{x}_r\|}\right) - \hat{y}\,(0-0) + \hat{z}\left(\frac{D}{\|\vec{x}_r\|}\right) \\ &= -\frac{D(2C+D)}{4F\|\vec{x}_r\|}\hat{x} + \frac{D}{\|\vec{x}_r\|}\hat{z}.\end{aligned} \tag{2.7}$$

Once the vectors $\hat{x}_r$, $\hat{y}_r$, $\hat{z}_r$ are obtained, the change of basis matrix from GCS to RCS is calculated simply by putting these vector as rows of said matrix. In order to obtain the focus coordinates in the RCS, the vector [(0, 0, F) − (center of the RA)] needs to be transformed. The center of the reflectarray is

$$\left(\frac{x_1 + x_2}{2},\, 0,\, \frac{z_1 + z_2}{2}\right) = \left(\frac{2C+D}{2},\, 0,\, \frac{C^2 + (C+D)^2}{8F}\right). \tag{2.8}$$

Then, the vector to be transformed is

$$\vec{v} = (0,\, 0,\, F) - \left(\frac{x_1 + x_2}{2},\, 0,\, \frac{z_1 + z_2}{2}\right) = \left(-\frac{2C+D}{2},\, 0,\, \frac{8F^2 - C^2 - (C+D)^2}{8F}\right). \tag{2.9}$$

Finally, the coordinates of the focus (feed) in the reflectarray coordinate system will be

$$\begin{pmatrix} x_f \\ y_f \\ z_f \end{pmatrix}_{(RCS)} = \begin{pmatrix} \frac{D}{\|\vec{x}_r\|} & 0 & \frac{D(2C+D)}{4F\|\vec{x}_r\|} \\ 0 & 1 & 0 \\ -\frac{D(2C+D)}{4F\|\vec{x}_r\|} & 0 & \frac{D}{\|\vec{x}_r\|} \end{pmatrix} \begin{pmatrix} -\frac{2C+D}{2} \\ 0 \\ \frac{8F^2 - C^2 - (C+D)^2}{8F} \end{pmatrix}_{(GCS)}. \tag{2.10}$$

2.2.2. Number of reflectarray elements

Given the reflectarray periodicity (a, b), being a the periodicity in the $\hat{x}_r$ axis and b in the $\hat{y}_r$ axis, the maximum number of elements in each axis can be calculated. The reflectarray length along $\hat{x}_r$ is given by $\|\vec{x}_r\|$, defined in (2.5), so the number of elements in that axis

will be

$$N_x = \left[\frac{\|\vec{x}_r\|}{a} \right], \tag{2.11}$$

where $[\circ]$ denotes the nearest integer function. As the paraboloid has symmetry of revolution, it will be extended in the $\hat{y}_r$ axis $y = \pm D/2$, (see Figure 2.1), hence the number of elements in that direction will be

$$N_y = \left[\frac{D}{b} \right]. \tag{2.12}$$

2.2.3. Radiation angle

Another parameter of interest is the radiation angle, which in general is (θ_0, φ_0). From the GCS point of view, a beam-focused reflectarray will collimate the rays from the feed in the $\hat{z}$ axis and thus $\varphi_0 = 0$. The angle formed by $\hat{z}$ (or equivalently, $\hat{z}_a$) and $\hat{z}_r$ will be the pointing angle (see Figure 2.1), which can be easily obtained as the dot product of the two angles,

$$\hat{z} \cdot \hat{z}_r = \|\hat{z}\| \, \|\hat{z}_r\| \cos\theta_0 = \cos\theta_0 \Rightarrow \theta_0 = \arccos\left(\hat{z} \cdot \hat{z}_r\right). \tag{2.13}$$

Vector $\hat{z}_r$ was previously obtained in (2.7), and taking into account that the norm of the unitary vectors is one, the dot product will be

$$\hat{z} \cdot \hat{z}_r = (0,0,1) \begin{pmatrix} -\frac{D(2C+D)}{4F\|\vec{x}_r\|} \\ 0 \\ \frac{D}{\|\vec{x}_r\|} \end{pmatrix} = \frac{D}{\|\vec{x}_r\|} \Rightarrow \theta_0 = \arccos\left(\frac{D}{\|\vec{x}_r\|}\right), \tag{2.14}$$

where $\|\vec{x}_r\|$ has been obtained in (2.5).

2.2.4. Targonsky condition

When designing directive reflectarrays for far field applications, the pointing direction of the main beam changes with frequency. This effect is known as beam squint and it also exists in offset parabolic reflectors. It can be minimized by imposing [124]

$$\theta_i = \theta_0, \tag{2.15}$$

where θ_i is the pointing angle of the feed over the reflectarray surface and θ_0 the radiation angle (see Figure 2.2). When imposing this condition, the point x_i where the feed is pointing at on the reflectarray surface will change. Usually, x_i is chosen to minimize the spillover [125] by imposing an almost constant illumination taper at the reflectarray contour edge. Thus, if the Targonski condition is met the spillover will not be minimized for a given feed.

In order to calculate the new x_i point, Figure 2.2 will be used as reference. The feed coordinates are $(x_f, 0, z_f)$ (with $y_f = 0$, since the feed is considered to be in the XZ plane) and the incident and radiation angles fulfill $\theta_i = \theta_0$. The distance of the focus with regard to x_i will be

$$x_{\text{off}} = z_f \tan\theta_0 > 0, \tag{2.16}$$

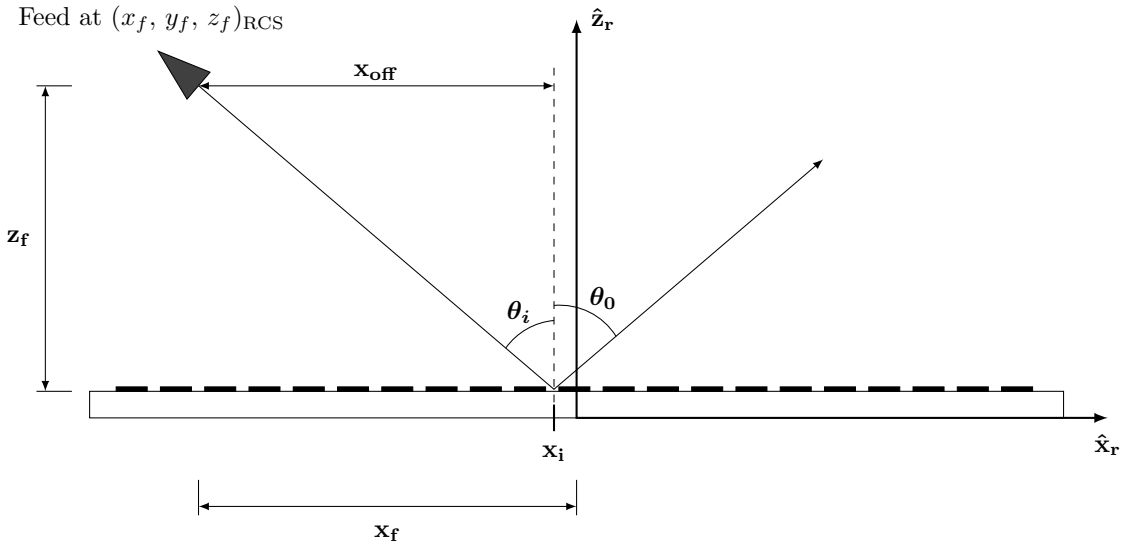

Figure 2.2: *Illustration of the Targonski condition to minimize the beam squint.*

and it is always a positive value. Then, taking into account the position of the feed, it follows

$$x_i = x_f + x_{\mathrm{off}}. \tag{2.17}$$

According to Figure 2.1, x_f will be always negative in the RCS, and thus x_i can be positive or negative depending on the values of x_f and x_{off}.

2.3. Analysis of reflectarrays based on local periodicity

Once the geometry of the antenna has been characterized and the reflectarray parameters derived from the parabolic reflector equivalent model, the tangential field on the surface of the reflectarray needs to be computed. This will be done first by analyzing the field radiated by the feed antenna, which will be modeled with an ideal far field model, suitable for directive antennas such as horns. The analysis will consider a dual linear polarized reflectarray whose working polarization will depend on the polarization of the feed, which can be X- or Y-polarized, as seen in Figure 2.3.

Then, the reflectarray will be analyzed using a full-wave analysis based on local periodicity and the Floquet theorem in order to obtain the reflection coefficient matrix that relates the incident with the reflected field. This full-wave analysis takes into account mutual coupling between elements, the field reflected by the substrate and ground plane, the field reradiated by the metallizations, and substrate losses.

With this method of analysis, three sources of cross-polarization are taken into account: the crosspolar component due to the incident field from the feed (if a real model were used), the geometry through the projection of the incident field onto the reflectarray surface and the crosspolarization introduced by the reflectarray element.

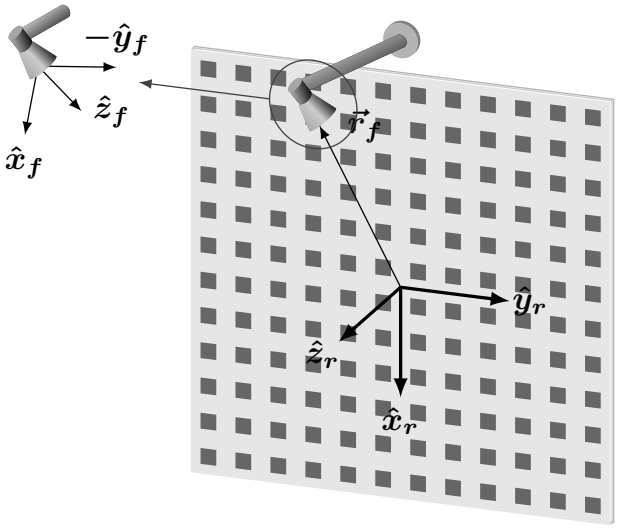

Figure 2.3: *Scheme of a general printed reflectarray.*

2.3.1. Feed model

Before addressing the actual analysis of the reflectarray antenna, the incident field on its surface needs to be calculated. It depends on the position and radiation pattern of the feed as shown in Figure 2.3. Usually, a horn antenna is used as feed and its radiation pattern can be modeled as a function. The model used is the one proposed in [78], where the following expressions for the horn far field are provided for an X- and Y-polarized feed horn expressed in the Feed Coordinate System (FCS) ($\hat{x}_f$, $\hat{y}_f$, $\hat{z}_f$),

$$\vec{E}^X = jA_0\frac{k_0}{2\pi r}e^{-jk_0r}\left[C_X\left(\theta\right)\cos\varphi\,\hat{\theta} - C_Y\left(\theta\right)\sin\varphi\,\hat{\varphi}\right], \tag{2.18a}$$

$$\vec{E}^Y = jA_0\frac{k_0}{2\pi r}e^{-jk_0r}\left[C_X\left(\theta\right)\sin\varphi\,\hat{\theta} + C_Y\left(\theta\right)\cos\varphi\,\hat{\varphi}\right], \tag{2.18b}$$

where k_0 is the wavenumber in vacuum and A_0 is a constant that depends on the radiated power. According to Figure 2.3, when the feed horn is X-polarized, the electric field is aligned with the $\hat{x}_f$ axis. Conversely, for a Y-polarized feed horn, the electric field is aligned with the $\hat{y}_f$ axis. $C_X(\theta)$ and $C_Y(\theta)$ are functions that give the feed horn pattern in the XZ and YZ planes of the FCS respectively,

$$C_X(\theta) = \cos^{q_x}\theta, \tag{2.19a}$$

$$C_Y(\theta) = \cos^{q_y}\theta. \tag{2.19b}$$

Both axial symmetric and non-symmetric radiation patterns can be modeled with (2.18), considering $q = q_x = q_y$ or $q_x \neq q_y$ in (2.19), respectively. The q factor gives the beamwidth in the main planes of the feed radiation patterns and thus the directivity of the feed (see Figure 2.4). This ideal model only characterizes the main lobe of the radiation pattern of the feed, as seen in Figure 2.4. Thus, it is only suitable for directive antennas, such us horns, where the side lobes are low, or when the projection of the side lobes lay outside

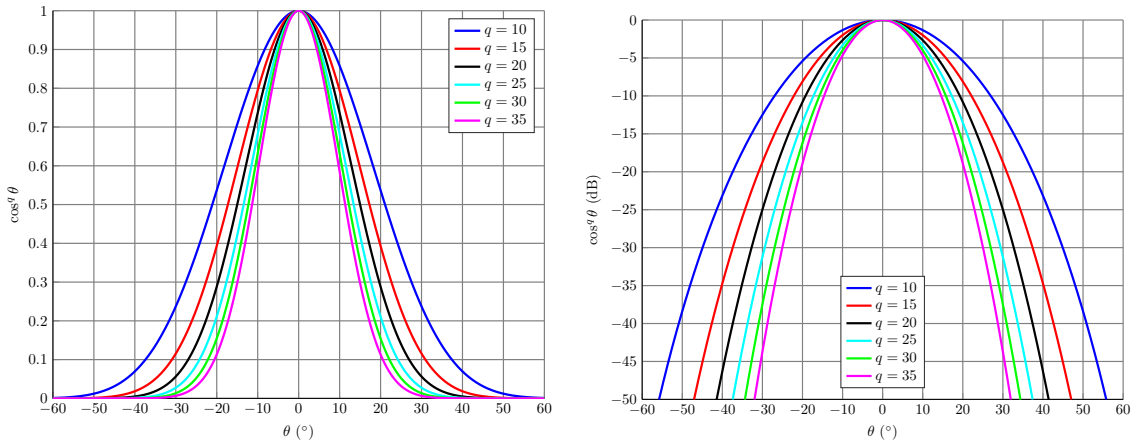

(a) *(b)*

Figure 2.4: *Radiation pattern given by a* $\cos^q\theta$ *function for different* q *values. (a) Natural units. (b) Decibels.*

the surface of the reflectarray, i.e., its surface is only illuminated by the main lobe. In those cases, this model provides good enough results to use it in the analysis, design and synthesis of reflectarrays [2].

Since the function $\cos^q\theta$ is proportional to the amplitude of the electric field

$$\left|\vec{E}\right| \propto \cos^q\theta, \tag{2.20}$$

the power (gain) will be proportional to the squared function

$$\left|\vec{E}\right|^2 \propto \cos^{2q}\theta, \tag{2.21}$$

so the normalized gain of the horn will be equal to

$$G(\theta) = 10\log\left(\cos^{2q}\theta\right) = 20\,q\log\left(\cos\theta\right), \tag{2.22}$$

for the main lobe of the radiation pattern. Isolating the variable yields

$$q = \frac{G(\theta)}{20\log\left(\cos\theta\right)}. \tag{2.23}$$

This way, evaluating the normalized gain for several θ angles belonging to the main beam and applying (2.23), a table of q values is obtained, which should be similar for θ angles where the main beam can be approximated by a cosine function. For the two main planes, two different values of q are be obtained, as shown in (2.19). Sometimes, an averaged q value is used,

$$q = \frac{q_x + q_y}{2}, \tag{2.24}$$

if q_x and q_y are similar [2,81]. This factor also changes with frequency since the directivity of the horn antenna also does, so if the analysis is made at several frequencies, the feed model needs to be obtained at each frequency [81].

The power radiated by the feed model is needed in order to compute the gain of the reflectarray antenna. Since this feed model is ideal both the ohmic losses and the back radiation are considered to be zero, and the sidelobes are neglected. However, for feed horns the losses are typically in the order of 0.05 dB and thus negligible, the back radiation is also very small and the level of the sidelobes will not significantly affect the final result. As a result, the total power radiated by the feed can be computed as

$$P_{\text{feed}} = \int_{\theta=0}^{\pi/2} \int_{\varphi=0}^{2\pi} \frac{\left|\vec{E}^{X/Y}(\theta,\,\varphi)\right|^2}{2\eta_0} r^2 \sin\theta \, d\theta \, d\varphi, \tag{2.25}$$

where $\vec{E}^{X/Y}(\theta,\,\varphi)$ is the field radiated by the ideal horn given by (2.18), and where X and Y indicates the considered polarization from the feed. The squared amplitudes for both polarizations are

$$\left|\vec{E}^{X}\right|^2 = \left|\vec{E}^{Y}\right|^2 = A_0^2 \, \frac{k_0^2 \cos^{2q}\theta}{4\,\pi^2\, r^2}, \tag{2.26}$$

where an axial symmetric pattern for the feed is considered. Substituting (2.26) in (2.25) it follows

$$P_{\text{feed}} = A_0^2 \, \frac{\pi}{\eta_0 \, \lambda_0^2 \, (2q+1)}. \tag{2.27}$$

The field radiated by the feed given by (2.18) is expressed in spherical coordinates in the FCS (see Figure 2.3). However, the incident field should be expressed in Cartesian coordinates of the RCS ($\hat{x}_r$, $\hat{y}_r$, $\hat{z}_r$). Thus, the field is first transformed to the Cartesian coordinates of the FCS applying the following transformation

$$\begin{pmatrix} E_x^{X/Y} \\ E_y^{X/Y} \\ E_z^{X/Y} \end{pmatrix}_{(\text{FCS})} = \begin{pmatrix} \sin\theta\cos\varphi & \cos\theta\cos\varphi & -\sin\varphi \\ \sin\theta\sin\varphi & \cos\theta\sin\varphi & \cos\varphi \\ \cos\theta & -\sin\theta & 0 \end{pmatrix} \begin{pmatrix} 0 \\ E_\theta^{X/Y} \\ E_\varphi^{X/Y} \end{pmatrix}_{(\text{FCS})}. \tag{2.28}$$

Note that this transformation is carried out for each element of the reflectarray, since the incident angle $(\theta,\,\varphi)$ from the feed changes with the position of the element. Then, the Cartesian components are transformed from FCS to RCS using [126]

$$\begin{pmatrix} E_x^{X/Y} \\ E_y^{X/Y} \\ E_z^{X/Y} \end{pmatrix}_{(\text{RCS})} = A \cdot \begin{pmatrix} E_x^{X/Y} \\ E_y^{X/Y} \\ E_z^{X/Y} \end{pmatrix}_{(\text{FCS})} = \begin{pmatrix} a_{11} & a_{12} & a_{13} \\ a_{21} & a_{22} & a_{23} \\ a_{31} & a_{32} & a_{33} \end{pmatrix} \begin{pmatrix} E_x^{X/Y} \\ E_y^{X/Y} \\ E_z^{X/Y} \end{pmatrix}_{(\text{FCS})}, \tag{2.29}$$

where the columns of the A matrix are the director cosines of the FCS expressed in the RCS. Thus, A defines the transformation of the field components from FCS to RCS and is the same for all the reflectarray elements. The feed is placed at $(x_f,\,y_f,\,z_f)$ and it is oriented in such a way that points to a certain position in the reflectarray surface,

$(x_i,\, y_i,\, 0)$. Then, the $\hat{z}_f$ axis is defined as

$$\vec{z}_f = (x_i - x_f,\, y_i - y_f,\, -z_f) \Longrightarrow \hat{z}_f = \frac{\vec{z}_f}{\|\vec{z}_f\|}. \tag{2.30}$$

In general, the feed will be placed in a position not contained in the symmetry planes of the reflectarray, and thus it will not be possible for the $\hat{x}_f$ and $\hat{y}_f$ feed axis to be orthogonal to the $\hat{y}_r$ and $\hat{x}_r$ reflectarray axis at the same time, which is desirable to use dual orthogonal polarization. In this general case, only one linear polarization will be used.

- X polarization, which must comply $\vec{x}_f \cdot \hat{y}_r = 0$. Apart from this condition, it also has to fulfill that $\vec{x}_f$ must be orthogonal to $\hat{z}_f$, i.e. $\vec{x}_f \cdot \hat{z}_f = 0$, so it immediately follows that $\vec{x}_f$ is orthogonal to $\hat{y}_r$ and $\hat{z}_f$, or that

  $$\hat{x}_f = \hat{y}_r \times \hat{z}_f. \tag{2.31}$$

  From here, $\hat{y}_f$ can be calculated as the cross product of $\hat{x}_f$ and $\hat{z}_f$ as

  $$\hat{y}_f = \hat{z}_f \times \hat{x}_f. \tag{2.32}$$

- The case for Y polarization is very similar. Now, it must comply $\vec{y}_f \cdot \hat{x}_r = 0$, and that the $\vec{y}_f$ vector is orthogonal to $\hat{z}_f$, i.e. $\vec{y}_f \cdot \hat{z}_f = 0$, so, similarly to the previous case, it follows

  $$\hat{y}_f = \hat{z}_f \times \hat{x}_r. \tag{2.33}$$

  Now, $\hat{x}_f$ is obtained as

  $$\hat{x}_f = \hat{y}_f \times \hat{z}_f. \tag{2.34}$$

Once the vectors $(\hat{x}_f,\, \hat{y}_f,\, \hat{z}_f)$ are obtained, they can be related to matrix A in (2.29). Indeed, the columns of matrix A are the vectors $(\hat{x}_f,\, \hat{y}_f,\, \hat{z}_f)$,

$$\hat{x}_f = (a_{11},\, a_{21},\, a_{31}), \tag{2.35a}$$

$$\hat{y}_f = (a_{12},\, a_{22},\, a_{32}), \tag{2.35b}$$

$$\hat{z}_f = (a_{13},\, a_{23},\, a_{33}). \tag{2.35c}$$

For the case in which the feed is contained in the symmetry planes of the reflectarray, such as in the case shown in Figure 2.1, the two conditions developed above are equivalent, since the fulfillment of one of them implies the fulfillment of the other.

2.3.2. Tangential field on the surface of the reflectarray

2.3.2.1. Electric field

In the previous section, an ideal feed model was analyzed that provides the incident electric field on the surface of the reflectarray, which can be written for both linear polarizations

as

$$\vec{E}_{\text{inc}}^{X/Y}(x,\, y) = E_{\text{inc},x}^{X/Y}(x,\, y)\,\hat{x} + E_{\text{inc},y}^{X/Y}(x,\, y)\,\hat{y}, \tag{2.36}$$

where the superscripts designate the polarization of the feed according to the FCS and the subscripts the field component with regard to the RCS (e.g. E_x^Y would be the $\hat{x}$ component of the projected field over the reflectarray surface when the feed radiates in Y polarization). Similarly, the reflected tangential electric field on the surface of the reflectarray can be written as follows,

$$\vec{E}_{\text{ref}}^{X/Y}(x,\, y) = E_{\text{ref},x}^{X/Y}(x,\, y)\,\hat{x} + E_{\text{ref},y}^{X/Y}(x,\, y)\,\hat{y}. \tag{2.37}$$

The relation between the incident and reflected tangential electric fields at each element $(m,\, n)$ of the reflectarray is given by a matrix of reflection coefficients that characterizes that element,

$$\vec{E}_{\text{ref}}^{X/Y}(x_m,\, y_n) = R^{mn} \cdot \vec{E}_{\text{inc}}^{X/Y}(x_m,\, y_n), \tag{2.38}$$

where $(x_m,\, y_n)$ are the coordinates of the $(m,\, n)$th element and

$$R^{mn} = \begin{pmatrix} \rho_{xx}^{mn} & \rho_{xy}^{mn} \\ \rho_{yx}^{mn} & \rho_{yy}^{mn} \end{pmatrix}. \tag{2.39}$$

The components of R^{mn} are complex and fully characterize the behavior of the element. The components ρ_{xx} and ρ_{yy} are known as direct coefficients while ρ_{xy} and ρ_{yx} are the cross coefficients. The direct coefficients mostly affect the copolar radiation pattern for each corresponding polarization (ρ_{xx} for X polarization and ρ_{yy} for Y polarization), while both direct and cross coefficients are important in the computation of the crosspolar far field. This latter fact can be easily seen by developing (2.38),

$$E_{\text{ref},\,x}^{X/Y} = \rho_{xx}\, E_{\text{inc},\,x}^{X/Y} + \rho_{xy}\, E_{\text{inc},\,y}^{X/Y}, \tag{2.40a}$$

$$E_{\text{ref},\,y}^{X/Y} = \rho_{yx}\, E_{\text{inc},\,x}^{X/Y} + \rho_{yy}\, E_{\text{inc},\,y}^{X/Y}. \tag{2.40b}$$

Assuming X polarization, the copolar reflected field is given by (2.40a) while the crosspolar one is given by (2.40b). Regarding (2.40a), the following inequalities always occur,

$$\left.\begin{aligned} |\rho_{xx}| &\gg |\rho_{xy}| \\ \left|E_{\text{inc},\,x}^{X}\right| &\gg \left|E_{\text{inc},\,y}^{X}\right| \end{aligned}\right\} \Longrightarrow \left|\rho_{xx}\, E_{\text{inc},\,x}^{X}\right| \gg \left|\rho_{xy}\, E_{\text{inc},\,y}^{X}\right|. \tag{2.41}$$

According to this, the copolar reflected field can be approximated by

$$E_{\text{ref},\,x}^{X} \approx \rho_{xx}\, E_{\text{inc},\,x}^{X}. \tag{2.42}$$

On the other hand, for the case of the crosspolar reflected field, it holds that

$$|\rho_{yx}| \ll |\rho_{yy}| \qquad \text{and} \qquad \left|E_{\text{inc},\,x}^{X}\right| \gg \left|E_{\text{inc},\,y}^{X}\right|, \tag{2.43}$$

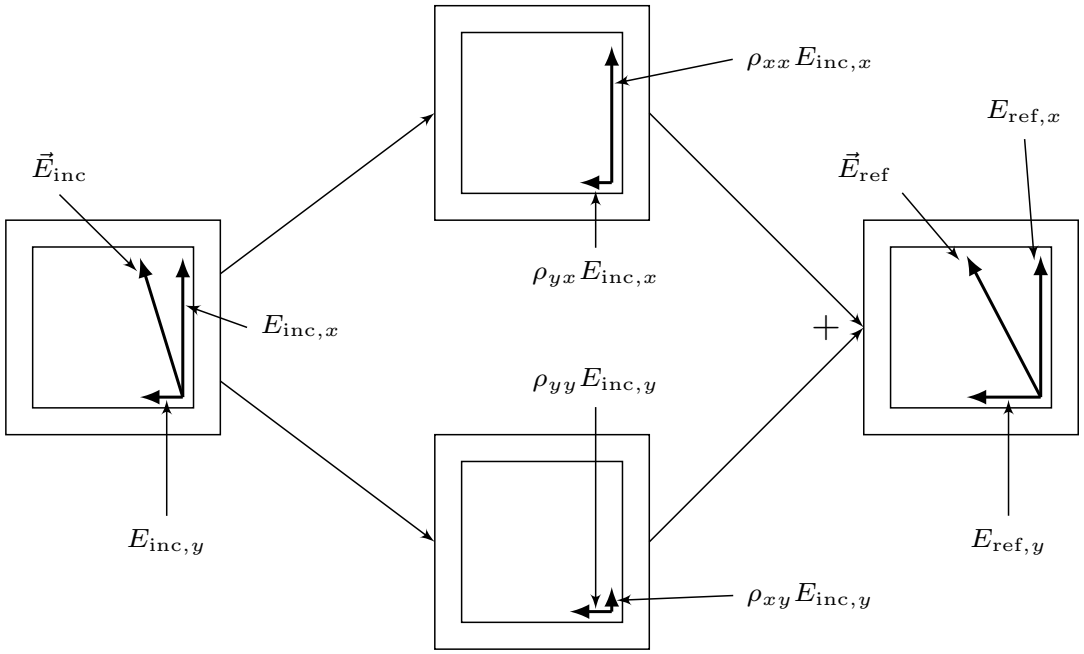

Figure 2.5: *Decomposition of the incident field from a feed with no crosspolarization. It shows the contributions to the crosspolarization from the field projection onto the reflectarray surface and the crosspolarization introduced by the reflectarray element.*

so no term can be neglected in the sum. However, for the total reflected field, it follows

$$\left|E^X_{\mathrm{ref},\,x}\right| \gg \left|E^X_{\mathrm{ref},\,y}\right|, \tag{2.44}$$

and since for the copolar radiation pattern the copolar reflected field is dominant, only (2.42) is needed to correctly predict the copolar pattern with minimum error.

The two addends of the crosspolar reflected field have different sources. While $\rho_{yx}\,E^X_{\mathrm{inc},x}$ is produced by the crosspolarization introduced by the element due to ρ_{yx}, $\rho_{yy}\,E^X_{\mathrm{inc},y}$ is produced by the projection of the incident field from the feed onto the reflectarray surface. They are graphically shown in Figure 2.5 and the effect is that the desired field component remains almost the same while the crosspolarization considerably increases its value. If a real feed is considered, its crosspolar contribution would add to both addends.

A similar discussion can be carried out for the Y polarization, where the following inequalities in (2.40b) will be fulfilled,

$$\left.\begin{array}{c} |\rho_{yy}| \gg |\rho_{yx}| \\ \left|E^Y_{\mathrm{inc},\,y}\right| \gg \left|E^Y_{\mathrm{inc},\,x}\right| \end{array}\right\} \Longrightarrow \left|\rho_{yy}\,E^Y_{\mathrm{inc},\,y}\right| \gg \left|\rho_{yx}\,E^Y_{\mathrm{inc},\,x}\right|. \tag{2.45}$$

As in the previous case, the copolar reflected field can be approximated by just one term of the sum,

$$E^Y_{\mathrm{ref},\,y} \approx \rho_{yy}\,E^Y_{\mathrm{inc},\,y}. \tag{2.46}$$

However, none of the terms of the crosspolar reflected field can be neglected since it holds

that

$$|\rho_{xy}| \ll |\rho_{xx}| \qquad \text{and} \qquad \left|E^{Y}_{\text{inc},\,y}\right| \gg \left|E^{Y}_{\text{inc},\,x}\right|. \tag{2.47}$$

And as it happened for the X polarization, now the copolar far field can be correctly predicted by (2.46).

Also, as in the previous case, the crosspolar reflected field for Y polarization has two sources: the crosspolarization of the element, which produces one addend ($\rho_{xy}\, E^{Y}_{\text{inc},y}$, through ρ_{xy}); and the reflectarray geometry through the projection of the incident field onto the reflectarray surface, producing the other addend ($\rho_{xx}\, E^{Y}_{\text{inc},x}$, through $E^{Y}_{\text{inc},x}$). The crosspolarization of a real feed would contribute to both addends of the crosspolar reflected field.

The approximations in the reflected field given by (2.42) and (2.46) are used in phase-only synthesis schemes, since it allows an important simplification of the R^{mn} matrix. Indeed, in this case the reflectarray element is treated as an ideal phase shifter where there are no losses and no crosspolarization introduced by the element. These two conditions are expressed by

$$|\rho_{xx}| = |\rho_{yy}| = 1 \qquad \text{(no losses)} \tag{2.48a}$$

$$|\rho_{xy}| = |\rho_{yx}| = 0 \qquad \text{(no element crosspolarization)}, \tag{2.48b}$$

and the R^{mn} matrix in (2.39) is simplified to

$$R^{mn} = \begin{pmatrix} e^{j\phi^{mn}_{xx}} & 0 \\ 0 & e^{j\phi^{mn}_{yy}} \end{pmatrix}, \tag{2.49}$$

where ϕ is the phase of the corresponding reflection coefficient. Now, the only two components of the reflection coefficients matrix are the phases of the direct coefficients. Since the incident field is fixed once the feed and its position are chosen, only the phases of ρ_{xx} and ρ_{yy} will conform the copolar radiation pattern as desired, for X and Y polarizations, respectively. This approximation has been widely used in the design of reflectarray antennas [2], although it does not allow a direct control of the crosspolar far field in the synthesis process, since the important contribution of ρ_{xy} and ρ_{yx} is not taken into account. This causes that the crosspolar pattern cannot be accurately predicted with the simplification of (2.49), as explained before with regard to the crosspolar reflected field, for which both contributions are similarly important.

In order to be able to predict the crosspolar component of the radiation pattern, the full R^{mn} matrix needs to be computed. Although there are more factors that affect the crosspolar far field, it is important to correctly characterize the crosspolarization introduced by the reflectarray element.

2.3.2.2. Magnetic field

On the other hand, the tangential reflected magnetic field is computed at each reflectarray element assuming a locally incident plane wave coming from the feed, using the following expression [127]:

$$\vec{H}_{\text{ref}}^{X/Y}(x_m, y_n) = \frac{\vec{k}_{\text{ref}} \times \vec{E}_{\text{ref}}^{X/Y}(x_m, y_n)}{\omega\mu_0}, \tag{2.50}$$

with $\omega = 2\pi f_0$ and $\vec{k}_{\text{ref}}$

$$\vec{k}_{\text{ref}} = k_x\hat{x} + k_y\hat{y} + k_z\hat{z}, \tag{2.51}$$

being

$$k_x = -k_0 \sin\theta^{mn} \cos\varphi^{mn}, \tag{2.52a}$$

$$k_y = -k_0 \sin\theta^{mn} \sin\varphi^{mn}, \tag{2.52b}$$

$$k_z = +k_0 \cos\theta^{mn}, \tag{2.52c}$$

where $(\theta^{mn}, \varphi^{mn})$ is the incident angle of the plane wave coming from the feed for the (m, n)th element. $\vec{k}_{\text{ref}}$ corresponds to the reflected propagative wave in the specular reflection direction, in the absence of grating lobes.

In order to compute the cross product in (2.50), all three components of the electric field are needed, but (2.38) only provides two, namely E_x and E_y. The E_z component can be obtained through the plane wave relation

$$\vec{k}_{\text{ref}} \cdot \vec{E}_{\text{ref}} = 0. \tag{2.53}$$

Solving (2.53), it immediately follows that

$$E_{\text{ref},z} = \frac{-k_{\text{ref},x}\, E_{\text{ref},x} - k_{\text{ref},y}\, E_{\text{ref},y}}{k_{\text{ref},z}}, \tag{2.54}$$

which allows to solve (2.50), obtaining the reflected tangential magnetic field on the reflectarray surface and yielding

$$\begin{aligned} \vec{H}_{\text{ref}}^{X/Y}(x_m, y_n) = \frac{1}{\omega\mu_0}\Big[& \big(k_{\text{ref},y}\, E_{\text{ref},z}^{X/Y}(x_m, y_n) - k_{\text{ref},z}\, E_{\text{ref},y}^{X/Y}(x_m, y_n)\big)\hat{x} \\ & - \big(k_{\text{ref},x}\, E_{\text{ref},z}^{X/Y}(x_m, y_n) - k_{\text{ref},z}\, E_{\text{ref},x}^{X/Y}(x_m, y_n)\big)\hat{y} \\ & + \big(k_{\text{ref},x}\, E_{\text{ref},y}^{X/Y}(x_m, y_n) - k_{\text{ref},y}\, E_{\text{ref},x}^{X/Y}(x_m, y_n)\big)\hat{z}\Big]. \end{aligned} \tag{2.55}$$

For the computation of the far fields only the tangential field is needed, finally having

$$H_{\text{ref},x}^{X/Y} = \frac{k_{\text{ref},y}\, E_{\text{ref},z}^{X/Y} - k_{\text{ref},z}\, E_{\text{ref},y}^{X/Y}}{\omega\mu_0}, \tag{2.56a}$$

$$H_{\text{ref},y}^{X/Y} = -\frac{k_{\text{ref},x}\, E_{\text{ref},z}^{X/Y} - k_{\text{ref},z}\, E_{\text{ref},x}^{X/Y}}{\omega\mu_0}. \tag{2.56b}$$

2.3.3. Efficient computation of the R-matrix with the Method of Moments

The computation of the reflection coefficients matrix is the most expensive task in the analysis of the reflectarray, since a full wave electromagnetic simulation software is needed. There are a number of commercially available software packages that can be used for this purpose, such as HFSS, CST, FEKO, etc. These programs can be used in two different ways to analyze a reflectarray. First, given a full design, the whole antenna can be simulated in order to obtain both near and far fields as desired. The advantage is that all effects such as mutual coupling, all kind of losses, diffraction, etc, are taken into account. However, this approach, by its own nature, requires huge amounts of memory and computing times, which makes it impractical in most cases, either for analysis or synthesis. The other approach consists in analyzing each element of the reflectarray assuming local periodicity using the Floquet theorem. This method of analysis embeds each element in an infinite array comprised of the same element and is excited by a plane wave, in general with oblique incidence. It takes into account losses of the dielectric, metal (if it is not PEC) and mutual coupling among elements. This way, the R^{mn} matrix can be extracted for each element and the reflected field computed. Although this approach is certainly faster than the previous one, it is still slow if it is to be applied to reflectarrays with a moderate number of elements. This is due to the nature of the software used, since they are general-purpose software and do not take advantage of the nature of the problem. Also, they cannot be used easily within homemade software in order to implement synthesis and optimization algorithms.

The approach followed in this thesis consists in the use of specially designed homemade software based on the Floquet theorem in order to analyze multilayered reflectarray elements [54, 76]. It takes into account the coupling among elements and the losses of the dielectric substrate. Since this software is specifically designed for this task, it is extremely fast in comparison with commercially available software. Also, it can be easily integrated with other homemade software, in particular, the software developed for this thesis. However, since each package is targeted for a specific reflectarray element (patches [54], dipoles [76], etc.), each unit cell would require to rewrite the core of the software to adapt it to the new problem.

In particular, the unit cell employed in this thesis is shown in Figure 2.6 and its method of analysis is described in detail in [76]. This tool was used in the analysis, design and manufacture of reflectarray antennas for space applications [42, 43] with good results. As it can be seen in Figure 2.6, the tool can handle several geometric parameters to set up the unit cell, in addition to other parameters related to the material, MoM and Floquet theorem (such us number of modes, convergence criteria, etc.). In practice, when doing optimizations, most of these variables will be fixed, since only a few of them are important in the reflectarray optimization. Usually, the substrate material is chosen beforehand, so the thickness of the different layers and relative permittivity are fixed. Also, the periodicity is usually fixed to allow the maximum variation in the size of the elements while avoiding the appearance of grating lobes [2, 43]. For the case of the dipole widths and separation

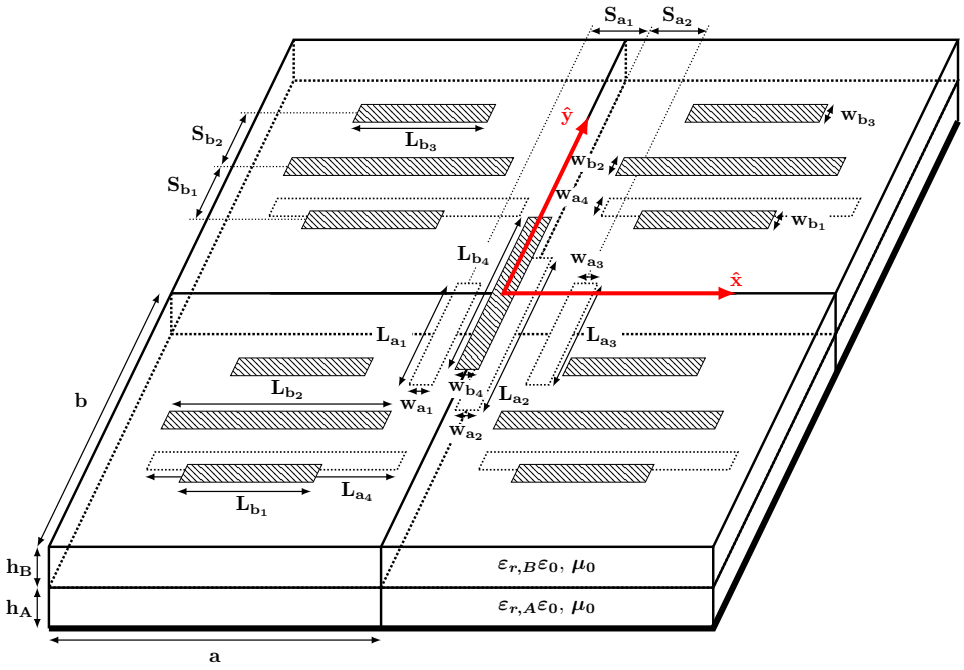

Figure 2.6: *Reflectarray unit cell based on parallel and coplanar dipoles in two different layers of metallizations for dual-polarized reflectarrays.*

between dipoles, a parametric study is usually carried out in order to obtain the optimum values [42, 43]. Hence, only the dipole lengths will be used in the reflectarray optimization in future chapters.

Another reflectarray element that will be employed in an antenna design consists of different layers of stacked patches and is shown in Figure 2.7 for a case of three stacked layers (although this number could be different). Its method of analysis is described in [2, 54] and it is based on the Floquet theorem and the use of the Generalized Scattering Matrix (GSM) in order to analyze each layer separately, obtaining its GSM, and then doing a cascade of different GSM to obtain the GSM of the whole element. It has been widely used for reflectarray designs [2, 19, 80, 81, 115, 128], obtaining good agreement between simulations and measurements. However, only the cell of Figure 2.6 is used in crosspolar optimizations in following chapters.

2.3.4. Sources of crosspolarization

The reflected field computed in (2.38) is used as a source to compute the far field radiated by the reflectarray antenna and it considers three sources of polarization. Firstly, although the feed model previously analyzed is ideal and presents no far field crosspolar component [125], if a real model or measurements [82, 88] were used, the crosspolar component of the feed would be taken into account in the incident field. Secondly, due to the projection of the incident field on the surface of the reflectarray, a crosspolar component will appear even in the case of using an ideal feed model with no crosspolarization. And thirdly, the element of the reflectarray introduces further crosspolarization through the terms ρ_{xy} and ρ_{yx} of the reflection coefficients matrix R^{mn}. All these three components will be taken into

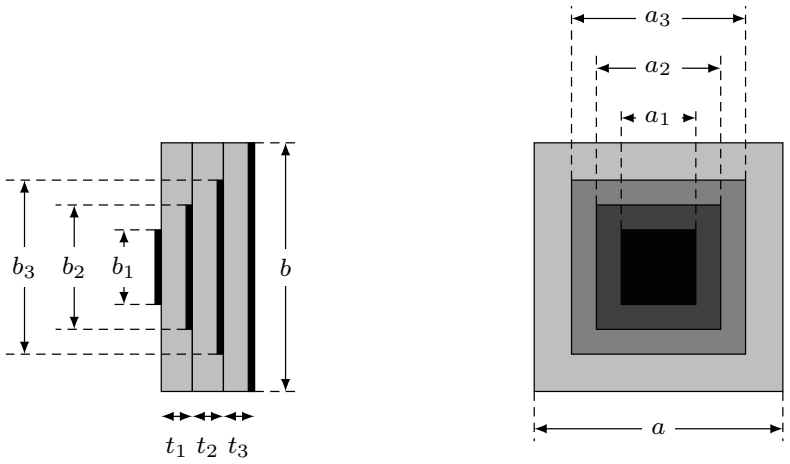

Figure 2.7: *Reflectarray unit cell based on stacked patches of different size.*

account when optimizing the crosspolar component in following chapters. From the three crosspolar sources, the most relevant when optimizing the antenna is the one generated by the element, since it varies with the dimensions of the geometry employed. The other two remain constant through the synthesis process. Hence, a good model of the unit cell is necessary to accurately characterize the crosspolar far field for its optimization.

Traditionally, these three components have been the only ones that were taken into account when computing the far fields from reflectarrays [2]. However, some discrepancies might arise when comparing measurements with simulations due to other sources not taken into account. The diffraction effects can be easily avoided by imposing an illumination at the reflectarray edges lower than −12 dB. It is also common to compute the radiation patterns using the Second Principle of Equivalence [2], and although this technique gives good results for the copolar and to some extent for the crosspolar pattern, the use of the the First Principle of Equivalence provides more accurate results [43,88], in which case the tangential magnetic field is needed [43]. Finally, the support structures should be taken into account [88] in case they are not properly covered by absorbents since their scatter field will affect the crosspolar component (but barely the copolar due to the high level of the field with regard to the crosspolar).

2.3.5. Effect of the dielectric frame

When manufacturing a reflectarray breadboard, it is very common that a dielectric frame is included. This frame is also backed by a ground plane but has no metallizations, and is employed to screw the breadboard to the supporting structure. Even though the field level at the edge of the reflectarray is quite low, usually below the optimum level of −10 dB, −12 dB which optimizes illumination efficiency [129] in order to minimize diffraction effects [2], modeling the frame is important to correctly characterize the radiated fields. The dielectric frame can be analyzed very efficiently by MoM since there are no metallizations and the analysis is greatly simplified [127]. The dielectric frame will present some losses due to the dielectric tangent loss, although they will be very low. More important is the phase shift introduced by the frame at each position, which will vary with the angle of

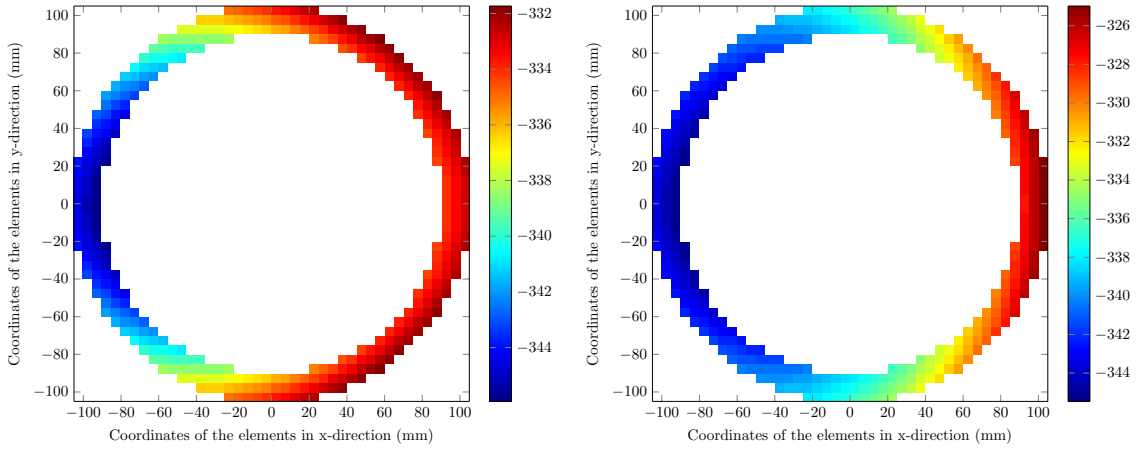

(a) *(b)*

Figure 2.8: *Phase shift introduced by the dielectric frame for (a) X polarization and (b) Y polarization.*

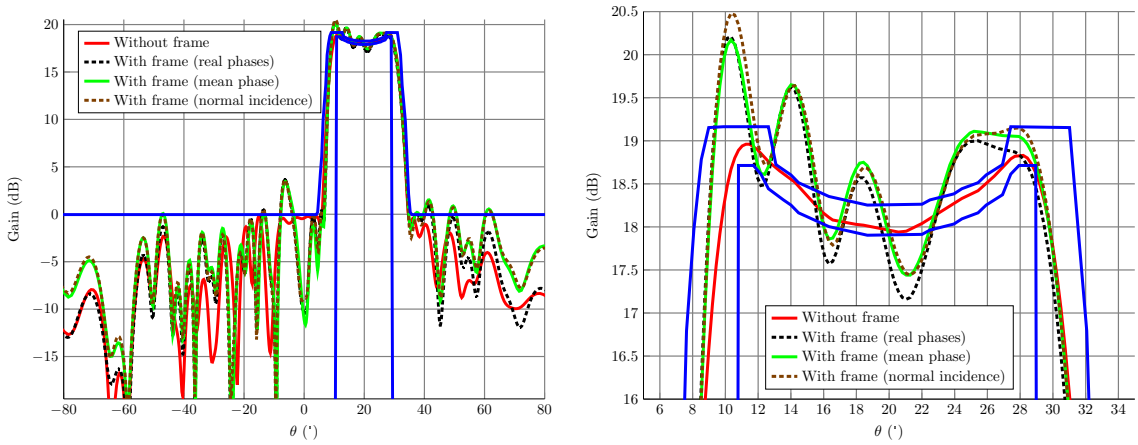

(a) *(b)*

Figure 2.9: *Effect of the inclusion of the dielectric frame in the reflectarray analysis for a reflectarray with isoflux antenna synthesized without frame. (a) Main cut in θ for $\varphi = 0$ for X polarization. (b) Zoom in the coverage area.*

incidence from the feed and can modify the copolar and crosspolar patterns when compared with the analysis with no dielectric frame. Also, as shown in Figure 2.8, the phase shift is different for each polarization, not only changing the distribution of the phase in the dielectric frame, but also the total range.

The frame is specified as a number of elements added as extra rows and columns to the edge of the reflectarray. For instance, the frame shown in Figure 2.8 was generated adding six extra rows (three at the upper edge and three at the lower edge) and six extra columns (three at the left edge and three at the right edge). Usually, a frame comprised of one, two or three extra elements at each side is enough [43], but there are cases in which the frame is comprised of an elevated number of extra rows and columns, such as in [80], which should be conveniently taken into account.

To show an example of how the dielectric frame affects the copolar pattern, it was added

to the phase distribution of a reflectarray which was previously synthesized without the frame. Also, to avoid other effects, the reflectarray is analyzed considering the elements as ideal phase shifters. The result is shown in Figure 2.9, where the main cut in θ is shown for X polarization, with and without dielectric frame taken into account in the analysis. After the phase-only synthesis, the isoflux pattern complies with the template specification, as demonstrated by the red solid line. However, if the dielectric frame shown in Figure 2.8 is added to the analysis, not only the side lobes change, increasing their values, but also the coverage area is strongly affected, adding a ripple of about 4 dB in this particular case.

The effect of the dielectric frame will increase when the frame is larger. Conversely, the effect will be smaller if the frame is narrower. In any case, it might affect differently to other shaped beams, although since the effect is not known beforehand, the reflectarray analysis should take into account the dielectric frame added to the antenna. Moreover, although it was not shown, the dielectric frame also affects the crosspolar radiation pattern.

2.4. Efficient computation of the far field radiated by reflectarray antennas

2.4.1. Far field radiated by a planar aperture

Reflectarray antennas are classified as aperture antennas and thus there are several ways of computing their radiation pattern, for instance, by using the plane wave spectra or equivalent currents, as described in [85] or [130]. In any case, all methods yield the same results and the far fields always depend on the tangential field on the aperture. For instance, using the formulation provided by [130], the far fields can be expressed according to the three Principles of Equivalence in electromagnetics. The use of one of them will depend on the knowledge one have of the electric and/or magnetic fields on the aperture. Applying the First Principle of Equivalence (also known as Love's Equivalence Principle), the radiated far fields are

$$E_\theta^{X/Y} = \frac{jk_0e^{-jk_0r}}{4\pi r}\left[P_x^{X/Y}\cos\varphi + P_y^{X/Y}\sin\varphi - \eta\cos\theta\left(Q_x^{X/Y}\sin\varphi - Q_y^{X/Y}\cos\varphi\right)\right], \quad (2.57a)$$

$$E_\varphi^{X/Y} = -\frac{jk_0e^{-jk_0r}}{4\pi r}\left[\cos\theta\left(P_x^{X/Y}\sin\varphi - P_y^{X/Y}\cos\varphi\right) + \eta\left(Q_x^{X/Y}\cos\varphi + Q_y^{X/Y}\sin\varphi\right)\right], \quad (2.57b)$$

while for the Second Principle of Equivalence (or Electric Conductor Equivalence Principle) they are

$$E_\theta^{X/Y} = \frac{jk_0e^{-jk_0r}}{2\pi r}\left(P_x^{X/Y}\cos\varphi + P_y^{X/Y}\sin\varphi\right), \quad (2.58a)$$

$$E_\varphi^{X/Y} = -\frac{jk_0e^{-jk_0r}}{2\pi r}\cos\theta\left(P_x^{X/Y}\sin\varphi - P_y^{X/Y}\cos\varphi\right), \quad (2.58b)$$

and for the Third Principle of Equivalence (or Magnetic Conductor Equivalence Principle)

$$E_\theta^{X/Y} = -\frac{jk_0\eta_0e^{-jk_0r}}{2\pi r}\cos\theta\left(Q_x^{X/Y}\sin\varphi - Q_y^{X/Y}\cos\varphi\right), \quad (2.59a)$$

$$E_{\varphi}^{X/Y} = -\frac{jk_0\eta_0 e^{-jk_0 r}}{2\pi r}\left(Q_x^{X/Y}\cos\varphi + Q_y^{X/Y}\sin\varphi\right), \tag{2.59b}$$

where P and Q are known as the spectrum functions and are computed as the Fourier transform of the electric and magnetic fields over an infinite aperture S which contains the antenna aperture

$$P_x^{X/Y}(u,\,v) = \iint_S E_{\mathrm{ref},x}^{X/Y}(x,\,y)\,e^{jk_0(ux+vy)}\,dx\,dy, \tag{2.60a}$$

$$P_y^{X/Y}(u,\,v) = \iint_S E_{\mathrm{ref},y}^{X/Y}(x,\,y)\,e^{jk_0(ux+vy)}\,dx\,dy, \tag{2.60b}$$

$$Q_x^{X/Y}(u,\,v) = \iint_S H_{\mathrm{ref},x}^{X/Y}(x,\,y)\,e^{jk_0(ux+vy)}\,dx\,dy, \tag{2.60c}$$

$$Q_y^{X/Y}(u,\,v) = \iint_S H_{\mathrm{ref},y}^{X/Y}(x,\,y)\,e^{jk_0(ux+vy)}\,dx\,dy, \tag{2.60d}$$

with $u = \sin\theta\cos\varphi$, $v = \sin\theta\sin\varphi$, k_0 the free-space wavenumber and $\eta = \mu_0 c_0$ the vacuum impedance.

It is very common to work only with the electric tangential field on the surface of the reflectarray [2], so the Second Principle of Equivalence in (2.58) is used. However, in the case of also having the magnetic field, the use of the First Principle in (2.57) is preferred since it provides more accurate results in the computation of the radiation patterns for the case of reflectarray antennas [2,43,88]. If there were perfect knowledge of both electric and magnetic fields over the infinite surface S, the three formulations of (2.57), (2.58) and (2.59) would provide the same radiation patterns for $z > 0$ [130]. However, that is not usually the case and some approximations are used, such as considering only a finite surface, sampling the field, using the plane wave approximation between the electric and magnetic fields, etc.

In this regard, since the extension of surface S in (2.60) is over an infinite plane, the radiated patterns expressed as the Fourier transform of the tangential fields is exact [85]. However, an approximation needs to be made in order to compute the radiation patterns of the aperture. Surface S is usually reduced to the surface of the aperture, i.e., fields in the aperture plane outside the aperture are considered negligible.

Finally, from the spherical components of the far field, the copolar and crosspolar components are computed applying Ludwig's third definition of crosspolarization [131]. For the Y polarization they are defined as

$$\begin{pmatrix} E_{\mathrm{cp}}^{Y} \\ E_{\mathrm{xp}}^{Y} \end{pmatrix} = \begin{pmatrix} \sin\varphi & \cos\varphi \\ \cos\varphi & -\sin\varphi \end{pmatrix} \begin{pmatrix} E_{\theta}^{Y} \\ E_{\varphi}^{Y} \end{pmatrix}, \tag{2.61}$$

while for the X polarization a rotation of 90° must be added to φ to account for X axis

rotation with regard to the Y axis,

$$\begin{pmatrix} E_{\text{cp}}^{X} \\ E_{\text{xp}}^{X} \end{pmatrix} = \begin{pmatrix} \cos\varphi & -\sin\varphi \\ -\sin\varphi & -\cos\varphi \end{pmatrix} \begin{pmatrix} E_{\theta}^{X} \\ E_{\varphi}^{X} \end{pmatrix}. \tag{2.62}$$

2.4.2. Gain, directivity and antenna efficiency

The antenna gain can be easily computed using the input power of the feed horn P_{feed}, according to

$$G^{X/Y}(\theta,\,\varphi) = \frac{\left|\vec{E}^{X/Y}(\theta,\,\varphi)\right|^2 4\,\pi\,r^2}{2\,\eta_0\,P_{\text{feed}}}. \tag{2.63}$$

In the case of an ideal far field model of the feed, the parameter P_{feed} was computed in (2.27). If a real feed horn were considered, P_{feed} would be substituted by the power radiated by the horn. Since the antenna requirements are usually given in copolar gain, the copolar and crosspolar patterns are expressed in gain using the following expressions,

$$G_{\text{cp}}^{X/Y}(\theta,\,\varphi) = \frac{\left|E_{\text{cp}}^{X/Y}(\theta,\,\varphi)\right|^2 4\,\pi\,r^2}{2\,\eta_0\,P_{\text{feed}}}, \tag{2.64a}$$

$$G_{\text{xp}}^{X/Y}(\theta,\,\varphi) = \frac{\left|E_{\text{xp}}^{X/Y}(\theta,\,\varphi)\right|^2 4\,\pi\,r^2}{2\,\eta_0\,P_{\text{feed}}}. \tag{2.64b}$$

The gain computed by (2.64) includes the spillover and the substrate losses in the reflectarray if they were included in the analysis of the reflectarray elements.

Similarly, the directivity of a reflectarray antenna is defined as

$$D(\theta,\,\varphi) = \frac{\left|\vec{E}^{X/Y}(\theta,\,\varphi)\right|^2 4\,\pi\,r^2}{2\,\eta_0\,P_{\text{RA}}}, \tag{2.65}$$

where the parameter P_{RA} is the power radiated by the reflectarray, computed considering the field radiated by the reflectarray obtained with one of the Principles of Equivalence,

$$P_{\text{RA}} = \int_{\theta=0}^{\pi/2}\int_{\varphi=0}^{2\pi} \frac{\left|\vec{E}^{X/Y}\,(\theta,\,\varphi)\right|^2}{2\,\eta_0}\,r^2\sin\theta\,d\theta\,d\varphi. \tag{2.66}$$

As in the case of the gain, the copolar and crosspolar directivities can be defined by taking into account the copolar or crosspolar components of the radiated field, resulting in

$$D_{\text{cp}}^{X/Y}(\theta,\,\varphi) = \frac{\left|E_{\text{cp}}^{X/Y}(\theta,\,\varphi)\right|^2 4\,\pi\,r^2}{2\,\eta_0\,P_{\text{RA}}}, \tag{2.67a}$$

$$D_{\text{xp}}^{X/Y}(\theta,\,\varphi) = \frac{\left|E_{\text{xp}}^{X/Y}(\theta,\,\varphi)\right|^2 4\,\pi\,r^2}{2\,\eta_0\,P_{\text{RA}}}. \tag{2.67b}$$

Finally, from the comparison of the gain and the directivity, the efficiency of the

reflectarray antenna is obtained as

$$\varepsilon_{\mathrm{RA}} = \frac{G_{\max}}{D_{\max}}. \tag{2.68}$$

Note that this efficiency takes into account all the substrate losses, the spillover and the aperture illumination.

2.4.3. Efficient computation of the spectrum functions

The most time consuming operation in the computation of the radiated far fields by a planar aperture is the spectrum functions defined in (2.60), which can be obtained as the Fourier transforms of the tangential fields on the aperture. If the tangential field corresponds to an analytical expression that is easy to integrate, the spectrum function in (2.60) can be quickly obtained in an exact fashion. However, it is more common to have the fields sampled over a grid of $N = N_x \cdot N_y$ cells, which in the case of the reflectarray antenna would correspond to the reflectarray elements or cells. In this case, the spectrum function can be calculated as a sum of the integrals in each cell as

$$P(u,\, v) = \sum_{i=1}^{N} \left[\iint_{S_i} E(x,\, y)\, e^{jk_0(ux+vy)}\, dx\, dy \right], \tag{2.69}$$

where for the sake of simplicity a generic spectrum function P and tangential electric field E were used, since the operations involved will be identical for both components, x and y and for both fields, E and H, as well as both polarizations X and Y. In (2.69), S_i is the surface of cell i.

At this point some assumptions are made. First, the field at each cell is considered to be constant. This is a good approximation when the samples are close to each other, i.e. the cell surface is small with regard to the surface S. And second, the cell is rectangular with dimensions $a_i \times b_i$. This last assumption is convenient because it facilitates the analytical operations with (2.69) and it is very common to have the fields sampled in that manner when analysing arrays. With these assumptions in mind, (2.69) can be rewritten as

$$P(u,\, v) = \sum_{i=1}^{N} \left[E_i \int_{x=x_i-a_i/2}^{x_i+a_i/2} \int_{y=y_i-b_i/2}^{y_i+b_i/2} e^{jk_0(ux+vy)}\, dx\, dy \right] \tag{2.70}$$

where E_i is the constant field in the cell i, $(x_i,\, y_i)$ are the coordinates of the center of each cell in which the surface is divided and $(a_i,\, b_i)$ is the local periodicity of each cell. If the discretization is periodic, the local periodicity of all cells will be the same. On the contrary, if the discretization is non-uniform, each cell will have a different local periodicity, depending on its distance to the neighboring cells.

The function

$$f(x, y) = e^{jk_0(ux+vy)} \tag{2.71}$$

is multiplicatively separable since it can be expressed as

$$f(x,\, y) = g(x)\, h(y) = e^{jk_0 ux}\, e^{jk_0 vy}. \tag{2.72}$$

Hence, the integral in (2.70) can be solved applying Fubini's theorem separating the double integral into a product of two single integrals. After solving the integrals, the spectrum function is

$$P(u,\, v) = \sum_{i=1}^{N} \left[E_i\, K_i(u,\, v)\, e^{jk_0(ux_i + vy_i)} \right], \tag{2.73}$$

with

$$K_i(u,\, v) = a_i\, b_i \operatorname{sinc}\left(\frac{k_0\, u\, a_i}{2} \right) \operatorname{sinc}\left(\frac{k_0\, v\, b_i}{2} \right), \tag{2.74}$$

and the sinc function defined as

$$\operatorname{sinc}(x) = \frac{\sin(x)}{x}. \tag{2.75}$$

When the grid is uniform, $K_i(u,\, v)$ is the same for all cells and (2.73) can be calculated by means of a 2D FFT very efficiently with a time complexity of $\mathcal{O}\,(M \log M)$, being $M = M_u \cdot M_v$ the number of points in the UV grid [2]. In principle, the FFT computes the transform in a grid with the same number of points as the source, i.e. $M_u = N_x$ and $M_v = N_y$. Nevertheless, the spectrum functions can be computed in a larger number of $(u,\, v)$ points by extending the grid on the tangential fields plane ($M_u > N_x,\ M_v > N_y$) and setting the amplitude to zero for all the elements outside the original plane [2]. This is done to have better resolution of the computed far fields. For the aperiodic case, (2.73) cannot be directly computed with the NUFFT, since K_i depends on the spectral variables u and v. Some manipulations are needed, which will be detailed later.

Since the development of the efficient computation of (2.73) is different for the periodic and aperiodic (or non-uniform) case, they will be treated separately in following sections, although bearing in mind that the periodic case is a particular case of the aperiodic one.

2.4.3.1. Periodic case

For the uniform grid, all the local periodicities are the same, that is, it holds that

$$a_i = a \qquad \text{and} \qquad b_i = b. \tag{2.76}$$

This means that function $K(u,\, v)$ no longer depends on the i index and (2.73) can be expressed as

$$P(u,\, v) = K(u,\, v) \sum_{i=1}^{N} \left[E_i\, e^{jk_0(ux_i + vy_i)} \right]. \tag{2.77}$$

The first step to be able to compute (2.77) as a 2D FFT, is to relate the physical coordinates of each element (x_i, y_i) with the integer indices (m, n). In this regard, the single summation in (2.77) with index i goes over all the elements of the reflectarray. It

can be expanded to a double sum with indices (m, n) instead of i as

$$P(u,v) = K(u,v) \sum_{m=0}^{N_x-1} \sum_{n=0}^{N_y-1} \left[E^{mn}\, e^{jk_0(ux_m+vy_n)} \right], \tag{2.78}$$

where $N = N_x \cdot N_y$, (x_m, y_n) are the coordinates of the (m,n)th element center and E^{mn} the constant field at the (m,n)th element. Taking into account that the RCS is placed at the center of the reflectarray, the coordinates (x_m, y_n) are related to the integer indices (m,n) through the following expressions (see Figure 2.10):

$$x_m = -\frac{N_x\, a}{2} + (m + 1/2)\, a = \frac{a}{2}\left(-N_x + 2m + 1\right), \qquad m = 0, 1, \ldots, N_x - 1, \tag{2.79a}$$

$$y_n = -\frac{N_y\, b}{2} + (n + 1/2)\, b = \frac{b}{2}\left(-N_y + 2n + 1\right), \qquad n\ = 0, 1, \ldots, N_y - 1. \tag{2.79b}$$

Substituting (2.79) in (2.78) it follows,

$$P(u,v) = K(u,v) \sum_{m=0}^{N_x-1} \sum_{n=0}^{N_y-1} \left[E^{mn}\, e^{jk_0\left[u\frac{a}{2}(-N_x+2m+1)+v\frac{b}{2}(-N_y+2n+1)\right]} \right]. \tag{2.80}$$

Developing the exponent in (2.80) and taking out the common factor which does not depend on the (m,n) indices,

$$P(u,v) = K(u,v)\, K'(u,v) \sum_{m=0}^{N_x-1} \sum_{n=0}^{N_y-1} \left[E^{mn}\, e^{jk_0(uma+vnb)} \right], \tag{2.81}$$

being

$$K'(u,v) = e^{-j\frac{k_0}{2}[u(N_x-1)a+v(N_y-1)b]}. \tag{2.82}$$

By inspecting (2.81), it is clear that it can be efficiently computed by means of a 2D FFT. However, more manipulations are needed. The general expression of the 2D DFT is

$$F(p,q) = \mathrm{DFT2}\left[f(m,n)\right] = \sum_{m=0}^{M-1} \sum_{n=0}^{N-1} \left[f(m,n)\, e^{-j\frac{2mp\pi}{M}} e^{-j\frac{2nq\pi}{N}} \right], \tag{2.83a}$$

$$f(m,n) = \mathrm{IDFT2}\left[F(p,q)\right] = \frac{1}{MN} \sum_{m=0}^{M-1} \sum_{n=0}^{N-1} \left[F(p,q)\, e^{j\frac{2mp\pi}{M}} e^{j\frac{2nq\pi}{N}} \right]. \tag{2.83b}$$

Equation (2.83b) is very similar to (2.81). Thus, the spectrum function can be written as an inverse Fourier transform by applying the following unknown changes,

$$u = \frac{2\pi}{N_x\, a\, k_0}\, p, \qquad p = 0, 1, \ldots, N_x - 1, \tag{2.84a}$$

$$v = \frac{2\pi}{N_y\, b\, k_0}\, q, \qquad q = 0, 1, \ldots, N_y - 1, \tag{2.84b}$$

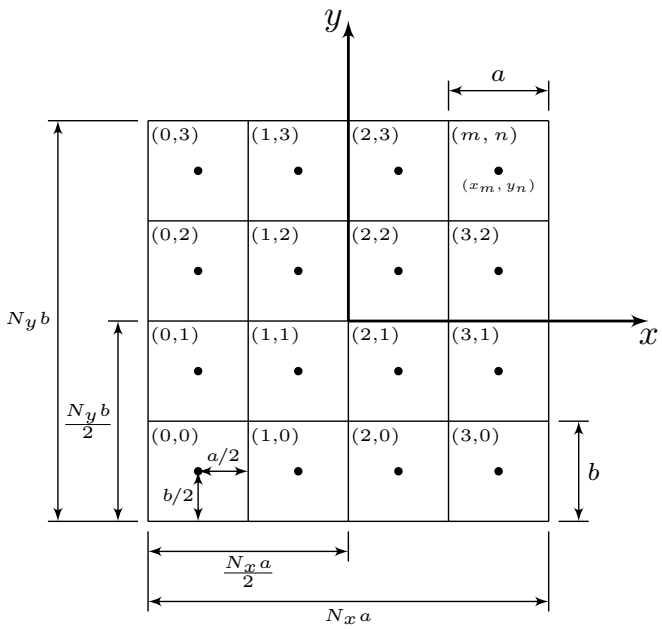

Figure 2.10: *Reflectarray dimensions for change of index from i to (m, n).*

to (2.81), having

$$P(p,q) = K(p,q)\, K'(p,q) \sum_{m=0}^{N_x-1} \sum_{n=0}^{N_y-1} \left[E^{mn} e^{j\frac{2mp\pi}{N_x}} e^{j\frac{2nq\pi}{N_y}} \right], \tag{2.85}$$

or equivalently

$$P(p,q) = N_x \cdot N_y \cdot K(p,q) \cdot K'(p,q) \cdot \mathrm{IDFT2}\left[E^{mn}\right]. \tag{2.86}$$

The same expression as in (2.86) applies for components $\hat{x}$ and $\hat{y}$ of both polarizations for both fields, electric and magnetic, only changing E^{mn} in (2.86) by the corresponding field.

One important aspect of the discrete Fourier transform is that the number of points in the two domains (source domain or reflectarray aperture with $N_x \times N_y$ points and spectral domain or far field mesh with $M_u \times M_v$ points) are the same, and since it is the tangential field the one that is transformed, the number of points in both meshes will be $N_x \times N_y$. Usually, this number of points is not sufficient to obtain good resolution of the far fields in the UV grid. Nevertheless, the spectrum functions can be computed in a larger number of points by extending the grid on the tangential fields plane ($M_u > N_x$, $M_v > N_y$) and setting the amplitude equal to zero for all the elements outside the original plane. In order to speed up computations, it is desirable that M_u and M_v are a power of 2, although new FFT algorithms are also optimized when the number of points in the transform are composite with factors 2, 3, 5, 7 and 11 [132].

Another important point is the spatial region where the radiated field is computed. Ideally, the far fields should be obtained in the whole visible region, defined by the values of (u, v) that fulfill $u^2 + v^2 \leq 1$. However, according to (2.84), the range for which u and

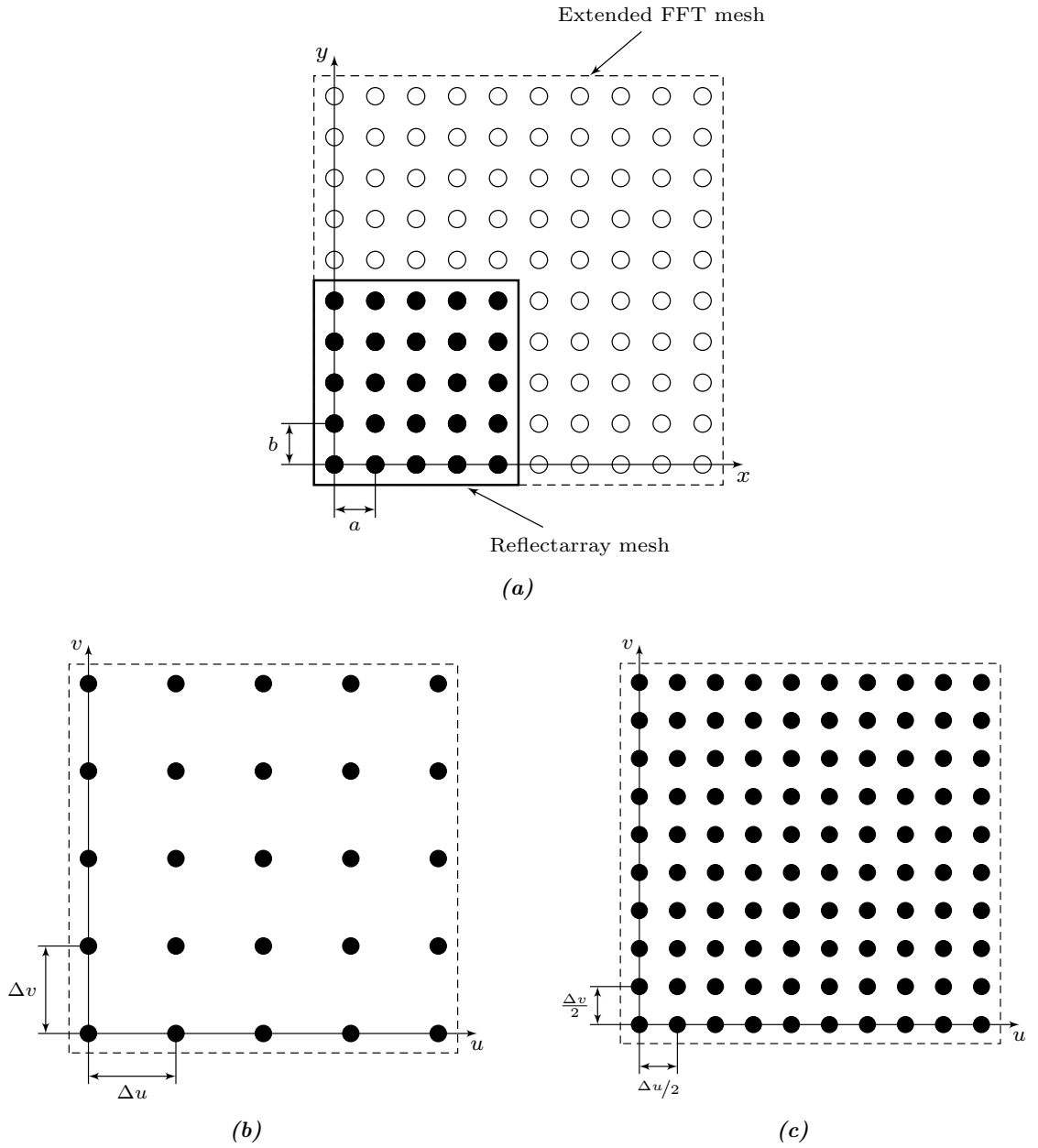

Figure 2.11: *Meshes used for the Discrete Fourier Transform in the source and UV domains. (a) Source domain, showing the reflectarray and extended meshes. (b) UV mesh considering the original reflectarray mesh. (c) UV mesh considering an extended mesh with double size of the reflectarray.*

v are defined in the computation of (2.86) is

$$0 \leq u < \frac{\lambda_0}{a} \qquad \text{and} \qquad 0 \leq v < \frac{\lambda_0}{b}. \tag{2.87}$$

Note that terms of $-1/(N_x\, a\, k_0)$ and $-1/(N_y\, b\, k_0)$ have been neglected from (2.87), according to the strict limits imposed in (2.84).

Equation (2.87) shows that the radiated far fields are computed only for positive values of the UV grid. In order to compute the radiation pattern also for negative values in the

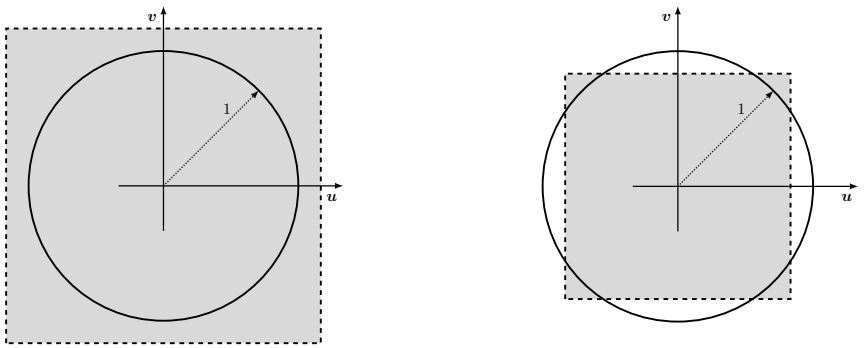

Figure 2.12: *Visible region inside the unit circle and region where the far field is computed in grey. (a) Periodicities larger than half a wavelength. (b) Periodicities smaller than half a wavelength.*

UV grid, the following conditions must be accomplished,

$$-\frac{\lambda_0}{2a} \leq u < \frac{\lambda_0}{2a} \qquad \text{and} \qquad -\frac{\lambda_0}{2b} \leq v < \frac{\lambda_0}{2b}. \tag{2.88}$$

Hence, a shift in the p and q indices is necessary to center the mesh of the 2D FFT and the visible region. Such displacement is

$$p' = p - \frac{N_x}{2} \qquad \text{and} \qquad q' = q - \frac{N_y}{2}, \tag{2.89}$$

and it is only necessary to add it to the terms inside the IDFT2. Finally, including the displacement in the spectral function, its final expression is [2]

$$P(p,q) = N_x \cdot N_y \cdot K(p,q) \cdot K'(p,q) \cdot \text{IDFT2}\left[E^{mn}\, e^{-j\pi(m+n)}\right]. \tag{2.90}$$

With the shift in (2.89) the radiation pattern is computed in the UV grid within the limits of (2.88). Those limits depend on the periodicity and two possibilities arise. If the periodicity is larger than half a wavelength ($a, b > \lambda_0/2$), the far field will be computed in a grid which exceeds the visible region as shown in Figure 2.12(a). The points outside the visible region have complex (θ, φ) angles and thus they are not valid. On the other hand, for periodicities smaller than half a wavelength ($a, b < \lambda_0/2$), the radiation pattern will not be computed in the whole visible region. In any case, since the visible region is defined by a circle and the far field is computed in a rectangular grid, even in this case the far field can be computed for complex angles, as shown in Figure 2.12(b).

2.4.3.2. Aperiodic case

As it has been shown in the previous section, when the grid is uniform, the spectrum function can be efficiently computed by means of a 2D FFT. If $N = N_x \cdot N_y$ is the number of elements of the reflectarray and $M = M_u \cdot M_v$ with $M_u > N_x$ and $M_v > N_y$ the number of points in the UV grid in which the far fields are computed, the time complexity for the computation of one spectrum function using the FFT algorithm is $\mathcal{O}(M \log M)$, in

contrast to the complexity $\mathcal{O}(NM)$ that would take a direct evaluation of the spectrum function as defined in (2.77). However, when the grid is non-uniform and the general expression of P is (2.73) the FFT can no longer be applied. Also, the NUFFT cannot be used because $K_i(u,v)$ is a function of the spectral variables, u and v. For the particular case of the array factor, that is, when $K_i = 1$ the NUFFT could be directly applied to efficiently evaluate the sum. However, the array factor provides less accurate results since it does not take into account the $K_i(u,v)$ factor. Also, as stated before, a direct evaluation of P is not efficient and would take considerable amounts of time, specially for large arrays with good resolution in the far field. Hence, in order to use the NUFFT algorithm, some manipulations to (2.73) have to be made.

Developing $K_i(u,v)$ in (2.74) using the definition of sinc yields

$$K_i(u,v) = \frac{4}{k_0^2\, u\, v} \sin\left(\frac{k_0\, u\, a_i}{2}\right) \sin\left(\frac{k_0\, v\, b_i}{2}\right). \tag{2.91}$$

Now, expressing the sine functions according to Euler's formula, operating, grouping the exponentials and substituting in (2.73) produces

$$\begin{aligned} P(u,v) = \frac{-1}{k_0^2\, u\, v} \sum_{i=1}^{N} \Bigg[E_i \Big(& e^{jk_0(u\, a_i/2 + v\, b_i/2)} - e^{jk_0(u\, a_i/2 - v\, b_i/2)} \\ & - e^{jk_0(-u\, a_i/2 + v\, b_i/2)} + e^{jk_0(-u\, a_i/2 - v\, b_i/2)} \Big) e^{jk_0(u x_i + v y_i)} \Bigg]. \end{aligned} \tag{2.92}$$

By inspecting (2.92) it is clear that $P(u,v)$ can be expressed as the sum of four summations

$$\begin{aligned} P(u,v) = \frac{-1}{k_0^2\, u\, v} \Big[& F\left(u,v\,;x^+,y^+\right) - F\left(u,v\,;x^+,y^-\right) \\ & - F\left(u,v\,;x^-,y^+\right) + F\left(u,v\,;x^-,y^-\right) \Big], \end{aligned} \tag{2.93}$$

with

$$F(u,v\,;x,y) = \sum_{i=1}^{N} E_i\, e^{jk_0(u x_i + v y_i)}, \tag{2.94}$$

and

$$x^{\pm} = x \pm {}^{a_i}\!/_2 \qquad ; \qquad y^{\pm} = y \pm {}^{b_i}\!/_2. \tag{2.95}$$

The NUFFT algorithm computes efficiently expressions of the following form [133,134],

$$f(\vec{s}_k) = \sum_{i=1}^{N} c_i\, e^{\pm j\, \vec{s}_k \cdot \vec{p}_i}, \tag{2.96}$$

where $\vec{s}_k$ is a vector of the Fourier or spectral variables and $\vec{p}_i$ are the physical coordinates of the sources c_i. Identifying the summation of (2.94) with the general expression of (2.96) it is clear that each of the four summations of (2.93) can be computed efficiently by one NUFFT. In contrast, the single summation of (2.73) cannot be computed by NUFFT because c_i in (2.96) does not depend on the spectral variables as in (2.73). Hence, each spectrum function can be computed with four NUFFT with an overall time complexity of

$\mathcal{O}(M \log M)$.

Taking into account the final expression of P in terms of the NUFFT in (2.93), there is a singularity when $u = 0$ or $v = 0$. This problem arises as a consequence of decomposing the sinc functions into exponentials. It can be circumvented by avoiding computing the spectrum functions when $u = 0$ or $v = 0$, or computing only both rects using (2.73).

One particularity of the NUFFT algorithm is that its time complexity is precision-dependent. A more accurate description of its time complexity [135] is

$$\mathcal{O}\left(M \log M + M \log^2 \xi^{-1}\right), \tag{2.97}$$

where ξ is the desired accuracy which bounds the error of the obtained solution as [135]

$$\frac{||\tilde{P} - P||}{||P||} \leq \xi, \tag{2.98}$$

being P the exact value and $\tilde{P}$ the computed value using the NUFFT algorithm. If it is necessary to compute the rects $u = 0$ and $v = 0$, a time complexity of $\mathcal{O}(N \cdot M_v)$ for $u = 0$ and $\mathcal{O}(N \cdot M_u)$ for $v = 0$ must be added. Then, the time complexity would be

$$\mathcal{O}\left(M \log M + M \log^2 \xi^{-1} + N\left(M_u + M_v\right)\right), \tag{2.99}$$

which is still faster than the direct evaluation of (2.73). Usually, $M_u = M_v$, and thus the time complexity can be written as

$$\mathcal{O}\left(M \log M + M \log^2 \xi^{-1} + N\sqrt{M}\right). \tag{2.100}$$

Since the uniform grid is a particular case of the non-uniform one, the spectrum functions can always be computed with the NUFFT. When the grid period is bigger than half a wavelength, for instance when analysing an array with such periodicity, using the FFT to compute the far fields presents the limitation that they cannot be obtained in the whole visible region, as shown before. If there is the need to compute the far field in the whole UV grid, a direct computation of (2.73) with a time complexity of $\mathcal{O}(NM)$ must be performed. However, due to the generality of the NUFFT provided by (2.96), it allows to compute the far field in the entire visible region without regard to the periodicity and preserving the $\mathcal{O}(M \log M)$ complexity.

2.4.4. Generalization for continuous incident field

One of the assumptions made in the previous formulation was that the field at each rectangular cell was constant. This allowed to analytically solve the integral in (2.70) by means of Fubini's theorem. However, the formulation in the previous section can be generalized assuming a smooth function for the tangential field at each cell, $E_i(x, y)$, so it is narrowband. The following generalization is independent of the type of reflectarray element (i.e. rectangular patch, parallel dipoles, ...) and only requires that the unit cell is rectangular, as in the previous section.

In principle, $E_i(x,y)$ is only defined at cell i, where it is integrated. Hence, it can take any value outside cell i. Without loss of generality, we can define a new function $\tilde{E}_i(x,y)$ as a periodic function in $x,y \in \mathbb{R}$, with period $a_i \times b_i$, being its periodic value $E_i(x,y)$. Equation (2.69) can thus be expressed as

$$P(u,v) = \sum_{i=1}^{N} \left[\iint_{S_i} \tilde{E}_i(x,y)\, e^{jk_0(ux+vy)}\, dx\, dy \right]. \tag{2.101}$$

Since $\tilde{E}_i(x,y)$ is periodic, it has a representation in terms of a Fourier series

$$\tilde{E}_i(x,y) = \sum_{k=-\infty}^{\infty} \sum_{l=-\infty}^{\infty} c_{k,l,i}\, e^{+j2\pi\left(x\frac{k}{a_i}+y\frac{l}{b_i}\right)}, \tag{2.102}$$

$$c_{k,l,i} = \frac{1}{a_i\, b_i} \int_{x=x_i-\frac{a_i}{2}}^{x_i+\frac{a_i}{2}} \int_{y=y_i-\frac{b_i}{2}}^{y_i+\frac{b_i}{2}} \tilde{E}_i(x,y)\, e^{-j2\pi\left(x\frac{k}{a_i}+y\frac{l}{b_i}\right)}\, dx\, dy, \tag{2.103}$$

with $k,l \in \mathbb{Z}$. Because $\tilde{E}_i(x,y)$ is assumed to be narrowband (since the incident field is smooth, its associated function will be narrowband, and hence the same will occur to the tangential field), the summation in (2.102) can be truncated to a finite number of values with a small error in the representation of the function, thus having

$$\tilde{E}_i(x,y) \approx \sum_{k=-K_1}^{K_1} \sum_{l=-L_1}^{L_1} c_{k,l,i}\, e^{+j2\pi\left(x\frac{k}{a_i}+y\frac{l}{b_i}\right)} = \sum_{k,l} c_{k,l,i}\, e^{+j2\pi\left(x\frac{k}{a_i}+y\frac{l}{b_i}\right)}, \tag{2.104}$$

with $k \in [-K_1, K_1] \in \mathbb{Z}$ and $l \in [-L_1, L_1] \in \mathbb{Z}$. Hence, $\tilde{E}_i(x,y)$ can be represented by $K \cdot L = (2K_1+1)(2L_1+1)$ Fourier harmonics. Substituting (2.104) in (2.101) yields

$$P(u,v) \approx \sum_{i=1}^{N} \left[\iint_{S_i} \left(\sum_{k,l} c_{k,l,i}\, e^{+j2\pi\left(x\frac{k}{a_i}+y\frac{l}{b_i}\right)} \right) e^{jk_0(ux+vy)}\, dx\, dy \right]. \tag{2.105}$$

Using the linearity of integration, the double integral and the sum can be interchanged,

$$P(u,v) \approx \sum_{i=1}^{N} \left[\sum_{k,l} \left(\iint_{S_i} c_{k,l,i}\, e^{+j2\pi\left(x\frac{k}{a_i}+y\frac{l}{b_i}\right)} e^{jk_0(ux+vy)}\, dx\, dy \right) \right]. \tag{2.106}$$

The following step is to solve the integral in a period. The integration limits in (2.106) are the same as in (2.70). Also, as in (2.70), the integrand is a separable function,

$$f(x,y) = e^{j2\pi x\frac{k}{a_i}}\, e^{j2\pi y\frac{l}{b_i}} e^{jk_0ux} e^{jk_0vy} = e^{jx\left(k_0u+\frac{2\pi k}{a_i}\right)}\, e^{jy\left(k_0v+\frac{2\pi l}{b_i}\right)} = g(x)h(y), \tag{2.107}$$

so Fubini's theorem can be used again to solve the double integral, separating it into a product of two single integrals which are identically solved, yielding

$$P(u,v) \approx \sum_{i=1}^{N} \left[\sum_{k,l} \left(c_{k,l,i}\, K_{k,l,i}(u,v)\, e^{jx_i\left(k_0u+\frac{2\pi k}{a_i}\right)}\, e^{jy_i\left(k_0v+\frac{2\pi l}{b_i}\right)} \right) \right], \tag{2.108}$$

with

$$K_{k,l,i}(u,v) = a_i\, b_i \,\mathrm{sinc}\left(\frac{k_0\, u\, a_i}{2} + \pi\, k\right) \mathrm{sinc}\left(\frac{k_0\, v\, b_i}{2} + \pi\, l\right). \tag{2.109}$$

Finally, the two sums can be interchanged due to the linearity of the sum,

$$P(u,v) \approx \sum_{k,l} \left[\sum_{i=1}^{N} \left(c_{k,l,i}\, K_{k,l,i}(u,v)\, e^{jx_i\left(k_0 u + \frac{2\pi k}{a_i}\right)}\, e^{jy_i\left(k_0 v + \frac{2\pi l}{b_i}\right)}\right)\right]. \tag{2.110}$$

Again, and as in the previous case, the development can be done for a periodic and aperiodic case, leading to the use of the FFT or NUFFT algorithms, respectively.

2.4.4.1. Periodic case

For the periodic case, the periodicity of all elements is the same, so (2.76) holds. The coefficients $c_{k,l,i}$ still depend on the i index and (2.110) can be rewritten as

$$P(u,v) \approx \sum_{k,l} K_{k,l}(u,v) \left[\sum_{i=1}^{N} \left(c_{k,l,i}\, e^{jx_i\left(k_0 u + \frac{2\pi k}{a}\right)}\, e^{jy_i\left(k_0 v + \frac{2\pi l}{b}\right)}\right)\right]. \tag{2.111}$$

In (2.111), the exponential in the innermost sum can be regrouped to separate the terms that depend on the spectral variables u and v, having

$$P(u,v) \approx \sum_{k,l} K_{k,l}(u,v) \left[\sum_{i=1}^{N} \left(c_{k,l,i}\, e^{j2\pi\left(\frac{x_i k}{a} + \frac{y_i l}{b}\right)}\, e^{jk_0(x_i u + y_i v)}\right)\right]. \tag{2.112}$$

Defining

$$d_{k,l,i} = c_{k,l,i}\, e^{j2\pi\left(\frac{x_i k}{a} + \frac{y_i l}{b}\right)}, \tag{2.113}$$

and substituting (2.113) in (2.112)

$$P(u,v) \approx \sum_{k,l} K_{k,l}(u,v) \left[\sum_{i=1}^{N} \left(d_{k,l,i}\, e^{jk_0(x_i u + y_i v)}\right)\right]. \tag{2.114}$$

Equation (2.114) is very similar to (2.77), where the sum was expressed as a 2D DFT and later solved with the 2D FFT algorithm. In this case, following the same steps as in Section 2.4.3.1, (2.114) can be expressed as a linear combination of KL DFT to obtain one spectrum function.

2.4.4.2. Aperiodic case

For the aperiodic case, the steps are similar to those in Section 2.4.3.2. The $K_{k,l,i}(u,v)$ function in (2.109) is decomposed taking into account the definition of sinc in (2.75), obtaining

$$K_{k,l,i}(u,v) = \frac{4\, a_i\, b_i\, c_{k,l,i}}{(a_i\, k_0\, u + 2\,\pi\, k)\,(b_i\, k_0\, v + 2\,\pi\, l)} \sin\left(\frac{a_i\, k_0\, u}{2} + \pi\, k\right) \sin\left(\frac{b_i\, k_0\, v}{2} + \pi\, l\right). \tag{2.115}$$

Now, the sine functions are expressed using the Euler's formula, operating, grouping the exponentials and substituting in (2.110) the following result is obtained

$$\begin{aligned} P(u,v) \approx \sum_{k,l} \Big[& F_{k,l}^{0,0}(u,v;x^+,y^+) - F_{k,l}^{0,1}(u,v;x^+,y^-) \\ & - F_{k,l}^{1,0}(u,v;x^-,y^+) + F_{k,l}^{1,1}(u,v;x^-,y^-) \Big], \end{aligned} \tag{2.116}$$

with

$$F_{k,l}^{n_1,n_2}(u,v;x,y) = \sum_{i=1}^{N} d_{k,l,i}^{n_1,n_2}\, e^{jk_0(ux_i+vy_i)}, \tag{2.117}$$

being

$$d_{k,l,i}^{n_1,n_2} = \frac{-a_i\, b_i\, c_{k,l,i}\, e^{j\pi\left[k\left(\frac{2x_i}{a_i}+(-1)^{n_1}\right)+l\left(\frac{2y_i}{b_i}+(-1)^{n_2}\right)\right]}}{(a_i k_0 u + 2\pi k)(b_i k_0 v + 2\pi l)}, \tag{2.118}$$

and $x^{\pm}$, $y^{\pm}$ the same as in (2.95).

In this case, the spectrum function is obtained as a linear combination of $4KL$ NUFFT that depend on the Fourier coefficients of (2.103).

2.4.4.3. Computation of the Fourier coefficients

The only remaining issue is to compute those coefficients. If the function $\tilde{E}_i(x,y)$ can be provided analytically and can be integrated solving (2.103), then the coefficients $c_{k,l,i}$ are immediately obtained. Another method is to have the field within the cell sampled in a uniform grid of $R_x \times R_y$ points. This way, the double integral in (2.103) can be evaluated as a double summation

$$c_{k,l,i} = \frac{\Delta x\, \Delta y}{a_i\, b_i} \sum_{p=0}^{R_x-1} \sum_{q=0}^{R_y-1} E_{r,s,i}\, e^{-j2\pi\left(x\frac{k}{a_i}+y\frac{l}{b_i}\right)}, \tag{2.119}$$

which can be expressed as a 2D DFT and hence computed efficiently as a 2D FFT. As a final remark, if the field in the unit cell is sampled in a non-uniform grid, the coefficients $c_{k,l,i}$ could still be computed efficiently by means of the NUFFT by following the procedure developed in a previous section for aperiodic reflectarrays.

2.4.5. Numerical examples

In this section numerical examples are provided for the efficient computation of the spectrum functions with constant field on each cell. Since the NUFFT can be used with uniform and non-uniform grids, both cases are treated and compared with the use of FFT and direct evaluation of (2.73). The computed far fields are obtained using Ludwig's third definition [131] and are radiated by a planar reflectarray of $N_x \times N_y$ rectangular cells.

2.4.5.1. Uniform grid with large period and pencil beam pattern

In the first case, a periodic reflectarray of 50×50 elements that generates a pencil beam pattern is analyzed. It has a periodicity of $(a,b) = (0.8\lambda, 0.7\lambda)$ at 35 GHz. The beam

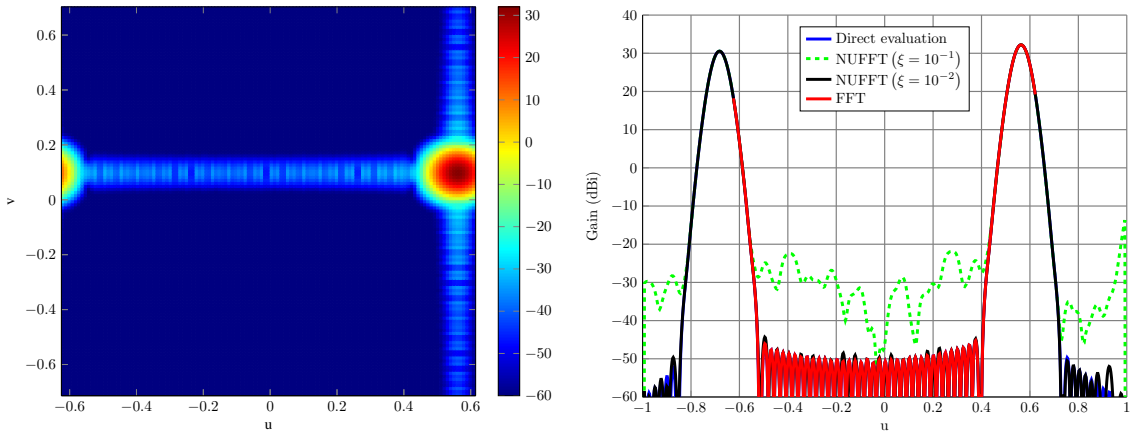

(a) *(b)*

Figure 2.13: *Copolar radiation pattern in gain (dBi) of a periodic reflectarray which generates a pencil beam pattern with a grating lobe. (a) 3D copolar pattern computed with the FFT. (b) Main cut computed by different methods. Lines blue and black are superimposed.*

pointing direction is $(\theta, \varphi) = (35°, 10°)$. Due to the large period and extreme pointing direction, a grating lobe is produced. This is an extreme case of theoretical interest to show some capabilities of the developed method. The analysis with FFT only allows to compute the far field within the region $u \in [-0.63, 0.63]$ and $v \in [-0.71, 0.71]$ according to (2.88). Figure 2.13(a) shows the computed 3D radiation pattern with FFT for the copolar component. As it can be seen, the FFT cannot compute the radiated field in the whole visible region and, in this particular case, the two beams (principal beam and grating lobe) are not fully calculated.

However, if the spectrum functions are calculated with a direct evaluation or the NUFFT, the far field can be obtained in the whole visible region. Figure 2.13(b) shows the main cut of the far field of Figure 2.13(a) computed with different methods: the FFT, a direct evaluation of the spectrum functions and the NUFFT with two different values of the parameter ξ. While the FFT does not compute the whole cut, as also shown in Figure 2.13(a), the NUFFT and direct evaluation do. However, in the case of the NUFFT, a low value of ξ can cause the radiation pattern not to be calculated accurately. Nevertheless, with a low value as $\xi = 10^{-2}$, the error is less than two decimal digits for the copolar directivity calculated in dB, taking as an exact value the directivity computed with a direct evaluation of (2.73). Lower values of ξ would produce more accurate results for the radiation pattern at the expense of higher computing times, although the real impact would be negative since $\xi = 10^{-2}$ is sufficient for a good estimation of the far field while providing a fast computation of the spectrum function.

2.4.5.2. Non-uniform grid

This case corresponds to a non-uniform reflectarray defined to radiate a pencil beam pattern at $(\theta, \varphi) = (20°, 20°)$. The periodicity profile has been chosen to vary between 0.06λ and 1.28λ at 30 GHz to test an extreme case of aperiodicity (even though in realistic

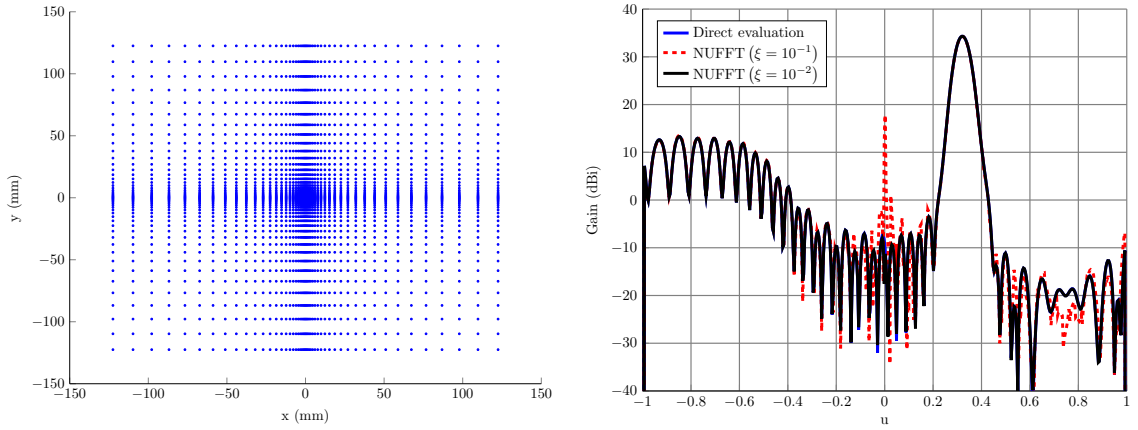

(a) *(b)*

Figure 2.14: *(a) Distribution of the samples for the aperiodic array analysis. (b) Main cut of the copolar pattern of an aperiodic array computed by different methods. Lines blue and black are superimposed.*

examples the minimum periodicity will be around 0.3λ, the value of 0.06λ has been chosen to show the capabilities of the technique). Figure 2.14(a) shows the distribution of the cells, being each dot the center of the corresponding rectangular cell. Figure 2.14(b) depicts the main cut of the aperiodic reflectarray copolar pattern. Due to the high periodicity in most of the elements (see Figure 2.14(a)), there are pseudo-grating lobes. In this case it can be observed that there is low accuracy around $u = 0$ and other points with low level of radiated field for $\xi = 10^{-1}$. Nevertheless, for $\xi = 10^{-2}$ the NUFFT provides a result which is almost the same as the direct evaluation of the spectrum functions.

2.4.6. Efficiency study

With the method developed for the efficient analysis of aperiodic reflectarrays, four NUFFT need to be used to obtain each spectrum function when the field at each cell is considered constant, in contrast with one FFT for the periodic case. Also, according to (2.97), the NUFFT is slower than the FFT and is also precision-dependent. In this section, a study of computing times is carried out for a periodic case to compare both methods along with the direct evaluation. The two spectrum functions of the Second Principle of Equivalence are computed for different rectangular reflectarrays with $N_x = N_y = 10, 30, 50, 70$ elements and UV grids of $M_u = M_v = 256, 512, 1024$ points. The NUFFT is evaluated for $\xi = 10^{-x}$, with $x = 1, 2, 3, 4, 5, 6$.

Figure 2.15(a) shows the results when fixing the UV grid. The times for the FFT and NUFFT remain flat because the source grid (N) is artificially increased to have the same number of points than the UV grid (M). However, this is not the case for the direct evaluation where the computing times quickly grow with the number of elements. Only for small number of elements is the direct evaluation faster than the NUFFT with moderate precision ($\xi = 10^{-4}$), since the direct evaluation considers only N sources rather than M as the (NU)FFT algorithm. Figure 2.15(b) shows the results when fixing the size of the

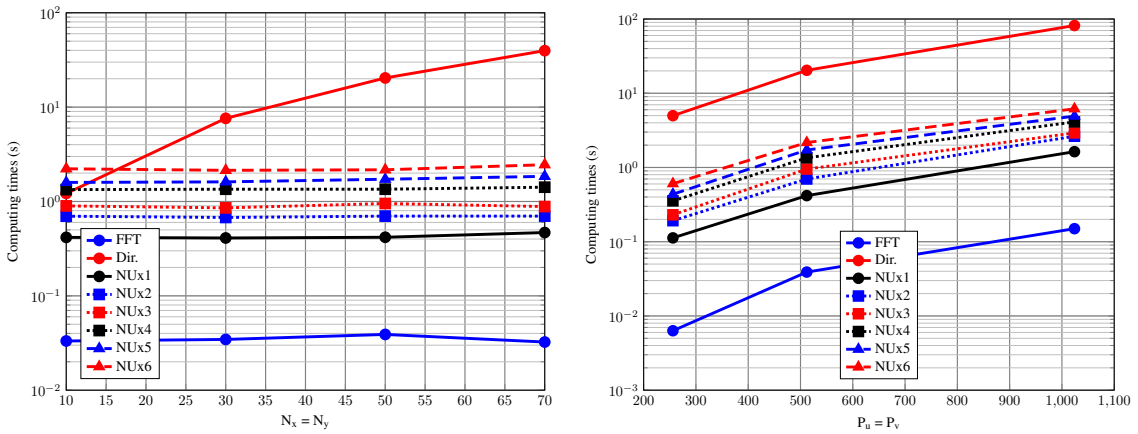

Figure 2.15: *Computing times study for the NUFFT. (a) Varying number of source samples and UV grid fixed to $M = 512 \times 512$ points. (b) Varying number of $M = P_u \times P_v$ points and number of source samples fixed to $N = 50 \times 50$.*

reflectarray. Now, the grid used by the FFT and NUFFT effectively increases and thus the computing times increase with M, although they remain two and one order of magnitude lower than the direct evaluation, respectively, showing the gain in computing times of the new formulation developed based on the use of the NUFFT.

2.5. Computation of the near field radiated by a reflectarray antenna

In the previous section it was described how to efficiently compute the radiation pattern of reflectarray antennas by using the FFT algorithm in the computation of the spectrum functions for the periodic case and the NUFFT for the aperiodic one. Also, a generalization of those formulations for the case when a continuous incident field is considered was developed. All these techniques allow to efficiently and accurately analyze the reflectarray for far field applications, which is the main niche of this type of antenna [2]. However, in recent years there have appeared some near field applications involving reflectarrays such as RFID [136], imaging [137] and even virus sanitizing [138]. For these three applications, the reflectarrays are designed for near field focusing at one or several points in space. In addition, reflectarray antennas can be a potential substitute of parabolic reflectors for Compact Antenna Test Ranges (CATR), since they are also able to collimate the waves from the feed to form a plane wave front. This is particularly interesting at high frequencies, where the surface error required for the parabolic surface is very low. Reflectarrays have been demonstrated at 94 GHz [80,139], showing that manufacturing errors in printed elements lower than ± 1 micron (< 1 %) can be achieved, which provides accurate control in the reflected field.

In this section, a simple model to compute the near field for reflectarray antennas is presented. The aim of this model is to use it as an analysis tool in the synthesis and optimization of its near field in order to increase the size of the quiet zone for CATR

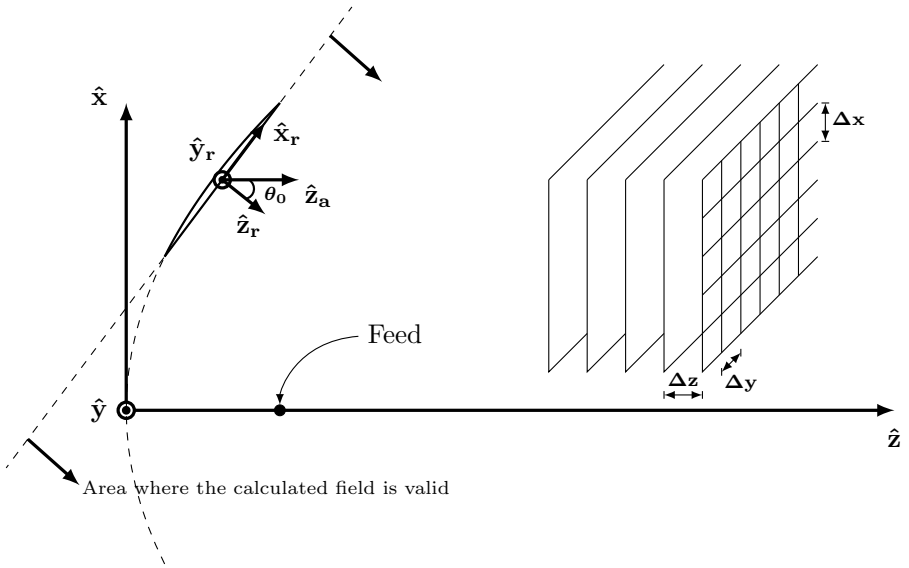

Figure 2.16: *Planes where the reflectarray near field will be computed.*

applications. Since the reflectarray geometry is based on a equivalent parabolic reflector, as shown in Figure 2.1, the near field will be computed in planes parallel to the pointing direction, so the quiet zone can be easily estimated. This model will be validated both by means of simulations with commercial software and by measurements of a reflectarray. In a following chapter, it will be used within an optimizing algorithm to improve the performance of the quiet zone. Although this new model is used in the present work for the estimation and optimization of the quiet zone, it can be used to analyze the reflectarray near field for any other application.

2.5.1. A simple near field radiation model for reflectarray antennas

With the aim of being able to analyze the quiet zone generated by the reflectarray, the near field radiated by the reflectarray needs to be computed in the whole half space in front of the reflectarray. Taking as reference Figure 2.16, the space will be divided in planes perpendicular to the reflectarray pointing direction (which will be (θ, φ) in general taking as reference the RCS, although in this particular case the pointing direction is $(\theta_0, 0)$ since $\hat{z}_a \parallel \hat{z}$). In order to obtain the near field in a volume, it will be computed in planes (corresponding to different wave fronts) separared Δz, with z constant. At the same time, each plane will be discretized in a grid, as shown in Figure 2.16.

At each point in space, the near field will be computed as contributions of the far field radiated by each element of the reflectarray, which will be modeled as a small rectangular aperture of dimensions $a \times b$ (only periodic reflectarrays will be considered, although the analysis could be extended to aperiodic ones). Hence, applying the Second Principle of Equivalence in (2.58) and the approximation that the field at each reflectarray element is constant, the far field radiated by each element can be obtained. In this regard, the

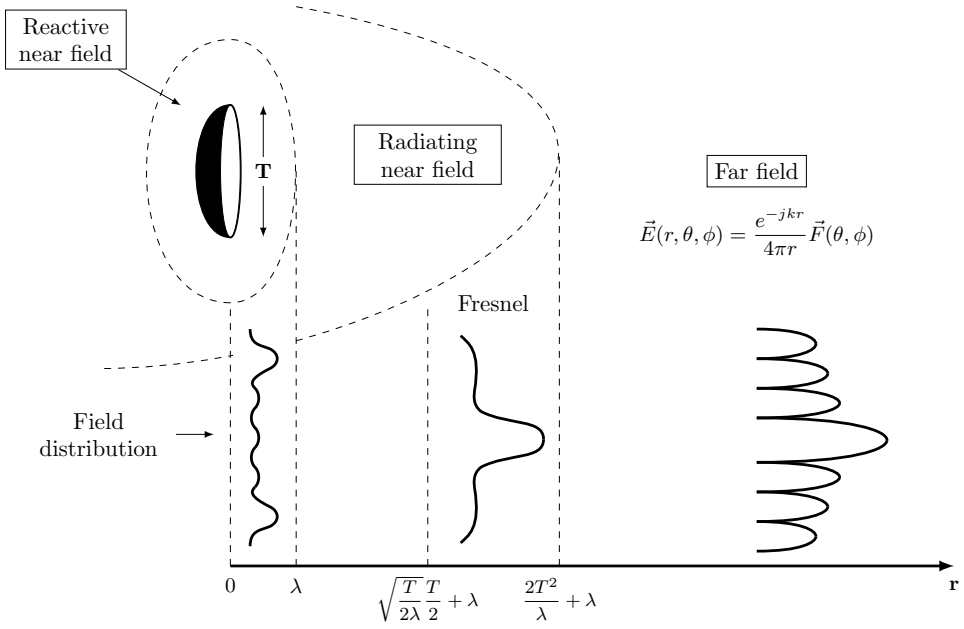

Figure 2.17: *Radiating regions of an antenna whose maximum dimension is T.*

spectrum function for element i is

$$\begin{aligned} P(u,v) &= \iint_{S_i} E_i(x,y)\, e^{jk_0(ux+vy)}\, dx\, dy = E_i \iint_{S_i} e^{jk_0(ux+vy)}\, dx\, dy \\ &= E_i \cdot a \cdot b \cdot \operatorname{sinc}\left(\frac{k_0\, u\, a}{2}\right) \operatorname{sinc}\left(\frac{k_0\, v\, b}{2}\right), \end{aligned} \tag{2.120}$$

where the double integral was solved following identical steps as in the previous far field sections, and along the Second Principle of Equivalence in (2.58) allows to compute the far field radiated by the element in front of the reflectarray. Furthermore, taking into account that the size of each element is around 0.5λ in both dimensions, considering Figure 2.17 [140], the far field distance for the reflectarray element will be

$$r = \frac{2T^2}{\lambda} + \lambda = \frac{2\left(a^2+b^2\right)}{\lambda} + \lambda = \frac{2\left(0.25\lambda^2+0.25\lambda^2\right)}{\lambda} + \lambda = 2\lambda, \tag{2.121}$$

where T was chosen as the maximum dimension of the element, corresponding to its diagonal, when $a = b = 0.5\lambda$ as particular case. This distance would be the minimum distance to consider the far field radiated by the element. However, a distance of 2λ might be too small, and it would be convenient to be larger, of several wavelengths. In practice, this distance should also avoid the feed (see Figure 2.16).

Although the field radiated by the element has been already characterized, there remain some considerations. The far field has been obtained in spherical coordinates in the RCS and it should be transformed to Cartesian coordinates in the GCS, in planes perpendicular to the pointing direction $\hat{z}_a$, as shown in Figure 2.16. The grid where the near field is to be computed is defined in the Pointing Coordinate System (PCS), $(\hat{x}_a, \hat{y}_a, \hat{z}_a)$, which can be obtained with a rotation of the RCS, $(\hat{x}_r, \hat{y}_r, \hat{z}_r)$. In general, this can be done by a general rotation given by three angles θ, φ and ψ as described in [141]. The definition of

angles θ and φ is the usual in spherical coordinates while ψ defines a rotation around axis $\hat{z}'$, as shown in Figure 2.18.

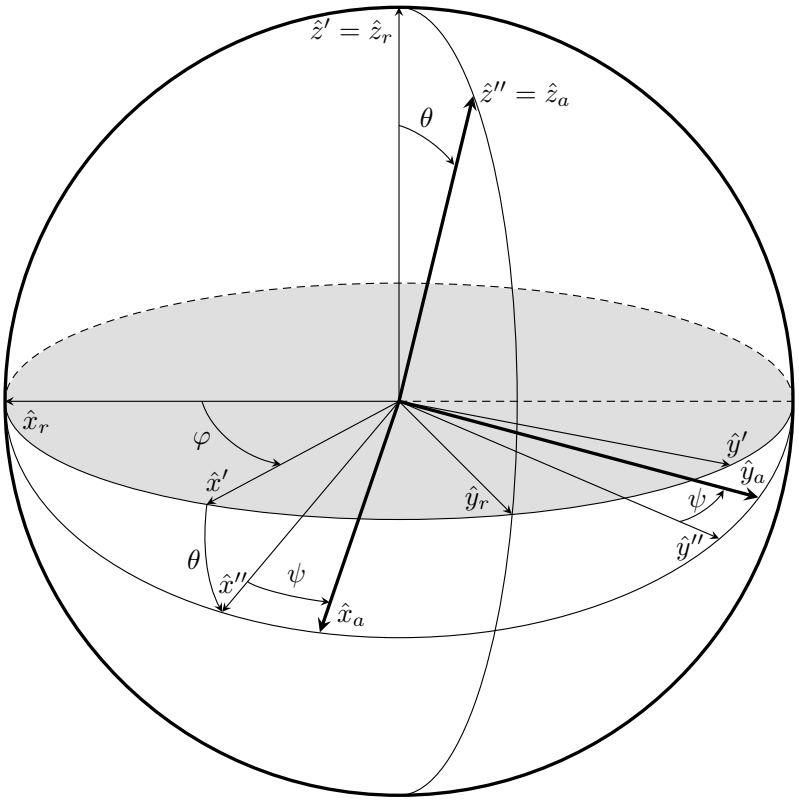

Figure 2.18: *Rotation of the coordinate system $(\hat{x}_r, \hat{y}_r, \hat{z}_r)$ specified by the angles θ, φ and ψ to obtain $(\hat{x}_a, \hat{y}_a, \hat{z}_a)$.*

The unit vectors of the rotated coordinate system are defined as [141]

$$\hat{x}_a = \hat{\theta}\cos(\varphi - \psi) - \hat{\varphi}\sin(\varphi - \psi), \tag{2.122a}$$

$$\hat{y}_a = \hat{\theta}\sin(\varphi - \psi) + \hat{\varphi}\cos(\varphi - \psi), \tag{2.122b}$$

$$\hat{z}_a = \hat{r}, \tag{2.122c}$$

where

$$\hat{\theta} = \hat{x}_r\cos\theta\cos\varphi + \hat{y}_r\cos\theta\sin\varphi - \hat{z}_r\sin\theta, \tag{2.123a}$$

$$\hat{\varphi} = -\hat{x}_r\sin\varphi + \hat{y}_r\cos\varphi, \tag{2.123b}$$

$$\hat{r} = \hat{x}_r\sin\theta\cos\varphi + \hat{y}_r\sin\theta\sin\varphi + \hat{z}_r\cos\theta. \tag{2.123c}$$

Substituting the unit vectors of (2.123) in (2.122) yields

$$\begin{aligned}\hat{x}_a = {} & \hat{x}_r\left[\cos\theta\cos\varphi\cos(\varphi - \psi) + \sin\varphi\sin(\varphi - \psi)\right] + \\ & \hat{y}_r\left[\cos\theta\sin\varphi\cos(\varphi - \psi) - \cos\varphi\sin(\varphi - \psi)\right] - \\ & \hat{z}_r\sin\theta\cos(\varphi - \psi),\end{aligned} \tag{2.124a}$$

$$\begin{aligned}\hat{y}_a = {} & \hat{x}_r\left[\cos\theta\cos\varphi\sin(\varphi-\psi)-\sin\varphi\cos(\varphi-\psi)\right]+\\ & \hat{y}_r\left[\cos\theta\sin\varphi\sin(\varphi-\psi)+\cos\varphi\cos(\varphi-\psi)\right]-\\ & \hat{z}_r\sin\theta\sin(\varphi-\psi),\end{aligned} \tag{2.124b}$$

$$\hat{z}_a = \hat{x}_r\sin\theta\cos\varphi+\hat{y}_r\sin\theta\sin\varphi+\hat{z}_r\cos\theta. \tag{2.124c}$$

The change of coordinates matrix from the RCS to the PCS is

$$\begin{pmatrix} \cos\theta\cos\varphi\cos(\varphi-\psi) & \cos\theta\sin\varphi\cos(\varphi-\psi) & -\sin\theta\cos(\varphi-\psi)\\ +\sin\varphi\sin(\varphi-\psi) & -\cos\varphi\sin(\varphi-\psi) & \\ \cos\theta\cos\varphi\sin(\varphi-\psi) & \cos\theta\sin\varphi\sin(\varphi-\psi) & -\sin\theta\sin(\varphi-\psi)\\ -\sin\varphi\cos(\varphi-\psi) & +\cos\varphi\cos(\varphi-\psi) & \\ \sin\theta\cos\varphi & \sin\theta\sin\varphi & \cos\theta \end{pmatrix}. \tag{2.125}$$

Since the angle ψ defines a rotation around the $\hat{z}_a$ axis (which is the same a $\hat{z}'$, see Figure 2.18), it is not necessary. Then, setting $\psi = 0$ and regrouping terms, the matrix will take the form

$$\begin{pmatrix} x' \\ y' \\ z' \end{pmatrix} = \begin{pmatrix} \cos\theta\cos^2\varphi+\sin^2\varphi & \cos\varphi\sin\varphi(\cos\theta-1) & -\sin\theta\cos\varphi \\ \cos\varphi\sin\varphi(\cos\theta-1) & \cos\theta\sin^2\varphi+\cos^2\varphi & -\sin\theta\sin\varphi \\ \sin\theta\cos\varphi & \sin\theta\sin\varphi & \cos\theta \end{pmatrix}\begin{pmatrix} x \\ y \\ z \end{pmatrix}, \tag{2.126}$$

where $(x,\, y,\, z)$ is a point in the RCS and $(x',\, y',\, z')$ a point in the PCS.

Equation (2.126) gives the change of coordinates from the RCS to the PCS when the reflectarray radiates in an arbitrary direction (θ, φ). Since we are interested in the inverse rotation, the transpose matrix will be used. Also, this matrix can be used for a general case, but since the reflectarray radiates in the direction $(\theta_0, 0)$ it can be further simplified, finally obtaining

$$\begin{pmatrix} x' \\ y' \\ z' \end{pmatrix} = \begin{pmatrix} \cos\theta_0 & 0 & -\sin\theta_0 \\ 0 & 1 & 0 \\ \sin\theta_0 & 0 & \cos\theta_0 \end{pmatrix}\begin{pmatrix} x \\ y \\ z \end{pmatrix}. \tag{2.127}$$

To recapitulate, the near field radiated by the reflectarray will be computed in planes parallel to the pointing direction of the antenna as contribution of the far fields radiated by each element of the reflectarray, which are modeled as small apertures. However, the grid in which the field is computed is defined in the PCS (equivalent to the GCS, with the exception of a translation) in Cartesian coordinates for convenience, while the far field radiated by the elements is computed in the RCS in spherical coordinates. Then, the steps to obtain the near field are as follows:

1. Perform a change of coordinates of the grid point from PCS to RCS using (2.127).

2. After computing the element far field in the transformed point, perform a change of coordinates from spherical to cartesian with the usual transformation matrix.

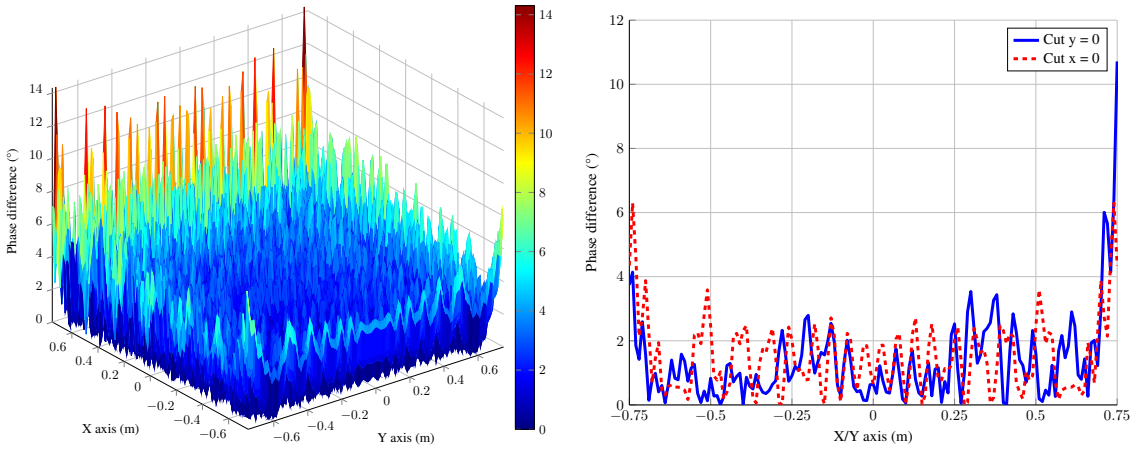

(a) *(b)*

Figure 2.19: *Difference for phase of component $\hat{x}$ in X polarization between the software developed and GRASP in a plane* 1 m *away from the reflectarray. (a) 3D representation. (b) Main cuts.*

3. Add contributions from all reflectarray elements, computing them following steps 1 and 2.

4. Perform a change of coordinates from RCS to PCS using the transpose of (2.127).

This way, the near field is computed in one point in space. Steps 1-4 are repeated in order to compute it in all desired points, in general in a volume. Each plane in space can be divided in rows and columns. Hence, four nested loops have to be implemented: three to go over all space and another for the elements of the reflectarray. In order to speed up computations, each plane can be parallelized, dividing the rows or columns among all available CPU units. Because the near field at each point is computed independently, it is straightforward to accomplish the parallelization, for instance by using OpenMP [142].

2.5.2. Model validation

2.5.2.1. Simulations

In order to validate the model, a homemade software has been implemented. GRASP v9 [143] has been used to validate it. Although reflectarrays cannot be directly analyzed with GRASP, a tabular planar source is defined using the tangential electric field computed with (2.38) as source and its radiation is evaluated. The considered test case is a reflectarray working at 10 GHz, with $C = 3.33\lambda$, $D = 50\lambda$, $F/D = 1$, $a = b = 0.5\lambda$. The feed is modeled as a $\cos^q \theta$ function [78] with $q = 8.2$, which provides an illumination taper of -9 dB at the reflectarray edge and complies with the Targonski condition [124] i.e., that the incident angle is equal to the reflected angle in order to minimize the beam squint, as detailed in Section 2.2.4.

For the near field, it is convenient to define a copolar and crosspolar fields. For the case of far field patterns, the copolar and crosspolar components were defined with Ludwig's third definition [131]. Now, in the near field, the copolar component is defined as the

Table 2.1: *Maximum values of the differences in amplitude and phase between the simulations in GRASP and the homemade software for X polarization.*

	X POLARIZATION			
	$\hat{x}$ comp.		$\hat{y}$ comp.	
	Amp. (dB)	*Phase (°)*	*Amp. (dB)*	*Phase (°)*
50 m.	−46.9	1.3	−40.7	29.1
5 m.	−34.6	7.1	−25.6	42.8
1 m.	−27.4	14.3	−22.7	—

desired field component for a given polarization, which corresponds to the $\hat{x}$ component in X polarization, and to the $\hat{y}$ component in Y polarization. Conversely, the crosspolar component will be the non-desired component, corresponding to the $\hat{y}$ and $\hat{x}$ components in X and Y polarization, respectively.

A number of near field planes were computed with the same size as the equivalent aperture, being the minimum distance tested 33.3λ (1 m), less than the equivalent aperture value, D. The differences between the results of GRASP and the software developed decrease for larger distances, as it is to be expected, since the near field is computed as far field contributions and for larger distances the far field approximation is more suitable. For the closest plane and the copolar component, the maximum difference in amplitude is always below −19 dB for both polarizations, while in the case of the phase, the difference remains below 14° in the whole plane. However, the maximum difference in phase occurs at the edges of the plane, as it can be seen in Figure 2.19. Still, the difference remains below 4° at the center of the plane, where the quiet zone is generated.

Tables 2.1 and 2.2 summarize the results of the software validation. They show the maximum values of the differences in amplitude and phase between the GRASP simulation and that of the homemade software using the new model for three different near field planes. With regard to the amplitude maximum error, for X polarization the $\hat{x}$ component presents an error of −27.4 dB and the $\hat{y}$ component of −22.7 dB. For the case of Y polarization, they are −19.3 dB and −26.5 dB for the $\hat{x}$ and $\hat{y}$, respectively. The copolar component for each polarization has a lower maximum error than the crosspolar. In principle, this makes sense since the relative amplitude between this component and the copolar one is much lower and thus more sensitive (usually, more than 20 dB below the copolar). In any case, the values obtained for the errors are within acceptable values in order to use the software as quiet zone predictor. Error in amplitude for both copolar and crosspolar as well as phase for the desired component are low. For the phases, in some cases there are 360° jumps, so the maximum error is not shown. Nevertheless, this only happens for the crosspolar component in the closest plane.

Table 2.2: *Maximum values of the differences in amplitude and phase between the simulations in GRASP and the homemade software for Y polarization.*

	Y POLARIZATION			
	$\hat{x}$ comp.		$\hat{y}$ comp.	
	Amp. (dB)	*Phase (˚)*	*Amp. (dB)*	*Phase (˚)*
50 m.	−44.5	12.9	−47.5	1.3
5 m.	−27.0	27.9	−34.1	6.5
1 m.	−19.3	—	−26.5	12.5

2.5.2.2. Measurements

Using a planar measurement setup [144] a reflectarray [128] has been measured. The reflectarray was designed to work in dual polarization at 20 and 30 GHz, although near field measurements are only carried out at 20 GHz. The beam is tilted $\theta_0 = 20°$ for both polarizations so in order to measure planes parallel to the pointing direction, the reflectarray is tilted 20°. Also, for this frequency, the phase center of the feed horn antenna is placed at $(-40, 0, 195)$ mm. in the RCS. Further details on the characteristics of the reflectarray can be consulted in [128]. A photograph of the measurement setup is shown in Figure 2.20.

The measurements were taken on a plane at 391 mm from the center of the reflectarray, which corresponds to $z = 100$ mm in the measurement setup coordinate system [144]. Figure 2.21 shows the measurements in amplitude and phase. The values of the X and Y axis correspond to the placement of the antenna in the measurement setup coordinate system [144]. The shape of the amplitude is due to the illumination taper of the feed in the surface of the reflectarray. The phase measurement clearly shows the phase front with the shape of the antenna aperture. In both images, some interferences can be seen for lower values of X which are due to the support structure and horn.

Figures 2.22 and 2.23 show the main cuts of the measurements shown in Figure 2.21 for the amplitude and phase along with the simulation of the reflectarray considering ideal phase shifters and MoM [54]. There is good agreement between simulations and measurements. From the phase cuts, it can be seen how the phase in the asymmetric cut is slightly tilted. This phenomena is due to certain tolerances in the measurement setup (floor slightly tilted, wooden support not perfectly manufactured) and reflectarray manufacturing process (which can make the beam not to exactly point at $\theta_0 = 20°$). Also, diffraction from the edges of the reflectarray as well as from the support structure of the horns and the horns themselves introduce some interference in the asymmetric cut that are not taken into account by the simulation software, as it can be seen in Figures 2.22 and 2.23. Finally, the evanescent modes, not taken into account in either simulation, might slightly affect the near field.

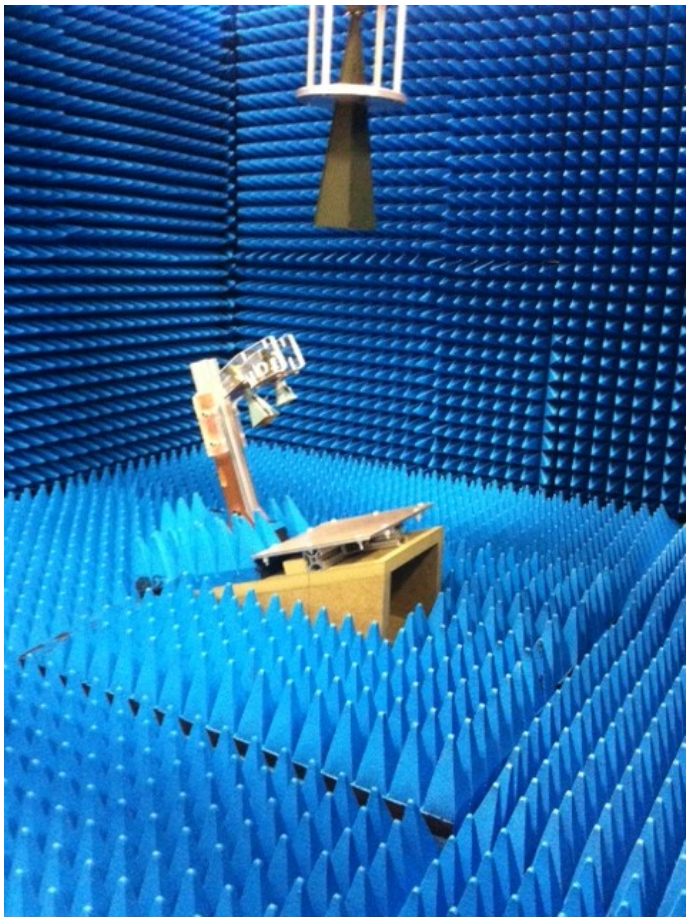

Figure 2.20: *Photograph of the measurement setup with the reflectarray tilted 20˚.*

2.6. Conclusions

In this chapter, the single-offset reflectarray geometry has been thoroughly described and analyzed. Starting from the geometry of a single-offset parabolic reflector, defined by the equivalent aperture D, focal distance F and clearance C, the geometry of the reflectarray is established and all of its parameters derived; in particular, the feed coordinates in the reflectarray own coordinate system, the maximum number of reflectarray elements in each dimension, the radiation angle and the point on the surface of the reflectarray to which the feed must point in order to minimize the beam squint, also known as the Targonski condition.

Once the geometry has been characterized, a technique for the analysis of reflectarray antennas based on local periodicity is presented. First, a feed model based on the $\cos^q \theta$ function is presented, and the field on the surface of the reflectarray is derived from this model. The reflectarray element is analyzed by the Method of Moments using the Floquet theorem, taking into account mutual coupling between adjacent elements, the field reflected by the metallizations and ground plane, substrate losses and the real angle of incident from the feed. This way, the reflected field on the surface of the reflectarray is accurately computed, although it could be improved by taking into account the real incident field [82] by measuring the feed or by simulating it with a full-wave simulator,

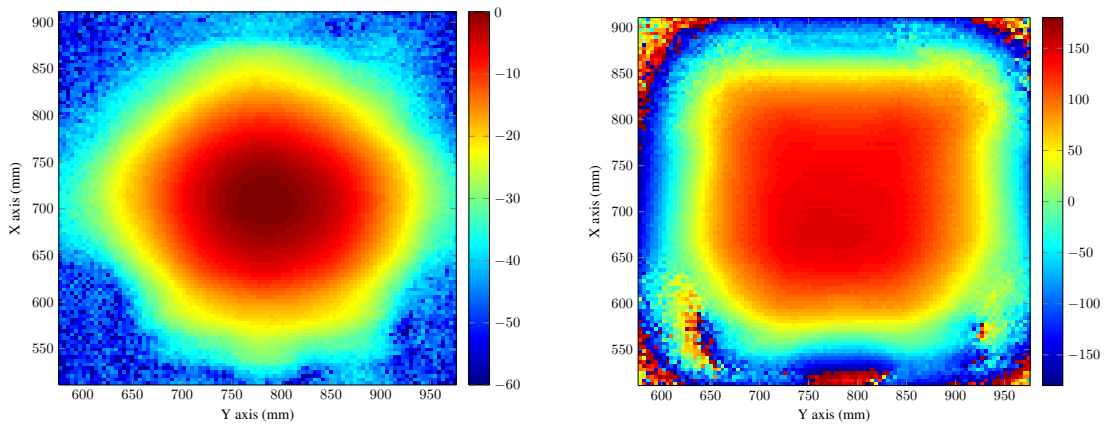

Figure 2.21: *Near field measurements at 20 GHz on a plane 391 mm away from the reflectarray center. Support structure and horns are placed on the lower X axis. (a) Amplitude. (b) Phase.*

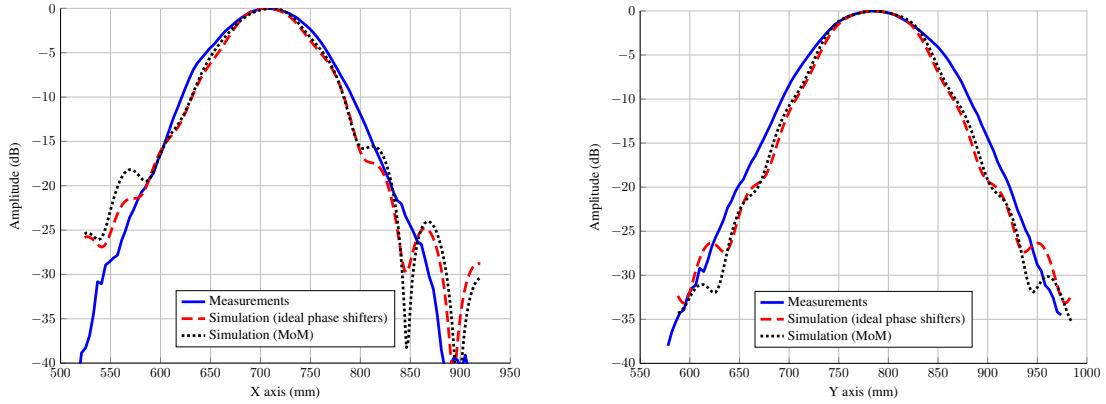

Figure 2.22: *Main cuts of the amplitude measurements along with simulations of the reflectarray for (a) asymmetric and (b) symmetric planes.*

and also by using improved techniques for the analysis for the incident field [84]. Also, the reflectarray analysis is completed by taking into account a dielectric frame which is usually added to screw the reflectarray breadboard into the supporting structures.

From the reflected tangential field on the reflectarray surface, the far fields are efficiently obtained. The most time consuming operation in the calculation of the radiation patterns is the computation of the spectrum functions, which are the Fourier transform of the tangential field. The Fourier transform can be efficiently computed by the FFT algorithm, although the FFT can only be applied when the reflectarray is periodic. In such case, the formulation is developed and it is shown that the region where the far fields are computed in a efficient fashion depend on the periodicity of the reflectarray. When the reflectarray is aperiodic, the FFT no longer applies and a new efficient technique using the NUFFT has been developed in order to maintain the scaling of the FFT algorithm in the reflectarray analysis. Also, the analysis technique is further generalized for the case when a continuous incident field is considered, taking into account that the impinging incident

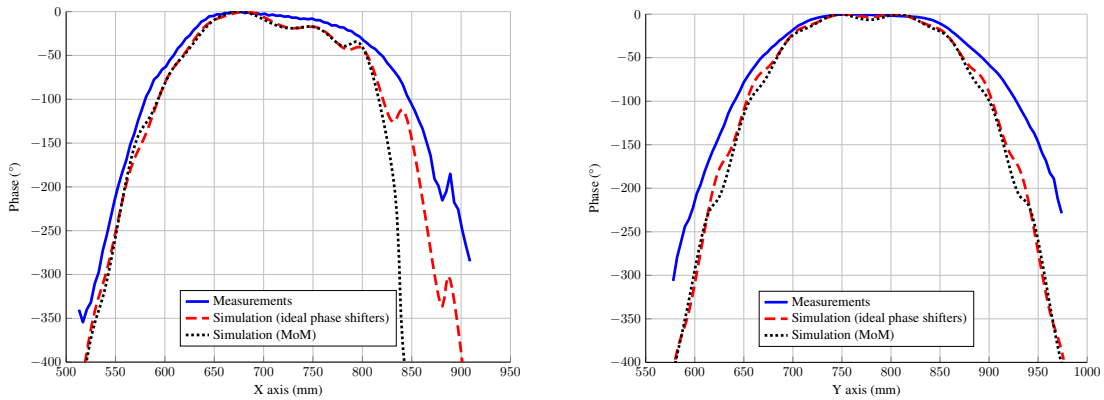

Figure 2.23: *Main cuts of the phase measurements along with simulations of the reflectarray for (a) asymmetric and (b) symmetric planes.*

field from the feed is smooth and hence narrowband. Numerical examples are provided that demonstrate the performance of the analysis technique for aperiodic reflectarrays as well as a computing time study which shows the efficiency of the technique with regard to a direct evaluation of the spectrum functions.

Finally, a near field model of the reflectarray is proposed and validated. As in the case of the far field analysis, the starting point is the tangential field on the surface of the reflectarray, but this time the near field in front of the antenna is obtained as far field contributions of each reflectarray element. In contrast to other works in the literature, where the array elements are considered to be punctual isotropic sources, here the reflectarray element is modeled as a small aperture. The model is then validated through simulations with commercial software and measurements, showing good results. Due to the nature of the model, it is more precise when the field is computed further from the reflectarray surface, since the far field assumption for the elements of the antenna is better approximated.

CHAPTER 3

Efficient pattern synthesis of reflectarrays based on the Fast Fourier Transform

3.1. Introduction

The design of directive reflectarrays with a pencil beam pattern is straightforward. According to the array theory [2], for the reflectarray to radiate in a direction (θ_0, φ_0), the following progressive phase distribution should be achieved by the reflected tangential field:

$$\phi\left(x_m, y_n\right) = -k_0 \sin\theta_0 \cos\varphi_0 \, x_m - k_0 \sin\theta_0 \sin\varphi_0 \, y_n, \tag{3.1}$$

where k_0 is the free space wavelength and $(x_m,\, y_n)$ the coordinates of the $(m,\, n)$th reflectarray element center. Taking into account that the phase of the incident field from the feed is $-k_0\, d_i$, with d_i the distance form the feed to each reflectarray element, the phase distribution of the reflection coefficients that should be implemented by the reflectarray elements is:

$$\phi_R(x_m, y_n) = k_0 \left(d_i - \left(x_m \cos\varphi_0 + y_n \sin\varphi_0\right) \sin\theta_0\right). \tag{3.2}$$

In order to implement the phases of (3.2), the element dimensions (dipoles lengths, patches dimensions, ...) are adjusted in such a way that the phase of the corresponding reflection coefficient matches the required phase shift in the required polarization (phase of ρ_{xx} for X polarization and ρ_{yy} for Y polarization).

However, when more complex radiation patterns are required, the use of a synthesis algorithm is mandatory. For the reflectarray case, the synthesis of radiation patterns is constrained by the radiation pattern of the feed, which fixes the amplitude of the incident field on each reflectarray element, and only the phase distribution can be modified. The most typical approach for the reflectarray beam shaping is the Phase-Only Synthesis (POS), whose output is the phase of the reflected field at each reflectarray element (or equivalently, the phase of the reflection coefficients) that provides the required shaped

beam. Then, the element dimensions will be adjusted to match the obtained phase distribution, as commented above.

The algorithm described in this chapter for the synthesis of reflectarray antennas is the Intersection Approach (IA), which in the most general case is described in [89] and can be applied to any kind of antenna. However, due to the nature of the reflectarray antennas, some particularizations can be made to the algorithm [94, 95] in order to take advantage of the analysis based on the FFT, obtaining a very powerful algorithm while keeping a very high numerical efficiency. This algorithm will be referred to as IA-POS. Since for the POS case the most time consuming operation of the IA is the FFT, the algorithm is very fast and allows the synthesis of very large reflectarrays in very short amounts of time [2]. However, this version of the IA is based on a POS, so it only deals with copolar patterns and there is no control over the crosspolar ones. Hence, a generalization of the IA formulation for reflectarrays will be developed that includes crosspolar specifications. This new formulation synthesizes a distribution of reflection coefficient matrices, instead of phases, since to obtain the crosspolar pattern the full matrix is needed, as explained in the previous chapter. This new algorithm will be denoted as IA-XP.

3.2. Intersection Approach for phase-only synthesis

The majority of pattern synthesis methods consists on the optimization of a functional defined as an error function. However, there is a simpler understanding of the problem: finding the intersection of two sets, or at least, the minor distance between them [89, 95]. The IA is based on this approach and was first developed, in the case of antennas, for arrays in which both amplitude and phase could vary along the surface of the antenna [94]. Although dynamics constraints have been implemented for array synthesis [145], where several phase distributions were obtained with one amplitude distribution, reflectarrays impose a tighter restriction, since the amplitude distribution is fixed by the incident field from the feed and not by the synthesis process. Still, the IA developed for reflectarrays provide excellent results for pattern synthesis.

The IA considers two sets: 1) the set of the radiation patterns that can be obtained with the reflectarray (set $\mathcal{R}$) and 2) the set of the radiation patterns that comply with the requirements (set $\mathcal{M}$) [89, 95]. Formally, both sets are sets of functions, which model radiation patterns [94], although for clarity, only their radiation pattern nature will be mentioned, as in [2]. Each iteration of the algorithm consists of a pair of operations, namely forward ($\mathcal{F}$) and backward ($\mathcal{B}$) projections, as follows:

$$\vec{E}_{i+1} = \mathcal{B}\left[\mathcal{F}\left(\vec{E}_i\right)\right], \tag{3.3}$$

where $\vec{E}$ is the radiated field by the antenna. The forward projection projects the far field radiated by the antenna onto the set of far fields that comply with the specifications. The backward projection projects the far field that fulfills the specifications onto the set of far fields that can be radiated by the reflectarray. The aim of the sequence defined in (3.3) is to find a radiation pattern that belongs simultaneously to both sets. If that is

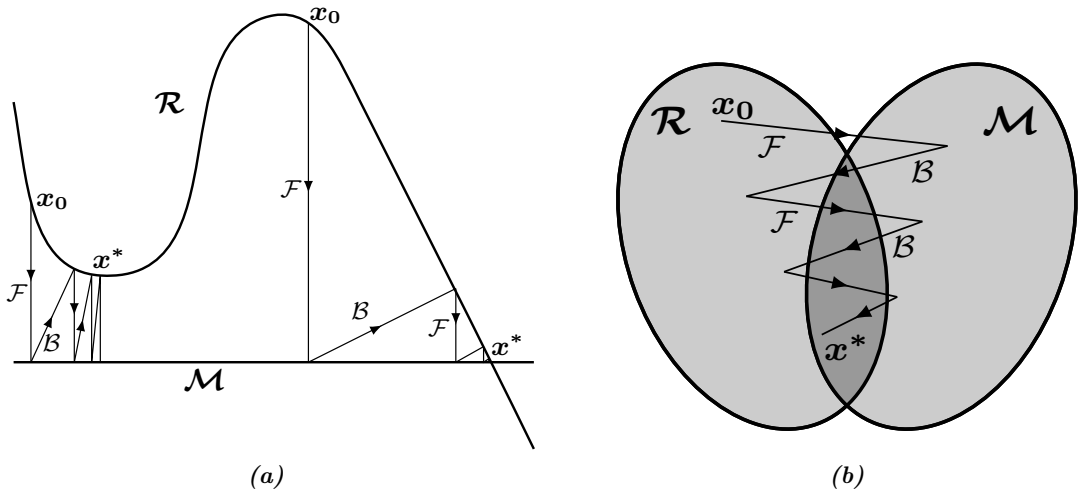

Figure 3.1: *Sketch of the Intersection Approach between two sets for (a) one dimension and (b) general case.*

not possible because the intersection is empty, a radiation pattern should be found whose distance to the set of patterns that fulfill the specifications is minimal [89]. Also, the IA is a local optimizer and as such the starting point is of the utmost importance since it will determine the correct convergence of the algorithm [89].

Figure 3.1(a) shows a sketch of the algorithm applied to one-dimensional sets. There, x_0 denotes the starting point of the algorithm and x^* the solution reached. In this case, the projection operators are the orthogonal projection of one curve to the other. As it can be seen, depending on the starting point, the algorithm can reach a non-desired local minima. Also, the steps provided by the algorithm become smaller as it reaches a solution (not necessarily the optimum one).

A flow chart of the implemented algorithm is shown in Figure 3.2. The aim of the algorithm is to obtain the phase distribution of the reflection coefficients that generates the desired radiated field. Hence, the first step is to compute the far fields from the initial reflected field, which can be one that generates a properly focused pencil beam [2]. After that, the forward projection is divided into two steps. The template normalization will define the synthesis as fixed or float gain, depending on how the templates are set. Then, using the templates, the radiated field is projected onto the set of fields that comply with the specifications.

Then, the backward projector is applied, which is divided in three steps. In the first step, the reflected field is recovered applying the inverse transform to the one used to compute the far fields. In general, the recovered reflected field will not be possible to generate by the reflectarray antenna, so it will be projected onto the set of possible radiation patterns (actually, possible reflected fields, but a possible reflected field generates a possible radiation pattern) by imposing certain restrictions. Afterwards, the possible radiated field is computed.

At this stage, the current computed far field is evaluated and depending on whether it fulfills the specifications or not, the algorithm will continue to iterate or it will stop, recovering the phase distribution from the last computed possible reflected field. Typically,

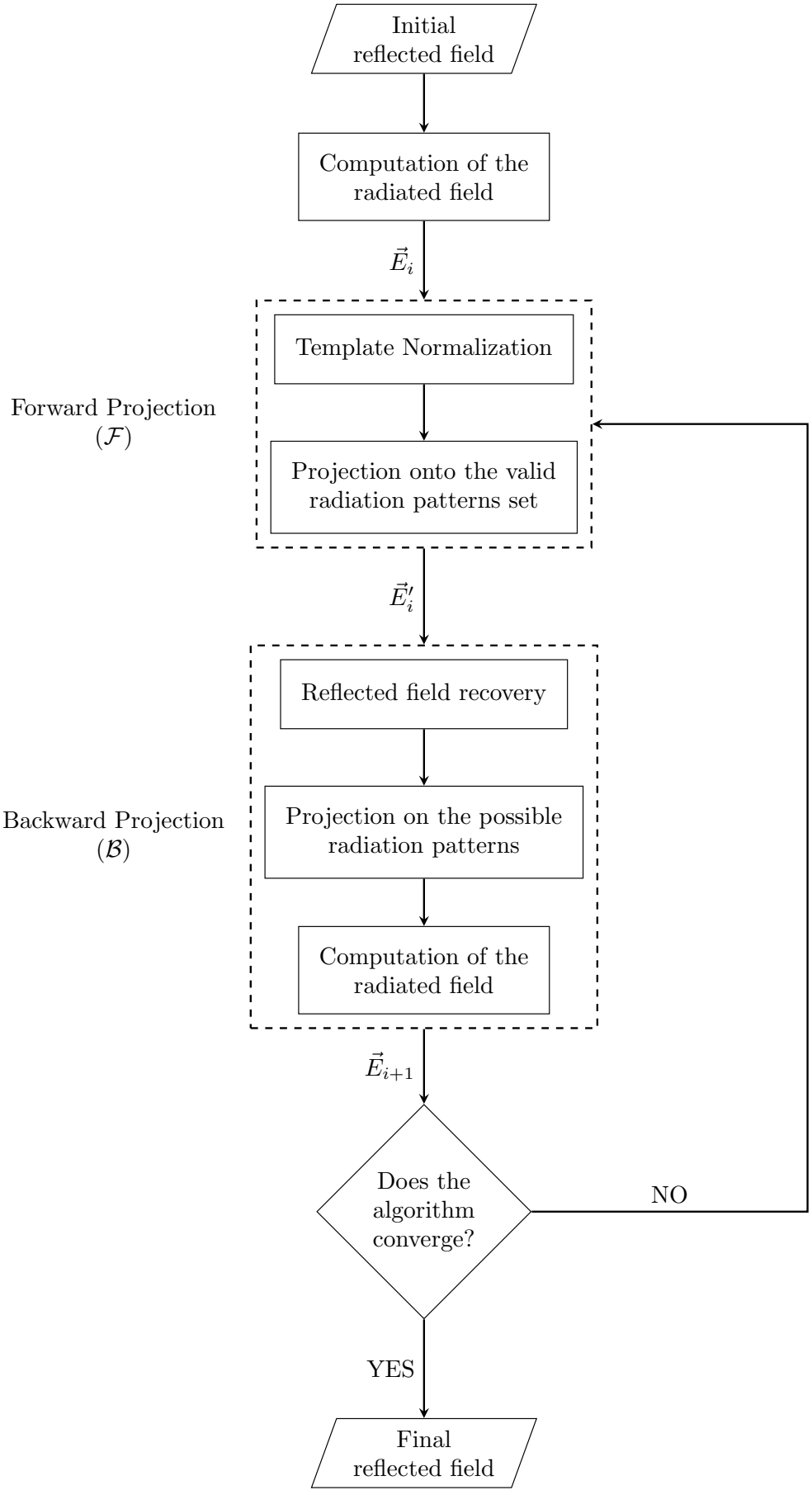

Figure 3.2: *Flow chart of the Intersection Approach for Phase-Only Synthesis.*

convergence is achieved by imposing a minimum desirable error higher than zero, although sometimes it is done by inspection of the current radiation pattern. Also, the algorithm might diverge if the specifications are too restrictive or the starting point is not good enough. In any case, the algorithm can be set to either stop when a minimum error is accomplished or until a maximum number of iterations are reached. Details of the different building blocks are discussed in the following sections.

3.2.1. Computation of the far field

The phase-only synthesis can be carried out either using the First or the Second Principles of Equivalence. Although POS only deals with copolar requirements, the copolar pattern is slightly different when computed and compared with both Principles, being the First Principle more accurate than the Second. Here, the formulation for both Principles of Equivalence will be presented for POS, starting with the Second Principle since its results are necessary for the formulation with the First Principle.

However, the algorithms presented in this chapter can only work with the Second Principle of Equivalence due to limitations in the formulation to recover the field at the aperture from the far fields. This limitation and others will be overcome in future chapters using more advanced algorithms, but the formulation for POS using both Principles will be presented here for completeness.

3.2.1.1. Using the Second Principle of Equivalence

The computation of the far field radiated by a reflectarray antenna has been described in detail in the previous chapter. Here, the process is the same in essence, but some approximations have been assumed in order to adapt it to the synthesis process. The reflected field was defined as

$$\vec{E}_{\text{ref}}^{X/Y}(x,\, y) = E_{\text{ref},x}^{X/Y}(x,\, y)\,\hat{x} + E_{\text{ref},y}^{X/Y}(x,\, y)\,\hat{y}, \tag{3.4}$$

so the incident and reflected fields are related through the matrix R^{mn} as

$$\vec{E}_{\text{ref}}^{X/Y}(x_m,\, y_n) = R^{mn} \cdot \vec{E}_{\text{inc}}^{X/Y}(x_m,\, y_n). \tag{3.5}$$

As discussed in the previous chapter, R^{mn} matrix includes the direct and cross coefficients for the two components of the incident field. Also, these components are complex numbers and are different for each reflectarray element. However, for POS, ideal phase shifters are considered, instead of real elements, and the cross polarization is not taken into account. In this case, the reflection coefficient matrix is reduced to:

$$R^{mn} = \begin{pmatrix} e^{j\phi_{xx}^{mn}} & 0 \\ 0 & e^{j\phi_{yy}^{mn}} \end{pmatrix}. \tag{3.6}$$

Thus, the reflected field can be expressed as

$$E^{X/Y}_{\text{ref},\,x} = e^{j\phi^{mn}_{xx}}\, E^{X/Y}_{\text{inc},\,x}, \tag{3.7a}$$

$$E^{X/Y}_{\text{ref},\,y} = e^{j\phi^{mn}_{yy}}\, E^{X/Y}_{\text{inc},\,y}. \tag{3.7b}$$

In (3.7) it is considered that no crosspolarization is produced by the element; but there is another source of crosspolar radiation: the geometry. This crosspolarization is produced due to the incidence angle of the polarization plane of the impinging wave on the reflectarray element. However, it is interesting to have the synthesis process independent for both polarizations, since modifying one dimension of the element affects more to the corresponding polarization (such is the case, for instance, of patches or dipoles) in the copolar pattern. Hence, the cross component of the incident wave is assumed to be zero ($\hat{y}$ component in X polarization and $\hat{x}$ component in Y polarization), resulting in the following reflected field components:

$$E^{X}_{\text{ref},\,x} = e^{j\phi^{mn}_{xx}}\, E^{X}_{\text{inc},\,x}, \tag{3.8a}$$

$$E^{Y}_{\text{ref},\,y} = e^{j\phi^{mn}_{yy}}\, E^{Y}_{\text{inc},\,y}. \tag{3.8b}$$

On the other hand, the spectrum functions were computed as two-dimensional IDFT. Taken into account the reflected field of (3.8), the expressions for the spectrum functions are

$$P^{X}_{x}(p,q) = N_x \cdot N_y \cdot K(p,q) \cdot K'(p,q) \cdot \text{IDFT2}\left[E^{X}_{\text{ref},\,x}\right], \tag{3.9a}$$

$$P^{Y}_{y}(p,q) = N_x \cdot N_y \cdot K(p,q) \cdot K'(p,q) \cdot \text{IDFT2}\left[E^{Y}_{\text{ref},\,y}\right], \tag{3.9b}$$

where the constants K and K' were defined in (2.74) and (2.82) in (u,v) coordinates and the change of variables to (p,q) was defined in (2.84). The steps for the efficient computation of the IDFT2 with the FFT algorithm were also detailed in the previous chapter.

Taking into account the spectrum functions of (3.9) and the Second Principle of Equivalence, the $\hat{\theta}$ and $\hat{\varphi}$ components of the far field for X polarization are

$$E^{X}_{\theta} = \frac{j\, k_0\, e^{-jk_0 r}}{2\pi r} \cos\varphi\, P^{X}_{x}, \tag{3.10a}$$

$$E^{X}_{\varphi} = -\frac{j\, k_0\, e^{-jk_0 r}}{2\pi r} \cos\theta \sin\varphi\, P^{X}_{x}, \tag{3.10b}$$

while for Y polarization the radiated fields are given by the equations

$$E^{Y}_{\theta} = \frac{j\, k_0\, e^{-jk_0 r}}{2\pi r} \sin\varphi\, P^{Y}_{y}, \tag{3.11a}$$

$$E^{Y}_{\varphi} = \frac{j\, k_0\, e^{-jk_0 r}}{2\pi r} \cos\theta \cos\varphi\, P^{Y}_{y}. \tag{3.11b}$$

Finally, applying Ludwig's third definition of crosspolarization, the copolar and crosspolar components are obtained using (2.61) and (2.62). For the case at hand, only the copolar component is needed for both polarizations, which can be expressed as

$$E_{\mathrm{cp}}^{X} = \frac{j\, k_0\, e^{-jk_0 r}}{2\pi r}\, P_x^X \, \left(\cos^2\varphi + \sin^2\varphi\cos\theta\right), \tag{3.12a}$$

$$E_{\mathrm{cp}}^{Y} = \frac{j\, k_0\, e^{-jk_0 r}}{2\pi r}\, P_y^Y \, \left(\sin^2\varphi + \cos^2\varphi\cos\theta\right). \tag{3.12b}$$

In classical implementations of pattern synthesis in array and reflectarray antennas, only the array factor is taken into account to produce the required pattern shaping, assuming that the effect of the element radiation pattern is negligible. However, in the present implementation, the pattern synthesis is applied to the copolar far field of the antenna, taking into account the constant K in (3.9), which accounts for the effect of the element modeled as a small rectangular aperture (also known as active element pattern), instead of an isotropic punctual source as is the case in the array factor. This methodology provides more accuracy in the synthesis process.

3.2.1.2. Using the First Principle of Equivalence

The First Principle of Equivalence requires the computation of the reflected tangential magnetic field. From the reflected field of (3.8) derived before, the magnetic field is computed by applying (2.50)–(2.54) to (3.8), particularized for each polarization. For polarization X, the reflected electric field has the following two components:

$$E_{\mathrm{ref},\,x}^{X} = e^{j\phi_{xx}^{mn}}\, E_{\mathrm{inc},\,x}^{X}, \tag{3.13a}$$

$$E_{\mathrm{ref},\,y}^{X} = 0. \tag{3.13b}$$

Thus, the $\hat{z}$ component according to (2.54) is

$$E_{\mathrm{ref},\,z}^{X} = -\frac{k_{\mathrm{ref},\,x}\, E_{\mathrm{ref},\,x}^{X}}{k_{\mathrm{ref},\,z}}. \tag{3.14}$$

The magnetic field is then obtained as:

$$\begin{aligned}\vec{H}_{\mathrm{ref}}^{X}(x_m, y_n) = \frac{\vec{k}_{\mathrm{ref}} \times \vec{E}_{\mathrm{ref}}^{X}(x_m, y_n)}{\omega\mu_0} = \frac{1}{\omega\mu_0}\Bigg(& k_{\mathrm{ref},\,y}\, E_{\mathrm{ref},\,z}^{X}(x_m, y_n)\,\hat{x} \\ & - \Big(k_{\mathrm{ref},\,x}\, E_{\mathrm{ref},\,z}^{X}(x_m, y_n) - k_{\mathrm{ref},\,z}\, E_{\mathrm{ref},\,x}^{X}(x_m, y_n)\Big)\hat{y} \\ & - k_{\mathrm{ref},\,y}\, E_{\mathrm{ref},\,x}^{X}(x_m, y_n)\,\hat{z}\Bigg).\end{aligned} \tag{3.15}$$

As only the tangential magnetic field is needed, we finally have:

$$H_{\mathrm{ref},\,x}^{X} = \frac{k_{\mathrm{ref},\,y}\, E_{\mathrm{ref},\,z}^{X}}{\omega\mu_0}, \tag{3.16a}$$

$$H^X_{\text{ref},\,y} = \frac{-k_{\text{ref},\,x}\,E^X_{\text{ref},\,z} + k_{\text{ref},\,z}\,E^X_{\text{ref},\,x}}{\omega\mu_0}. \tag{3.16b}$$

Notice that when using the Second Principle of Equivalence there was only one component of the reflected electric field, and thus one spectrum function, per polarization after applying the POS simplifications. This was convenient because this way the copolar far field could be controlled independently for each polarization with the phase of one reflection coefficient, namely ρ_{xx} for X polarization and ρ_{yy} for Y polarization. However, for the magnetic field there are now two components in the tangential field, and thus two spectrum functions (having a total of three spectrum functions in the computation of the far field with the First Principle of Equivalence, taking also into account the electric field). Nevertheless, since the simplifications in the electric field apply, both components of the tangential magnetic field only depend on one reflection coefficient, again ρ_{xx} for X polarization and ρ_{yy} for Y polarization, maintaining the independence between the two polarizations as with the other Equivalence Principle.

In the case of the Y polarization, the reflected electric field has the following components:

$$E^Y_{\text{ref},\,x} = 0, \tag{3.17a}$$

$$E^Y_{\text{ref},\,y} = e^{j\phi^{mn}_{yy}}\,E^Y_{\text{inc},\,y}. \tag{3.17b}$$

Thus, the $\hat{z}$ component according to (2.54) is

$$E^Y_{\text{ref},\,z} = -\frac{k_{\text{ref},\,y}\,E^Y_{\text{ref},\,y}}{k_{\text{ref},\,z}}. \tag{3.18}$$

The magnetic field is then obtained as:

$$\begin{aligned}\vec{H}^Y_{\text{ref}}(x_m, y_n) &= \frac{\vec{k}_{\text{ref}} \times \vec{E}^X_{\text{ref}}(x_m, y_n)}{\omega\mu_0} \\ &= \frac{1}{\omega\mu_0}\Bigg(\Big(k_{\text{ref},\,y}\,E^Y_{\text{ref},\,z}(x_m, y_n) - k_{\text{ref},\,z}\,E^Y_{\text{ref},\,y}(x_m, y_n)\Big)\hat{x} \\ &\quad - k_{\text{ref},\,x}\,E^Y_{\text{ref},\,z}(x_m, y_n)\,\hat{y} - k_{\text{ref},\,x}\,E^Y_{\text{ref},\,y}(x_m, y_n)\,\hat{z}\Bigg).\end{aligned} \tag{3.19}$$

As only the tangential magnetic field is needed, we finally have:

$$H^Y_{\text{ref},\,x} = \frac{k_{\text{ref},\,y}\,E^Y_{\text{ref},\,z} - k_{\text{ref},\,z}\,E^Y_{\text{ref},\,y}}{\omega\mu_0}, \tag{3.20a}$$

$$H^Y_{\text{ref},\,y} = \frac{-k_{\text{ref},\,x}\,E^Y_{\text{ref},\,z}}{\omega\mu_0}. \tag{3.20b}$$

Once the tangential field has been obtained, the spectrum functions P^X_x, P^Y_y, $Q^{X/Y}_x$ and $Q^{X/Y}_y$ are computed following the steps provided in the previous chapter. Since for

the POS the spectrum functions P_y^X and P_x^Y are zero, the simplified far fields for X polarization are

$$E_\theta^X = \frac{jk_0e^{-jk_0r}}{4\pi r}\left[P_x^X\cos\varphi - \eta\cos\theta\left(Q_x^X\sin\varphi - Q_y^X\cos\varphi\right)\right], \tag{3.21a}$$

$$E_\varphi^X = -\frac{jk_0e^{-jk_0r}}{4\pi r}\left[P_x^X\sin\varphi\cos\theta + \eta\left(Q_x^X\cos\varphi + Q_y^X\sin\varphi\right)\right], \tag{3.21b}$$

while for Y polarization are

$$E_\theta^Y = \frac{jk_0e^{-jk_0r}}{4\pi r}\left[P_y^Y\sin\varphi - \eta\cos\theta\left(Q_x^Y\sin\varphi - Q_y^Y\cos\varphi\right)\right], \tag{3.22a}$$

$$E_\varphi^Y = -\frac{jk_0e^{-jk_0r}}{4\pi r}\left[-P_y^Y\cos\varphi\cos\theta + \eta\left(Q_x^Y\cos\varphi + Q_y^Y\sin\varphi\right)\right]. \tag{3.22b}$$

Finally, applying Ludwig's third definition of crosspolarization, the copolar and crosspolar components are obtained using (2.61) and (2.62). For the case at hand, only the copolar component is needed for both polarizations, which can be expressed as

$$E_{\text{cp}}^X = \cos\varphi\,E_\theta^X - \sin\varphi\,E_\varphi^X, \tag{3.23a}$$

$$E_{\text{cp}}^Y = \sin\varphi\,E_\theta^Y + \cos\varphi\,E_\varphi^Y. \tag{3.23b}$$

3.2.1.3. Differences between the First and Second Principles

When possible, the use of the First Principle of Equivalence for the analysis, synthesis and design of reflectarray antennas is recommended since it provides more accurate results [43,88]. Although the main differences in the radiation patterns are in the crosspolar component, there are also some differences in the copolar pattern.

Figure 3.3 shows the main cut of a shaped beam reflectarray with an isoflux pattern which was synthesized using the IA-POS with the Second Principle of Equivalence. As

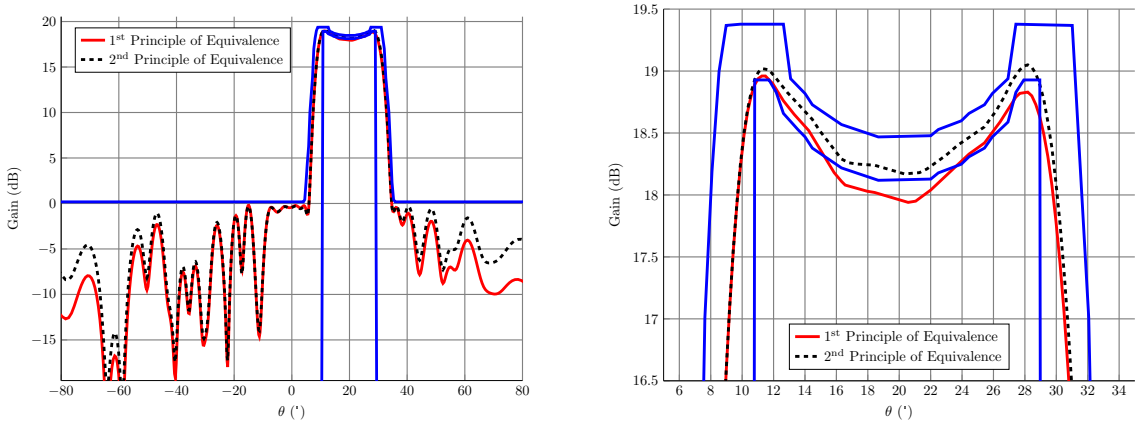

Figure 3.3: *Differences in the copolar pattern of an isoflux beam shaped reflectarray for the First and Second Equivalence Principles. (a) Cut in θ for $\varphi = 0°$. (b) Zoom in the coverage area.*

it can be seen, the synthesized pattern correctly fulfills the template. However, if the radiation pattern is computed using the First Principle of Equivalence and compared with the pattern obtained with the Second Principle, there are some differences. The side lobes present similar values for angles close to broadside, although they diverge for large angles. More importantly, in the coverage area there is a drop in gain of about 0.23 dB at $\theta = 20°$, where the antenna is pointing. Even though the shape of the copolar gain would agree with the template when computed with the First Principle, is notable that the predicted gain is lower than with the Second Principle. Thus, it might be interesting to use the POS formulation of the First Principle of Equivalence to synthesize reflectarrays whose application demands a correct prediction of the gain, such as space applications [19, 20], among others.

3.2.1.4. Inclusion of the dielectric frame

In the previous chapter the effect of the dielectric frame in the radiation patterns was evaluated, and it was concluded that it was necessary to include it in the analysis since the effects were important even in the copolar pattern. Hence, its inclusion in the synthesis process is also recommended, along with the use of the First Principle of Equivalence, to correctly synthesize the copolar pattern. However, when including the dielectric frame in the synthesis, some considerations need to be taken into account.

First, the dielectric has to be analyzed with MoM beforehand in order to extract the corresponding phase shift of the elements without metallizations that comprise the dielectric frame. For this case, only the phases are needed since it is the only information needed for POS, disregarding losses due to the dielectric and cross coefficients. And second, the dielectric phases will remain unaltered during the whole synthesis process, since there are no metallizations that will modify the phase shift introduced by the frame.

3.2.2. Forward projection

This projection is divided in two steps. First, the templates that give the requirements in the copolar radiation patterns are normalized through a constant C_n. Then, the projection in the set of the radiation patterns that fulfill the requirements is carried out.

3.2.2.1. Normalization of the requirement templates

The requirements of the copolar radiation patterns are usually given in gain. However, the projection is carried out in radiated field units, so the following equation that relates the gain and the radiated field must be used:

$$G(u,v) = \frac{|E(u,v)|^2\, 2\pi r^2}{\eta_0\, P_{\text{feed}}}. \tag{3.24}$$

Using (3.24), the gain templates are transformed to radiated field templates, resulting in

$$|T_{\max}(u,v)| = \sqrt{\frac{G_{\max}(u,v)\,\eta_0\, P_{\text{feed}}}{2\pi r^2}}, \tag{3.25a}$$

$$|T_{\min}(u,v)| = \sqrt{\frac{G_{\min}(u,v)\,\eta_0\,P_{\text{feed}}}{2\pi r^2}}, \tag{3.25b}$$

where $G_{\max}$ and $G_{\min}$ are the maximum and minimum requirement templates in copolar gain, given in natural units; P_{feed} the power given by the feed in watts, and $T_{\max}$ and $T_{\min}$ the requirement field templates in natural units.

Now, two possibilities arise. The synthesis can be performed either in fixed or float gain. If the synthesis is carried out in fixed gain, (3.25) are the final templates used in the synthesis process. This method can be useful to further refine a previous synthesis, as it will be shown in a subsequent chapter, devoted to crosspolar optimization. The other possibility is to carry out the synthesis in float gain, which is the preferred method, since it adapts automatically the templates to the maximum gain that can be obtained with the antenna (reflectarray in this case). For the float gain synthesis, the templates are normalized to the field radiated in a determined direction (u_0, v_0) which belongs to the maximum gain region. Thus, a normalizing constant C_n is defined as

$$C_n = \frac{|E_{\text{cp}}(u_0,v_0)|}{|T_{\text{av}}|}, \tag{3.26}$$

where T_{av} is the average value of the maximum and minimum templates in the desired direction

$$T_{\text{av}} = \frac{T_{\text{cp,max}}(u_0,v_0) + T_{\text{cp,min}}(u_0,v_0)}{2}. \tag{3.27}$$

The normalizing constant C_n is applied to the maximum and minimum templates in the following fashion:

$$T^n_{\max}(u,v) = T_{\max}(u,v)\cdot C_n, \tag{3.28a}$$

$$T^n_{\min}(u,v) = T_{\min}(u,v)\cdot C_n. \tag{3.28b}$$

The normalization process is the same for both polarizations and different templates can be used, as it would be the case of dual-polarized antennas with different shaped beams. This normalization process defines a float gain synthesis where the middle point of the templates at (u_0, v_0) is placed at the same level as the field. This method provides slightly better results than the fixed gain synthesis where the templates are not normalized [95], since it provides the shaping of the beam with the maximum gain that can be achieved for the defined antenna dimensions.

3.2.2.2. Projection onto the set of valid radiation patterns

Once the templates have been conveniently normalized, the copolar component of the field radiated by the reflectarray should accomplish

$$T^n_{\min}(u,v) \leq |E_{\text{cp}}(u,v)| \leq T^n_{\max}(u,v), \tag{3.29}$$

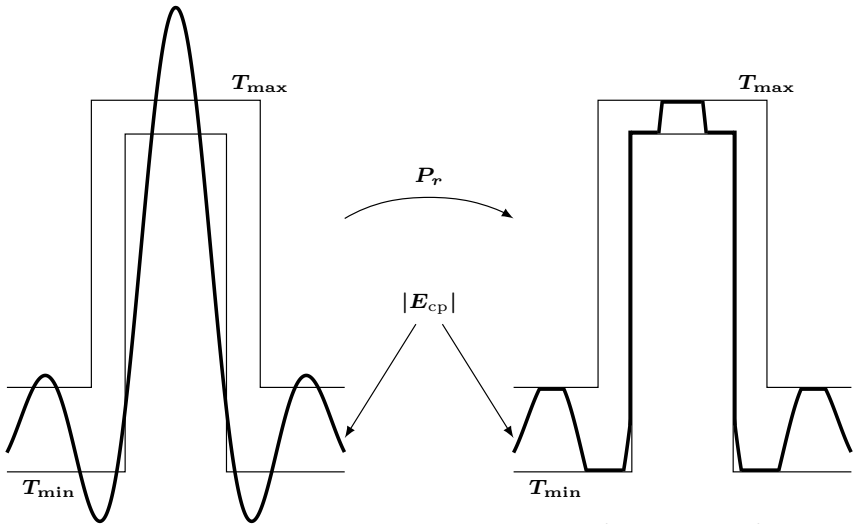

Figure 3.4: *Projection onto the set of valid radiation patterns.*

for either polarization. This condition can be fulfilled by the P_r operator, defined for all (u, v) for a generic electric field component as

$$P_r\left(E(u,v)\right) = \begin{cases} T^n_{\max}(u,v) \cdot \arg\left(E(u,v)\right), & T^n_{\max}(u,v) < |E(u,v)| \\ T^n_{\min}(u,v) \cdot \arg\left(E(u,v)\right), & T^n_{\min}(u,v) > |E(u,v)| \\ E(u,v), & \text{otherwise,} \end{cases} \tag{3.30}$$

where $\arg(\cdot)$ gives the phase of its complex argument. With this operator only the amplitude of the field is changed. The phase remains unaltered. The result of this operation is the field E',

$$E'(u,v) = P_r\left(E(u,v)\right). \tag{3.31}$$

For the sake of simplicity, a generic E field component and template T were used in (3.30) and (3.31), but they should be applied to the copolar component of both polarizations with their respective normalized templates. This projection is shown graphically in Figure 3.4.

3.2.3. Backward projection

The backward projection ($\mathcal{B}$), that is, the projection from the set of valid radiation patterns ($\mathcal{M}$) which fulfill the specifications, onto the set of possible radiation patterns ($\mathcal{R}$), is divided in three steps. First, the reflected field on the reflectarray surface is recovered, then amplitude and phase constraints are imposed, and finally the possible radiation pattern is computed.

3.2.3.1. Recovery of the reflected field

The first step in the implementation of the backward projection is the most complex, since the inverse process of the computation of the radiated far fields has to be carried

out. Once the P_r operator in (3.30) is applied, a trimmed copolar far field is obtained. Then, the spectrum functions can be directly recovered by isolating P in (3.12) using the Second Principle of Equivalence, having

$$P_x^X = E_{\text{cp}}^X \frac{2\pi r}{j\, k_0\, e^{-jk_0 r}} \frac{1}{\cos^2\varphi + \sin^2\varphi \cos\theta}, \tag{3.32a}$$

$$P_y^Y = E_{\text{cp}}^Y \frac{2\pi r}{j\, k_0\, e^{-jk_0 r}} \frac{1}{\sin^2\varphi + \cos^2\varphi \cos\theta}. \tag{3.32b}$$

In (3.32) there is a singularity when $\theta = \pi/2$ rad and $\varphi = \pi/2$ rad for X polarization, and $\theta = \pi/2$ rad and $\varphi = 0$ rad for Y polarization, although it is in the limit of the visible region in both cases ($\theta = \pi/2$ rad). In order to avoid numerical instabilities (e.g. overflows when $\theta \to \pi/2$ rad or divisions by zero), computations should avoid values of θ close to that value. In any practical realization of the algorithm, this is easy to accomplish due to the coarse discretization of the UV grid, which in most cases will not exceed from 512×512 or 1024×1024 points.

Notice that isolating the P functions is possible since each equation in (3.12) only has one variable using the Second Principle of Equivalence. However, this step of the Backward Projection is not possible working with the First Principle of Equivalence, for which each copolar pattern depends on three spectrum functions, P_x or P_y, depending on the polarization, and Q_x and Q_y, as shown in (3.21) and (3.22). Thus, using the First Principle it is not possible to recover the three spectrum functions from the copolar component of the far field. This is the reason why the IA-POS must be implemented with the Second Principle of Equivalence.

When calculating the far field from the reflected field, the spectrum function could be expressed as 2D IDFT as in (3.9). At this point, it is straightforward to recover the reflected field

$$E_{\text{ref},x}^X = \text{DFT2}\left[\frac{P_x^X(p,q)}{N_x \cdot N_y \cdot K(p,q) \cdot K'(p,q)}\right], \tag{3.33a}$$

$$E_{\text{ref},y}^Y = \text{DFT2}\left[\frac{P_y^Y(p,q)}{N_x \cdot N_y \cdot K(p,q) \cdot K'(p,q)}\right], \tag{3.33b}$$

taking into account the change of variables described in (2.84).

3.2.3.2. Projection onto the set of possible radiation patterns

When the reflected field is recovered by (3.33), it is computed in a grid with the same number of points as the far field, which is usually larger than the grid corresponding to the reflectarray elements, as discussed in the previous chapter. Hence, the recovered field that lies outside the reflectarray boundaries must be set to zero. This is an inherent constraint of the algorithm derived from the fact that it uses the FFT to recover the reflected field.

In general, the amplitude of the recovered reflected field can take any value, even values greater than the original reflected field, which cannot be accomplished by passive reflectarrays. In fact, the amplitude of the reflected field is the same as the incident field

(assuming no losses), and it remains fixed along the synthesis process. Hence, the next constraint is to generate a reflected field with the amplitude of the incident field but the phases of the recovered reflected field. This can be expressed mathematically through the P_t operator as

$$P_t\left[E_{\text{ref}}(x_m,\, y_n)\right] = \left|E_{\text{inc}}(x_m,\, y_n)\right| \cdot \arg\left[E_{\text{ref}}(x_m,\, y_n)\right], \tag{3.34}$$

which would be applied to recover the reflected field for both polarizations.

With the definition of the P_t operator in (3.34), only the phases are free to vary in an entire 360° cycle in each iteration of the IA. This behavior is very useful in the first stages of the synthesis process since a quick convergence can be obtained. However, when a refinement is required, a wide variation in phase could be not recommended. In those cases, the algorithm can be improved by introducing a phase constraint in the P_t operator, limiting the maximum variation in phase with regard to the initial phase distribution. Then, the P_t operator is modified as

$$P_t\left[E_{\text{ref}}(x_m,\, y_n)\right] = \left|E_{\text{inc}}(x_m,\, y_n)\right| \cdot e^{j\phi(x_m,\, y_n)}, \tag{3.35}$$

where the phase term $\phi(x_m,\, y_n)$ is defined for each reflectarray element $(m,\, n)$ depending on the variation suffered during a cycle of the algorithm,

$$\phi(x_m, y_n) = \begin{cases} \arg\left(E_{\text{ref}}(x_m, y_n)\right) & \forall (m,n) \;/\; \Delta\phi(x_m, y_n) < \Delta\phi_{\max}, \\ \arg\left(E_{\text{ref},0}(x_m, y_n)\right) + \Delta\phi_{\max} & \forall (m,n) \;/\; \Delta\phi(x_m, y_n) \geq \Delta\phi_{\max}, \end{cases} \tag{3.36}$$

where

$$\Delta\phi(x_m, y_n) = \left|\arg\left(E_{\text{ref}}(x_m, y_n)\right) - \arg\left(E_{\text{ref},0}(x_m, y_n)\right)\right|, \tag{3.37}$$

$\Delta\phi_{\max}$ is the maximum allowable phase variation and $\arg\left(E_{\text{ref},0}(x_m, y_n)\right)$ is the phase of the reflected field at the starting point of the synthesis process. With the introduction of this phase constraint, the convergence becomes slower, but a better control on the phase distribution is obtained.

If the dielectric frame is taken into account in the synthesis process, the phases for the elements belonging to the frame must not change at any iteration of the IA. Thus, the P_t operator is further modified as

$$P_t\left[E_{\text{ref}}(x_m,\, y_n)\right] = \begin{cases} \left|E_{\text{inc}}(x_m,\, y_n)\right| \cdot e^{j\phi(x_m,\, y_n)} & / \; (m,n) \notin \text{diel. frame}, \\ \left|E_{\text{inc}}(x_m,\, y_n)\right| \cdot e^{j\arg\left(E_{\text{ref},0}(x_m, y_n)\right)} & / \; (m,n) \in \text{diel. frame}, \end{cases} \tag{3.38}$$

where $\phi(x_m,\, y_n)$ and $\arg\left(E_{\text{ref},0}(x_m, y_n)\right)$ are the same as before.

3.2.3.3. Computation of the radiated field

Finally, the backward projection is completed with the computation of the field radiated by the reflectarray, considering the new reflected field distribution after applying the P_t operator in (3.34), (3.35) or (3.38) on the recovered reflected field. This step has already

been described in Section 3.2.1, and for the IA-POS the Second Principle of Equivalence must be used.

3.2.4. Variable number reduction

The starting point in the synthesis process is very important in order to avoid undesirable convergence to local minima, since the IA is a local optimizer. The case of reflectarrays is particularly critical, since the number of degrees of freedom can be very large (hundreds or thousands of elements). Thus, a radiation pattern similar to the required one would be desirable as a starting point. Another possibility is to start from a properly focused pencil beam and to introduce some control in the optimization algorithm.

In order to improve the convergence of the synthesis method in the case of reflectarrays, the number of unknowns should be reduced, reducing the number of degrees of freedom. As a consequence, the number of local minima becomes lower and the convergence of the algorithm is improved. This strategy can be carried out by a progressive synthesis of the reflectarray from the center to the edges, which can be also explained as the variation of the size of the reflectarray during the synthesis process (starting from an electrically smaller antenna). This progressive synthesis can be carried out by changing the directivity of the feed, starting from a high directivity feed. In this case, the field level at the edges of the reflectarray is extremely low and only the elements at the center of the reflectarray contribute significantly to the beam shaping. Although the physical size of the reflectarray has not changed, the effective size is smaller. The effective size of the reflectarray is progressively increased with the reduction of the feed directivity. The number of unknowns is progressively increased in the algorithm, which is carried out through a number of steps, avoiding undesired local minima. This technique can be easily implemented by modifying the feed directivity, which in the case of an ideal $\cos^q \theta$ feed model is done varying the q-factor of the function, starting with a high q value and ending with the q value which models the required feed horn. This technique is referred to as a fictitious reduction of unknowns.

3.2.5. Convergence criteria

The IA consists of an iterative approximation to the solution until a minimum is found. The algorithm converges to a minimum, but it can be a local minimum. In fact, a convergence to the global minimum is quite unlikely, especially when the starting point is far from the required solution. In the algorithm, the last step of each iteration is the evaluation of the convergence, treated as a distance. If the distance between the solutions in two consecutive iterations of the algorithm is under a given threshold, the process is falling in a local minima and it finishes. Thus, this criteria can be expressed as

$$\| |E_{\mathrm{cp},i}| - \mathcal{B}\left[\mathcal{F}\left(E_{\mathrm{cp},i}\right)\right] \| = \| |E_{\mathrm{cp},i}| - |E_{\mathrm{cp},i+1}| \| < d. \tag{3.39}$$

The norm function used to compute the distance between the solutions of two consec-

utive iterations is defined as

$$\|f\|^2 = \iint_{\Omega} |f(u,v)|^2 \, du\, dv, \tag{3.40}$$

where Ω is the UV area that belongs to the visible region. The double integral in (3.40) can be easily implemented by a double summation since the UV grid is already discretized to compute the radiation patterns.

3.2.6. Phase-only synthesis considerations

When performing phase-only synthesis, the only variables to be optimized are the phases of the reflection coefficients ρ_{xx}^{mn} and ρ_{yy}^{mn}. The approximations made to obtain the copolar far field patterns using the tangential field of (3.8) have proven to be valid in the case of reflectarray antennas [95], providing a copolar pattern which is very close to the exact one.

Usually, the reflectarray is required to be placed at far field distance of the feed, in which case the feed can be modeled as a $\cos^q \theta$ function [78], with very accurate results [19, 128]. This feed model can also be used in the preliminary steps of the synthesis process and later use full wave simulations of the feed in order to accurately predict the far field [20, 42, 146]. However, the copolar far fields obtained using both methods are very similar between each other. In any case, the algorithm described in the present work allows to use the real incident field from the feed, either by full wave simulations or near field measurements. The incident field is fixed throughout the synthesis process and only the phase shift that the reflectarray elements have to introduce is optimized in order to obtain the required copolar pattern.

Due to the simplifications made on the R^{mn} matrix, the crosspolar pattern that could be computed using (3.9) would not take into account the crosspolarization introduced by the reflectarray elements, which in practice is an important contribution to the crosspolar pattern. As it was explained before in detail, the copolar pattern obtained with the simplifications applied to the R^{mn} matrix is still accurate. However, the crosspolar pattern is not, hence a phase-only synthesis only deals with copolar requirements.

Once the synthesis is finished and the phases of ρ_{xx}^{mn} and ρ_{yy}^{mn} are obtained, a design can be carried out that takes into account the real element behavior. By using full wave simulations based on local periodicity [29, 54, 76], the full R^{mn} matrix is computed, taking into account mutual coupling between elements. During this step, a zero finding routine is used that calls iteratively a full wave simulator to adjust the required phase shift for each element. Because the synthesized phases are accurately adjusted using this procedure, the resulting phase distribution will have a small error with regard to those obtained after the POS, and hence the copolar pattern will be very close to the one synthesized.

3.2.7. Example

In this section, an application example of the IA will be shown for an isoflux pattern. Since this pattern will be used in following chapters for other optimizations, a procedure

for its generation will be detailed.

3.2.7.1. Isoflux pattern

The goal of the isoflux pattern is to provide coverage with constant energy flux on the surface of the Earth. A sketch of the Earth-satellite geometry is shown in Figure 3.5. There, R_e is the radius of the Earth, $d_{\min}$ and $d_{\max}$ are minimum and maximum distances from the satellite to the Earth surface, and $\theta_{\max}$ the maximum coverage angle.

The attenuation curve due to free space propagation is given by the Friis formula [129]

$$A = 20\log(f) + 20\log(d) + 32.5, \tag{3.41}$$

where A is the attenuation given in dB, f is the frequency in MHz and d is the distance from the satellite to the surface of the Earth in Km. If (x_s, y_s) are the satellite coordinates and (x_e, y_e) are the coordinates of a point in the Earth surface, d is calculated as

$$d = \sqrt{(x_s - x_e)^2 + (y_s - y_e)^2}. \tag{3.42}$$

The distance from the satellite to the surface of the Earth is given by its orbit, so $d_{\min}$ is known. Then, $d_{\max}$ is calculated using the Pythagorean theorem and $\theta_{\max}$ is obtained as

$$\cos\theta_{\max} = \frac{d_{\max}}{d_{\min} + R_e}. \tag{3.43}$$

Considering the origin of coordinates the center of the Earth, the points of its surface will follow the equation

$$x^2 + y^2 = R_e^2. \tag{3.44}$$

Then, the linear equation from the satellite to a point in the surface of the Earth can be expressed as

$$y = mx + n, \tag{3.45}$$

with $m = -\tan\theta$ and $n = -m\,(d_{\min} + R_e)$. Substituting (3.45) in (3.44), the following quadratic equation is obtained:

$$(1 + m^2)\,x^2 + 2\,m\,n\,x - \left(R_e^2 - n^2\right) = 0. \tag{3.46}$$

By solving (3.46) two solutions are obtained, which correspond to the intersection of

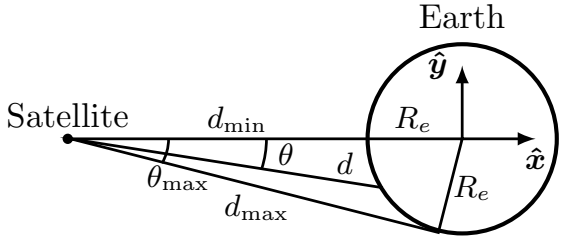

Figure 3.5: *Sketch of the Earth-satellite geometry.*

the straight line d with the Earth circumference. The one with $x < 0$, according to Figure 3.5, is selected; and then y is obtained with (3.44). This solution corresponds to the point (x_e, y_e) in (3.42), which along with the known satellite position (x_s, y_s) enable the calculation of the attenuation given by (3.41).

The attenuation curve is computed in a single plane, but since it is symmetric in φ, it is straightforward to obtain the attenuation in the whole Earth surface in spherical coordinates. It is common to perform reflectarray synthesis in the UV plane [2], knowing that $u = \sin\theta\cos\varphi$ and $v = \sin\theta\sin\varphi$.

The obtained attenuation pattern can be used directly as radiation pattern template if a symmetric antenna geometry is used. Apart from the attenuation curve, side lobe levels, ripple and a transition zone should also be specified. However, it is more common to use single-offset configurations [2], such as the one shown in Figure 2.1. The reflectarray radiates at an angle $\theta = \theta_0$ with regard to its own coordinate system, RCS. Hence, the centered templates have to be rotated by applying a proper transformation.

The template for the centered configuration in (θ, φ) coordinates is referenced to the RCS $(\hat{x}_r, \hat{y}_r, \hat{z}_r)$ of Figure 2.1. Each point of the template is transformed from spherical coordinates to cartesian coordinates

$$x_{\mathrm{RA}} = \sin\theta_{\mathrm{RA}}\cos\varphi_{\mathrm{RA}}, \tag{3.47a}$$

$$y_{\mathrm{RA}} = \sin\theta_{\mathrm{RA}}\sin\varphi_{\mathrm{RA}}, \tag{3.47b}$$

$$z_{\mathrm{RA}} = \cos\theta_{\mathrm{RA}}, \tag{3.47c}$$

and then the following transformation is applied

$$\begin{pmatrix} x_{\mathrm{ANT}} \\ y_{\mathrm{ANT}} \\ z_{\mathrm{ANT}} \end{pmatrix} = \begin{pmatrix} \cos\theta_0 & 0 & \sin\theta_0 \\ 0 & 1 & 0 \\ -\sin\theta_0 & 0 & \cos\theta_0 \end{pmatrix} \begin{pmatrix} x_{\mathrm{RA}} \\ y_{\mathrm{RA}} \\ z_{\mathrm{RA}} \end{pmatrix}. \tag{3.48}$$

Then, the cartesian coordinates will be transformed to spherical coordinates and from there to UV coordinates, with the usual operations.

3.2.7.2. Antenna specifications

The reflectarray is made up of 1528 elements disposed in a regular circular grid of 44×44 cells. The working frequency is 30 GHz and the periodicity is 4 mm $\times$ 4 mm (0.4λ). The reflectarray is fed by a horn antenna whose phase center is placed at $(-40, 0, 195)$ mm with regard to the reflectarray coordinate system (see Figure 2.1). The feed is modeled as a $\cos^q\theta$ function following [78] with a q-factor of 14.8, which produces an illumination taper of -12 dB at the reflectarray edges. The requirements for the isoflux pattern are specified by a reflectarray with $\theta_0 = 20°$, side lobe level of -19 dB and 0.25 dB of allowable ripple, placed on a satellite in geostationary orbit.

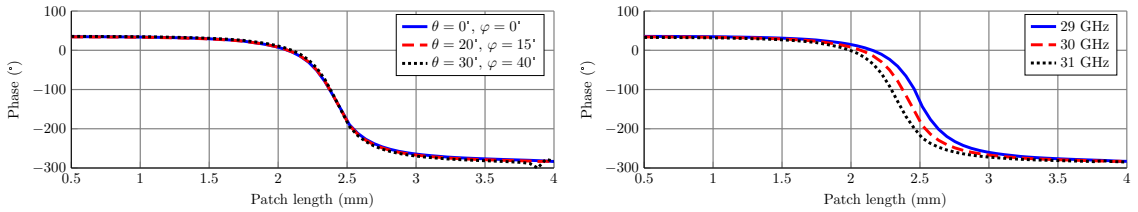

(a) *(b)*

Figure 3.6: *Phase range of the unit cell as a function of patch length for a periodicity of* 0.4λ *at 30 GHz. (a) For different incidence angles at 30 GHz. (b) For different frequencies at* $(\theta, \varphi) = (20°, 15°)$.

3.2.7.3. Unit cell study

The reflectarray chosen element is the rectangular microstrip patch backed by a ground plane [147]. Since only a single layer is used, the provided phase range of the cell will be lower than 360° [2]. Hence, it is important to study the element in order to delimit the phase range as a function of the patch size.

The Arlon 25N substrate is selected, with a relative permittivity $\varepsilon_r = 3.38$, thickness $h = 18$ mil and loss tangent $\tan\delta = 0.0025$ at 10 GHz. Figure 3.6 shows the phase variation of the unit cell as a function of the patch length for different angles of incidence and frequencies. In this study, the patches are squares. The results show that, in this particular case, the incidence angle barely affects the phase shift introduced by the element. When the frequency is shifted, the phase variation is non-linear, since for dimensions lower than 2 mm and higher than 3 mm it barely changes, but between 2 and 3 mm the phase is shifted with frequency.

In order to maximize the available phase range avoiding extreme values of the patch lengths (which would compromise the local periodicity assumption when carrying out the design [2]), the patch length is restricted to vary in the range 1.7 to 3.2 mm, which provides a phase range of about 300°.

3.2.7.4. Pattern synthesis and design

The reflectarray synthesis is carried out with the IA algorithm in several stages as described before, starting with a high value of q in order to artificially reduce the number of variables. Each step of the synthesis reduces the q-factor until its value reaches that of the horn feed. The starting point is a pencil beam pattern pointing at $(\theta, \varphi) = (20°, 0°)$. Also, since the generation of the isoflux template is parameterized, in the first steps of the synthesis the allowed ripple will be higher in order to facilitate convergence, and as the algorithm is approaching the solution, the ripple will be gradually reduced until the prescribed template value is achieved. Table 3.1 shows the number of iteration for each q-factor at each step of the synthesis of the isoflux pattern.

Since the selected unit cell only provides a phase range of 300°, the IA needs to be modified in order to impose a phase range restriction. In the general framework of the IA applied to array synthesis, the reflectarray is a particular case in which the amplitude

Table 3.1: *Number of iterations for each q-factor and its associated taper at each step of the synthesis of the isoflux pattern.*

***q*-factor**	**Taper (dB)**	**# it.**
80	60.0	20
60	45.3	40
50	38.0	40
40	30.6	50
30	23.2	60
20	15.9	30
15	12.2	60
14.8	12.0	130

is fixed by the incident field of the feed, and now the phase is also constrained in order to match the available phase range from the unit cell, allowing it to vary only from 0° to −300° to match the provided phase shift by the unit cell, shown in Figure 3.6.

Once the synthesis is finished and the required phase distribution is obtained, the patch lengths are adjusted element by element using the Method of Moments (MoM) [54] and a zero-finding routine. In this process, the real angle of incidence from the feed to each element of the reflectarray is used, in order to take into account possible phase shifts due to the incidence angle. Also, the MoM employs the Floquet theorem to analyze the unit cell, which embeds the analyzed element within an infinite array comprised of the same element, taking into account mutual coupling and the reflected field from the ground. It is thus important that the patch size variation is smooth in order to fulfill the local periodicity assumption of the analysis technique. Also, the design produces slightly rectangular patches, since the reflection coefficients are to some extent different for both polarizations, and the synthesized phases for both polarizations are not completely identical.

3.2.7.5. Results

The synthesis was carried out for both polarizations, obtaining a dual-linear polarized reflectarray with an isoflux pattern in both polarizations. The results for both polarizations are similar, and only the patterns for X polarization are shown. Figure 3.7 shows the synthesized phases with a total phase range of 300° imposed during the synthesis process. As reference, a synthesis with no phase constraints was also performed with the phase distributions shown in Figure 3.8.

Figure 3.9 shows the results between the synthesis with and without phase constraints. When the phase is free to vary in the whole 360° range, a smooth coverage area can be obtained. However, restricting the phase range to 300° causes the algorithm not to converge properly, and there is a ripple in the coverage zone. It is also shown the simulation after the design was made, simulating the patches with MoM [54], and there is little variation in the copolar component with regard to the simulation with ideal phase shifters.

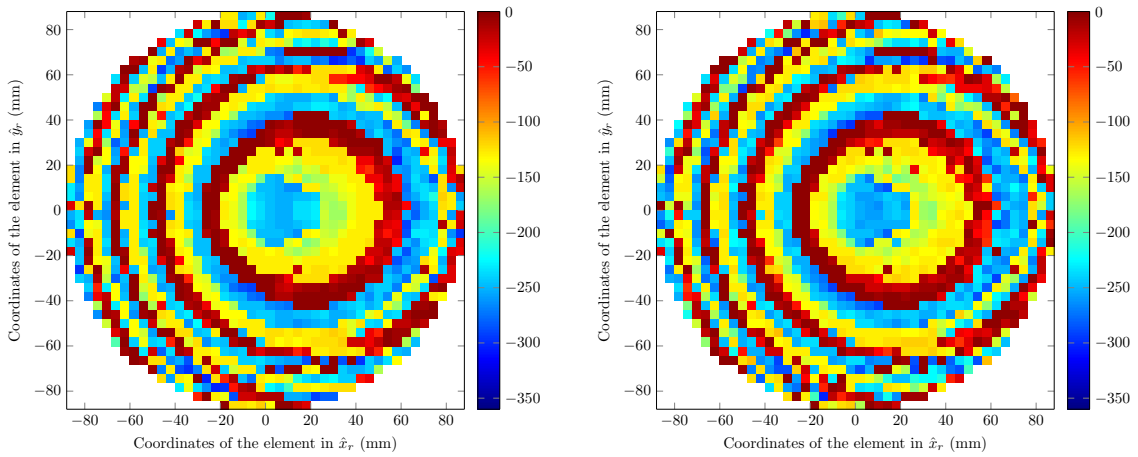

(a) *(b)*

Figure 3.7: *Synthesized phases for an isoflux pattern with a phase restriction of 300°. (a) X polarization. (b) Y polarization.*

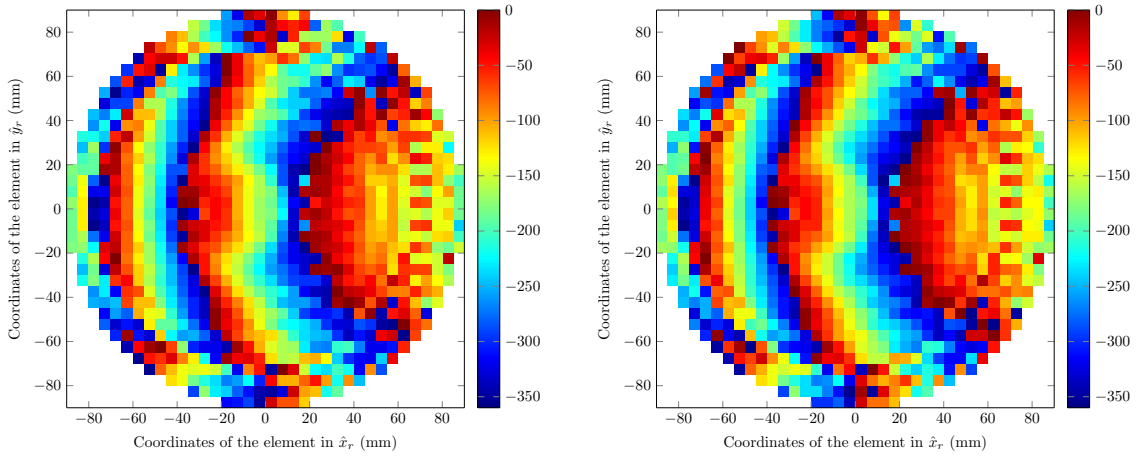

(a) *(b)*

Figure 3.8: *Synthesized phases for an isoflux pattern without phase restriction. (a) X polarization. (b) Y polarization.*

After the phase-only synthesis, the reflectarray was manufactured and measured. Figure 3.10 shows a picture of the prototype with the supporting structure, which secures the position of the feed and the reflectarray breadboard. The antenna was measured in a spherical far-field range anechoic chamber at 30 GHz and the measurements are shown in Figures 3.11 and 3.12. The deterioration in the coverage area is attributed to several causes. First, in the synthesis process the corners of the reflectarray were not taken into account. Also, the coverage area is very sensitive to variations in the height and relative permittivity of the substrate. New simulations were performed for a square reflectarray and different values of the parameters of the substrate. A better agreement between simulations and measurements was obtained than with the circular reflectarray (see Figure 3.12). Side lobes are also affected by reflections in the supporting structure and diffraction in the edge of the breadboard, which were not taken into account.

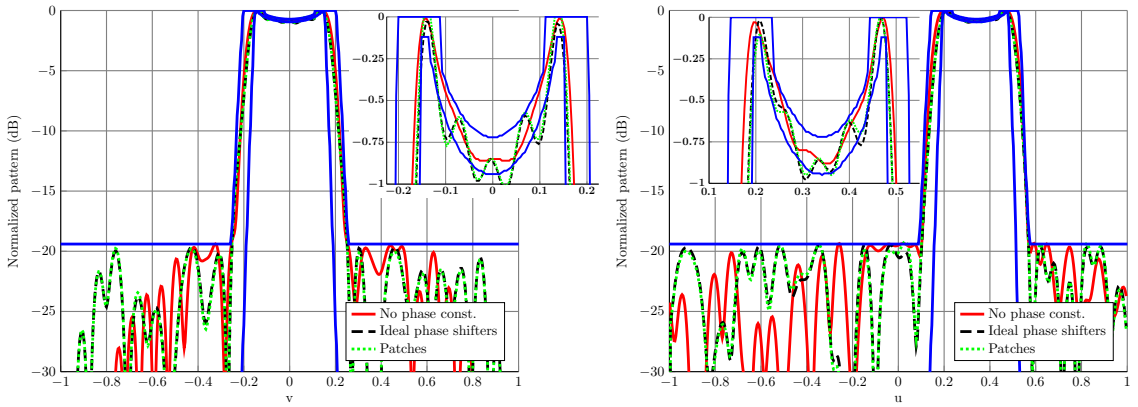

Figure 3.9: *Main cuts of the synthesized isoflux pattern for three different simulations for X polarization: reference simulation (no phase constraints, red solid), simulation with ideal phase shifters (phase constraints, dashed black) and design simulation (phase constraints, dotted green). (a)* $u = 0.34$. *(b)* $v = 0$.

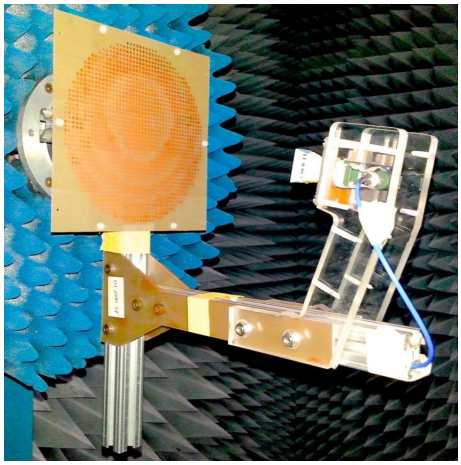

Figure 3.10: *Picture of the prototype in the anechoic chamber.*

These issues can be minimized by choosing a more appropriate antenna geometry, which reduces the interference of the supporting structure, and by employing a rectangular reflectarray instead of a circular one, having more variables to adjust the pattern and taking into account the corners of the breadboard. Also, decreasing the illumination at the edge would reduce the diffraction effects.

3.3. Efficient generalization of the Intersection Approach with far field crosspolar requirements

The main disadvantage of the Intersection Approach algorithm presented in the previous section is that it only performs a phase-only synthesis, which means that it only deals with the copolar pattern and there is no control over the crosspolar one. One of the first attempts to reduce the crosspolar radiation pattern in reflectarrays was presented in [114] and later used in [115]. It is based on properly adding a constant to the reflectarray phase

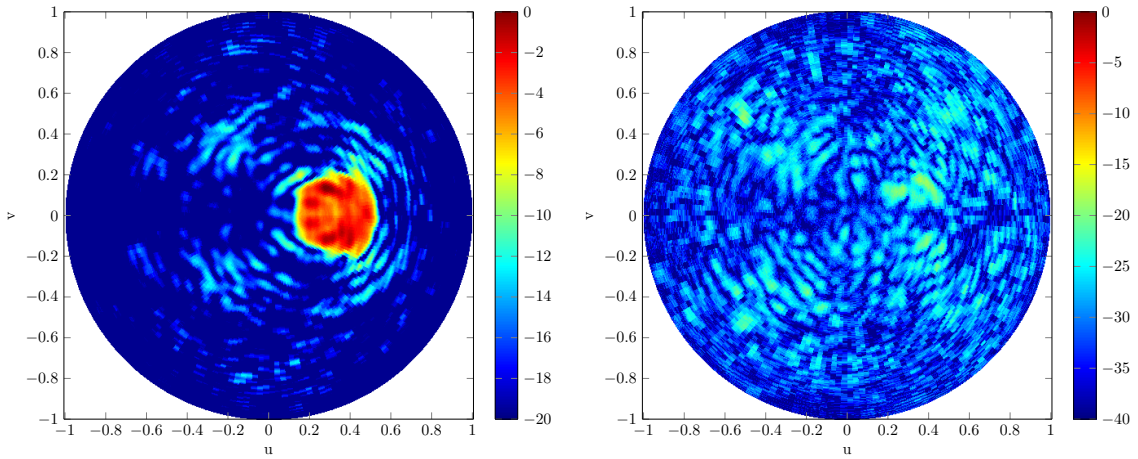

Figure 3.11: *3D measured pattern for X polarization. (a) Copolar. (b) Crosspolar.*

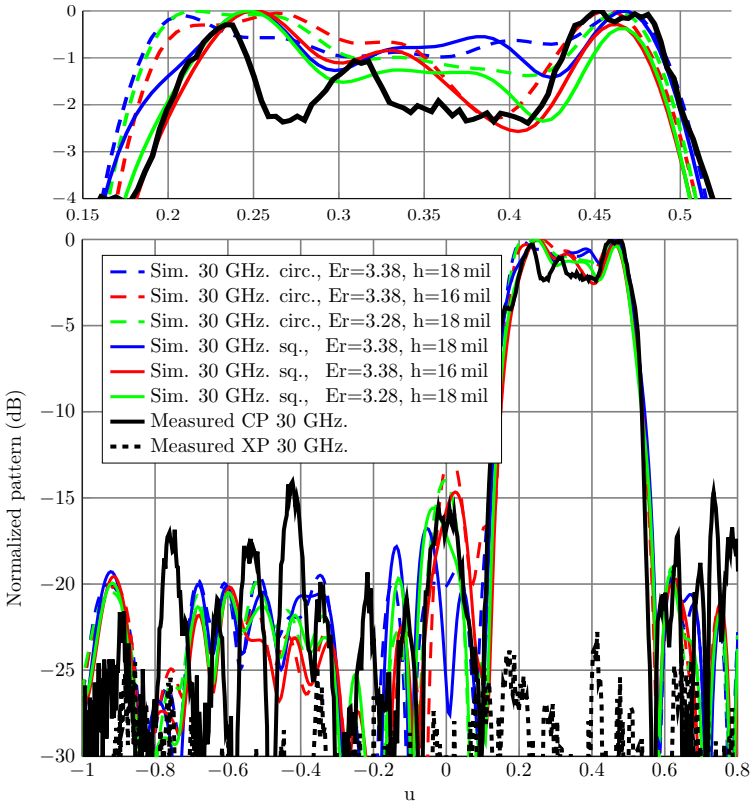

Figure 3.12: *Measurement and simulations for $v = 0$ for X polarization.*

distribution in order to enforce 180° phase shifts and amplitude nulls in the reflection cross coefficients that contribute more to the crosspolar pattern. However, it is not flexible since it only tries to reduce the contribution of the cross coefficients after the synthesis is done instead of synthesizing the crosspolar pattern to a desired value. This latter approach was followed in [116–118], using the IA general framework [89] with the Broyden-Fletcher-Goldfarb-Shanno (BFGS) [100] algorithm as the backward projector. It directly optimized the geometry of the antenna using MoM, resulting in a very slow algorithm. Also, it only

dealt with single-polarized reflectarrays. More recently, some works have appeared that deal with dual-polarized reflectarrays with crosspolar constraints. For instance, in [17], a faceted dual-polarized reflectarray with crosspolar suppression is presented, where after a POS pattern is obtained, the crosspolar component is suppressed and the currents on the surface of the reflectarray are obtained. From there, the matrix of reflection coefficients are computed, which fully characterize the reflectarray element. In [18] another faceted reflectarray is designed using a different approach. The reflectarray is directly optimized [119] using a gradient-based minimax algorithm and it also uses a phase-only synthesis as starting point, but in this case the initial reflectarray phase distribution is retrieved from a shaped reflector design.

In this section, a generalization of the IA algorithm presented in the previous section is developed for the synthesis of planar dual-polarized reflectarrays with crosspolar requirements. It will be denoted as IA-XP. As in [17], it synthesizes the matrix of complex reflection coefficients, although in a more flexible fashion since it is based on the IA framework of [116–118], allowing to perform the synthesis in one step without requiring a previous POS (although a previous POS would improve the starting point, which could improve the convergence of the algorithm as in any local optimizer [89]), and allowing the design of dual-polarized antennas while preserving the algorithm efficiency by using the FFT in both projections. In contrast with POS, where the phases are free to take any value, the matrices of reflection coefficients might take values which are impossible to obtain with passive reflectarrays. Hence, a lossless and lossy passive two-port network analysis of the reflectarray unit cell is carried out as part of an effort to impose constraints to obtain feasible reflection coefficients for passive reflectarrays. From this study, the restriction equations are derived for both cases involving reflection coefficient amplitudes and phases. Numerical examples are provided that show the capabilities of the algorithm to synthesize reflection coefficients with restrictions.

For this generalization, the IA framework remains the same, and it is based on the iterative process described by (3.3). Also, the same flow chart as the one shown in Figure 3.2 still applies. The difference lies in the redefinition of both projectors (namely, the forward $\mathcal{F}$ and backward $\mathcal{B}$ projectors) to include the crosspolar requirements. Despite this redefinition, the divisions in different steps of each projector remain the same as well. However, the IA-XP also presents the limitation that must be implemented with the Second Principle of Equivalence for the computation of the far field, since using the First Principle would not allow to recover the reflected field using the FFT in the backward projector, as it happened in the case of the IA-POS.

3.3.1. Computation of the far field

A detailed description of the computation of the far field radiated by a reflectarray antenna has already been described in the previous chapter using the First and Second Principles of Equivalence. However, as it happened in the POS case, only the Second Principle is suitable for this algorithm, as it will be shown later on. For the POS case, some simplifications in the R^{mn} matrix were applied, in which the reflectarray elements were

considered as ideal lossless phase shifters; as well as others in the reflected field. As a result, only the copolar pattern could be considered in the synthesis process and the two polarizations were synthesized independently from each other. In order to include crosspolar requirements it is necessary to use the full R^{mn} matrix, with no simplifications. This way, the cross coefficients are not zero, and account for an important contribution to the crosspolar pattern. Then, the reflected field at each element (m, n) is given by

$$\vec{E}_{\text{ref}}^{X/Y}(x_m, y_n) = R^{mn} \cdot \vec{E}_{\text{inc}}^{X/Y}(x_m, y_n), \tag{3.49}$$

with

$$R^{mn} = \begin{pmatrix} \rho_{xx}^{mn} & \rho_{xy}^{mn} \\ \rho_{yx}^{mn} & \rho_{yy}^{mn} \end{pmatrix}, \tag{3.50}$$

and $\vec{E}_{\text{inc}}^{X/Y}$ the incident field from the feed. Equation (3.49) provides the relation between the reflected field on the surface of the reflectarray with the incident field from the feed through the matrix of reflection coefficients for each element of the reflectarray. The reflected field can be also expressed as

$$\vec{E}_{\text{ref}}^{X/Y}(x, y) = E_{\text{ref},x}^{X/Y}(x, y)\,\hat{x} + E_{\text{ref},y}^{X/Y}(x, y)\,\hat{y}, \tag{3.51}$$

taking into account that the desired component for a given polarization X or Y is the $\hat{x}$ or $\hat{y}$ component, respectively.

Once the total tangential field has been obtained, the far field radiated by the antenna is computed. Using the Second Principle of Equivalence, the far field in spherical coordinates is given by [85]

$$E_{\theta}^{X/Y} = \frac{jk_0 e^{-jk_0 r}}{2\pi r}\left(P_x^{X/Y}\cos\varphi + P_y^{X/Y}\sin\varphi\right), \tag{3.52a}$$

$$E_{\varphi}^{X/Y} = -\frac{jk_0 e^{-jk_0 r}}{2\pi r}\cos\theta\left(P_x^{X/Y}\sin\varphi - P_y^{X/Y}\cos\varphi\right), \tag{3.52b}$$

with $P_x^{X/Y}$ and $P_y^{X/Y}$ being the spectrum functions. It is worth noting that when the synthesis process is carried out only for the copolar pattern (POS case), the simplifications in the reflected field cause that the far fields for both polarizations only require the computation of one spectrum function, P_x for X polarization and P_y for Y polarization (see (3.10), (3.11) and (3.12)). However, now both functions are necessary since also the crosspolar pattern has to be accurately computed. They can be calculated as

$$P_x^{X/Y}(u, v) = \iint_S E_{\text{ref},x}^{X/Y}(x, y)\, e^{jk_0(ux+vy)}\, dx\, dy, \tag{3.53a}$$

$$P_y^{X/Y}(u, v) = \iint_S E_{\text{ref},y}^{X/Y}(x, y)\, e^{jk_0(ux+vy)}\, dx\, dy, \tag{3.53b}$$

where S is the surface of the planar aperture. The calculation of P_x and P_y is the most time consuming problem in the computation of the radiated field. A direct evaluation of (3.53)

gives a time complexity of $\mathcal{O}(M^2)$, being M the number of points of the grid in the UV space. However, they can be expressed as a two-dimensional inverse Fourier transform and thus calculated efficiently by means of a two-dimensional inverse FFT (IFFT) with a time complexity of $\mathcal{O}(M \log M)$ as follows:

$$P_x = N_x\, N_y\, K\, K' \,\mathrm{IFFT}\left\{E_{\mathrm{ref},x} e^{-j\pi(m+n)}\right\}, \tag{3.54a}$$

$$P_y = N_x\, N_y\, K\, K' \,\mathrm{IFFT}\left\{E_{\mathrm{ref},y} e^{-j\pi(m+n)}\right\}, \tag{3.54b}$$

where N_x and N_y are the number of elements in the x and y directions, respectively; m and n integer indices of the reflectarray elements, K' is a phase-only term and K the amplitude of a single element radiation pattern. The detailed development was shown in the previous chapter.

Once the radiated far field is obtained with (3.52), the copolar and crosspolar components are obtained applying Ludwig's third definition of crosspolarization starting from the θ and φ components [131]. They are defined in the case of X polarization as

$$\begin{pmatrix} E^X_{\mathrm{cp}} \\ E^X_{\mathrm{xp}} \end{pmatrix} = \begin{pmatrix} \cos\varphi & -\sin\varphi \\ -\sin\varphi & -\cos\varphi \end{pmatrix} \begin{pmatrix} E^X_{\theta} \\ E^X_{\varphi} \end{pmatrix}, \tag{3.55}$$

and for Y polarization as

$$\begin{pmatrix} E^Y_{\mathrm{cp}} \\ E^Y_{\mathrm{xp}} \end{pmatrix} = \begin{pmatrix} \sin\varphi & \cos\varphi \\ \cos\varphi & -\sin\varphi \end{pmatrix} \begin{pmatrix} E^Y_{\theta} \\ E^Y_{\varphi} \end{pmatrix}. \tag{3.56}$$

3.3.2. Forward projection

The forward projection is again divided in two steps. The first step consists in the normalization of the templates that provide the requirements in copolar and crosspolar radiation patterns, which are usually given in gain. Hence, in order to carry out the synthesis, the gain templates must be converted to field templates, which can be simply done by taking the square root of the gain in natural units, as in (3.25) for the IA-POS. The templates are then normalized to the field radiated value in a determined direction (u_0, v_0) which belongs to the maximum gain region. Thus, a normalizing constant is defined as follows:

$$C_n = \frac{|E_{\mathrm{cp}}(u_0, v_0)|}{|T_{\mathrm{av}}|}, \tag{3.57}$$

where T_{av} is the average value of the maximum and minimum templates in the desired direction

$$T_{\mathrm{av}} = \frac{T_{\mathrm{cp,max}}(u_0, v_0) + T_{\mathrm{cp,min}}(u_0, v_0)}{2}. \tag{3.58}$$

The normalizing constant C_n has to be defined for both polarizations and is to be applied to both copolar and crosspolar templates in the following fashion

$$T^n_{\mathrm{cp,max}}(u,v) = T_{\mathrm{cp,max}}(u,v) \cdot C_n, \tag{3.59a}$$

$$T^n_{\mathrm{xp,max}}(u,v) = T_{\mathrm{xp,max}}(u,v) \cdot C_n. \tag{3.59b}$$

In the same way to (3.59), the minimum templates also have to be normalized. The normalization process is the same for both polarizations and different templates can be used, as it would be the case of dual-polarized antennas with different shaped beams. This normalization process defines a float gain synthesis where the middle point of the templates at (u_0, v_0) is placed at the same level as the field. This method provides slightly better results than the fixed gain synthesis where the templates are not normalized. With regard to the IA-POS, notice that C_n is computed only with the copolar field and templates, but is now applied to both copolar and crosspolar templates.

Once the templates have been normalized, both components of the radiated field should accomplish the following condition:

$$T^n_{\mathrm{cp,min}}(u,v) \leq |E_{\mathrm{cp}}(u,v)| \leq T^n_{\mathrm{cp,max}}(u,v), \tag{3.60a}$$

$$T^n_{\mathrm{xp,min}}(u,v) \leq |E_{\mathrm{xp}}(u,v)| \leq T^n_{\mathrm{xp,max}}(u,v). \tag{3.60b}$$

This condition can be fulfilled by the P_r operator, defined for all (u,v) as follows for a generic electric field component E:

$$P_r\left(E(u,v)\right) = \begin{cases} T^n_{\max}(u,v) \cdot \arg\left(E(u,v)\right), & T^n_{\max}(u,v) < |E(u,v)| \\ T^n_{\min}(u,v) \cdot \arg\left(E(u,v)\right), & T^n_{\min}(u,v) > |E(u,v)| \\ E(u,v), & \text{otherwise,} \end{cases} \tag{3.61}$$

where $\arg(\cdot)$ gives the phase of its complex argument. With this operator only the amplitude of the field is changed. The phase remains unaltered. The result of this operation is the field E',

$$E'(u,v) = P_r\left(E(u,v)\right). \tag{3.62}$$

For the sake of simplicity, a generic E field component and template T were used in (3.61) and (3.62), but they should be applied to the copolar and crosspolar components of both polarizations with their respective normalized templates. The result of the forward projection, $E'(u,v)$ given by (3.62), is a radiation pattern that fulfills the specifications but which, in general, cannot be radiated by the antenna (it belongs to the set $\mathcal{M}$).

3.3.3. Backward projection

The backward projection is implemented in three steps. First, the reflection coefficient matrices must be recovered. Starting from the trimmed copolar and crosspolar components according to Ludwig's third definition, the θ and φ components of the far field have to

be calculated. As the matrices that relate the θ and φ components with the copolar and crosspolar components in (3.55) and (3.56) are symmetric and orthogonal, their inverses are equal to themselves, so the far fields in spherical coordinates are easily obtained for both polarizations.

Now, the spectrum functions must be obtained from E_θ and E_φ. Re-expressing (3.52) in matrix form and calculating the inverse, P_x and P_y are found

$$\begin{pmatrix} P_x^{X/Y} \\ P_y^{X/Y} \end{pmatrix} = \frac{2\pi r}{jk_0 e^{-jk_0 r}} \begin{pmatrix} \cos\varphi & -\sin\varphi/\cos\theta \\ \sin\varphi & \cos\varphi/\cos\theta \end{pmatrix} \begin{pmatrix} E_\theta^{X/Y} \\ E_\phi^{X/Y} \end{pmatrix}. \tag{3.63}$$

In (3.63) there is a singularity when $\theta = \pi/2$ rad, although it is in the limit of the visible region. In order to avoid numerical instabilities (e.g. overflows when $\theta \to \pi/2$ rad or divisions by zero), computations should avoid values of θ close to that value. In any practical realization of the algorithm, this is easy to accomplish due to the coarse discretization of the UV grid, which in most cases will not exceed from 512×512 or 1024×1024 points.

As it happened with the IA-POS, recovering the spectrum functions is not possible when using the First Principle of Equivalence since there would be four spectrum functions per polarization, and only two far field components, having an underdetermined system with infinite solutions.

When calculating the far field from the reflected field, the spectrum functions could be expressed as 2D IFFT as in (3.54). At this point it is straightforward to recover the reflected field

$$E_{\text{ref},x} = \text{FFT}\left\{{}^{P_x}/_{N_x N_y KK'}\right\}\, e^{j\pi(m+n)}, \tag{3.64a}$$

$$E_{\text{ref},y} = \text{FFT}\left\{{}^{P_y}/_{N_x N_y KK'}\right\}\, e^{j\pi(m+n)}. \tag{3.64b}$$

The FFT recovers the reflected field in a grid with the same number of points as the UV grid. If this grid has more points than the actual reflectarray (i.e. to have better resolution of the radiated far fields), all the points of the recovered reflected field outside the physical reflectarray must be set to zero. This is an inherent constraint of the intersection approach algorithm and prevents it to converge in just one iteration when no other constraints are imposed. This also happened in the IA-POS.

Once the reflected field is recovered, along with the incident field, the reflection coefficients are recovered. Four equations can be extracted from (3.49), two for each polarization. As the unknowns are also four (the four reflection coefficients), one solution is obtained for dual-polarized antennas. This means that both polarizations are not independent anymore (as in contrast to the phase-only synthesis) in this version of the IA algorithm. The recovered reflection coefficients correspond to the Floquet fundamental mode when analyzed with an electromagnetic technique [2]. The solution to (3.49) is

$$\rho_{xy} = \frac{E_{\text{ref},x}^Y \cdot E_{\text{inc},x}^X - E_{\text{ref},x}^X \cdot E_{\text{inc},x}^Y}{E_{\text{inc},y}^Y \cdot E_{\text{inc},x}^X - E_{\text{inc},y}^X \cdot E_{\text{inc},x}^Y}, \tag{3.65a}$$

$$\rho_{xx} = \frac{E^X_{\text{ref},x} \cdot E^Y_{\text{inc},y} - E^Y_{\text{ref},x} \cdot E^X_{\text{inc},y}}{E^Y_{\text{inc},y} \cdot E^X_{\text{inc},x} - E^X_{\text{inc},y} \cdot E^Y_{\text{inc},x}}, \tag{3.65b}$$

$$\rho_{yx} = \frac{E^Y_{\text{ref},y} \cdot E^X_{\text{inc},y} - E^X_{\text{ref},y} \cdot E^Y_{\text{inc},y}}{E^Y_{\text{inc},x} \cdot E^X_{\text{inc},y} - E^X_{\text{inc},x} \cdot E^Y_{\text{inc},y}}, \tag{3.65c}$$

$$\rho_{yy} = \frac{E^X_{\text{ref},y} \cdot E^Y_{\text{inc},x} - E^Y_{\text{ref},y} \cdot E^X_{\text{inc},x}}{E^Y_{\text{inc},x} \cdot E^X_{\text{inc},y} - E^X_{\text{inc},x} \cdot E^Y_{\text{inc},y}}. \tag{3.65d}$$

The second step in the implementation of the backward projection is to impose constraints on the reflection coefficients. After solving for the reflection coefficients, the solution can give any value, in general with magnitudes (modulus) greater than one. Hence, some constraints have to be applied. The magnitudes must be smaller than one and the reflection coefficients have to meet the power balance. However, the more constraints there are the more difficult for the algorithm to converge. Furthermore, the fact that both polarizations are not independent from each other anymore reduces the degrees of freedom thus making it harder to converge and control. In the following section, restriction equations are derived in order to obtain feasible reflection coefficients for passive reflective elements when constraints are applied in this step of the backward projection. In addition to those constraints, if the dielectric frame is considered during the synthesis with the IA-XP, the reflection coefficient matrix of those elements must remain unchanged at each iteration. Those matrices should be computed using MoM before the first iteration of the algorithm in order to take into account the real effect of a dielectric frame.

Finally, the third step consists in the computation of the radiated far fields from the reflection coefficients and the incident field, as detailed previously. If the far fields fulfill the specifications (or are close enough), the synthesis process concludes. Otherwise, the iterative process continues by applying the forward projection, and then again the backward projection until a minimum user-defined error is achieved or a determined number of iterations reached. In this regard, the IA-POS convergence criteria of Section 3.2.5 is the same for the IA-XP, but integrating the four far fields in the visible region instead of only the two copolar components.

3.3.4. Efficiency of the algorithm

The presented algorithm is very efficient. Each iteration of the IA is comprised of one forward and one backward projection. The most expensive operation in each projection is the FFT/IFFT, with a time complexity of $\mathcal{O}(M \log M)$. Each projection has four calls to the FFT, since it has to compute four different radiation patterns, which makes a total of eight calls to the FFT. This is extremely fast in modern computers. Tests were carried out in an Intel Core i3-2100 with 4 CPU (two physical, two virtual) at 3.1 GHz, taking less than 0.5 s each iteration for a UV grid of 512×512 points. As for any local optimizer, convergence to a suitable solution depends on the starting point, specifications and antenna geometry [89].

3.3.5. Feasibility of the R matrix

When synthesizing radiation patterns with the algorithm described above, some restrictions have to be imposed depending on the antenna under consideration. For the case of passive reflectarrays, the reflected power will be at best equal to the incident power, when no losses are considered. This means that the magnitudes of the reflection coefficients cannot be greater than one, in natural units. However, imposing this condition does not mean that the obtained reflection coefficients after the synthesis process are feasible. The power balance must be met and perhaps other conditions.

Each cell of the reflectarray can be seen as a two port network, being port 1 the $\hat{x}$ component and port 2 the $\hat{y}$ component of the electric field. Both ports share the same physical space but are orthogonal to each other. A schematic view of this network is shown in Figure 3.13. This analogy is only valid on the surface of the cell, where the reflection coefficients are defined [2]. From this point of view, the incident and reflected fields are related through the R^{mn} matrix. However, in order to carry out the feasibility analysis considering the cell as a two port network an S-parameter matrix is needed [148], and R^{mn} is not an S-parameter matrix. As the characteristic impedances are unknown in Cartesian basis, it is best to carry out the analysis in the TE-TM basis.

3.3.5.1. Obtaining matrix S from matrix R

The relation between the TE-TM and Cartesian components for the fundamental Floquet harmonic is [2]

$$\hat{e}_{\mathrm{TE}} = -\sin\varphi\,\hat{x} + \cos\varphi\,\hat{y}, \tag{3.66a}$$

$$\hat{e}_{\mathrm{TM}} = \quad \cos\varphi\,\hat{x} + \sin\varphi\,\hat{y}, \tag{3.66b}$$

where (θ, φ) is the angle of incidence of the fundamental mode at each reflectarray element. Equation (3.66) is the equation system to change from Cartesian to TE-TM basis. The

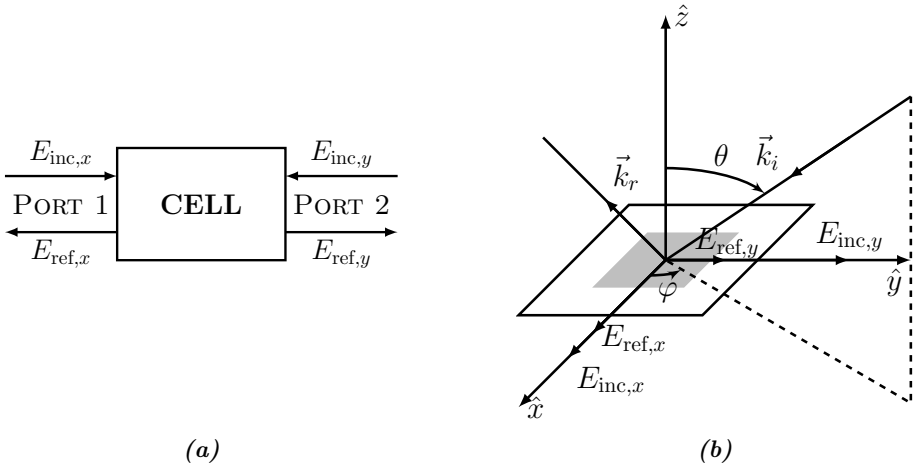

Figure 3.13: *Unit cell of the reflectarray seen as a two port network. (a) Black box representation. (b) Two ports sharing the same physical space.*

change of basis matrix is

$$B = \begin{pmatrix} -\sin\varphi & \cos\varphi \\ \cos\varphi & \sin\varphi \end{pmatrix}. \tag{3.67}$$

Matrix B is symmetric and orthogonal so $B^{-1} = B$. The R matrix in TE-TM basis is then

$$R_{\mathrm{TETM}} = B \cdot R \cdot B^{-1} = B \cdot R \cdot B = \begin{pmatrix} \rho_{\mathrm{TETE}} & \rho_{\mathrm{TETM}} \\ \rho_{\mathrm{TMTE}} & \rho_{\mathrm{TMTM}} \end{pmatrix}. \tag{3.68}$$

Matrix R_{TETM} relates the incident with the reflected electric fields in TE-TM basis. However, the characteristic impedances of the two ports (i.e. TE and TM) are not the same. From [148], the generalized S matrix in TE-TM basis is

$$S_{\mathrm{TETM}} = \begin{pmatrix} \rho_{\mathrm{TETE}} & \rho_{\mathrm{TETM}}\sqrt{\dfrac{Z_{\mathrm{TM}}}{Z_{\mathrm{TE}}}} \\ \rho_{\mathrm{TMTE}}\sqrt{\dfrac{Z_{\mathrm{TE}}}{Z_{\mathrm{TM}}}} & \rho_{\mathrm{TMTE}} \end{pmatrix}. \tag{3.69}$$

The impedances of the TE and TM fundamental modes are [2]

$$Z_{\mathrm{TE}} = \frac{\omega\mu}{k_{z0}} \quad ; \quad Z_{\mathrm{TM}} = \frac{k_{z0}}{\omega\epsilon}, \tag{3.70}$$

being $\omega = 2\pi f$ the angular frequency, μ and ϵ the permeability and permittivity of the medium and k_{z0}

$$k_{z0} = \sqrt{k_0^2 - k_{x0}^2 - k_{y0}^2} = k_0 \cos\theta. \tag{3.71}$$

We are only interested in the quotient of the impedances. By setting the medium to be the vacuum and calculating one of the quotients it follows:

$$\frac{Z_{\mathrm{TM}}}{Z_{\mathrm{TE}}} = \cos^2\theta. \tag{3.72}$$

Finally, the S matrix in TE-TM basis is

$$S_{\mathrm{TETM}} = \begin{pmatrix} \rho_{\mathrm{TETE}} & \rho_{\mathrm{TETM}}\cos\theta \\ \dfrac{\rho_{\mathrm{TMTE}}}{\cos\theta} & \rho_{\mathrm{TMTM}} \end{pmatrix}, \tag{3.73}$$

which is computed for each reflectarray element separately.

In order to alleviate the notation, from here on matrix S_{TETM} will be denoted as S and the indices TE and TM, which refer to the TE-TM ports, will be denoted as 1 and 2, respectively.

3.3.5.2. Lossless networks

A lossless passive network must fulfill [148, 149]

$$S^H S = I, \tag{3.74}$$

being S^H the conjugate transpose of S and I the identity matrix. Solving the system of (3.74) the conditions of the passive lossless network are extracted. In particular, the conditions of the power balance for the two ports are

$$|\rho_{11}|^2 + \frac{|\rho_{21}|^2}{\cos^2\theta} = 1, \tag{3.75a}$$

$$|\rho_{22}|^2 + |\rho_{12}|^2 \cos^2\theta = 1. \tag{3.75b}$$

However, from (3.74) another two equations are extracted that involve complex numbers. Both equations are equivalent and will yield the same phase condition. Hence, only one will be referenced. This equation is

$$\overline{\rho_{11}} \cdot \rho_{12} \cdot \cos\theta + \rho_{22} \cdot \overline{\rho_{21}} \cdot \frac{1}{\cos\theta} = 0, \tag{3.76}$$

where $\overline{\rho}$ is the complex conjugate of ρ. Passing the second addend to the right-hand side and taking arguments, the phase condition arises as

$$-\arg(\rho_{11}) + \arg(\rho_{12}) = \pi + \arg(\rho_{22}) - \arg(\rho_{21}). \tag{3.77}$$

Apparently, from (3.75) the magnitudes involved in the different power balances are independent from each other. However, taking magnitudes in (3.76) and substituting in (3.75) will give another relation for the magnitudes

$$|\rho_{11}| = |\rho_{22}|\,, \tag{3.78a}$$

$$|\rho_{21}| = |\rho_{12}| \cos^2\theta. \tag{3.78b}$$

Considering (3.75) and (3.78), only one magnitude is free to vary, and the other three are derived from it. For instance, taking $|\rho_{11}|$ as the free magnitude, it follows:

$$|\rho_{22}| = |\rho_{11}| \Longrightarrow |\rho_{21}| = \sqrt{1 - |\rho_{11}|^2}\cos\theta \Longrightarrow |\rho_{12}| = \frac{|\rho_{21}|}{\cos^2\theta}. \tag{3.79}$$

When doing optimizations with passive lossless two-port networks there are four free parameters regarding the reflection coefficients, one magnitude and three phases, since the phases have to fulfill (3.77). When applied to the task at hand (i.e. achieving feasible reflection coefficients in the intersection approach with crosspolar requirements) these conditions turn out to be too restrictive and no convergence is achieved with the crosspolar patterns. Instead, more relaxed conditions should be used in order to facilitate convergence.

3.3.5.3. Lossy networks

Lossy networks should provide more relaxed conditions for the feasibility of the reflection coefficients of the S matrix. Unfortunately, it is hard to find in the literature the conditions that lossy networks must fulfill, apart from the well-known power balance that states that

the reflected power must be equal or less than the incident power [148]. Thus, from a simple condition of the S matrix, the conditions of the reflection coefficients for a passive lossy network are developed from here on.

Any passive lossy network must fulfill the following condition [149]

$$A = I - S^H S \quad \text{is positive definite.} \tag{3.80}$$

For A to satisfy this condition, first it has to be hermitian. It is easy to demonstrate that A is hermitian for any given S matrix, being I the identity matrix, using basic matrix operations,

$$\begin{aligned} A^H &= \left[I - S^H S\right]^H = \left[\left[I - S^H S\right]^T\right]^* = \left[I^T - \left[S^H S\right]^T\right]^* = \left[I - S^T \left[S^H\right]^T\right]^* \\ &= I^* - \left[S^T\right]^* \left[\left[\left[S^T\right]^*\right]^T\right]^* = I - S^H S = A, \end{aligned} \tag{3.81}$$

where in the last step $\left[S^*\right]^T = \left[S^T\right]^*$.

As A has to be positive definite, the conditions of feasibility of the reflection coefficients can be extracted. A hermitian square matrix $A \in M_n$ is positive definite if [150]

$$z^H A z > 0 \quad \text{for all non zero } z \in \mathbb{C}^n. \tag{3.82}$$

The power balance equations can be extracted considering first $z = (1, 0)$ and then $z = (0, 1)$ in (3.82) with the matrix S of (3.73). This is the same as a property of positive definite matrices that states that if A is positive definite then all of its principal submatrices are positive definite [150]. The power balance conditions derived for the case being analyzed are then

$$|\rho_{11}|^2 + \frac{|\rho_{21}|^2}{\cos^2\theta} < 1, \tag{3.83a}$$

$$|\rho_{22}|^2 + |\rho_{12}|^2 \cos^2\theta < 1, \tag{3.83b}$$

which is the well known condition that the net reflected power is less than the net incident power.

There is, however, another condition that can be extracted from the fact that the determinant of any positive definite matrix is a positive real number [150]. The determinant of matrix A is then

$$\begin{aligned} \det(A) = 1 - |\rho_{11}|^2 - |\rho_{22}|^2 - |\rho_{12}|^2 \cos^2\theta - \frac{|\rho_{21}|^2}{\cos^2\theta} + \\ |\rho_{11}|^2 \cdot |\rho_{22}|^2 + |\rho_{12}|^2 \cdot |\rho_{21}|^2 - \\ 2\,\mathrm{Re}\left\{\rho_{11}\,\rho_{22}\,\overline{\rho_{12}}\,\overline{\rho_{21}}\right\} > 0. \end{aligned} \tag{3.84}$$

The real part of the complex number in (3.84) can be expressed as

$$\mathrm{Re}\left\{\rho_{11}\,\rho_{22}\,\overline{\rho_{12}}\,\overline{\rho_{21}}\right\} = |\rho_{11}|\,|\rho_{22}|\,|\rho_{12}|\,|\rho_{21}|\cos\alpha, \tag{3.85}$$

where

$$\alpha = \arg(\rho_{11}) + \arg(\rho_{22}) - \arg(\rho_{12}) - \arg(\rho_{21}). \tag{3.86}$$

Rearranging inequality (3.84) and using (3.85) the third condition arises as

$$\cos\alpha < \frac{1 - |\rho_{11}|^2 - |\rho_{22}|^2 - |\rho_{12}|^2\cos^2\theta - \dfrac{|\rho_{21}|^2}{\cos^2\theta} + B}{2\,|\rho_{11}|\,|\rho_{22}|\,|\rho_{12}|\,|\rho_{21}|}, \tag{3.87}$$

with $B = |\rho_{11}|^2 \cdot |\rho_{22}|^2 + |\rho_{12}|^2 \cdot |\rho_{21}|^2$. Equation (3.87) not only imposes a condition on the phases, but also implicitly on the magnitudes, since its right-hand side has to be within the range $(-1, 1]$ for the phases to be real.

As in the case of lossless networks, a condition for the phase of the reflection coefficients has been found. The amplitudes are free to vary as long as they meet the power balance and the determinant of matrix (3.80) has to be a positive real number (which imposes restrictions on both amplitudes and phases).

For networks of 3 or more ports, the conditions would also be derived from (3.80), although having analytical expressions is more complicated for the phases. Nevertheless, the power balance among all the ports have to hold, and can be expressed as

$$\sum_{i=1}^{N} |S_{ij}|^2 < 1, \quad j = 1, \ldots, N. \tag{3.88}$$

Finally, the principal minors of A should also be real positive [150]. By computing them and checking their positivity, the feasibility of the reflection coefficients would be established, since phases also play a role in their computation (the determinants of the principal submatrices, i.e. the principal minors, are calculated with complex numbers).

3.3.5.4. Verification of lossy network conditions

In order to test the conditions derived for passive lossy two-port networks, a frequency analysis of a reflectarray unit cell was carried out using MoM [76] to obtain the complex reflection coefficients. The unit cell is depicted in Figure 2.6 and consists of four parallel and coplanar dipoles for each polarization distributed in two layers, three in the upper layer and one in the bottom layer. The substrate of the upper layer has a height of 2.363 mm and a complex relative permittivity $\epsilon_r = 2.55 - j2.295 \cdot 10^{-3}$ while the substrate of the bottom layer has a height of 1.524 mm and a complex relative permittivity $\epsilon_r = 2.17 - j1.953 \cdot 10^{-3}$. The periodicity of the unit cell is 5 mm in both dimensions (half a wavelength at 30 GHz). The separation between the dipoles is 4 mm while their width is 0.5 mm. The lengths of the dipoles are 3.09, 4.56 and 3.09 mm for the set of parallel dipoles and 4.9 mm for the other dipole.

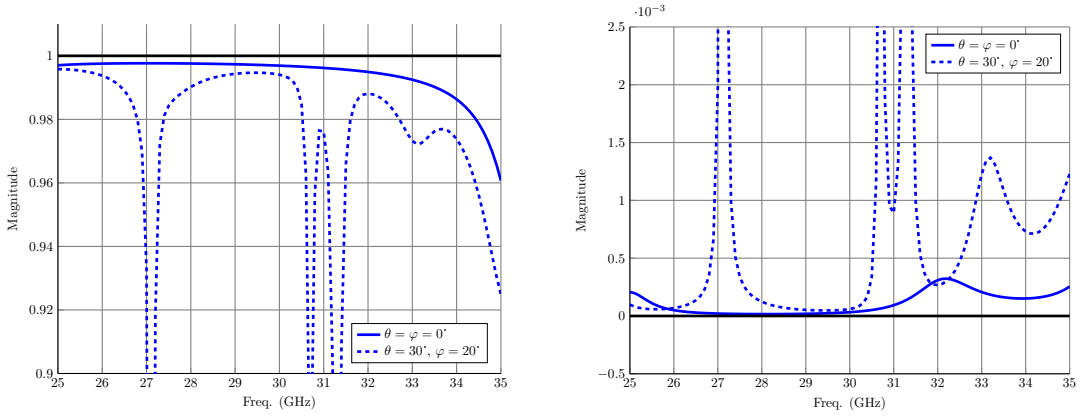

Figure 3.14: *Passive lossy two-port network conditions for a unit cell consisting of four parallel and coplanar dipoles for different incident angles. (a) Power balance for TE port. (b) Positive determinant condition.*

The reflection coefficients were processed in order to test the lossy network conditions of (3.83) and (3.84). Figure 3.14 shows the results simulated with MoM. It can be seen that, as a lossy network, in the power balance for the two TE-TM ports, the reflected power is less than the incident power due to losses in the substrate. Also, the determinant of matrix A in (3.80) is always positive. Note that for lossless passive networks the power balance condition equals to one and the determinant of matrix A is zero.

3.3.5.5. Realization constraints

When using the algorithm described in Section 3.3, the starting point is a set of given complex reflection coefficients. If the synthesis is aimed to a passive array, these reflection coefficients will meet the conditions of lossy networks. However, if the IA is left to run with no restrictions on the reflection coefficients, the algorithm might give coefficients that, in general, will not meet (3.83) and/or (3.84), taking any value with magnitudes greater than one and large ranges. This is not a problem in POS since the phase of ρ_{xx} and ρ_{yy} can take any value. Then, some restrictions can be enforced to reduce the range of variation of the coefficients or to make them feasible for passive reflectarrays. When restrictions apply, convergence is more difficult to achieve, especially with the crosspolar pattern, with regard to the case without restrictions. If the specification constraints are too demanding, the algorithm might diverge to undesired solutions in which case the specifications should be relaxed or the antenna geometry changed.

Since the lossless network conditions are too restrictive to achieve convergence, the lossy conditions should be chosen in order to obtain feasible coefficients. However, (3.83) and (3.84) are expressed in terms of reflection coefficients in TE-TM basis instead of Cartesian, so there is no direct procedure to impose them. One way is to transform the obtained Cartesian reflection coefficients into an S matrix in the TE-TM basis. Then, apply to those coefficients the feasibility restrictions and recover the Cartesian reflection coefficients. Also, in order to assure a better convergence, some reflection coefficients can

be allowed to be not feasible, for instance, only imposing the power balance constraint of (3.83) and leaving the other condition unchecked. As the algorithm approaches the solution, the number of non-feasible elements is reduced (if too many elements are non-realizable, the solution would not be valid and the synthesis should be restarted). This strategy was used to synthesize two different radiation patterns, one isoflux for global Earth coverage and a contoured beam for Direct-Broadcast Satellite (DBS) European coverage.

A better strategy to impose the realization constraints preserving the efficiency of the algorithm would be to use some electromagnetic model within the algorithm, such as ANN (Artificial Neural Network). ANNs have demonstrated their capabilities to accurately characterize the behavior of multilayered reflectarray cells providing at the same time fast computational speeds [66]. In order to use an ANN with the described algorithm, it should provide the full reflection coefficient matrix, including the crosspolar components. Recent work has proved the potential of such possibility [69].

3.3.5.6. Obtaining the element dimensions

Once the matrix of reflection coefficients is obtained for all the elements of the reflectarray antenna, it remains the task of finding the physical dimensions of the element to match the required coefficients. Although it is not the goal of the present work to carry out the actual design, some guidelines are presented.

As previously stated, the use of ANNs within the algorithm would improve the imposition of the realization constraints, but also deliver the physical dimensions associated to the given reflection coefficients [69]. A different approach might be the one used in POS, where after the phases are obtained, the dimensions are adjusted element by element, as described, for instance, in [2]. However, adjusting full matrices of reflection coefficients is more difficult than only phases, as some mismatch can be produced that alter the overall radiation pattern. In such case, a multi-step design approach can be followed, in which after the first time the dimensions are adjusted, the resulting reflection coefficients from the obtained geometry are used as starting point for a new synthesis. This approach was used in other context in order to obtain broadband reflectarrays [20], but it can be adapted to the new context. Finally, in some cases the approach followed in [17] can be used, in which the direct and cross reflection coefficients are independently adjusted by applying certain geometrical transformations to the reflectarray element.

3.3.6. Validation

3.3.6.1. Isoflux pattern

A sketch of the reflectarray is shown in Figure 2.3. It consists of a planar rectangular reflectarray with dual-linear polarization formed by 900 cells (30×30) and a feed horn modeled as a $\cos^q \theta$ function [78] with a *q-factor* of 25, which produces an illumination taper of -18.3 dB at the edges of the reflectarray. The feed horn points to the center of the reflectarray and its phase center is placed at $\vec{r}_f = (-71, 0, 154)$ mm with regard to the

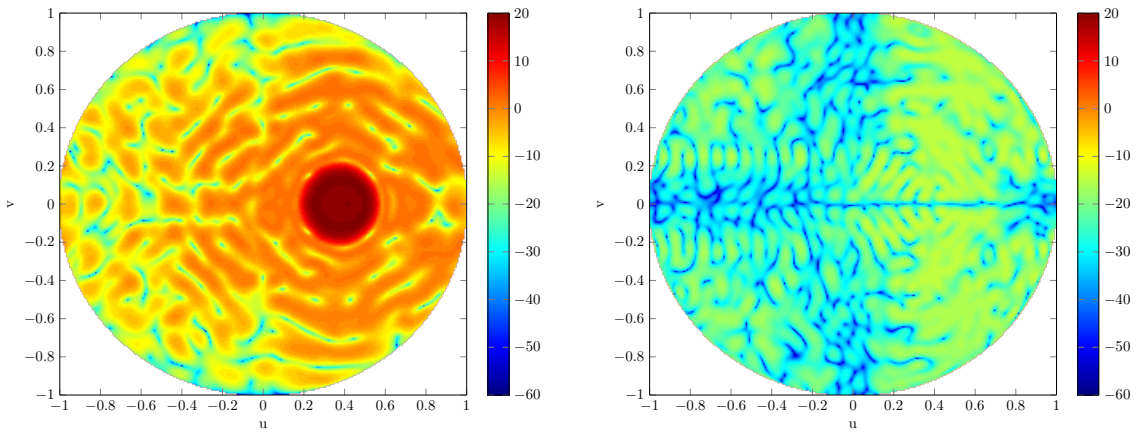

Figure 3.15: *Synthesized radiation patterns in gain (dBi) for X polarization with some restrictions on the reflection coefficients. (a) Copolar. (b) Crosspolar.*

center of the reflectarray. The working frequency is 30 GHz and the period of the unit cell is 5 mm × 5 mm, which is half a wavelength.

The first example corresponds to an isoflux pattern, which provides a homogeneous power density over the Earth surface. The chosen isoflux pattern would be radiated by a satellite in geostationary orbit, with a beam tilt of 22.6° regarding the reflectarray coordinate system (see Figure 2.3). The maximum allowed ripple is 1 dB and the sidelobe level was set to −19.2 dB.

For the first exemplary case, the magnitudes of ρ_{xx} and ρ_{yy} are limited to the range (0.95, 0.99) whereas the magnitudes of ρ_{xy} and ρ_{yx} can vary within the range (0.01, 0.65). This is an example of arbitrary restrictions, since they do not fulfill the power balance of (3.83) and (3.84) when transformed to TE-TM basis for some incident angles (θ, φ). The maximum crosspolar template was set 35 dB below the maximum of the copolar one.

Figure 3.15 shows the copolar and crosspolar synthesized isoflux pattern for X polarization. The crosspolar pattern component remains 33.5 dB below the maximum value of the copolar for all the visible region. The radiation patterns for Y polarization are very similar to those obtained for X polarization. Figure 3.16(a) shows the magnitude of ρ_{xx}, being its range of variation roughly (−0.45, 0) dB.

Another synthesis was made imposing the feasibility constraints for the power balance. Since these are tighter constraints than in the previous case, the crosspolar template has been relaxed from 35 dB to 30 dB below the maximum copolar value. Also, only 7% of the reflection coefficients are non-convergent, i.e., not feasible for a passive array realization. Overall, the algorithm produced a solution which mostly satisfies the new specification, although with a higher crosspolar level and secondary sidelobe levels with regard to the first case. Figure 3.17 shows the main cut along v for $u = 0.38$ comparing both synthesis. It can be seen how the crosspolar levels remain practically below the specified values in the templates and how for the second case, due to the tighter constraints, there appear some higher secondary lobes with a value of −16 dB. Again, patterns for Y polarization were similar to those obtained for X polarization. Figure 3.16(b) shows the magnitude in

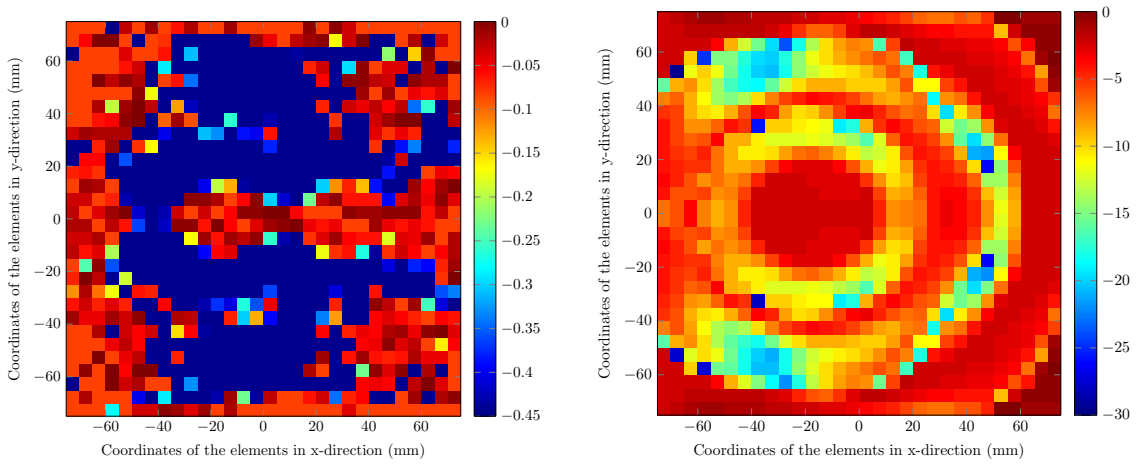

Figure 3.16: *Magnitude in dB of the synthesized ρ_{xx}. (a) First case with arbitrary restriction. (b) Second case with feasible coefficients.*

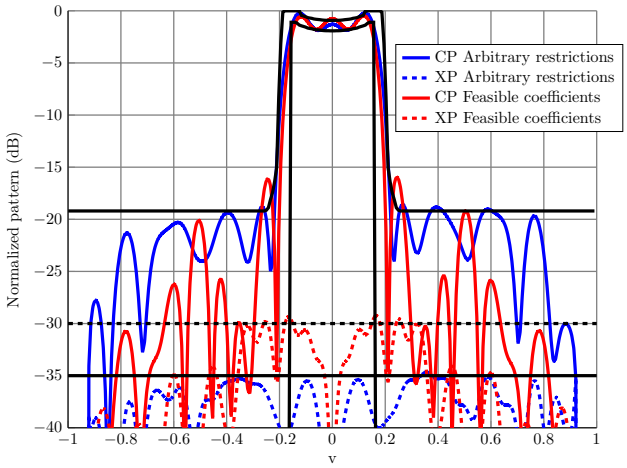

Figure 3.17: *Main cut in v (for $u = 0.38$) of the isoflux radiation pattern for X polarization.*

dB of ρ_{xx} for the second case. Now, it varies within a wider range than in the second test case shown in Figure 3.16(a). This is due to the fact that in the first test the restrictions were applied to the reflection coefficients in Cartesian basis, so their range can be tightly controlled; while now they are applied in TE-TM basis and then the Cartesian coefficients are recovered, only ensuring that the power balance is met at the element level while meeting the copolar and crosspolar far field specifications, according to Ludwig's third definition of crosspolarization [131].

3.3.6.2. Contoured beam

The next example corresponds to a contoured beam. It has been chosen a European coverage at 11.85 GHz which can be seen in Figure 3.18 [151]. It corresponds to a geostationary satellite in position 10° E longitude, 0° latitude. The minimum gain specified in the coverage region is 28 dBi. The coverage is enlarged to take into account typical pointing errors

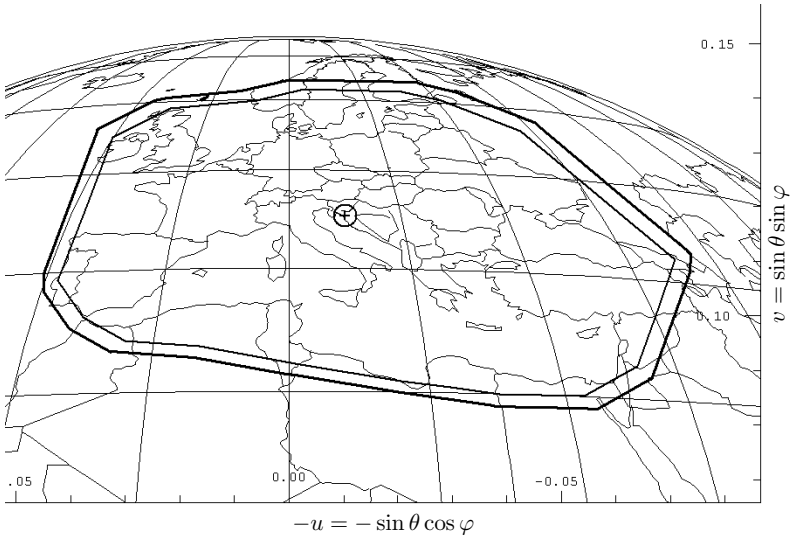

Figure 3.18: *European coverage.* (u, v) *are in the antenna coordinate system.*

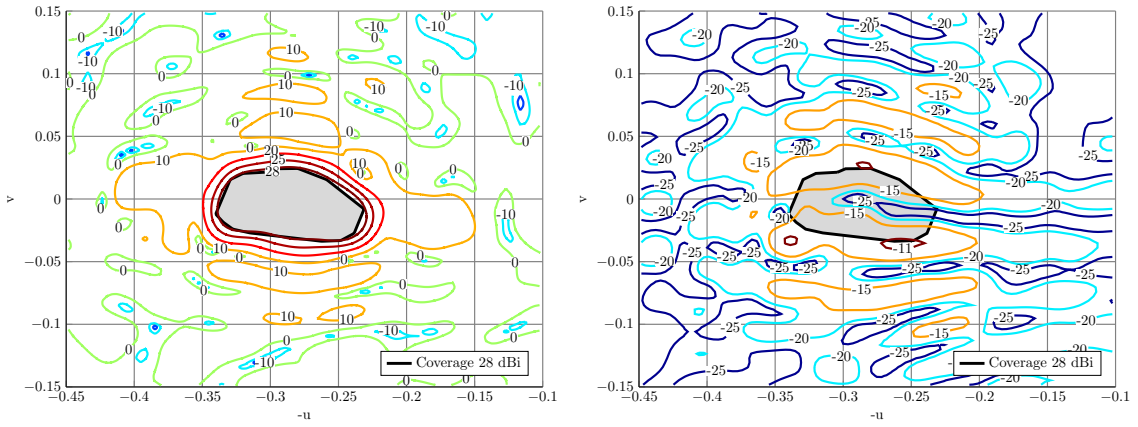

(a) ***(b)***

Figure 3.19: *Synthesized radiation patterns in gain (dBi) for X polarization with feasible reflection coefficients. Gray region specifies the coverage area.* (u, v) *are in the reflectarray coordinate system. (a) Copolar. (b) Crosspolar.*

(0.1° in roll, 0.1° in pitch and 0.5° in yaw). The coverage of Figure 3.18 is shown in the antenna coordinate system and before carrying out the synthesis it has to be transformed to the reflectarray coordinate system defined in Figure 2.3 [2].

The considered rectangular reflectarray antenna works in dual-linear polarization and is formed by 5180 cells (74×70). The feed horn modeled as a $\cos^q\theta$ function [78] with a *q-factor* of 23, which produces an illumination taper of -17.9 dB at the edges of the reflectarray. The feed horn points to the center of the reflectarray and its phase center is placed at $\vec{r}_f = (-358, 0, 1070)$ mm with regard to the center of the reflectarray. The working frequency is 11.85 GHz and the period of the unit cell is 14 mm $\times$ 14 mm, which is 0.55λ.

Figure 3.19 shows the synthesized copolar and crosspolar radiation patterns for X polarization. This time, only the simulation with feasible restrictions was carried out,

with less than 2.5% of the reflection coefficients being not feasible. The minimum XPD in the coverage area is 38.7 dB for X polarization and 38.8 dB for Y polarization, which presents a similar pattern to the one shown in Figure 3.19.

3.4. Conclusions

In this chapter, a phase-only synthesis algorithm of radiation pattern has been described. It is based on the Intersection Approach algorithm and has been adapted to the particular case of reflectarray antennas taking into account particularities of this type of antenna, such as the analysis techniques and the fixed amplitude from the feed. Regarding the analysis techniques, the POS formulation for the First Principle of Equivalences has been derived, and the inclusion of the dielectric frame in the synthesis has been possible by a convenient modification of the backward projector. The implementation of the algorithm is very efficient since the most time consuming operation is the Fourier transform of the tangential field, which can be efficiently computed by means of the FFT algorithm. Some mechanisms have also been introduced in order to control the convergence of the algorithm, including phase restrictions and a fictitious reduction of variables, both suitable for the synthesis of very large reflectarrays. As an example, a small reflectarray with an isoflux shaped pattern has been designed, manufactured and measured. The synthesis process included the reduction of variables and the synthesis in several steps to better control the convergence towards a suitable shaped pattern, and a phase restriction in order to adapt the algorithm to the limited phase range of the employed reflectarray element. Measurements and simulations were in good agreement.

The phase-only synthesis presents the advantage that it is a powerful and easy method to obtain shaped patterns for dual-polarized antennas. In the case of the reflectarrays, two phase distributions are obtained, one for each linear polarization, and then the geometry of the element is easily adjusted to match the required phase shift. The only consideration is to obtain a relatively smooth phase distribution so the local periodicity assumption used in the MoM analysis holds. However, the main disadvantage is that, due to the simplifications made, there is no direct control over the crosspolar component of the radiation pattern during the synthesis process. This can be problematic for applications that require a strict control of the crosspolar levels, such as satellite applications.

For that reason, the IA formulation has been extended to include crosspolar requirements in the synthesis process. Since one important contribution to the crosspolar pattern is the crosspolarization introduced by the reflectarray elements, the full reflection coefficient matrix has to be considered. Hence, the IA does not provide a phase distribution anymore but a distribution of reflection coefficient matrices. Now, eight variables are obtained (four complex numbers) instead of two as in the POS case (two real phases, one per polarization). Furthermore, the two polarizations are not independent anymore in the new formulation of the IA, so converge might be more difficult to achieve. In any case, since the reflection coefficients are free to vary, the values obtained are, in general, not feasible for passive reflectarrays. Hence, a formulation to derive the constraints for passive reflectarrays was developed, obtaining amplitude and phase conditions for the feasibility

of the reflection coefficients. In order to validate the algorithm, two examples were shown, one for an isoflux pattern for global Earth coverage and another one for a DBS mission with a European coverage.

The main disadvantage of the new IA formulation is the difficulty to obtain a reflectarray layout (i.e. the element dimensions) from the reflection coefficient matrices. Some guidelines have been laid out to obtain such layout from the R^{mn} matrix that could potentially solve this issue. Nevertheless, the fact is that using this approach (for both, the IA-POS and the IA-XP), the problem is divided into two: first the synthesis of the radiation pattern is carried out, obtaining either phases or matrices of reflection coefficients; and finally, the layout is obtained from the previous result. It turns out that adjusting the element dimensions to obtain a certain phase distribution is very easy, but the problem is significant when R^{mn} is the starting point. For this reason, a new approach is devised in the following chapters, directly optimizing the geometry of the reflectarray in order to achieve lower levels in the crosspolar pattern while maintaining the desired shaped for the copolar component.

CHAPTER 4

Efficient and scalable reflectarray phase-only synthesis based on the Levenberg-Marquardt Algorithm

4.1. Introduction

In the previous chapter, two algorithms for the synthesis of reflectarray antennas were described. First, the IA-POS was detailed, which only dealt with copolar patterns since the output of the algorithm was a distribution of phases, treating the reflectarray elements as ideal phase shifters. Hence, there was no control over the crosspolar pattern during the synthesis process. One of the highlights of the algorithm was its computational efficiency, since the most time consuming operation was the FFT, used to compute the copolar far fields and to recover the tangential reflected field. An efficient generalization of the IA-POS was developed to include the crosspolar requirements, obtaining the algorithm known as IA-XP. This led to the use of the full reflection coefficient matrix, R^{mn}, since the crosspolarization introduced by the elements is mandatory in the reflectarray analysis to accurately predict the crosspolar component of the far field during the pattern synthesis. The efficiency was maintained since the FFT was still the most computationally expensive operation in both projectors. However, the output of the IA-XP is the full matrix R^{mn}, which provides four complex variables (or equivalently, eight real variables) per reflectarray element, in contrast with the IA-POS in which there was only two real variables (one phase per polarization per element). The inconvenience is evident: adjusting the element geometry to match eight variables is much more difficult than to match only two. Due to this limitation, the solution to obtain a reflectarray layout was not further pursued with the IA-XP.

In light of these results, there are two strategies which can be followed in order to include crosspolar specifications in the synthesis process:

- Synthesize the reflection coefficient matrix (as in the IA-XP).

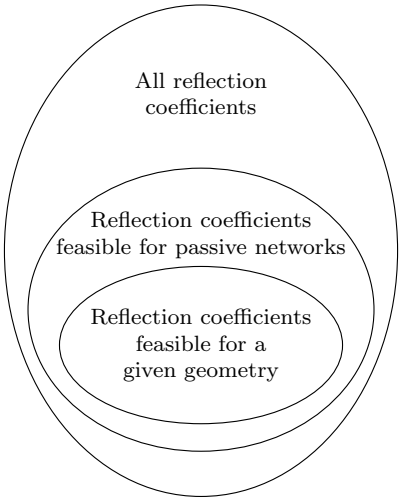

Figure 4.1: *Classification of reflection coefficients for passive reflectarray synthesis.*

- Synthesize the element geometry.

For the first point, apart from the inconvenience of matching more variables with a given element geometry, it is not guaranteed that it is possible to do so. The problem is divided into two: the synthesis of the radiation patterns and adjusting the reflectarray layout. If the reflection coefficients were free to vary, the algorithm would converge quickly. However, the obtained reflection coefficients were, in general, not feasible for passive networks. A formulation was developed to obtain constraints for lossless and lossy passive networks. This makes the algorithm convergence harder to achieve. However, even though after obtaining the desired radiation patterns applying suitable constraints to the R^{mn} matrix, the problem of synthesizing the reflection coefficients with a given element geometry is still there. Also, even though at this point is guaranteed that the reflection coefficients are feasible for passive networks, there is still the possibility that the employed reflectarray element is not able to match the required R^{mn} matrix, as it can be seen in Figure 4.1.

Even though the set of feasible reflection coefficients for passive networks is clearly smaller than the set of all reflection coefficients, it is not clear that all of them can be obtained by a reflectarray element. In any case, it is only guaranteed that, if A is the set of all reflection coefficients, B the set of feasible reflection coefficients for passive networks and C the set of reflection coefficients which can be obtained by a reflectarray element, then

$$A \supset B \supseteq C, \tag{4.1}$$

which even in the best case of $B = C$, matching the geometry to try to obtain the required reflection coefficients might be a problem difficult to solve. This was not a problem with the IA-POS since the ρ_{xx} and ρ_{yy} phases are well-behaved, and it is easy to adjust the reflectarray element geometry to match those phases [2].

In order to solve all these inconveniences of working with the matrix of reflection coefficients, it is desirable to have a synthesis algorithm which is able to work directly with the physical dimensions of the elements, in a way that working directly with those dimensions, the required radiation patterns are obtained. This approach guarantees a

feasible geometry at the expense of losing the IA efficiency. In a first approach to the crosspolar optimization of reflectarrays, the chosen algorithm is the Levenberg-Marquardt algorithm (LMA), which has been selected as a reasonable trade-off between complexity, robustness and performance on minimisation tasks [97, 152].

4.2. The Levenberg-Marquardt algorithm for far-field phase-only pattern synthesis

In this section, the LMA will be described for far field POS along with several improvements in its implementation that will allow its later extension to directly optimize the reflectarray geometry. Since the optimization of the reflectarray geometry will be done employing a full-wave analysis based on local periodicity in the optimization process, the LMA needs to be as fast as possible, since otherwise the optimization process would take too long to be of practical use. Some discussions regarding the proper choice of the LMA parameters, starting point and solution are presented. Finally, the algorithm is validated through an example of a LMDS radiation pattern, obtaining better results than others in the literature regarding both, radiation patterns and computing times.

Although the ultimate goal is the direct optimization of the reflectarray geometry with a full-wave analysis based on local periodicity to reduce the crosspolar component of the radiation patterns, this chapter is devoted to the LMA for POS, known as LMA-POS. The main reason to take a step back with regard to the IA-XP and come back to POS is that it will serve as a starting point to include several improvements in the LMA implementation in order to speed up its computation time. This is very important if this algorithm will be later used to optimize the reflectarray geometry using a full-wave analysis based on local periocidity. All of its building blocks will be described and strategies to speed up their computations will be detailed. Furthermore, some discussions regarding the proper choice of its parameters as well as the starting point and solution reached are provided. Then, the algorithm is validated with an example of a LMDS radiation pattern and its performance is compared with other works in the literature, improving both the obtained radiation patterns and computing times with regard to other implementation of the algorithm.

Another reason is that the LMA is very different from the IA in how it addresses the optimization. The IA tackled the problem by looking for the intersection of two sets, while the LMA is an algorithm which minimizes a cost function. In order to familiarize with the new algorithm, it is best to solve first an easier problem than the crosspolar optimization of reflectarrays, and hence the starting point is the POS with LMA, which later will lead to the crosspolar optimization with the LMA.

As a complementary contribution, the LMA-POS can be easily adapted to perform near field synthesis, taking advantage of all the improvements in the algorithm implementation. The reflectarray far field model needs to be substituted with the near field model described in Chapter 2 and the LMA cost function is also adapted to optimize both amplitude and phase. Test cases are provided at microwave and millimeter frequencies to validate the algorithm for NF synthesis.

4.2.1. The Levenberg-Marquardt algorithm

The Levenberg-Marquardt algorithm is an iterative algorithm used to solve non-linear least-square problems. It minimizes cost functions of the form

$$F(x) = \sum_{i=1}^{T} \left(r_i(x)\right)^2, \tag{4.2}$$

where $r(x)$ is known as residual and is discretized in T points. One of the most popular applications of the LMA is the curve fitting, where a model with a given number of parameters is adjusted to fit as best as possible a set of data points obtained from measurements. However, it can be adapted to solve any kind of problem provided a suitable cost function defined as in (4.2). In particular, the LMA has been used with success in the optimization of linear arrays [96] and planar arrays [152] in both far field and near field, including reflectarrays as well [97].

A flow chart of the algorithm is shown in Figure 4.2. After the initialization, the cost function is computed, which provides the error at the current iteration. If the error is smaller than a reference error, ϵ, the algorithm stops as convergence has been achieved. Otherwise it continues with the computations. The LMA is a modification of the Gauss-Newton algorithm, and as such, it computes a Jacobian matrix, which can be obtained either analytically or by finite differences. After the Jacobian has been computed, a set of normal equations is formed, which involves a big matrix multiplication with the Jacobian and a matrix-vector multiplication. Then, the equation system is solved, obtaining the updating vector to the solution.

The optimization of reflectarray antennas is considered a big problem, even when the reflectarray is a medium-sized antenna. This is due to the large number of points involved in the far field computation, the number of optimizing variables, the expensive operation of the matrix multiplication, and finally, finding the solution to the equation system. For these reasons, in the following sections each building block of the LMA will be detailed and adapted for the reflectarray optimization, devising strategies to accelerate computations and carry them out as efficiently as possible.

4.2.2. Cost function definition

In order to use the LMA, a proper cost function to minimize has to be defined. The same cost function as in [97] will be used, where the residuals are defined as

$$\begin{aligned} F_t^{X/Y} = C\left(\vec{r}_t\right) \Bigg[& \left(T^2_{\max}\left(\vec{r}_t\right) - \left|E^{X/Y}_{\mathrm{cp}}\left(\vec{r}_t\right)\right|^2\right)\left(T^2_{\min}\left(\vec{r}_t\right) - \left|E^{X/Y}_{\mathrm{cp}}\left(\vec{r}_t\right)\right|^2\right) + \\ & \left|T^2_{\max}\left(\vec{r}_t\right) - \left|E^{X/Y}_{\mathrm{cp}}\left(\vec{r}_t\right)\right|^2\right|\left|T^2_{\min}\left(\vec{r}_t\right) - \left|E^{X/Y}_{\mathrm{cp}}\left(\vec{r}_t\right)\right|^2\right| \Bigg], \end{aligned} \tag{4.3}$$

and thus, the cost function is

$$F^{X/Y} = \sum_{t=1}^{T} \left(F_t^{X/Y}\right)^2. \tag{4.4}$$

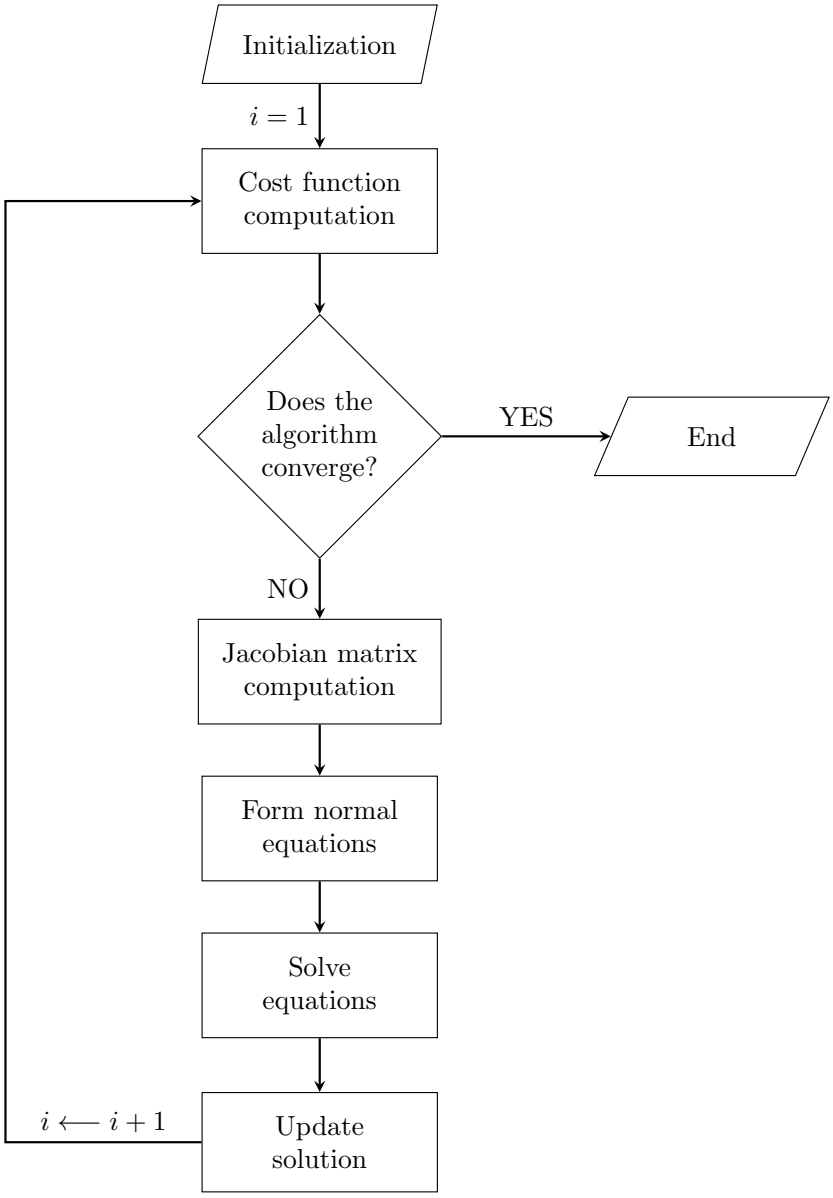

Figure 4.2: *Flow chart of the Levenberg-Marquardt Algorithm for Phase-Only Synthesis.*

In (4.3) and (4.4), each $t = 1, \ldots, T$ describes a $\vec{r}_t = (u, v)_t$ point in which the UV grid is discretized; $C(\vec{r}_t)$ is a weighting function; $E_{\text{cp}}^{X/Y}(\vec{r}_t)$ can be either of both copolar far fields, which are synthesized independently; and $F^{X/Y}$ is the total error, contributed by all the far field samples that lay outside the specified templates. This cost function penalizes the samples that lie outside the specified bounds (upper and lower) while it sets the error to zero when the samples are within bounds. Taking as reference Figure 4.3, the operations between the templates and the copolar field can be expressed as

$$F = a_1 \cdot a_2 + |a_1| \cdot |a_2|. \tag{4.5}$$

When the field is below the lower template, both a_1 and a_2 are positive, and (4.5) is reduced to

$$F = a_1 \cdot a_2 + a_1 \cdot a_2 = 2 \cdot a_1 \cdot a_2. \tag{4.6}$$

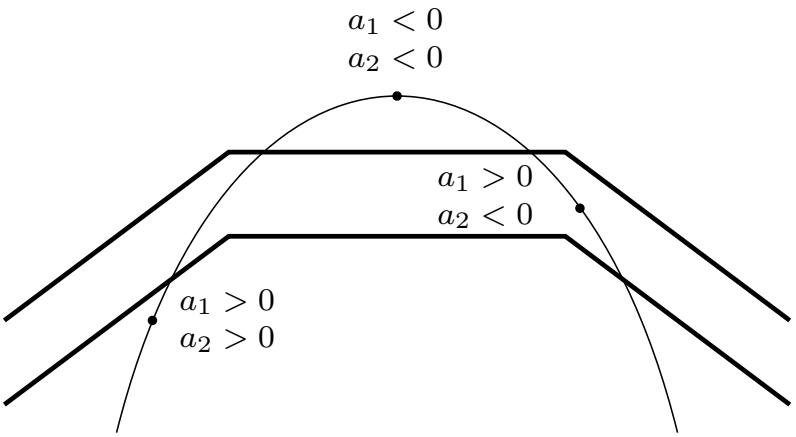

Figure 4.3: *Values of the cost function terms for different field points.*

Conversely, when the field is above the upper template, both a_1 and a_2 are negative, but their product is positive, so (4.5) is again reduced to (4.6). This operation gives the error when the field is not within the templates. However, when field is within specifications, a_1 is positive while a_2 is negative, hence having

$$F = a_1 \cdot a_2 + |a_1| \cdot |a_2| = 0. \tag{4.7}$$

The cost function in (4.4) represents a non-convex search space [152] due to the non-convexity of the lower bound [153] and multiple solutions are possible. There are potentially a large number of solutions with minimum error. If the lower and upper bounds are too confined, the specifications might be too stringent and the algorithm might not find a solution, either because it does not exist or because the starting point is too far off from the solution. In that case, the specifications should be relaxed and/or the antenna optics redefined.

In order to alleviate the notation, from here on a generic F_t will be used, avoiding the superscripts and knowing that it can represent the residual of either of both polarizations (F_t^X or F_t^Y).

4.2.3. Jacobian matrix calculation

The LMA requires the calculation of a Jacobian matrix, which is a $T \times P$ matrix, where P is the number of variables to be optimized. Any element (t, p) of the Jacobian is calculated as

$$J(t,p) = \frac{\partial F_t(\alpha)}{\partial \alpha_p}, \tag{4.8}$$

where $\alpha = (\alpha_1, \ldots, \alpha_P)$ is a vector with the optimization variables. Now, equation (4.8) can be evaluated analytically, as in [96, 97], as long as the analytical expression of the far field as a function of the optimization variables is provided. In [97], the partial derivatives are obtained deriving the cost function with respect to the tangent of the phases. However, in this work derivation is done with respect to the phases themselves, improving the

performance of the algorithm greatly by making it converge faster, as it will be shown later.

In the case where the analytical expressions cannot be used, the derivative can be calculated using finite differences of the form [100]

$$\frac{\partial F_t(\alpha)}{\partial \alpha_p} = \frac{F_t(\alpha + he_p) - F_t(\alpha - he_p)}{2h} + \mathcal{O}\left(h^2\right), \tag{4.9}$$

where h is a small positive scalar and e_p is the pth unit vector. Because the evaluation of the cost function (4.4) can be computationally expensive, a one-sided-difference can be used,

$$\frac{\partial F_t(\alpha)}{\partial \alpha_p} = \frac{F_t(\alpha) - F_t(\alpha - he_p)}{h} + \mathcal{O}\left(h\right), \tag{4.10a}$$

$$\frac{\partial F_t(\alpha)}{\partial \alpha_p} = \frac{F_t(\alpha + he_p) - F_t(\alpha)}{h} + \mathcal{O}\left(h\right), \tag{4.10b}$$

in order to reduce by half the number of cost function evaluations required. Also, a proper choice of h can minimize the error of the evaluation of the derivative in (4.9), (4.10). For the central difference the optimum choice of h [100] is

$$h = \sqrt[3]{u_r}, \tag{4.11}$$

while for the lateral difference is

$$h = \sqrt{u_r}, \tag{4.12}$$

with u_r being the unit round-off, whose value will depend on the precision of the real numbers used in the implementation of the algorithm. Note that for the central difference there is an error of $\mathcal{O}(h^2)$, while for the lateral one, the error is $\mathcal{O}(h)$. Since $h \in (0, 1)$, the error will be lower for the central difference, although the evaluation of the derivative will be twice as expensive, computationally speaking.

The finite differences can be implemented either in simple or double precision. In simple precision, each real number is represented with 4 bytes, while for double precision they are represented with 8 bytes. For both cases, the unit round-off is

$$\text{Simple precision: } u_r = 1.1920929 \cdot 10^{-7}, \tag{4.13a}$$

$$\text{Double precision: } u_r = 2.220446049250313 \cdot 10^{-16}. \tag{4.13b}$$

A good implementation would only work in double precision, so the values of h for the two types of finite differences will be

$$\text{Lateral: } h = \sqrt{u_r} = 1.490116 \cdots \cdot 10^{-8}, \tag{4.14a}$$

$$\text{Central: } h = \sqrt[3]{u_r} = 6.055454 \cdots \cdot 10^{-6}. \tag{4.14b}$$

Table 4.1: *Jacobian size in gigabytes (GB) with $N = 900$.*

	N	**2 N**	**4 N**	**6 N**	**8 N**	**10 N**
$\mathbf{T = 128 \cdot 128}$	0.11	0.22	0.44	0.66	0.88	1.10
$\mathbf{T = 256 \cdot 256}$	0.44	0.88	1.76	2.64	3.52	4.40
$\mathbf{T = 512 \cdot 512}$	1.76	3.52	7.03	10.55	14.06	17.58
$\mathbf{T = 4 \cdot 128 \cdot 128}$	0.44	0.88	1.76	2.64	3.52	4.40
$\mathbf{T = 4 \cdot 256 \cdot 256}$	1.76	3.52	7.03	10.55	14.06	17.58
$\mathbf{T = 4 \cdot 512 \cdot 512}$	7.03	14.06	28.13	42.19	56.25	70.31

Hence, the error in the evaluation of the finite differences would be of the order of

$$\text{Lateral: } h = \sqrt{u_r} = 1.490116 \cdots \cdot 10^{-8}, \tag{4.15a}$$

$$\text{Central: } h^2 = \sqrt[3]{u_r^2} = 3.666852 \cdots \cdot 10^{-11}. \tag{4.15b}$$

This means that using the central difference to evaluate the derivative, the cost function is evaluated twice as much as in the lateral difference, but it is only gained a precision of three decimal figures in decimal base, approximately [100]. If the cost function evaluation is time expensive, it would be convenient to analyze if it is better to use the lateral difference at the cost of losing some precision in the computations, since large amounts of time could be saved.

An important point to consider when computing the Jacobian matrix is the fact that the columns of J are independent from each other because the derivatives are calculated with respect to one variable. Hence, the evaluation of the Jacobian can be fully parallelized by means of OpenMP [142], computing one column per available thread. Furthermore, each column can be obtained by just two calls to the cost function when the central difference is used (one call for the lateral difference). Also, the far field is computed efficiently by means of the FFT, and only one FFT is needed per cost function call. This way, one of the most time-consuming operations of the algorithm is performed efficiently and will scale well with the number of available processors, allowing the optimization of large problems.

Finally, it is important to bear in mind that, depending on the number of points in which the far field is discretized and the number of optimizing variables, the size of the Jacobian matrix can grow very fast. An example in shown in Table 4.1, where a reflectarray of $N = 900$ elements is used as basis to estimate the Jacobian size (supposing $P = N$). Each Jacobian element is a real number, which in double precision is represented by 8 bytes. Large reflectarrays not only have many elements, greatly increasing the number of optimizing variables, they also require a high resolution in the UV grid since the beam width is usually small. Thus, the Jacobian size can be important. This issue will become more important when optimizing the crosspolar far field in the following chapter.

4.2.4. Solving the matrix equation

Once the Jacobian matrix is calculated, the LMA can be applied iteratively as

$$\left[J_i^T \cdot J_i + \mu_i \cdot \text{diag}\left(J_i^T \cdot J_i\right)\right] \cdot \delta_i = -J_i^T \cdot F_{t,i}, \tag{4.16}$$

which can be compactly written as

$$A_i \cdot \delta_i = b_i. \tag{4.17}$$

In (4.16), the subindex i represents the current iteration, diag$(\cdot)$ is the diagonal matrix, δ_i is the updating vector which satisfies the equality and μ_i is a real positive number. The choice of diag $\left(J_i^T \cdot J_i\right)$ instead of any other positive diagonal matrix, such as the identity, is to reduce the effects of poor scaling in the optimization variables by using and ellipsoidal trust region. This way, the algorithm is invariant under diagonal scaling of the components of α [100].

The matrix multiplication $J_i^T \cdot J_i$ and other matrix-vector operations can be computationally very expensive if the dimension is large. Nevertheless, these operations can be performed by routines from libraries such as OpenBLAS [154] or MKL [155], which take advantage of highly optimized and fully parallelized algorithms and low-level hardware operations in order to improve their performance and computing times. Also, since the resulting matrix is symmetric, only the upper or lower triangular part of it is computed, further reducing computing times.

In [97], (4.17) is solved by forming its normal equation applying the Conjugate Gradient Squared (CGS) method. This is unnecessary because (4.17) is already a square matrix system, and the CGS additionally solves another system of normal equations, thus squaring the condition number of matrix A_i, which can lead to poor convergence of the CGS depending on the initial Jacobian matrix. Nevertheless, it can be demonstrated that A_i is at least positive semidefinite, so a Cholesky factorization based solver can be used [150], which is the fastest exact solver for this type of problems [156] since it takes advantage of the symmetric nature of the matrix. Compared with other methods, the Cholesky factorization involves $P^3/3$ floating-point operations, while LU takes $2P^3/3$ and SVD $12P^3$ [156]. Although SVD is more robust, in this case the Cholesky factorization is enough, being 26 times faster than SVD and twice as fast as LU.

Since J_i is a matrix of size $T \times P$, the matrix $J_i^T \cdot J_i$ will be a square matrix of size $P \times P$. Moreover, the resulting matrix will be positive semidefinite, since

$$\forall J \in \mathbb{R}^{m \times n} \text{ and } \forall z \in \mathbb{R}^m, z^T J^T J z = \|Jz\|_2^2 \geq 0. \tag{4.18}$$

In addition, diag $\left(J_i^T \cdot J_i\right)$ is a matrix with numbers greater or equal to zero. Assuming a real matrix $J \in \mathbb{R}^{m \times n}$, then matrix $B = J^T J \in \mathbb{R}^{n \times n}$, with the elements of its main diagonal

$$B(i,i) = \sum_{j=1}^{m} J(j,i) \cdot J(j,i) = \sum_{j=1}^{m} \left(J(j,i)\right)^2, \ i = 1, \ \ldots, \ n. \tag{4.19}$$

Since the elements of the main diagonal of diag $\left(J_i^T \cdot J_i\right)$ are always greater or equal than zero and the parameter μ_i is always positive, the matrix $\mu_i \cdot \text{diag}\left(J_i^T \cdot J_i\right)$ will be positive semidefinite since all its eigenvalues are greater or equal to zero (its eigenvalues are the elements of the main diagonal, since it is a diagonal matrix [150, page 38]). Also, the sum of two positive semidefinite matrices is also positive semidefinite [150, page 398], so A_i is positive semidefinite.

A Cholesky factorization based solver is used to solve (4.17). The Cholesky decomposition is based on expressing A_i in the form

$$A_i = GG^T, \tag{4.20}$$

where G is a lower triangular matrix. Then, the system $A_i \cdot \delta_i = b_i$ is solved in two steps:

1. Solve $G \cdot y = b_i$, obtaining y.
2. Solve $G^T \cdot \delta_i = y$, obtaining δ_i.

It is easy to see that

$$b_i = G \cdot y = GG^T \cdot \delta_i = A_i \cdot \delta_i. \tag{4.21}$$

Solving each one of the triangular matrix systems is very easy.

After the matrix system is solved, the solution is updated as

$$\alpha_{i+1} = \alpha_i + \delta_i. \tag{4.22}$$

4.2.5. Choice of μ_0

The parameter μ in (4.16) is used to control the convergence of the algorithm. It controls the behavior of the algorithm ranging from the steepest descent when $\mu \to \infty$ and the Gauss-Newton method when $\mu = 0$ [101]. A small value of μ when the current solution is not near the minimum may cause the algorithm to diverge. Hence, it is recommended to start with a high value of μ and decrease it as the error diminishes. Conversely, if the error increases, it could be necessary to increase the value of μ to control the algorithm and prevent it from diverging to non-desired solutions. A new real parameter $\beta > 1$ is defined to control μ. If the last k_d iterations have decreased the error, μ is updated as $\mu_{i+1} = \mu_i/\beta$. On the other hand, if the last k_i iterations have increased the error, μ is updated as $\mu_{i+1} = \mu_i\beta$. If neither of both conditions are fulfilled, μ remains the same.

Parameters β, k_d and k_i are artificially introduced in the algorithm in order to control μ. On the one hand, β controls how fast μ is decreased when the error diminishes, and vice versa. A high value of β causes μ to decrease initially very fast, and could lead the algorithm to diverge, hence rapidly increasing the value of μ. These swings in μ can cause the algorithm to either diverge or converge to non-desired local minima. A low value of β (close to 1) causes the algorithm to converge slowly, specially when μ is high. It has been found that values of β between 1.05 and 1.5 provide a good trade-off for a good rate of convergence while keeping the algorithm from diverging. On the other hand, k_d and k_i control how tolerant the algorithm is to changes in μ when the error oscillates. When the

algorithm reaches a flat valley in the search space, the error might behave irregularly due to the low gradient of the hypersurface around the current position. In order to control μ in this situation, k_d and k_i come into play, having complementary roles. If the error starts decreasing, k_d prevents μ from decreasing too much if previously the error had increased. This tries to prevent the algorithm from diverging because it ensures that μ remains constant until the error decreases k_d consecutive iterations. Conversely, the error has to increase during k_i consecutive iterations in order to increase μ. This prevents μ from increasing too much making the converge slower once the error begins to decrease again. Some reasonable values for these two parameters are within the range from 2 to 5.

However, the problem of choosing μ_0 remains. Nevertheless, there is a suitable strategy to choose it. The optimization variables are the reflection coefficient phases. Hence, in order to have a reliable design, the phase distribution should be as smooth as possible, because that way the physical dimensions of the elements of the reflectarray would vary smoothly from one element to the next (which is necessary because the reflectarray analysis is based on a full-wave analysis assuming local periodicity [2, 29, 54, 76]). Following this, μ_0 should be high enough to allow the phase at the initial iterations to vary smoothly and not to make jumps to valleys of the search space with noisy phase distributions. Due to the dimensionality of the problem being P (usually of the order of hundreds or thousands of optimization variables, at least one per element of the reflectarray), it is very easy to make false steps into non-desired solutions during the first iterations of the algorithm, from which it will be virtually impossible to escape. For that reason, a high value of μ_0, about the same order of magnitude of P (for instance, between $0.5P$ and $5P$), is a good choice.

4.2.6. Starting point and solution

Another important issue is the starting point for the optimization process, which has been widely discussed in the literature [94, 95]. As the LMA is a local optimizer, the starting point is of the utmost importance, since it will determine if the achieved solution is good enough. It has been determined [95] that a good initial point is that of a pencil beam pattern properly focused. Also, a pencil beam pattern can provide a smooth enough initial phase distribution in the center of the reflectarray, where the field amplitude is higher [2], depending on the placing of the feed antenna. As an alternative, an analytical synthesis might be used to obtain a better starting point [81, 157], at the cost of a more complex initial formulation.

In this chapter, different aspects of the algorithm have been discussed that can prevent it from converging to a solution. First, the specifications should be reasonable; i.e., not too stringent, to allow the algorithm to converge from the first iteration. Also, the starting point should be good enough and μ_0 high to ensure a soft descend towards the solution. In practice, the final solution should not only have a low error, but also a smooth phase distribution. With regard to having a low error, it means that the copolar pattern is close to meet the specifications, which is the main goal of the synthesis. However, a smooth phase distribution is also needed for a real reliable design. Due to the local periodicity

assumption when analyzing the reflectarray unit cell [2], the design will perform better when the physical size of the reflectarray elements will vary smoothly across the surface of the antenna. The smoothness of the phase distribution is more critical in the center of the reflectarray were the illumination level is higher.

4.2.7. Validation

4.2.7.1. Antenna specifications

The considered planar reflectarray is rectangular and formed by 900 elements (in a regular grid of 30×30) and a feed horn modeled as a $\cos^q \theta$ function with a q-factor of 37, which produces an illumination taper of -19.5 dB at the edges of the reflectarray. The feed horn points to the center of the reflectarray and its phase center is placed at $\vec{r}_f = (-91, 0, 214)$ mm with regard to the center of the reflectarray. The working frequency is 25.5 GHz and the periodicity of the elements is 5.84 mm$\times$5.84 mm, which is approximately half a wavelength. Also, the far fields are discretized in a 128×128 UV grid, being $T = 16384$. Note that, according to Figure 2.3, the X polarization corresponds to the vertical polarization (V) because the electric field in the $\hat{x}$ direction is vertical, while the Y polarization corresponds to the horizontal polarization (H).

The chosen pattern is a central station for LMDS, which presents a 30°-sector beam in azimuth and a square cosecant beam in elevation [81]. Templates in the main cuts will be presented along with the results of the optimization in the next section.

4.2.7.2. Improvement of previous synthesis

In order to test the described procedure, a synthesis for a LMDS pattern was carried out. The first example uses as a starting point the final result of [81] for both polarizations, which employed the IA-POS after an analytical synthesis procedure to obtain the LMDS pattern. This constitutes an excellent initial radiation pattern since it is very close to the final specification. The LMA parameters are set to $\mu_0 = 1800$, $\beta = 1.05$, $k_d = 3$, $k_i = 2$ and $C(\vec{r}_t) = 1$. The initial error is 2.99 and 2.95 for vertical and horizontal polarizations, according to (4.4). The convergence is very similar for both polarizations. In the case of vertical polarization, after 500 iterations of the LMA, the error was $7.8 \cdot 10^{-10}$. The algorithm was left to complete 999 iterations. However, after iteration 500, approximately, it stagnates. The lowest error was $5.57 \cdot 10^{-10}$ at iteration 990. For the horizontal polarization, the lowest error was $3.78 \cdot 10^{-10}$ at iteration 995, stagnating around iteration 650.

The simulated radiation pattern for vertical polarization is shown in Figure 4.4. The main cuts for horizontal polarization are shown in Figure 4.5 along with the results of [81]. With a global error of the order of 10^{-10}, the radiated fields fit very well to the templates, improving back lobes and the coverage zone with regard to [81] while maintaining a similar shape of the synthesized phases, which are shown in Figure 4.6.

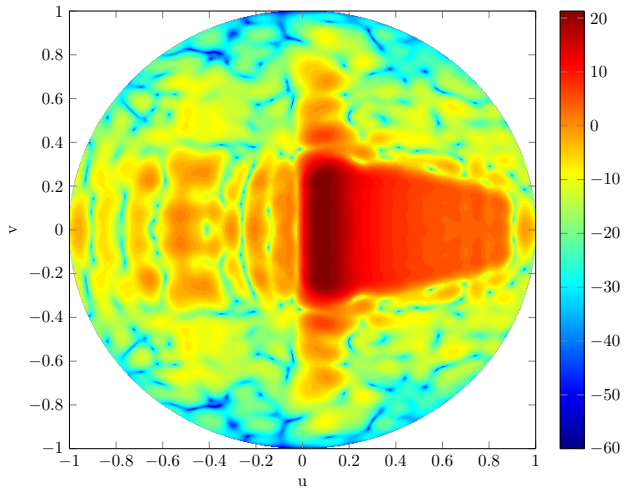

Figure 4.4: *Three dimensional synthesized radiation pattern in gain (dBi) for vertical polarization.*

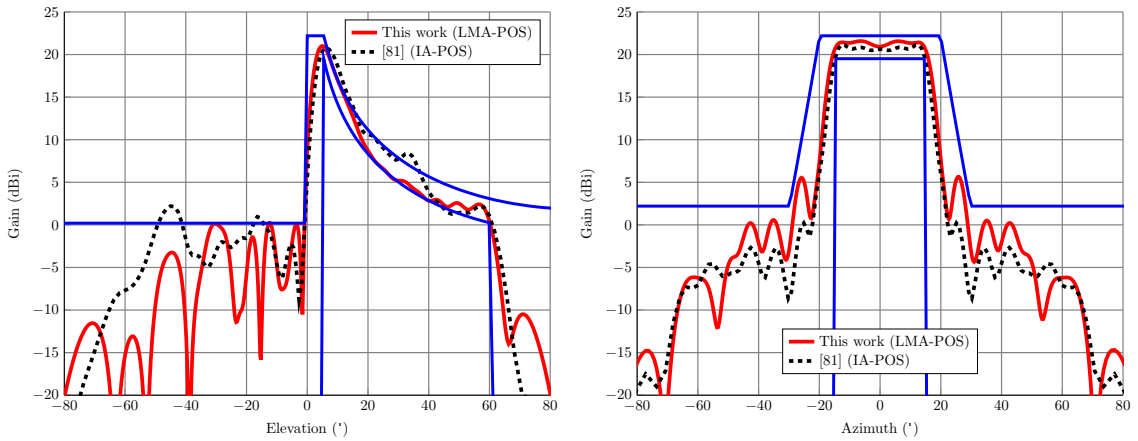

(a) ***(b)***

Figure 4.5: *Radiation pattern of the synthesized reflectarray considering an ideal model of the feed horn in dual polarization, comparing results of the IA-POS and LMA-POS. Main cuts for horizontal polarization in (a) elevation and (b) azimuth.*

4.2.7.3. Synthesis with a pencil beam as starting point

In order to compare more faithfully the results with [97], a new synthesis was carried out employing the same initial point; i.e., the phases of a pencil beam pattern pointing to $(\theta, \varphi) = (5.4°, 0.0°)$, which corresponds to the area of maximum gain in the templates. The LMA parameters for this case were $\mu_0 = 500$, $\beta = 1.1$, $k_d = 3$, $k_i = 2$ and $C(\vec{r}_t) = 1$. First, the H polarization was synthesized from the phase distribution of the pencil beam. The initial error was 53.00 and after the iteration 450 (where the error was $5.05 \cdot 10^{-7}$) it stagnates. The lowest error achieved was $3.87 \cdot 10^{-7}$ at iteration 998, out of 999. After the synthesis of the H polarization, the V polarization was synthesized starting with the synthesized phases of the H polarization. This resulted in an initial error of $7.03 \cdot 10^{-3}$ because the pattern is closer to the templates than the pencil beam, although higher than the final error for the H polarization because the incident field is different for both

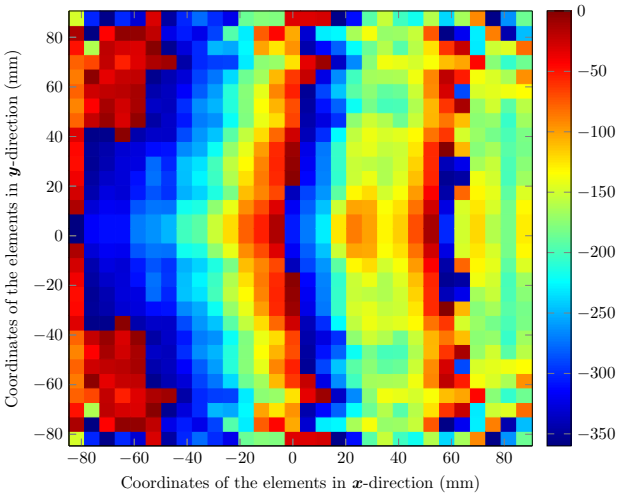

Figure 4.6: *Synthesized phase distribution of the reflection coefficient for the vertical polarization (degrees).*

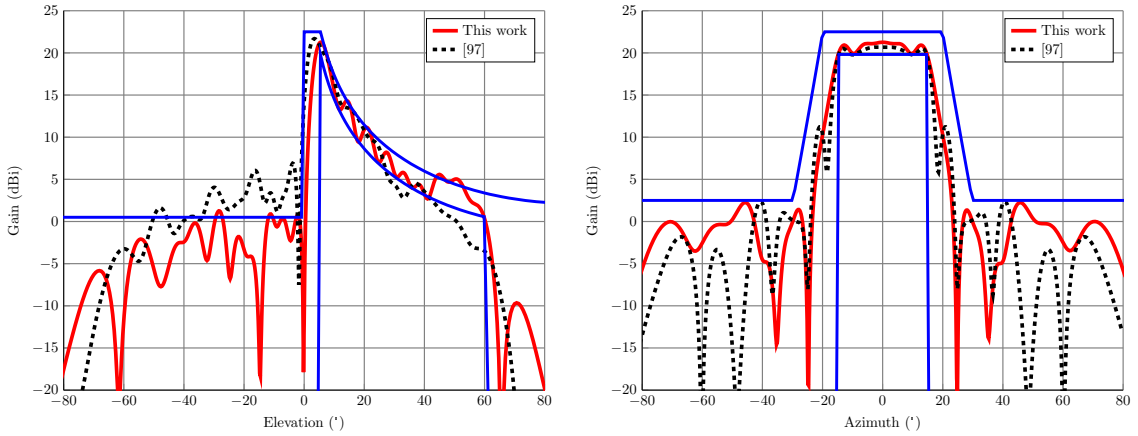

(a) ***(b)***

Figure 4.7: *Radiation pattern of the synthesized reflectarray considering an ideal model of the feed horn in dual polarization with starting point a pencil beam pattern. Main cuts for horizontal polarization in (a) elevation and (b) azimuth.*

polarizations. The lowest error achieved was $2.97 \cdot 10^{-9}$ at iteration 471. As comparison, the final error in [97] is $5.60 \cdot 10^{-3}$, which is several orders of magnitude higher than the error obtained in this work.

Figure 4.7 shows the main cuts for the horizontal polarization of the new synthesized radiation pattern. Because the starting point is not as good as in the previous case, the final pattern obtained now is slightly worse due to some points in the coverage area and back lobes not complying with the templates, although it greatly improves the results of [97]. In particular, the back lobes are reduced by about 6 dB and the coverage zone improves for large angles. Also, the results were obtained in less iterations (less than 500 vs. 3900, for each polarization) and with a final error several orders of magnitude lower, which accounts for the better results in the radiation patterns. Finally, Figure 4.8 shows the synthesized phase distribution when using a pencil beam patterns as starting point.

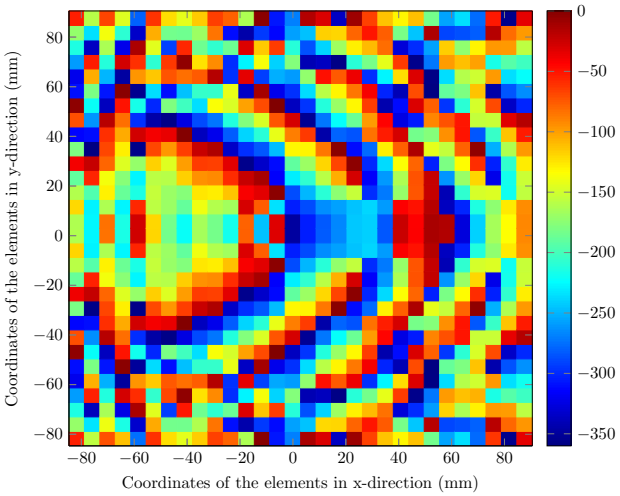

Figure 4.8: *Synthesized phase distribution of the reflection coefficient for the vertical polarization using a pencil beam as starting point (degrees).*

4.2.7.4. Improvement in computing times

With the optimizations detailed in previous sections, the computing times were greatly reduced. In [97], it is reported that each iteration takes less than a minute. Here, each iteration takes about 5.7 seconds using the same computer (Intel Core 2 Duo with a 2.4 GHz processor), which along with the improved convergence of the LMA, reduces significantly the computing times of the synthesis process. The time for each iteration is reduced approximately by a factor of 10. Moreover, taking into account that the synthesis process took less than 500 iterations for each polarization (about eight times faster), the overall improvement in computing times is by a factor of 80.

4.3. Levenberg-Marquardt algorithm for near field applications

4.3.1. Particularization of the Levenberg-Marquardt algorithm for near field optimization

The implemented LMA can also be used to synthesized a desired near field after a few modifications. Now, the analysis of the reflectarray changes, since we are interested in the near field and not the far field. A reflectarray near field model was introduced and validated in Section 2.5 and it will be the one used here. When synthesizing the far field, only the amplitude is taken into account since the far field phase can take any value. However, this is not the case in near field, specially for CATR applications, where both amplitude and phases are being optimized. Thus, the LMA cost function is redefined to account for both components of the near field. The LMA still minimizes cost functions of the form

$$F = \sum_{i=1}^{T} F_i^2. \tag{4.23}$$

However, for the optimization of the quiet zone, the amplitude and phase will be treated separately, specifying the requirements by means of maximum and minimum templates (as for the far field). Now, the cost function takes the form

$$F^{X/Y} = \sum_{i=1}^{N_z} \left(\sum_{t=1}^{T} \left(F_{t,\text{amp}}^{X/Y} \right)^2 + \sum_{t=1}^{T} \left(F_{t,\text{pha}}^{X/Y} \right)^2 \right), \tag{4.24}$$

where the subscript X/Y indicates the polarization that is being optimized, N_z is the number of near field planes perpendicular to axis $\hat{z}$ (see Figure 2.16), T is the total number of points in which each plane is discretized and F_t is the residual for either the amplitude or phase of the near field, which is defined as

$$\begin{aligned} F_t^{X/Y} = C(\vec{r}_t) \Bigg[& \left(M_U^2(\vec{r}_t) - \left| F_{x/y}^{X/Y}(\vec{r}_t) \right|^2 \right) \cdot \left(M_L^2(\vec{r}_t) - \right. \\ & \left. \left| F_{x/y}^{X/Y}(\vec{r}_t) \right|^2 \right) + \left| M_U^2(\vec{r}_t) - \left| F_{x/y}^{X/Y}(\vec{r}_t) \right|^2 \right| \cdot \\ & \left| M_L^2(\vec{r}_t) - \left| F_{x/y}^{X/Y}(\vec{r}_t) \right|^2 \right| \Bigg], \end{aligned} \tag{4.25}$$

where $\vec{r}_t = (x, y)_t$ is a point in a near field plane; C is a weighting function; M_U and M_L are the upper and lower masks or templates, respectively; and $F_{x/y}^{X/Y}$ can be either the amplitude or phase of the field, depending on the residual. The subscript x/y indicates the component of the field, and since only a copolar or desired component is being optimized, only F_x^X or F_y^Y will be considered. Note that (4.25) employs the squared absolute value of the amplitude and phase, which may cause that the field would not be distinguishable from its complex conjugate. In order to solve this ambiguity, the phase should be set in the range $[0, 2\pi]$ for the residual, so the error produced by conjugated field is not the same as the required field (which would be the case when setting the phase in the range $[-\pi, \pi]$).

When optimizing the far field, each column of the Jacobian accommodated all the points of the UV grid of one copolar component. Now, each column will accommodate both, phase and amplitude of N_z near field planes, which are discretized in T points. Hence, the new size of the Jacobian matrix is $(2 \cdot N_z \cdot T) \times P$. As it can be seen, now the Jacobian can be bigger due to the fact that several near field planes can be optimized at the same time and because two components of the field are being optimized, instead of just one.

4.3.2. Validation

4.3.2.1. Optimization of the quiet zone at 20 GHz

For the validation of the algorithm for the near field optimization, two examples will be presented, optimizing the quiet zone at two different frequencies. First, a quiet zone optimization at 20 GHz will be carried out. The geometry of the reflectarray is shown in Figure 2.16 and it is the same reflectarray described in [128]. It consists of a planar

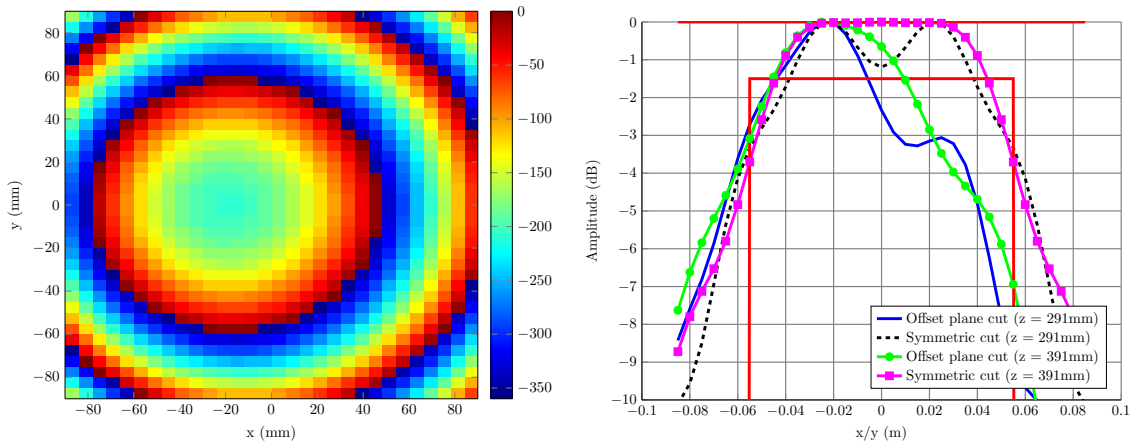

(a) *(b)*

Figure 4.9: *Starting point for the quiet zone optimization at 20 GHz. (a) Initial phase distribution for X polarization. (b) Main cuts of the initial radiated near field at two different planes.*

rectangular surface formed by 1080 elements (30×36) fed by a feed horn modeled as a $\cos^q \theta$ function [78] with $q = 8.2$ at 20 GHz. The focus is located at $(-85, 0, 180)$ mm in the reflectarray coordinate system and the radiation angle is $\theta_0 = 20°$. The periodicity of the reflectarray is 6 mm $\times$ 5 mm and its physical size is 180 mm $\times$ 180 mm. Taking these data into consideration, the projected aperture of the reflectarray will be

$$D = 180 \text{ mm} \cdot \cos\theta_0 = 169 \text{ mm}. \tag{4.26}$$

Since the reflectarray generates a planar phase front, the templates will be set to allow a maximum phase ripple of 10°. However, in order to facilitate the convergence of the algorithm, the amplitude template will be set for a ripple of 1.5 dB. Both templates will specify the respective ripples in a grid defined in ± 55 mm, which corresponds to a 65% of D. Also, the distance z of the planes will be measured taking the center of the reflectarray as origin, and along axis $\hat{z}_a$ (see Figure 2.16). The optimization will be carried out only for X polarization and planes avoiding the reflectarray and the feed in the $\hat{z}$ axis. The weighting function is set to $C = 1$.

The starting point of the optimization is shown in Figure 4.9. The starting phase distribution is given by (3.2) and is shown in Figure 4.9(a). This phase distribution generates the field shown in Figure 4.9(b) in two different planes along the $\hat{z}$ axis. It can be clearly seen how the amplitude taper affects the size of the quiet zone, especially in the offset plane cuts. Although the phases do not completely comply with the specifications, the most restrictive cut is due to the amplitude, and complies with the given specifications only in a 29.4% of D.

After the reflectarray is optimized, the phase distribution of Figure 4.10 was obtained. The main cuts of the generated the near field are shown in Figure 4.11 for the amplitudes and in Figure 4.12 for the phases. The amplitudes are effectively flattened while the phase ripple is reduced in the offset cut. Previously to the optimization, none of the cuts

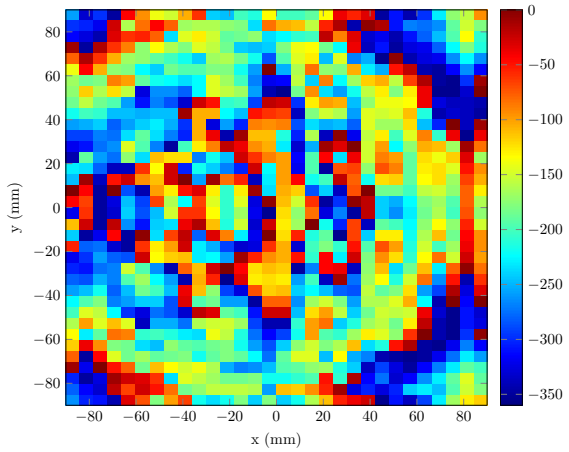

Figure 4.10: *Optimized phase distribution at 20 GHz for the reflectarray quiet zone improvement.*

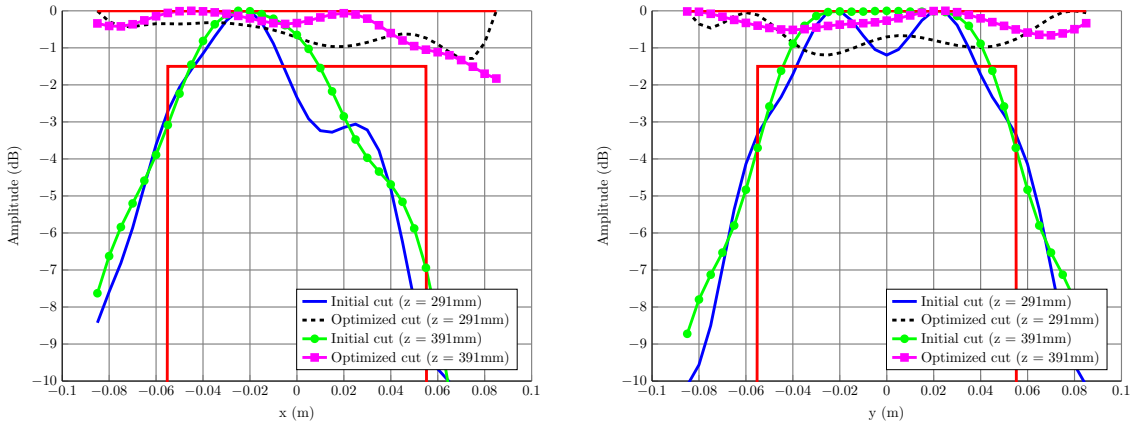

(a) ***(b)***

Figure 4.11: *Comparison for the (a) offset plane and (b) symmetric cuts of the initial and optimized near field amplitude.*

complied with the specifications (with the exception of the phases in the symmetric cut), but after it, all of them comply. Now, the most restrictive cut has been increased to a size of 88% of D, which is an increment of 200% in the size of the quiet zone in the main cuts.

Figure 4.13 shows the 3D near field for the plane at $z = 391$ mm before and after the optimization. The near field is effectively flattened in the whole area where the quiet zone was specified.

4.3.2.2. Reflectarray probe optimization at millimeter frequencies

For the next example, a similar optimization of the quiet zone has been carried out but this time at millimeter frequencies at 100 GHz. A planar rectangular reflectarray has been chosen consisting of 1080 elements (30×36) and illuminated by a feed horn modeled as a $\cos^q \theta$ function with a q-factor of 27, which produces an illumination taper of -18 dB at the edges of the reflectarray. The phase center of the feed horn is placed at $\vec{r}_f = (-17, 0, 36)$ mm with regard to the center of the reflectarray. The periodicity of the cells

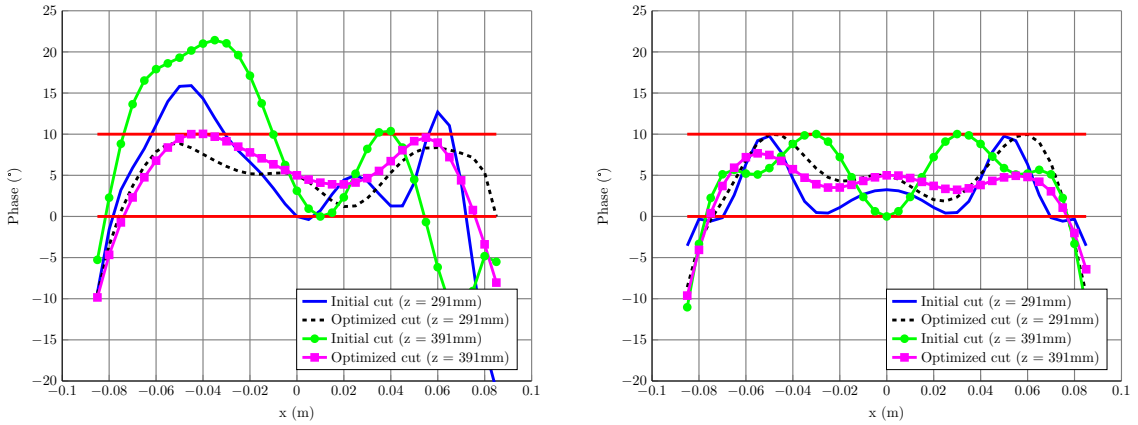

Figure 4.12: *Comparison for the (a) offset plane and (b) symmetric cuts of the initial and optimized near field phase.*

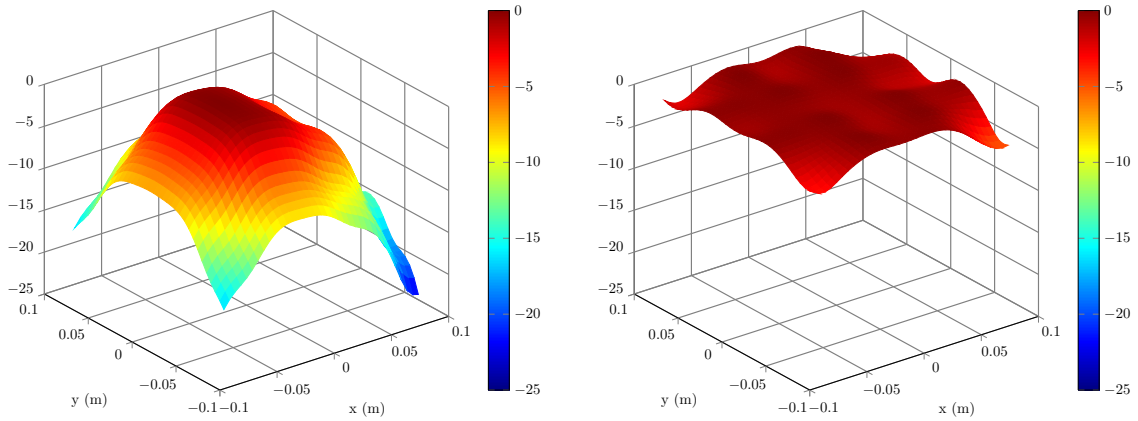

Figure 4.13: *Near field amplitude for* $z = 391$ mm *in 3D (a) before and (b) after the optimization.*

is 1 mm × 1 mm, which is a third of a wavelength at the working frequency.

After the synthesis is done and the phase distribution obtained for X polarization, a design will be carried out using as unit cell two stacked patches backed by a ground plane. The patches from the two layers have a fixed size ratio of 0.85, being the lower layer the one with bigger patches. The chosen substrate for both layers is quartz, with $\epsilon_r = 3.78$, $\tan\delta = 0.002$ and thickness 115 μm. This topology provides more than 360° phase shift to carry out the design using a zero-finding routine, as described in [2].

The starting point of the synthesis is a properly focused reflectarray. The initial phase distribution is obtained with (3.2) and produces a planar phase front. From this initial phase distribution, the algorithm will try to maintain the planar phase front while flattening the near field amplitude. Given the number of elements and periodicity, the

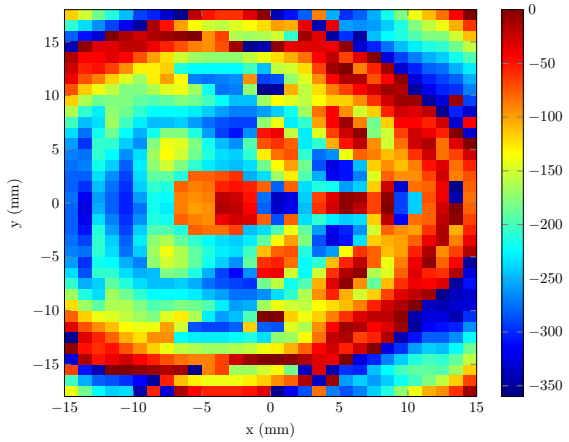

Figure 4.14: *Optimized phase distribution for the quiet zone synthesis at 100 GHz.*

equivalent aperture is

$$\begin{aligned} D = D_x \times D_y &= 30 \text{ mm} \cdot \cos\theta_0 \times 36 \text{ mm} \\ &= 28.2 \text{ mm} \times 36 \text{ mm} = 9.4\lambda \times 12\lambda. \end{aligned} \tag{4.27}$$

Although the typical amplitude ripple for CATR is 1 dB, in order to facilitate convergence of the algorithm due to the strong amplitude taper of the starting point, templates are set for an amplitude ripple of 1.5 dB in a width of 20 mm while for the phase the allowable ripple is set to 10° in 28 mm of width. The weighting function is set to $C = 1$.

Once the optimization process is finished, the phase distribution of Figure 4.14 is obtained, from which a reflectarray design is carried out following [2]. The main cuts of the radiated near field are shown in Figures 4.15 and 4.16, where the starting point is compared with the optimized near field for the POS (considering ideal phase shifters) and the design (simulating real patches with a full-wave221 Method of Moments assuming local periodicity). Due to the small electrical size of the reflectarray (equivalent aperture of $9.4\lambda \times 12\lambda$), the planar phase front is lost in the planes where the optimization is carried out ($z = 58.2$ mm and 78.2 mm from the center of the reflectarray). For this antenna, the planar phase front would be closer to the antenna aperture. The most restrictive cut for the starting point in $z = 58.2$ mm complies with the specification in a size of 9.3 mm (amplitude limiting the quiet zone), while for the other plane is 9.1 mm, also for the amplitude.

After the optimization, both the amplitude and phase are flattened in both planes, improving the size of the quiet zone, as it can be seen in Figures 4.15 and 4.16. They are flattened in the whole plane, as is shown in Figure 4.17 for the amplitude at $z = 78.2$ mm. Considering only the results for the design simulations (which are similar to the POS simulations), now the most restrictive cut in the plane $z = 58.2$ mm is still due to the amplitude, but with a size of 17.8 mm, which supposes an improvement of 91%. For the other plane, now the restriction is due to the phase, with a size of 21.9 mm, an improvement over the non-optimized near field of 140%.

The phases obtained in both test cases (Figures 4.10 and 4.14) are not very suitable

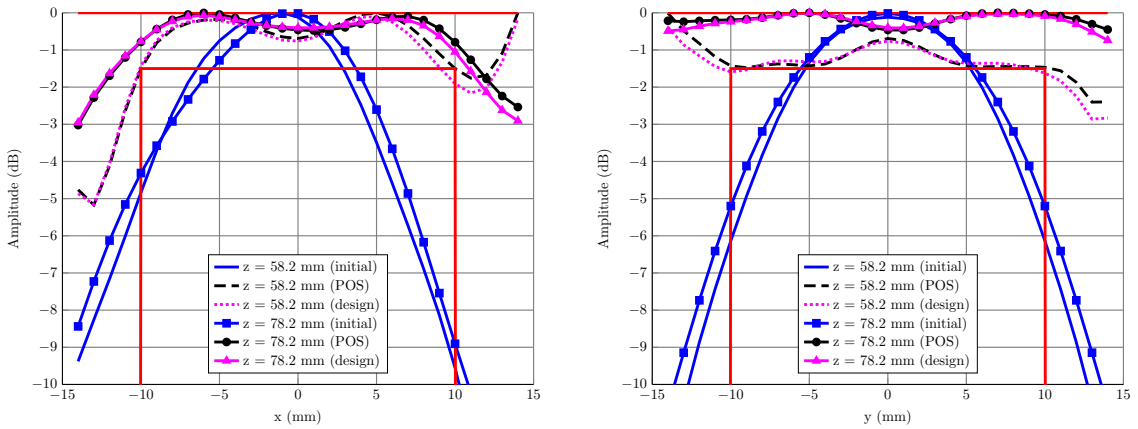

(a) *(b)*

Figure 4.15: *Comparison for the (a) offset plane and (b) symmetric cuts of the initial and optimized (POS and design) near field amplitude.*

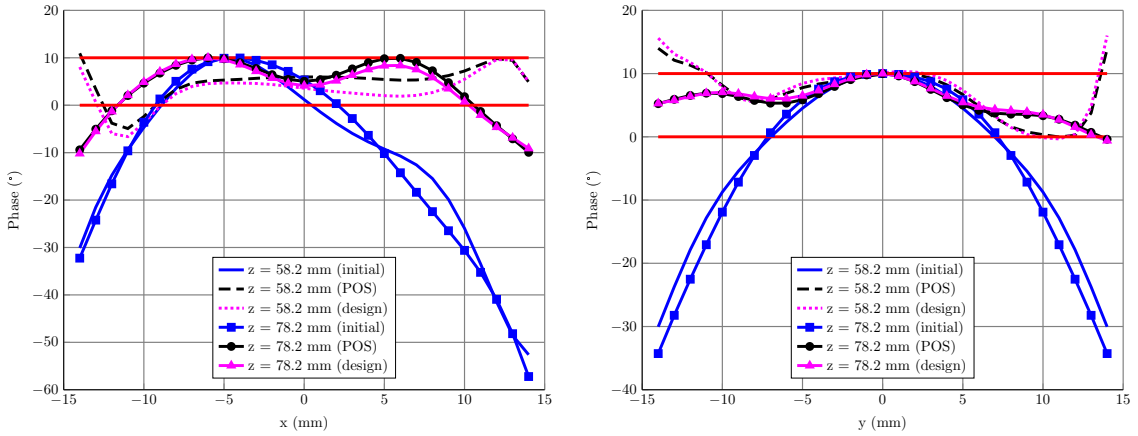

(a) *(b)*

Figure 4.16: *Comparison for the (a) offset plane and (b) symmetric cuts of the initial and optimized near field phase.*

for reflectarray design since they are not smooth and thus the design would present element with very different sizes, violating the local periodicity assumptions, leading to poor agreement between measurements and simulations. In this regard, the phase distribution of Figure 4.14 is better than the phases shown in 4.10. However, it still remains the task of finding better solutions for the near field optimization. A possible approach would be to model the reflectarray phases with spline functions, in such a way that by optimizing the spline coefficients, a smooth solution could be obtained.

4.4. Conclusions

An improved phase-only synthesis for reflectarrays based on the Levenberg-Marquardt algorithm with an ellipsoidal trust region has been developed, improving the accuracy and efficiency with regard to other works in the literature. By optimizing each building block

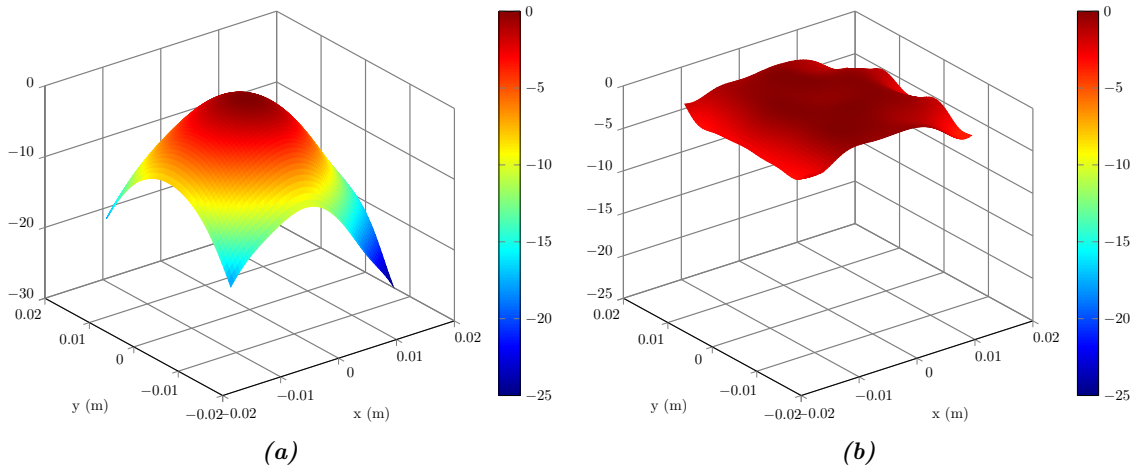

Figure 4.17: *Near field amplitude for $z = 78.2$mm in 3D (a) before and (b) after the optimization.*

of the algorithm, a great computational efficiency is achieved that will allow for more powerful synthesis techniques implemented with the same algorithm. For instance, it will be possible to implement a direct optimization of the geometry of the reflectarray through full-wave analysis based on local periodicity of the reflectarray unit cell [29, 54, 76] within reasonable computing times. This approach will be explored in the following chapter.

In particular, the Jacobian matrix is obtained through finite differences which allows to avoid using the analytical expressions for complex problems. By choosing the appropriate value of the increment in the finite difference equation, the error evaluating the derivative is minimized. Also, the columns of the Jacobian can be computed independently from each other, which allows to fully parallelize its evaluation. By deriving with respect to the reflection coefficient phases instead of the tangent of the phases, the convergence of the algorithm is improved. Further improvements were made regarding the choice of the solver for the equation system, where a Cholesky factorization based solver was selected to take advantage of the symmetry of the resulting matrix. Also, computationally expensive operations such as matrix and matrix-vector multiplications were performed using highly optimized and parallelized routines. Since the result of the matrix multiplication is symmetric, only the lower or upper triangular part needs to be computed. In addition, due to the intrinsic high dimensionality of the problem, a few guidelines have been laid out in order to control the evolution of the synthesis, which allows for a better control of the obtained solution. In particular, it has been shown how the initial point of the synthesis is a key factor in a local search optimizer such as the LMA. Also, a suitable choice of the parameters of the LMA is important in order to control the speed of convergence as well as the initial evolution of the algorithm, which can determine the path to a good or bad solution. Two test cases of a LMDS pattern were shown to validate the proposed solution. The performance of the algorithm has proven to be better than others in the literature. The results are more accurate, reducing back lobes and better controlling the coverage zone, while reducing the computing times by a factor of 80.

The LMA-POS was also adapted to perform near field optimizations with the reflect-

array near field modeled presented in Chapter 2. Apart from the change in the analysis tool, the cost function was adapted to take into account both amplitude and phase in the optimizations, since the goal was to improve the quiet zone generated by the reflectarray. For the first example, due to the high taper of the feed, the near field amplitude presented a strong taper, limiting the size of the quiet zone. After the optimization, the amplitude was flattened, while keeping the phase front within a range of variation of 10°. In the last example, the phase front was lost, but after the optimization, both the amplitude and phases were flattened, greatly improving the quiet zone size.

The implemented LMA will be extended in the next chapter to perform crosspolar optimization using a full-wave analysis technique within the optimization process.

CHAPTER 5

Direct optimization of reflectarrays using full-wave analysis based on local periodicity

5.1. Introduction

At this stage, three algorithms for the synthesis of radiation patterns have been discussed. First, the Intersection Approach for phase-only synthesis (IA-POS) was detailed, along with several modifications in order to control the synthesized phases and the convergence of the algorithm. The IA-POS has demonstrated to be very useful for the copolar pattern synthesis of reflectarrays of all sizes, including very large reflectarrays. The extreme efficiency of the algorithm lies in the fact that it is very fast since it takes advantage of the FFT algorithm in order to compute the far fields and to recover the tangential field. The FFT is the most time consuming operation of the algorithm, making it very fast. However, since it is a POS algorithm, there is no control over the crosspolar component of the far field and thus its formulation was extended to include crosspolar requirements in the IA-XP. In order to accurately compute the crosspolar far field, without the simplifications considered in the POS case, the full matrix of reflection coefficients must be used. Hence, instead of working with phase distributions as in the IA-POS, the output of the algorithm was a distribution of reflection coefficient matrices. Despite preserving the computational efficiency of the algorithm by using the FFT in both projectors to compute the radiation patterns and recover the tangential field, it presented the problem of finding a layout that matched the obtained reflection coefficient matrix for each reflectarray element, which could be really challenging and was not pursued in this work.

It was later discussed that a better approach to the crosspolar optimization of reflectarray antennas would be to directly optimize the geometry of the elements. However, the approach followed before would not be useful. Now, a general optimization algorithm was needed and hence the Levenberg-Marquardt algorithm (LMA) was chosen. However, before applying this algorithm to the direct optimization of reflectarrays, it was applied to

a POS in order to speed up the algorithm, presenting a number of improvements to have an efficient and scalable version of the LMA for reflectarray optimization that could take advantage of computers with multiple CPU units. The results provided to validate the algorithm showed an improved and faster version of the LMA-POS than other implementations in the literature, that was suitable for its extension for the direct optimization of the reflectarray geometry. Furthermore, the LMA-POS was also tested for the near field optimization of reflectarrays, with minimal changes in its structure (only in the analysis tool and cost function). It was used for the quiet zone optimization obtaining very promising results. This algorithm is very flexible and can be applied to many problems either for near or far field applications.

In this chapter, the knowledge acquired in previous chapters will be used in the crosspolar radiation pattern optimization by directly optimizing the reflectarray geometry. First, the LMA detailed in the previous chapter will be modified in order to include a full-wave analysis based on local periodicity of the reflectarray unit cell based on MoM. Since the full-wave analysis tool is very slow (relative to the rest of analysis operations), the algorithm will be further optimized in order to minimize the impact of MoM in the LMA. This version of the algorithm is denoted as LMA-XP. A test case of a LMDS pattern is used as validation. The LMDS pattern is first obtained with POS, in order to have a better starting point for the crosspolar optimization. The LMA-XP was applied, effectively lowering the crosspolar component while preserving the copolar shape within specifications.

Despite the good results obtained for a small-sized reflectarray, the LMA-XP might present limitations when applied to the optimizations of very large reflectarrays (several thousands of elements), due to the optimization being non-convex, which might lead to poor convergence due to the problem of traps (local minima). In order to improve the convergence, the generalized Intersection Approach framework is used [89], working with the squared field amplitude, which convexifies one of the sets, minimizing the impact of the trap problem. However, for the direct optimization, the backward projector needs to be modified to use a general optimization algorithm. Thus, the LMA is used as backward projector, taking advantage of all the previous work, and hence integrating the IA framework and LMA into a single optimizing algorithm with improved convergence for the crosspolar optimization, which in this context is known as IA-LMA-XP. This algorithm is able to provide better results in less iterations than the LMA-XP. Two test cases are shown to validate the new algorithm for the crosspolar optimization. The first one is a small reflectarray with an isoflux pattern for global Earth coverage, and the second a very large reflectarray with a European coverage for DBS applications. The developed algorithm is able to handle thousands of optimizing variables (as demonstrated in the two examples) within acceptable computing times in workstations.

5.2. Generalization of the Levenberg-Marquardt algorithm for crosspolar optimization

In this section, the LMA will be extended in order to allow the direct optimization of reflectarrays. All the improvements to the algorithm described in the previous chapter in

order to speed up the computations are kept, and some new are introduced in order to minimize the impact of introducing MoM in the optimization algorithm as analysis tool.

5.2.1. Differences with the phase-only synthesis

When doing POS the reflectarray analysis was simplified considering the elements as ideal phase shifters with no losses and no crosspolarization introduced by them. These two simplifications in the coefficient reflection matrix can be summarized by the following equations:

$$|\rho_{xx}| = |\rho_{yy}| = 1 \qquad \text{(no losses)}, \tag{5.1a}$$

$$|\rho_{xy}| = |\rho_{yx}| = 0 \qquad \text{(no element crosspolarization)}. \tag{5.1b}$$

This led to a synthesis algorithm in which only the copolar pattern could be synthesized, since an important contribution to the crosspolar pattern was not taken into account (the coefficients ρ_{xy} and ρ_{yx}).

Also, the far fields in spherical coordinates were computed considering only one spectrum function instead of two. This spectrum function was the Fourier transform of the tangential field component which was relevant for the given polarization, that is, the $\hat{x}$ component for X polarization and the $\hat{y}$ component for Y polarization. This simplification led to a synthesis method in which both polarizations were synthesized independently from each other. Furthermore, only one FFT per polarization was needed (two in total), instead of two (four in total) for the far fields computation.

It is clear that with these two simplifications, the computed crosspolar pattern cannot be synthesized since it is not properly computed, with regard to its computation with no such simplifications. However, some similar doubts can arise for the case of the copolar pattern. Fortunately, it has been demonstrated [2, 95] that the copolar patterns obtained with and without these two simplifications are very similar between them, and this simplified analysis is suitable for the copolar synthesis of reflectarray antennas, as has been demonstrated several times in the literature.

However, for the crosspolar optimization, neither of these two simplifications should be used, as it was also the case of the IA-XP algorithm. Nevertheless, in this chapter a different approach will be followed, since now the output of the algorithm will not be the matrices of reflection coefficients, but the reflectarray geometry. To obtain the R^{mn} matrix, several methods can be used, such as Method of Moments (MoM), Finite Element Method (FEM) or Finite Difference Time Domain (FDTD), all of them assuming local periodicity. They are full-wave analysis tools and are slow. Another approach would be to use ANN or SVM, which model the reflectarray element in order to predict its behavior for a given geometry. They are really fast analysis tools, but their training process can be very slow depending on the number of considered variables. Also, a look-up table has been previously used in some works, but it presents the same disadvantage of the ANN and SVM. Furthermore, if the reflectarray element is changed, or the substrate or working frequency, new ANN, SVM or look-up tables must be generated. On the other hand, using

a full-wave analysis tool directly in the optimization process would eliminate the need of generating an intermediate model, which is by definition less accurate than the model provided by the full-wave analysis tool. However, this is done at the expense of higher computing times in the optimization.

As it can be seen, the crosspolar optimization of reflectarrays is not an easy problem to solve from a computational point of view. Either way of approaching it (ANN/SVM/look-up table or directly using MoM/FEM/FDTD in the optimization) presents the problem of demanding high computing times for one task or another. The approach followed in this thesis is the inclusion of a MoM tool in the optimization process. It was chosen for several reasons. First, the analysis of the reflectarray elements with MoM (or other full-wave tools) is already an imperfect model. The ANN/SVM/look-up table are models of a model, which can further introduce inaccuracies in the analysis. Furthermore, in order to minimize the impact of an inaccurate model of the ANN/SVM/look-up table, considerable time needs to be invested in generating a proper model (for instance, a whole PhD thesis is devoted to develop an ANN model of a reflectarray unit cell, but the full R^{mn} was only obtained for a particular case of the reflectarray geometry, and not for all possible variations [63]). In addition, when doing an ANN/SVM/look-up table model, it is done for a certain element geometry (stacked patches, dipoles, rings, ...), substrate and frequencies. If one of those were to change, the model would need to be generated again, investing more time. However, it is true that once the model is obtained, the optimization process will be faster that when using MoM/FEM/FDTD directly in the optimizing algorithm.

With the approach followed in this thesis (incorporating MoM in the optimizing algorithm as analysis tool), more time is employed during the optimization, but there is no need to generate a new model of the reflectarray unit cell. However, more care has to be devoted to develop the algorithm in order to make it more efficient, since MoM will slow down the whole process. Nevertheless, all the potential improvements to the algorithm in order to speed up computations could also be used if, instead of MoM, the ANN/SVM/look-up table is used. Thus, focusing in strategies to speed up the algorithm computations (as done in the previous chapter) will result in benefits for both approaches.

The flow chart for the LMA-XP is the same as for the LMA-POS shown in Figure 4.2, since the algorithm is essentially the same and only the analysis tool is changed.

5.2.2. LMA cost function for crosspolar optimization

The cost function of the LMA needs to be adapted for the crosspolar optimization, since it will be slightly different than for the POS case. Now, four components of the far field need to be taken into account, the copolar and crosspolar fields for both polarizations. If each one of these far fields is discretized in T points in the UV grid, the cost function will take the form

$$F = \sum_{t=1}^{4T} F_t^2, \tag{5.2}$$

where the residual F accommodates the four far field components. In fact, (5.2) can also be expressed as

$$F = \sum_{t=1}^{T} \left[\left(F^X_{t,\,\mathrm{cp}}\right)^2 + \left(F^X_{t,\,\mathrm{xp}}\right)^2 + \left(F^Y_{t,\,\mathrm{cp}}\right)^2 + \left(F^Y_{t,\,\mathrm{xp}}\right)^2 \right], \tag{5.3}$$

where the residuals are defined as

$$\begin{aligned} F^X_{t,\,\mathrm{cp}} = C^X_{\mathrm{cp}}(\vec{r}_t) \Bigg[& \left(\left(T^X_{\mathrm{cp,max}}(\vec{r}_t)\right)^2 - \left|E^X_{\mathrm{cp}}(\vec{r}_t)\right|^2 \right) \left(\left(T^X_{\mathrm{cp,min}}(\vec{r}_t)\right)^2 - \left|E^X_{\mathrm{cp}}(\vec{r}_t)\right|^2 \right) + \\ & \left| \left(T^X_{\mathrm{cp,max}}(\vec{r}_t)\right)^2 - \left|E^X_{\mathrm{cp}}(\vec{r}_t)\right|^2 \right| \left| \left(T^X_{\mathrm{cp,min}}(\vec{r}_t)\right)^2 - \left|E^X_{\mathrm{cp}}(\vec{r}_t)\right|^2 \right| \Bigg], \end{aligned} \tag{5.4a}$$

$$\begin{aligned} F^X_{t,\,\mathrm{xp}} = C^X_{\mathrm{xp}}(\vec{r}_t) \Bigg[& \left(\left(T^X_{\mathrm{xp,max}}(\vec{r}_t)\right)^2 - \left|E^X_{\mathrm{xp}}(\vec{r}_t)\right|^2 \right) \left(\left(T^X_{\mathrm{xp,min}}(\vec{r}_t)\right)^2 - \left|E^X_{\mathrm{xp}}(\vec{r}_t)\right|^2 \right) + \\ & \left| \left(T^X_{\mathrm{xp,max}}(\vec{r}_t)\right)^2 - \left|E^X_{\mathrm{xp}}(\vec{r}_t)\right|^2 \right| \left| \left(T^X_{\mathrm{xp,min}}(\vec{r}_t)\right)^2 - \left|E^X_{\mathrm{xp}}(\vec{r}_t)\right|^2 \right| \Bigg], \end{aligned} \tag{5.4b}$$

$$\begin{aligned} F^Y_{t,\,\mathrm{cp}} = C^Y_{\mathrm{cp}}(\vec{r}_t) \Bigg[& \left(\left(T^Y_{\mathrm{cp,max}}(\vec{r}_t)\right)^2 - \left|E^Y_{\mathrm{cp}}(\vec{r}_t)\right|^2 \right) \left(\left(T^Y_{\mathrm{cp,min}}(\vec{r}_t)\right)^2 - \left|E^Y_{\mathrm{cp}}(\vec{r}_t)\right|^2 \right) + \\ & \left| \left(T^Y_{\mathrm{cp,max}}(\vec{r}_t)\right)^2 - \left|E^Y_{\mathrm{cp}}(\vec{r}_t)\right|^2 \right| \left| \left(T^Y_{\mathrm{cp,min}}(\vec{r}_t)\right)^2 - \left|E^Y_{\mathrm{cp}}(\vec{r}_t)\right|^2 \right| \Bigg], \end{aligned} \tag{5.4c}$$

$$\begin{aligned} F^Y_{t,\,\mathrm{xp}} = C^Y_{\mathrm{xp}}(\vec{r}_t) \Bigg[& \left(\left(T^Y_{\mathrm{xp,max}}(\vec{r}_t)\right)^2 - \left|E^Y_{\mathrm{xp}}(\vec{r}_t)\right|^2 \right) \left(\left(T^Y_{\mathrm{xp,min}}(\vec{r}_t)\right)^2 - \left|E^Y_{\mathrm{xp}}(\vec{r}_t)\right|^2 \right) + \\ & \left| \left(T^Y_{\mathrm{xp,max}}(\vec{r}_t)\right)^2 - \left|E^Y_{\mathrm{xp}}(\vec{r}_t)\right|^2 \right| \left| \left(T^Y_{\mathrm{xp,min}}(\vec{r}_t)\right)^2 - \left|E^Y_{\mathrm{xp}}(\vec{r}_t)\right|^2 \right| \Bigg], \end{aligned} \tag{5.4d}$$

where each $t = 1, \ldots, T$ describes a $\vec{r}_t = (u, v)_t$ point in which the UV grid is discretized; $C(\vec{r}_t)$ is a weighting function; and T is the template which specify the requirements for the optimization. In the most general case, each component of the far field can have different weighting functions with different values at each point, and also different templates. However, since this algorithm is specifically thought for crosspolar optimization, C_{xp} plays an important role. The crosspolar components present values which are very low with regard to the maximum copolar values, usually 20 dB or more below. Hence, in absence of a weighting function, the crosspolar error would be negligible and would not be optimized by the algorithm. For that reason, C_{xp} should be initialized to a value such that the crosspolar error is similar to the copolar error, optimizing both components at the same time.

5.2.3. Optimizing variables

The unit cell which will be used for the crosspolar optimization of reflectarray antennas is shown in Figure 5.1. It is comprised of two layers of metallization with four parallel and coplanar dipoles per polarization, having a total of eight dipoles. The full-wave Method of Moments which analyzes the cell is described in [76,127], and takes as input parameters all the variables shown in Figure 5.1, among others. So many variables provide, potentially, many degrees of freedom to carry out the optimization. However, the main disadvantage

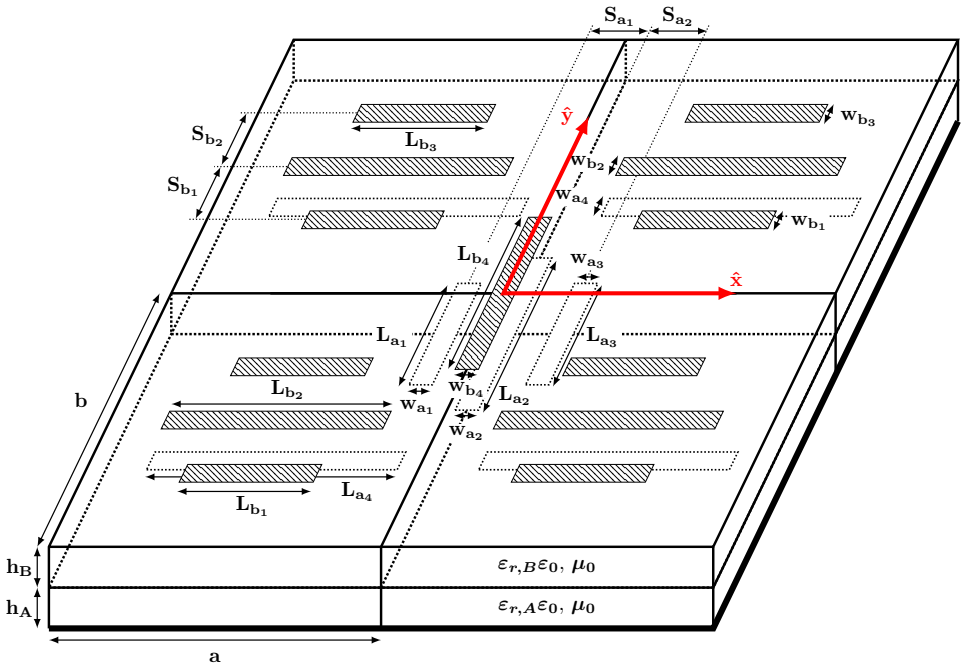

Figure 5.1: *Reflectarray unit cell based on parallel and coplanar dipoles in two different layers of metallizations for dual-polarized reflectarrays.*

is that, as the number of degrees of freedom increase, the search space grows exponentially as well as the number of non-desired local minima. As explained in Chapter 4, the cost function represents a non-convex search space, and thus it is very easy for the algorithm to reach a non-desired local minima. For POS, this issue can be avoided by choosing a proper starting point for the optimization, since the number of optimizing variables is much more smaller than in the present case. Nevertheless, from all the parameters shown in Figure 5.1, some of them should not be used in the optimization. For instance, the height (thickness) of the substrates and their relative permittivity could be optimized, considering the same values for all reflectarray elements. However, the resulting values after the optimization could not be available commercially or result in a very expensive material. In this case, it is better to fix those values beforehand. The optimization of parameters such as the periodicity would alter the physical size of the antenna for a fixed number of elements or, conversely, alter the total number of elements for a fixed physical size. It is cumbersome to optimize this kind of parameters and it is better to carry out a parametric study to choose a fixed value for them. In addition, other parameters, such as the width of the dipoles or the separation between them might not result flexible enough to justify the increase in memory and computing time usage with regard to the benefits in the optimization.

For the given geometry, the best optimizing variables are the dipole lengths [127], since they have a wide range of variation and directly control the phases of the main reflection coefficients (ρ_{xx} and ρ_{yy}). The amplitude and phase of ρ_{xy} and ρ_{yx} also vary in a wide range by only modifying the dipole lengths [127]. Moreover, having eight potential optimizing variables per reflectarray element is considered enough to carry out crosspolar optimization, provided a suitable starting point. In addition, it is not necessary to optimize

all eight variables at the same time. Since the memory and computing time of the LMA directly depend on the number of optimizing variables, it might be a good idea to fix some of them while optimizing others, reducing also the size of the search space and thus the potential non-desired local minima. One strategy could be to fix the lateral dipoles to have the same length, having a total of six variables per element. Another strategy would be to impose a fixed ratio for the dipoles of each polarization, in a way that all of them are scaled with regard to one another optimizing only two variables, one per polarization. Finally, it is not necessary to optimize all reflectarray elements. Similarly to the strategy followed in POS, the number of reflectarray elements which are optimized can be reduced. The difference with POS is that now the reduction in the number of optimizing variables is not fictitious anymore, since one can really choose which elements are optimized and which elements are not.

Finally, due to the generality of the algorithm, apart from crosspolar optimization it can also carry out copolar optimization, potentially obtaining better results than with POS, since now the reflectarray geometry is directly being modified. This strategy might be suitable for optimizing reflectarrays in a given bandwidth to obtain a suitable starting point for a future crosspolar optimization.

5.2.4. Further computational improvements to the algorithm

With the computational improvements to the LMA detailed in the previous chapter, an important ground was covered for its use for the direct reflectarray optimization. In short, those improvements were:

- Minimization of the evaluation error of the finite difference by properly choosing the step parameter h.
- Parallelization of the Jacobian matrix evaluation, by computing one column per available thread.
- Efficient computation of the reflectarray far fields by means of the FFT.
- Use of suitable libraries for the matrix-vector and matrix multiplications, which take advantage of highly efficient and fully parallelized algorithms with low-level hardware operations.
- Computation of a triangular part of a big matrix multiplication, instead of the full matrix, since the result is a symmetric matrix.
- Use of a Cholesky-based matrix equation solver, since the involved matrix is at least semidefinite positive. This kind of solver is the fastest exact solver for this kind of problem.

However, if MoM is included in the algorithm, more improvements are needed in the LMA in order to further speed up computations. They are included in the computations of the cost function and the Jacobian matrix evaluation, which are the building blocks calling the MoM routine.

5.2.4.1. Improvement in the LMA cost function implementation

For the POS case, the most time consuming operation when computing the far fields from the tangential field of the reflectarray is the FFT. However, now that the reflectarray is analyzed with MoM, the evaluation of the tangential field is slower, since a MoM call is required per reflectarray element. However, since the evaluation of a reflectarray element is independent from the rest (because the analysis assumes local periodicity), this operation can be easily parallelized using OpenMP [142]. This way, the evaluation of the tangential field is sped up, and can take advantage of modern CPU units, scaling well with the number of available processors. This parallelization of the cost function routine only applies when it is called the first time at the beginning of each LMA iteration, and not from the Jacobian evaluation routine, where another kind of parallelization is used.

5.2.4.2. Improvements in the Jacobian matrix evaluation

Despite the optimization in the Jacobian evaluation described in the previous chapter, it is still not enough to be practical when using MoM in the analysis of the reflectarray. In order to reduce the number of calls to the MoM routine, first a one-sided-difference is used in the evaluation of each column of the Jacobian, instead of the central difference, which is expressed as

$$\frac{\partial F_t(\alpha)}{\partial \alpha_p} = \frac{F_t(\alpha) - F_t(\alpha - he_p)}{h} + \mathcal{O}(h), \tag{5.5a}$$

$$\frac{\partial F_t(\alpha)}{\partial \alpha_p} = \frac{F_t(\alpha + he_p) - F_t(\alpha)}{h} + \mathcal{O}(h), \tag{5.5b}$$

being the optimum value for the increment h

$$h = \sqrt{u_r}, \tag{5.6}$$

with u_r the unit round-off which has the following value for double precision real numbers:

$$u_r = 2.220446049250313 \cdot 10^{-16}. \tag{5.7}$$

Any of the two lateral differences shown in (5.5) can be used in the computation of the Jacobian matrix. This reduces the calls to the cost function (and hence the calls to the MoM routine) by half.

Still, when calling the cost function in order to evaluate the lateral difference, all elements of the reflectarray are processed with MoM. Assuming that all reflectarray elements are optimized by the LMA, the Jacobian matrix has sN columns (where N is the number of reflectarray elements and s the number of optimizing variables per reflectarray element) and considering MoM as the dominant operation, the overall time complexity of evaluating the full matrix would be

$$\mathcal{O}(O_{\text{MoM}} \cdot s \cdot N \cdot N/L), \tag{5.8}$$

where L is the number of available processors, since one column is computed per available

thread; and

$$O_{\mathrm{MoM}} = \mathcal{O}\left(k_1 Z^2 + k_2 Z^3\right), \tag{5.9}$$

where Z is the number of unknowns in MoM, $k_1 Z^2$ is the term for filling the MoM matrix and $k_2 Z^3$ for inverting it. In the present case, 5 basis functions per dipole are used, thus having a 40×40 MoM matrix, which is very fast to invert. However, in this case the bottleneck is the matrix filling, which is much slower than the inversion [76].

The time complexity in (5.8) is not suitable for practical implementation. If analysing one element with MoM takes an average time of 0.1 s. and the reflectarray has $N = 900$ elements with $s = 6$ optimization variables per element, the time to evaluate the Jacobian matrix would be of the order of 135 h. (5.6 days) for $L = 1$ and 13.5 h. for $L = 10$. If the reflectarray has roughly 7000 elements as in [20], the time would escalate to 340 days and 34 days for $L = 1$ and $L = 10$, respectively.

In light of these results, it is obvious that the times involved in the Jacobian matrix evaluation are of no practical use. However, they can be greatly reduced by further minimizing the number of MoM calls. Each column of the Jacobian is obtained by a single call to the cost function, which returns a vector with all the components of the column. Furthermore, each column is calculated by deriving the cost function with respect to just one variable, resulting in just one element being modified. Hence, there is no need to recompute R^{mn} for all elements using MoM, but just one element per Jacobian column, reusing the rest of the reflection coefficients from the first call to the cost function at the beginning of each iteration of the LMA. This can be easily implemented by branching the cost function routine, detecting when it is used to evaluate the Jacobian matrix, computing only one element with MoM. With this improvement, the new time complexity of evaluating the Jacobian matrix is

$$\mathcal{O}\left(O_{\mathrm{MoM}} \cdot s \cdot N/L\right). \tag{5.10}$$

Using the same examples as before, the new improved computing times would be 9 and 70 min. for $L = 1$, which represent an important reduction from the previous 5.6 and 340 days, respectively.

5.2.5. Validation

In order to validate the algorithm, two antennas will be optimized with different radiation patterns. First, a small reflectarray comprised of 900 elements with an LMDS pattern will be optimized to reduce the crosspolar component of the far field. Then, in order to test the convergence of the algorithm, a large reflectarray comprised of 5180 elements with a European DBS coverage will be optimized and its results discussed.

5.2.5.1. LMDS pattern

For the first test case, a planar rectangular reflectarray has been chosen consisting of 900 elements (30×30) and illuminated by a feed horn modeled as a $\cos^q \theta$ function with a q-factor of 37, which produces an illumination taper of -19.7 dB at the edges of the

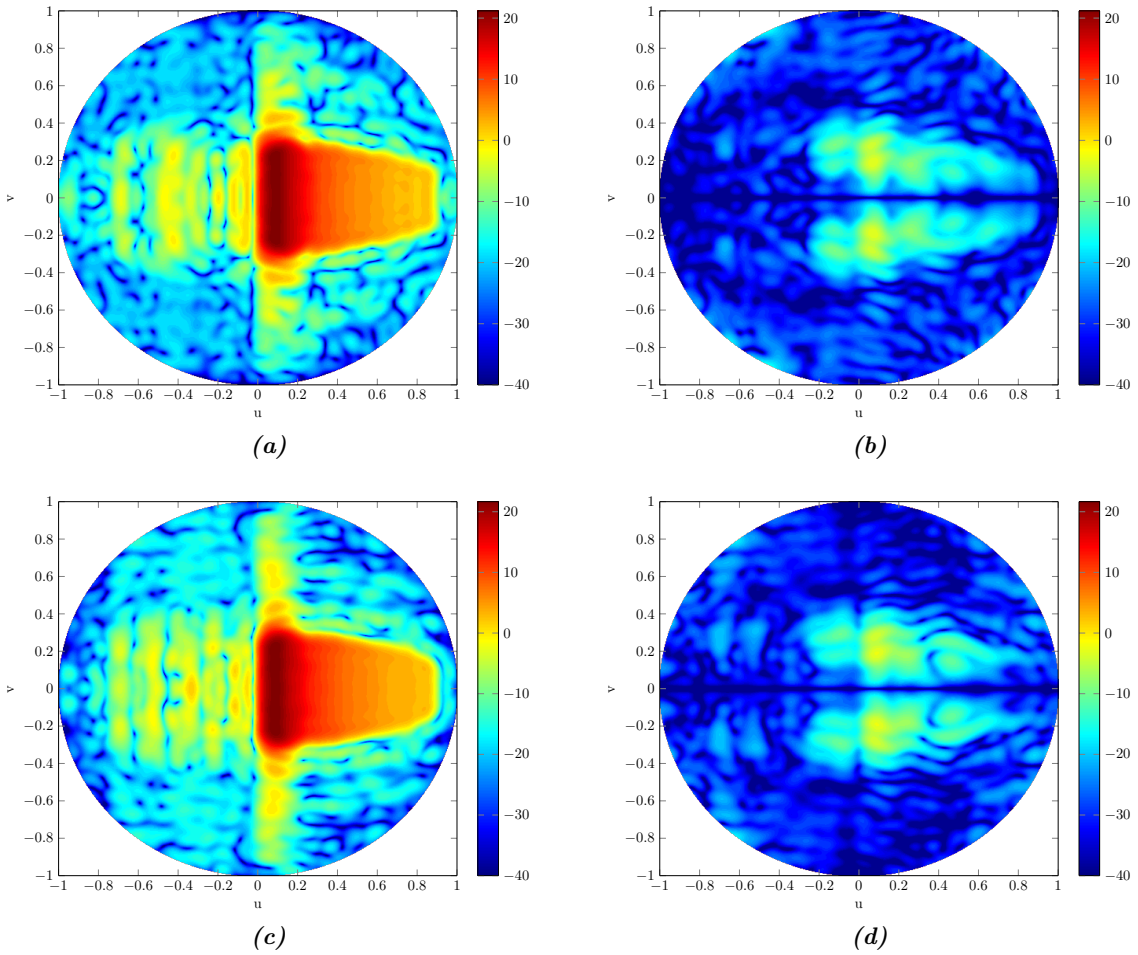

Figure 5.2: *Radiation patterns in gain (dBi) at the starting point. (a) Copolar (X polarization). (b) Crosspolar (X polarization). (c) Copolar (Y polarization). (d) Crosspolar (Y polarization).*

reflectarray. The phase center of the feed horn is placed at $\vec{r}_f = (-94, 0, 214)$ mm. with regard to the center of the reflectarray. The working frequency is 25.5 GHz and the periodicity of the cells is 5.84 mm $\times$ 5.84 mm, which is approximately half a wavelength. The chosen unit cell for the design is the one shown in Figure 5.1. Arlon CuClad 233LX, with $\varepsilon_r = 2.33$, $\tan\delta = 0.0013$ and thickness 0.787 mm has been chosen for the two layers of the substrate. The minimum and maximum crosspolar templates are set 200 dB and 35 dB below the maximum copolar value for both polarizations, respectively.

The starting point for the crosspolar optimization is the POS from [81]. From the phase distribution and using a zero-finding routine, the layout of the reflectarray is found [2]. Then, the algorithm will directly optimize the geometry analyzing the unit cell with MoM. The figure of merit to evaluate the improvement is the difference between the maximum value of the copolar and the crosspolar components, and will be denoted as CP-XP. For the case at hand, the initial CP-XP is 24.89 dB and 24.88 dB for the X and Y polarizations, respectively. Figure 5.2 shows the radiation pattern of the starting point for the X and Y polarizations, being both of them very similar.

The algorithm was tested in two different computers to better appreciate its scalable

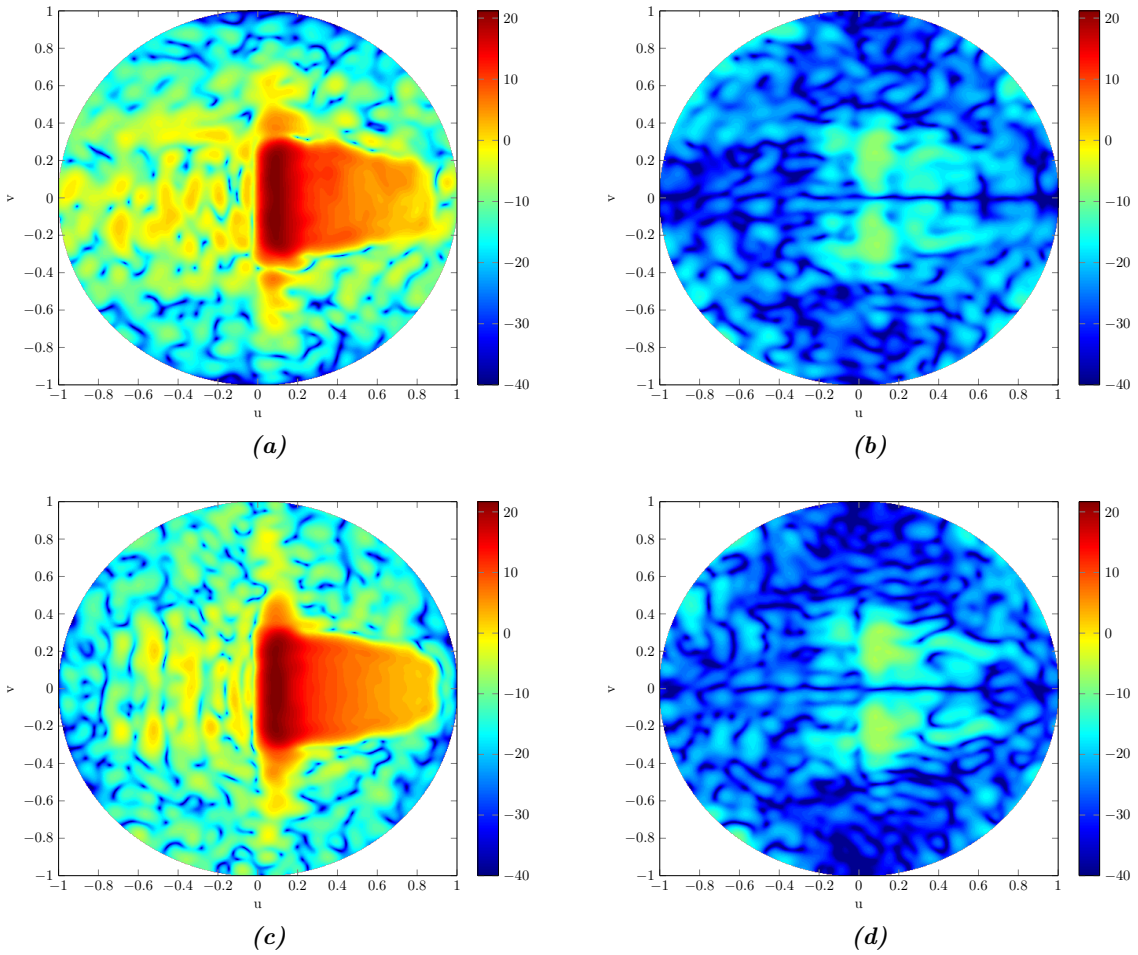

Figure 5.3: *Optimized radiation patterns in gain (dBi). (a) Copolar (X polarization). (b) Crosspolar (X polarization). (c) Copolar (Y polarization). (d) Crosspolar (Y polarization).*

capabilities. The first computer was an Intel Core i3-2100, with two physical and two virtual CPU working at 3.10 GHz, where the algorithm took around 360 seconds per iteration and 4.16 days to complete 999 iterations. The other computer was an Intel Xeon CPU E5-2650 v2 with 16 physical and 16 virtual CPU working at 2.6 GHz. In this case, the algorithm took around 53 seconds per iteration and 14.9 hours to complete 999 iterations.

The results after the optimization are shown in Figures 5.3, 5.4 and 5.5. The gain of the antenna remains the same and the copolar patterns mostly remain within the templates, as it can be seen in Figure 5.4. However, the crosspolar level is reduced. Now, CP-XP is 29.48 dB for X polarization and 28.82 dB for Y polarization, which supposes an improvement of the crosspolar component of 4.59 dB and 3.94 dB for X and Y polarizations, respectively. The reduction in the crosspolar component causes a more even distribution of the crosspolarization level in the whole visible region and the increment of the secondary lobes in the copolar pattern. The copolar radiation pattern for X polarization is slightly affected by the optimization process (compare Figures 5.2 and 5.3), although it almost complies with the specifications. The cost function could include a weighting function in

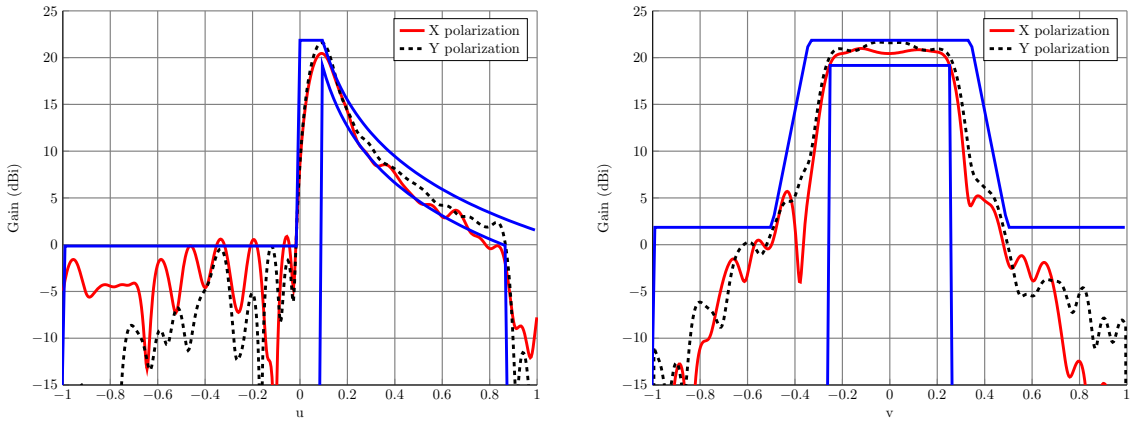

Figure 5.4: *Main cuts of the optimized radiation patterns. (a) Cut along u. (b) Cut along v.*

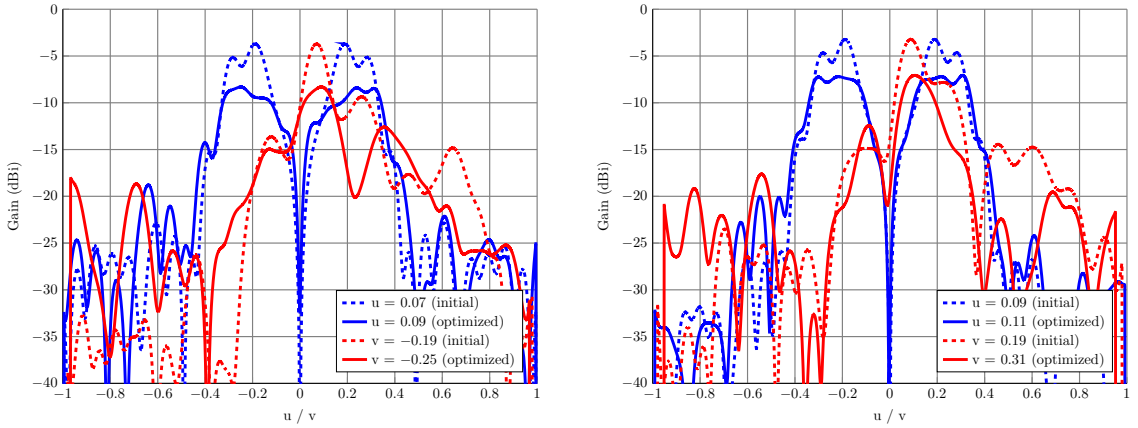

Figure 5.5: *Cuts along u and v of the crosspolar far field before and after the optimization. The cuts are taken at the point where the crosspolar level is maximum for each pattern. (a) X polarization. (b) Y polarization.*

order to balance the crosspolar reduction with the copolar deterioration, in those cases in which the copolar pattern is more affected. Finally, Figure 5.5 shows the crosspolar cuts before and after the optimization, where the crosspolar patterns present their maximum value, showing the reduction in the maximum value of the crosspolar pattern.

5.2.5.2. European DBS coverage

The second test case corresponds to a European DBS coverage shaped beam, as shown in Figure 5.6 [151]. The working frequency is 11.85 GHz and the satellite is placed in a geostationary orbit in position 10° E longitude, 0° latitude. The minimum gain specified in the coverage area is 28 dBi, which has been enlarged to take into account typical pointing errors (0.1° in roll, 0.1° in pitch, and 0.5° in yaw). The coverage shown in Figure 5.6 is specified in the antenna coordinate system and before carrying out the synthesis it needs

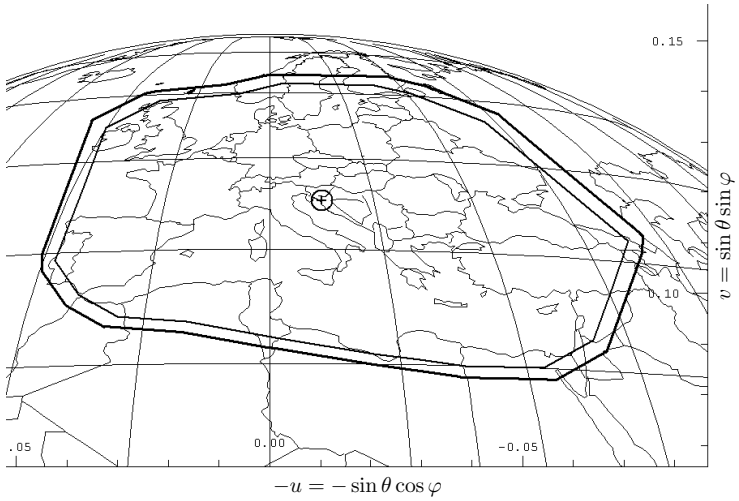

Figure 5.6: *European coverage.* (u, v) *are in the antenna coordinate system.*

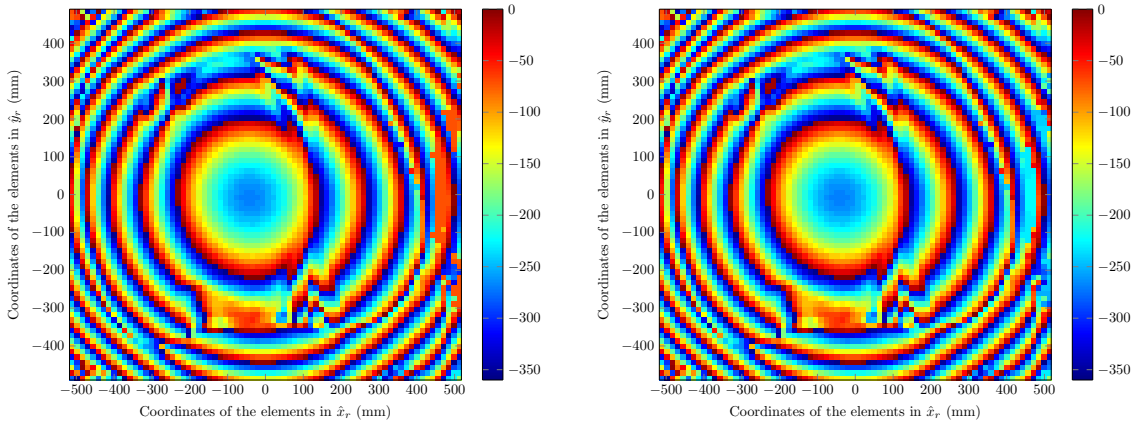

(a) ***(b)***

Figure 5.7: *Distribution phases for the design of the starting point for the reflectarray with European DBS coverage. (a) Polarization X. (b) Polarization Y.*

to be transformed to the reflectarray coordinate system defined in Figure 2.3 [2].

The reflectarray is square and formed by 5180 elements in a regular grid of 74×70 cells. The feed horn is modeled as a $\cos^q\theta$ function [78] with a q-factor of 23, which provides an illumination taper of -17.9 dB at the reflectarray edges. The feed horn is placed at $\vec{r}_f = (358, 0, 1070)$ mm with regard to the reflectarray center. The period of the unit cell is 14 mm $\times$ 14 mm, which is 0.55λ at the working frequency. Now, the substrate for the lower layer has a height of 2.363 mm and a complex relative permittivity $\epsilon_r = 2.55 - j2.295 \cdot 10^{-3}$, while the upper layer has a height of 1.524 mm and a complex relative permittivity $\epsilon_r = 2.17 - j1.953 \cdot 10^{-3}$.

For the starting point, a POS is carried out with the generalized Intersection Approach [89] starting with a properly focused reflectarray. After the POS, the phases shown in Figure 5.7 were obtained. The layout of the reflectarray is obtained using the unit cell shown in Figure 5.1 and a zero-finding routine, in such a way that the phases of ρ_{xx} and ρ_{yy} match the required phase shift for each element as imposed by Figure 5.7 [2].

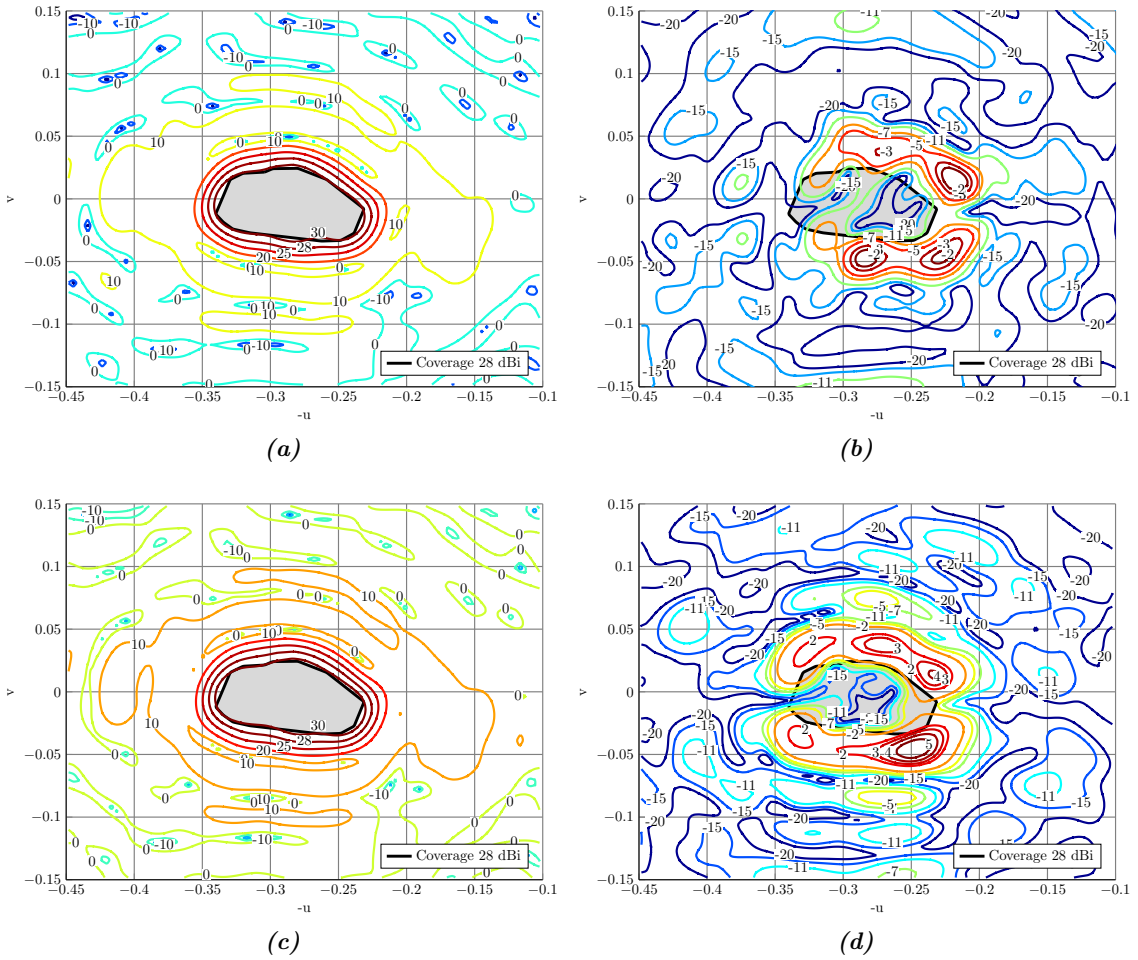

Figure 5.8: *Starting European coverage radiation pattern in gain (dBi) after POS. Gray region specifies the coverage area. (u, v) are in the reflectarray coordinate system. (a) Copolar (X polarization). (b) Crosspolar (X polarization). (c) Copolar (Y polarization). (d) Crosspolar (Y polarization).*

When the layout is simulated with MoM, the radiation patterns of Figure 5.8 are obtained, having 32.60 dBi and 0.88 dBi for the maximum copolar and crosspolar gain, respectively, for X polarization; while for Y polarization those values are 32.74 dBi and 5.98 dBi. As it can be seen, polarization X presents a better starting point for the optimization than the Y polarization.

The optimization is carried out in a region defined by $u \in [0.1, 0.45]$ and $v \in [-0.15, 0.15]$ around the coverage area, with a resolution of the far fields of 512×512 points for the FFT, having a total of 4047 points in the UV grid. All reflectarray elements are optimized at the same time, considering six dipoles as independent optimizing variables ($s = 6$) maintaining the unit cell symmetry, thus having a total number of optimizing variables of 31080. The crosspolar template is set 35 dB below the maximum copolar gain template, and the crosspolar component is scaled by a factor of 10^5 in natural units with the weighting function.

Several attempts were made to optimize the radiation pattern with the LMA-XP for the European DBS coverage, modifying several parameters such as the crosspolar weight

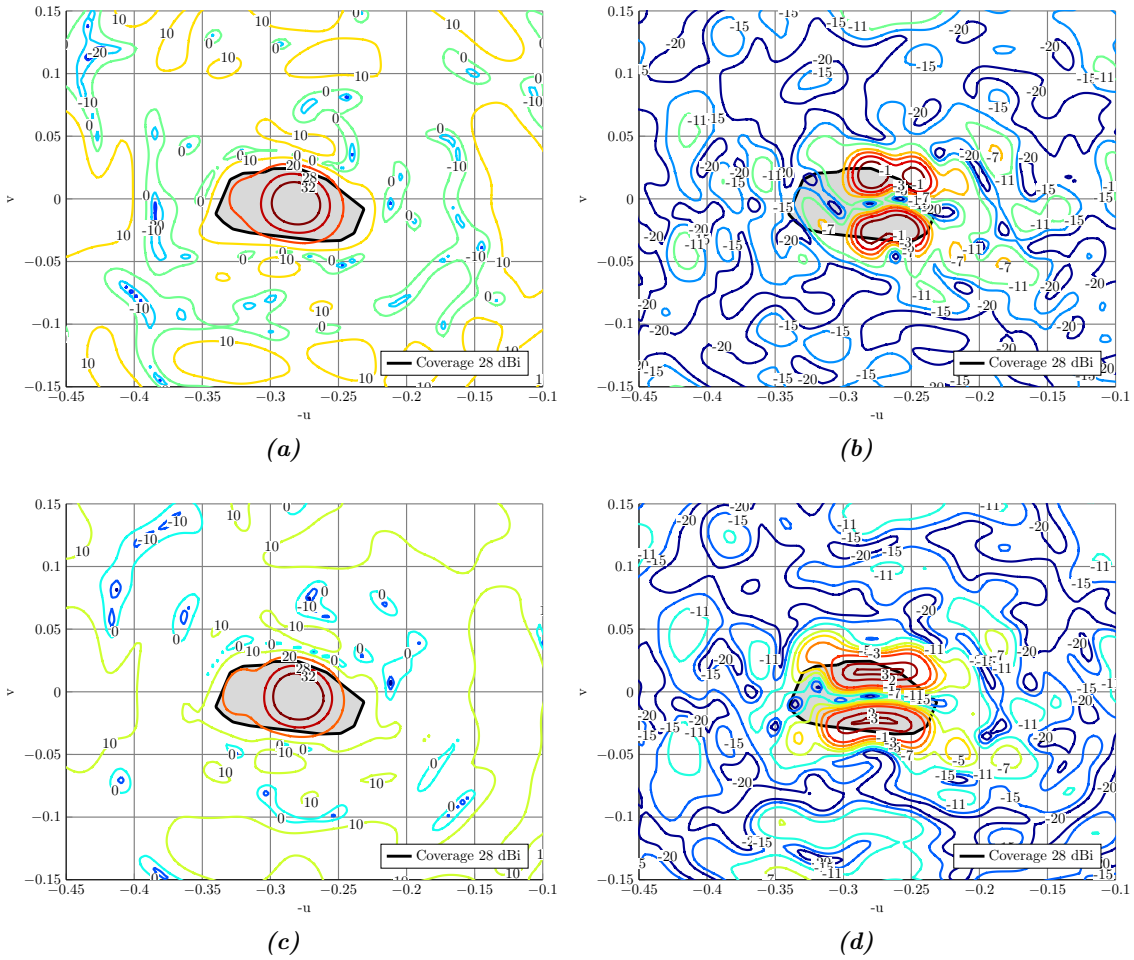

Figure 5.9: *European coverage radiation pattern in gain (dBi) after the optimization with the LMA-XP. Gray region specifies the coverage area. (u, v) are in the reflectarray coordinate system. (a) Copolar (X polarization). (b) Crosspolar (X polarization). (c) Copolar (Y polarization). (d) Crosspolar (Y polarization).*

in the cost function, allowing more ripple in the coverage zone and allowing higher side lobes in the copolar pattern, without obtaining good results. In all instances the algorithm converged to undesired local minima, obtaining similar and poor results. As an example, Figure 5.9 shows the results when the crosspolar template was set 30 dB below the maximum copolar gain, the allowed ripple in the copolar pattern was 3 dB and the side lobe levels were set 15 dB below the maximum copolar level, all set to facilitate convergence. The crosspolar pattern was scaled by a factor of 10^4 in natural units. The results shown belong to iteration 178 of the LMA-XP. (Original specifications for the optimization were: crosspolar template 35 dB below the maximum copolar value, copolar ripple of 2 dB, side lobe levels of -30 dB and scaling factor for the crosspolar component of 10^5 in natural units, for which the algorithm also diverged with similar results.) As it can be seen comparing Figures 5.8 and 5.9, the crosspolar component for Y polarization reduced its maximum value from 5.98 dB to 3.08 dB, although the crosspolar pattern for X polarization deteriorated, increasing its maximum original value of -0.88 dB to 1.27 dB, while the coverage area was seriously affected for both polarizations, not fulfilling specifications

in most of the area.

It is important to note that, regardless of possible improvements in the crosspolar levels, if the coverage area is affected as much as in this case, the obtained layout would not be useful. In addition, the maximum crosspolar values were outside the coverage area before the optimization, as it can be seen in Figure 5.8. However, after the optimization, even though in the case of Y polarization this value is reduced, is now situated, for both polarizations, inside the coverage area, which seriously penalizes the performance of the antenna.

5.2.6. Conclusions and discussion

The Levenberg-Marquardt algorithm has been adapted to optimize the crosspolar component of reflectarray antennas using MoM based on local periodicity in the computations. Because the MoM routine is slow, the algorithm has been fully optimized in order to take advantage of the resources available. In particular, all building blocks of the algorithm have been conveniently parallelized and optimized in order to reduce the number of MoM calls. An optimization has been carried out in two different computers in order to assess the scalability of the proposed technique. An LMDS radiation pattern has been chosen as a test case in which the crosspolar far field has been reduced 4.59 dB and 3.94 dB for the X and Y polarizations, respectively, while mostly preserving the copolar pattern within specifications.

Another example of a reflectarray with a European coverage for DBS applications was tested. The reflectarray was comprised of 5180 elements and 31080 variables were optimized. However, the algorithm converged to undesired local minima and poor results were obtained. Several optimizations were tried to optimize this configuration, always obtaining similar poor results. Despite the good results optimizing the crosspolar component of a small-sized reflectarray, the algorithm does not provide good results when confronted to larger reflectarrays due to the high number of variables involved. This happens due to local minima which the LMA encounters during the optimization process. It could be partially solved by employing a similar mechanism in the IA-POS, in which the number of degrees of freedom was reduced by increasing the q-factor in the feed model. Here, the number of optimizing variables could be reduced, resulting in a similar approach. Furthermore, by reducing the number of optimizing variables not only the degrees of freedom are reduced, hence reducing the amount of local minima; but also the computing times and memory usage. However, as it was mentioned in the previous chapter when describing the LMA, it performs a non-convex optimization due to the non-convexity of the lower bound used in the cost function [152, 153]. This problem will limit the performance of the algorithm for large reflectarrays, even when the strategy of reducing the number of optimizing variables is employed.

A better strategy is proposed to overcome the limitations of the LMA-XP for large reflectarrays, which consists in using another algorithm in order to improve the convergence properties of the LMA. For that purpose, a generalized Intersection Approach algorithm for the crosspolar optimization of reflectarrays with MoM based on local periodicity is

described and compared with the LMA-XP detailed in this section.

5.3. The generalized Intersection Approach for direct crosspolar optimization

In this section, the Intersection Approach framework is employed in a more generalized approach [89] in order to improve the convergence for the crosspolar optimization of reflectarrays by working directly with MoM. Although the IA was extensively detailed in a previous chapter, first for POS and later for the synthesis of R^{mn} matrices (IA-POS and IA-XP, respectively), it will be briefly summarized again from the point of view of improving its convergence properties.

5.3.1. Convergence improvement

The IA considers two sets, the set of the radiation patterns that can be obtained with the reflectarray (set $\mathcal{R}$) and the set of radiation patterns that comply with the specifications (set $\mathcal{M}$). At each iteration of the algorithm, the following operation is performed:

$$\vec{E}_{i+1} = \mathcal{B}\left[\mathcal{F}\left(\vec{E}_i\right)\right], \tag{5.11}$$

where $\vec{E}$ is the radiated far field by the antenna. $\mathcal{F}$ is the forward projector which projects the far field radiated by the antenna (belonging to the $\mathcal{R}$ set) onto the set of fields that comply with the specifications ($\mathcal{M}$ set). Conversely, $\mathcal{B}$ is the backward projector which projects the far field that fulfills the specifications onto the set of far fields that can be radiated by the reflectarray. The goal of (5.11) is to find a radiation pattern that belongs simultaneously to both sets, or if that is not possible, to find a radiation pattern whose distance to the set of patterns that fulfill the requirements is minimal. Also, the IA is a local optimizer and as such the starting point is of the utmost importance since it will determine the correct converge of the algorithm [89].

The potential local minima reached by local optimizers are commonly known as traps. In the IA framework, there are two main sources of traps [89]: the number of degrees of freedom, which in this case will be the number of optimizing variables; and the non-convexity of the involved sets. The latter problem can be addressed by working with the squared field amplitude instead of the field itself. The gain is also suitable since it is proportional to the squared field amplitude,

$$G \propto \left|\vec{E}\right|^2, \tag{5.12}$$

and the specifications are usually given in gain. This improves the convergence of the algorithm since it convexifies the set $\mathcal{M}$ of radiation patterns that comply with the specifications [89]. However, this leads to a redefinition of the backward projector in the IA-POS and IA-XP since the FFT cannot be used anymore. It causes the algorithm to lose the efficiency derived from the FFT being the most time consuming operation, and

needing to use some optimization algorithm, which in the case of the present thesis is the LMA.

For the first problem the solution is to reduce the number of variables in the first steps of the synthesis process. This has been implemented in the IA-POS with a fictitious reduction of variables modifying the illumination taper of the feed [95]. Nevertheless, since the reflectarray geometry is optimized with the LMA, the variable reduction is not fictitious anymore, since one can choose which variables will be optimized and which will not.

In order to alleviate the notation, the compact notation for both polarizations will be avoided and generic gains and templates will be used when possible, although keeping in mind that the process is done for both polarizations and components of the far field.

5.3.2. Forward projection

The forward projector is divided in two steps, being the first one optional. In the first step, the templates are normalized to the value of the gain of the far fields in a given direction. Then, the fields are trimmed using those normalized templates, obtaining a far field which complies with the specifications, but cannot, in general, be radiated by a passive reflectarray.

The requirements of the copolar radiation pattern are usually given in gain, with a maximum and minimum value. If these templates remain unaltered (i.e., the first step is skipped), the synthesis is carried out in *fixed gain*. This method can be useful to further refine a previous synthesis. Alternatively, they can be normalized to the gain in a given (u_0, v_0) direction which belongs to the maximum gain region. It is then said that the synthesis is carried out in *float gain* [95]. This method is more useful when a synthesis is started from scratch (e.g. when doing POS) since it adapts automatically the templates to the maximum gain that can be obtained with the reflectarray. In this case, a normalizing constant is defined as

$$C_n = \frac{G_{\mathrm{cp}}\left(u_0, v_0\right)}{T_{\mathrm{av}}}, \tag{5.13}$$

where T_{av} is the average value of the maximum and minimum copolar templates in the (u_0, v_0) direction

$$T_{\mathrm{av}} = \frac{T_{\mathrm{cp,max}}(u_0, v_0) + T_{\mathrm{cp,min}}(u_0, v_0)}{2}. \tag{5.14}$$

C_n is defined for both polarizations independently to adapt the template to the current gain of each polarization. Then, it is applied to both copolar and crosspolar templates as

$$T^n_{\mathrm{cp}}(u, v) = T_{\mathrm{cp}}(u, v) \cdot C_n, \tag{5.15a}$$

$$T^n_{\mathrm{xp}}(u, v) = T_{\mathrm{xp}}(u, v) \cdot C_n. \tag{5.15b}$$

The normalization in (5.15) is applied to the minimum and maximum templates of both polarizations. This normalization process sets the middle point of the templates at (u_0, v_0) at the same level of the gain in that direction.

Once the templates have been normalized, both components of the radiated field should accomplish the following condition in both polarizations

$$T^n_{\mathrm{cp,min}}(u,v) \leq G_{\mathrm{cp}}(u,v) \leq T^n_{\mathrm{cp,max}}(u,v), \tag{5.16a}$$

$$T^n_{\mathrm{xp,min}}(u,v) \leq G_{\mathrm{xp}}(u,v) \leq T^n_{\mathrm{xp,max}}(u,v). \tag{5.16b}$$

This condition can be fulfilled by the P_r operator, defined for all (u,v) as follows for a generic gain G,

$$P_r\left(G\right) = \begin{cases} T^n_{\max}(u,v), & T^n_{\max}(u,v) < G(u,v) \\ T^n_{\min}(u,v), & T^n_{\min}(u,v) > G(u,v) \\ G(u,v), & \text{otherwise,} \end{cases} \tag{5.17}$$

The result of this operation is the gain G',

$$G'(u,v) = P_r\left(G(u,v)\right). \tag{5.18}$$

For the sake of simplicity, a generic G gain component and normalized template T^n were used in (5.17) and (5.18), but they should be applied to the copolar and crosspolar components of both polarizations with their respective normalized templates. Also, the forward projector only works with the gain (which is proportional to the squared field amplitude) and the far field phase does not play any role, being able to take any value. In contrast to the IA-POS and IA-XP, where the far field phase remained unchanged, now there is no such constraint, improving the converge of the algorithm.

5.3.3. Backward projection

Since the forward projection works with the squared field amplitude (gain) instead of the field itself, the FFT to recover the source field cannot be used. In any case, since the goal is to directly optimize the geometry of the reflectarray to improve the crosspolar far field, an optimization algorithm will be used. Now, the $\mathcal{B}$ operator is defined as the minimization of the distance of an element $m \in \mathcal{M}$ to the set $\mathcal{R}$,

$$\mathrm{dist}\left(m, \mathcal{R}\right). \tag{5.19}$$

For the minimization of the distance in (5.19), at this stage we have the element m as the trimmed gain $G'(u,v)$ of (5.18) and the current reflectarray geometry which generates a gain pattern that belongs to the $\mathcal{R}$ set, $G(u,v)$. As a distance definition, the Euclidean norm for square-integrable functions can be used, which can be easily implemented by the weighted Euclidean metric

$$d = \mathrm{dist}^2\left(G'(u,v),\ G(u,v)\right) = \iint_{\Omega} w(u,v)\left(G'(u,v) - G(u,v)\right)^2 du\, dv, \tag{5.20}$$

where $w(u,v)$ is a weighting function and Ω is the area belonging to the visible region

$(u^2+v^2 \leq 1)$ where the far fields are optimized. This area can be the whole visible region or located around the coverage zone. Since the radiated fields are already discretized in the UV grid, the integral in (5.20) can be approximated by a sum for the UV points which lie in Ω,

$$d = \sum_{u,v} w(u,v) \left(G'(u,v) - G(u,v)\right)^2 \Delta u \, \Delta v = \sum_{u,v} \left[C(u,v) \left(G'(u,v) - G(u,v)\right)\right]^2, \quad (5.21)$$

where

$$C(u,v) = \sqrt{w(u,v)\Delta u \Delta v}, \quad (5.22)$$

and Δu and Δv are the steps in the discretized UV grid in u and v, respectively.

On the other hand, the LMA minimizes cost functions of the form [101]

$$F(x) = \sum_{i=1}^{M} \left(r_i(x)\right)^2, \quad (5.23)$$

where $r(x)$ is known as residual, which is discretized in M points. Comparing (5.21) with (5.23) it is clear that

$$r(u,v) = C(u,v) \left(G'(u,v) - G(u,v)\right), \quad (5.24)$$

so the LMA naturally minimizes the distance between the two gain patterns.

The generic gains G and G' need to accommodate the copolar and crosspolar components for both polarizations. They can be implemented as vectors of size $4M \times 1$, where M is the number of points in which each component of the gain is discretized. Also, since the relative value of the crosspolar component is significantly lower than the copolar gain, in order to properly reduce its starting value it might be convenient to scale the crosspolar residual by means of the weighting function contained in $C(u,v)$. Finally, it is not necessary to attain a minimum (generally local) of (5.19), only to decrease the distance at each iteration of the IA, so very few iterations of the LMA are needed.

The LMA described in the previous chapter is used here to directly optimize the reflectarray geometry. It also includes the optimizations described in this very same chapter when it was used in a standalone version (known as LMA-XP) to directly optimize the reflectarray geometry. The only change in the LMA is the definition of cost function, which now is (5.21). The implemented new algorithm is now known as IA-LMA-XP and is able to handle thousands of optimizing variables obtaining good results due to its improved convergence properties derived from the use of the squared field amplitude and the elimination of the far field phase constraint (which now can take any value), provided a suitable starting point. Also, in order to control computing times and memory usage, the number of optimizing variables can be reduced as well as the number of points in the UV grid where the optimization is performed, carrying it out, for instance, only around the coverage area instead of in the whole visible region.

5.3.4. Validation

In order to validate the algorithm described in this section, two shaped patterns for satellite applications are optimized in order to lower their crosspolar levels while maintaining the copolar pattern within specifications. The patterns are an isoflux pattern for global Earth coverage and a European coverage for DBS application [151]. In both cases, a POS is done using the IA-POS [95] and then a design is obtained following [2], using the reflectarray element of Figure 5.1. The unit cell is comprised of two layers of metallizations with four parallel and coplanar dipoles for each polarization, and is described in detail in [43, 127].

These two designs are used as starting point for the crosspolar optimization. The copolar template is the same as the one used in the POS, and the crosspolar template is defined as a certain constant value below the maximum copolar level, for the whole region where the optimization is carried out.

5.3.4.1. Isoflux pattern

The first test case is an isoflux pattern for global Earth coverage. In Chapter 3 was detailed how to obtain a parametrized isoflux pattern, which in this case has been particularized for $\theta_0 = 20°$, a geostationary orbit, side lobe level 19 dB below the maximum copolar level and 0.35 dB of allowable ripple in the coverage area.

The reflectarray is circular, with 1020 total elements placed in a rectangular grid with 36 elements along the diameter in both reflectarray axes. The feed horn is modeled as a $\cos^q \theta$ function [78] with a q-factor of 14.8, which provides an illumination taper of -12 dB at the reflectarray edges. The feed horn is placed at $\vec{r}_f = (40, 0, 195)$ mm with regard to the reflectarray center. The working frequency is 30 GHz and the period of the unit cell is 5 mm $\times$ 5 mm (0.5λ). The substrate for both layers of the unit cell is the same, with a height of 0.787 mm and a complex relative permittivity $\epsilon_r = 2.33 - j3.029 \cdot 10^{-3}$. The starting point for the crosspolar optimization is the POS carried out in Chapter 3, whose phases are shown in Figure 3.8. A design using the cell of Figure 5.1 is done following [2], which will be optimized.

The optimization is carried out in the whole visible region, with a resolution of the far fields of 256×256 points for the FFT, having a total of 51543 points in the UV grid and using the First Principle of Equivalence. All of the reflectarray elements are optimized at the same time, considering all dipoles as independent optimizing variables ($s = 8$), so the total number of optimizing variables is 8160. The optimization is carried out in fixed gain, setting the required gain to 18.35 dB in the center of the coverage zone. The crosspolar template is set 35 dB below the maximum copolar gain template, and the crosspolar component is scaled by a factor of 100 in natural units with the weighting function. The LMA is set to perform three iterations per iteration of the IA.

The results obtained after the optimization are compared to the starting point in Figures 5.10 and 5.11. On the one hand, Figure 5.10 shows the results for the copolar pattern. There were two goals: to maintain the copolar specification (isoflux shape) while reducing the crosspolar component, and to increase the gain for Y polarization while maintaining the X polarization gain. As it can be seen, the starting point has around

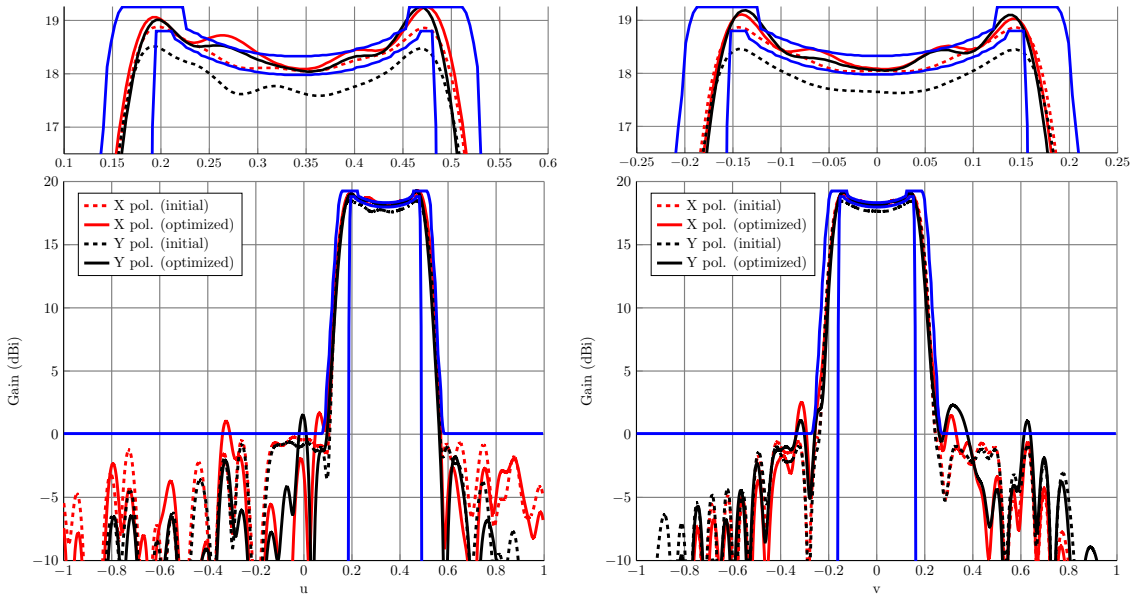

(a) *(b)*

Figure 5.10: *Main cuts for the copolar pattern for both polarizations before and after the crosspolar optimization. The copolar gain for Y polarization is increased during the optimization. (a) Cut along u for $v = 0$. (b) Cut along v for $u = 0.34$.*

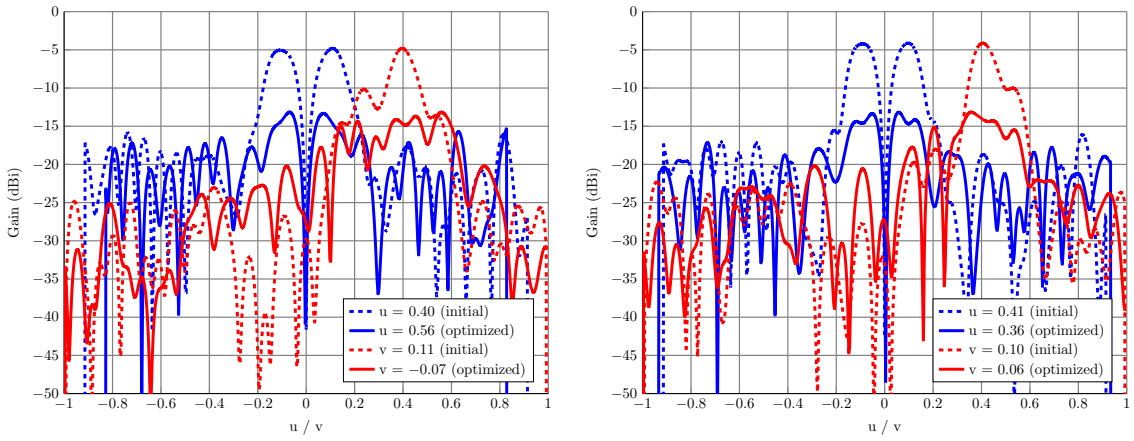

(a) *(b)*

Figure 5.11: *Cuts along u and v of the crosspolar far field before and after the optimization. The cuts are taken at the point where the crosspolar level is maximum for each pattern. (a) X polarization. (b) Y polarization.*

0.4 dB less in gain for Y polarization than the other in the coverage area. However, after the optimization, the gains for both polarizations become similar while mostly preserving the copolar shape within specifications.

On the other hand, Figure 5.11 shows some cuts in (u, v) of the crosspolar patterns. The cuts correspond to the points were the crosspolar is maximum, for both polarizations, even though they are not the same for the patterns before and after the optimization. For the X polarization, the initial maximum crosspolar level is -4.81 dBi, and is reduced by 8.36 dB to -13.17 dBi after the optimization. For the Y polarization, initially there is

a maximum level of −4.12 dBi for the crosspolar component and is reduced an amount of 9.05 dB to −13.17 dBi. This important crosspolar reduction is achieved while keeping the gain of the copolar pattern (and slightly increasing it in the case of Y polarization) and its shape. The trade-off is a slight increase in the side lobes, as seen in Figure 5.10 and a redistribution of the lobes in the crosspolar component, which is now more uniform towards higher levels in the whole UV grid.

5.3.4.2. European DBS coverage

The second test case corresponds to a European DBS coverage shaped beam, as shown in Figure 5.12 [151]. The working frequency is 11.85 GHz and the satellite is placed in a geostationary orbit in position 10° E longitude, 0° latitude. The minimum gain specified in the coverage area is 28 dBi, which has been enlarged to take into account typical pointing errors (0.1° in roll, 0.1° in pitch, and 0.5° in yaw). The coverage shown in Figure 5.12 is specified in the antenna coordinate system and before carrying out the synthesis it needs to be transformed to the reflectarray coordinate system defined in Figure 2.3 [2].

The reflectarray is square and formed by 5180 elements in a regular grid of 74 × 70 cells. The feed horn is modeled as a $\cos^q\theta$ function [78] with a q-factor of 23, which provides an illumination taper of −17.9 dB at the reflectarray edges. The feed horn is placed at $\vec{r}_f = (358, 0, 1070)$ mm with regard to the reflectarray center. The period of the unit cell is 14 mm × 14 mm, which is 0.55λ at the working frequency. Now, the substrate for the lower layer has a height of 2.363 mm and a complex relative permittivity $\epsilon_r = 2.55 - j2.295 \cdot 10^{-3}$, while the upper layer has a height of 1.524 mm and a complex relative permittivity $\epsilon_r = 2.17 - j1.953 \cdot 10^{-3}$.

The optimization is carried out in a region defined by $u \in [0.1, 0.45]$ and $v \in [-0.15, 0.15]$ around the coverage area, with a resolution of the far fields of 512×512 points for the FFT, having a total of 4047 points in the UV grid. All reflectarray elements are optimized at the same time, considering six dipoles as independent optimizing variables ($s = 6$) maintaining the unit cell symmetry, thus having a total number of optimizing variables of

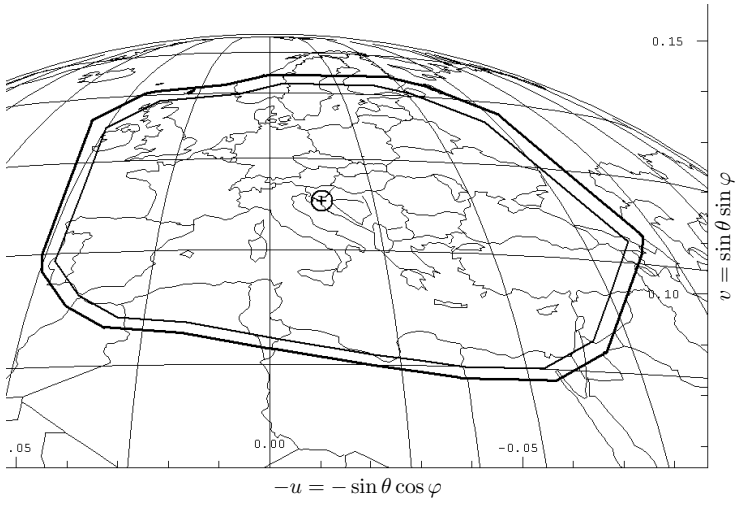

Figure 5.12: *European coverage. (u, v) are in the antenna coordinate system.*

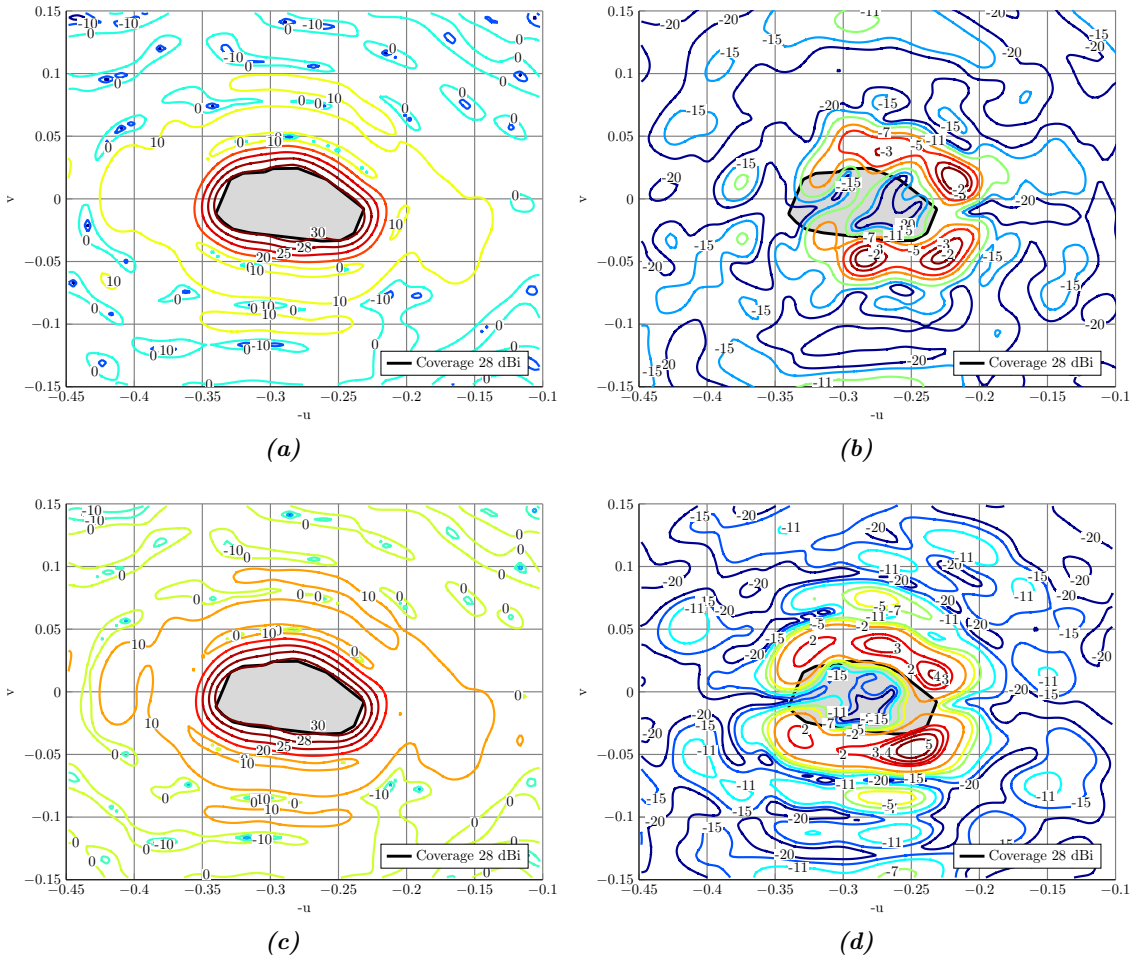

Figure 5.13: *Starting European coverage radiation pattern in gain (dBi) after POS. Gray region specifies the coverage area. (u, v) are in the reflectarray coordinate system. (a) Copolar (X polarization). (b) Crosspolar (X polarization). (c) Copolar (Y polarization). (d) Crosspolar (Y polarization).*

31080. The optimization is carried out in fixed gain, setting the required gain to 31.90 dB in the direction $(u_0, v_0) = (0.28, 0)$, allowing a ripple of 2 dB. The crosspolar template is set 35 dB below the maximum copolar gain template, and the crosspolar component is scaled by a factor of 10^5 in natural units with the weighting function. The LMA is set to perform three iterations per iteration of the IA.

The starting point is the same as the one used in the LMA-XP optimization, where the obtained phases after the POS are shown in Figure 5.7. After the layout was obtained using the unit cell of Figure 5.1, the simulated radiation patterns with MoM are shown again in Figure 5.13 for both linear polarizations. The gain requirements are fulfilled in the whole extended coverage region (see Figure 5.12), having a maximum copolar gain of 32.60 dBi and maximum crosspolar gain of -0.88 dBi for X polarization, while for Y polarization those values are 32.74 dBi and 5.98 dBi for the maximum copolar and crosspolar gain, respectively. As it can be seen, the starting point for Y polarization is much worse than for X polarization, since the crosspolar pattern has a maximum value almost 7 dB higher.

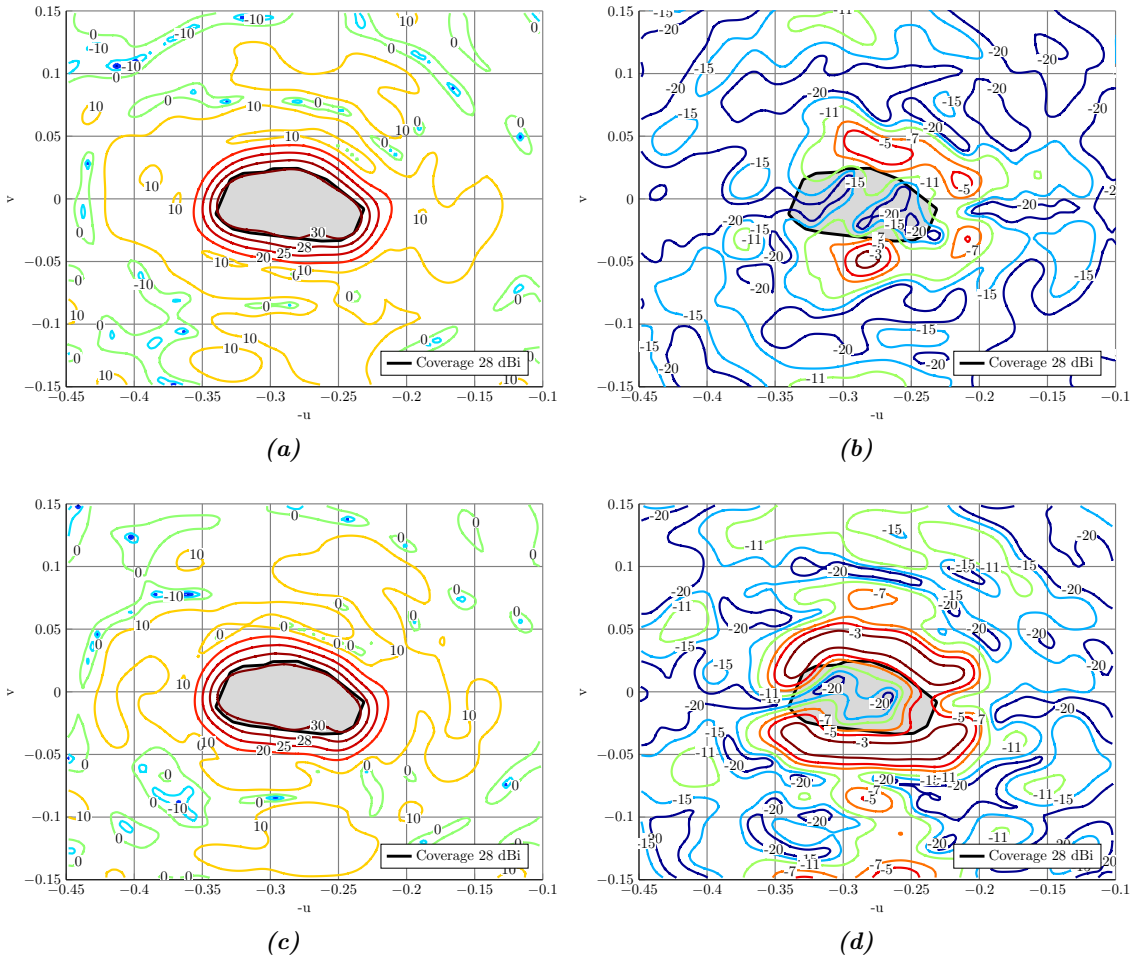

Figure 5.14: *Optimized European coverage radiation pattern in gain (dBi) with the IA-LMA-XP. Gray region specifies the coverage area. (u, v) are in the reflectarray coordinate system. (a) Copolar (X polarization). (b) Crosspolar (X polarization). (c) Copolar (Y polarization). (d) Crosspolar (Y polarization).*

Figure 5.14 shows the optimized radiation pattern for both polarizations. For X polarization, the coverage zone is barely affected, and presents a maximum copolar gain of 32.13 dBi and a maximum crosspolar gain of −2.20 dBi (reduced an amount of 1.32 dB). In the case of the Y polarization, the maximum copolar gain is 31.47 dBi while the maximum crosspolar gain is −2.20 dBi. Paying attention to the 30 dB contour, the pattern is slightly worsen, but the specifications comply for a gain of 28 dBi in the whole coverage region, while the maximum crosspolar gain has been substantially reduced (an amount of 8.18 dB).

A better parameter to analyze the crosspolar component of the radiation pattern is the crosspolar discrimination (XPD), which is defined, for the coverage area, as the difference, point by point, of the copolar and crosspolar components in dBi. Figure 5.15 shows the XPD before and after the optimization for both polarizations. Due to the initial low value for the crosspolar component, the $\mathrm{XPD}_{\mathrm{min}}$ for X polarization is 33.46 dB, and it barely improves after the optimization, obtaining a value of 33.94 dB (0.48 dB higher). However, for Y polarization, the initial value of $\mathrm{XPD}_{\mathrm{min}}$ was 25 dB and it improved to

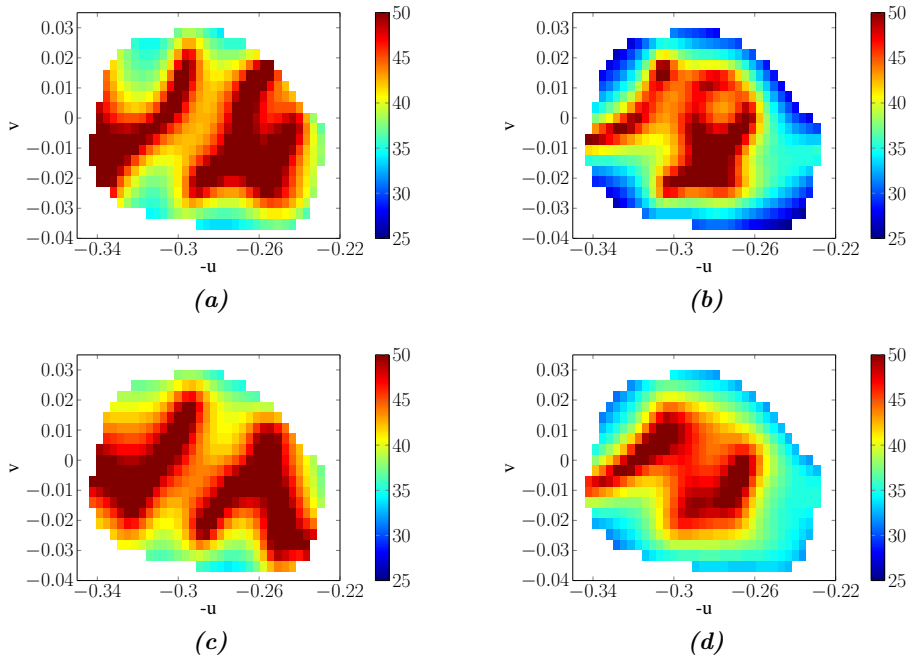

Figure 5.15: *XPD before and after the optimization for the European coverage shaped beam. (a) Pol. X before ($XPD_{\min} = 33.46$ dB). (b) Pol. Y before ($XPD_{\min} = 25.00$ dB). (c) Pol. X after ($XPD_{\min} = 33.94$ dB). (d) Pol. Y after ($XPD_{\min} = 30.76$ dB).*

30.76 dB after the optimization (5.76 dB higher), despite defining the crosspolar template as a constant value in a bigger region than the coverage zone and not directly optimizing the XPD parameter.

Another parameter, stricter than XPD, is the crosspolar isolation (XPI), which is defined, for the coverage area, as the difference between the minimum copolar gain and the maximum crosspolar gain, both in dBi. For the case at hand, the initial XPI is 32.06 dB and 23.88 dB for X and Y polarizations, respectively. After the optimization, the new values for XPI are 32.62 dB (improvement of 0.56 dB) and 29.73 dB (improvement of 5.85 dB), for X and Y polarizations, respectively. As it happened to the XPD parameter, the XPI is greatly improved for Y polarization, but not for X polarization, since the starting point was already good.

5.3.5. Convergence improvement over the LMA-XP

The main goal of switching from the LMA-XP to the IA-LMA-XP was to improve the convergence of the algorithm, to obtain better results in less iterations and to be able to handle larger problems with success. The two examples shown to validate the IA-LMA-XP proof the latter assertion. In order to compare both algorithms, a number of optimizations were carried out for a LMDS pattern for different UV grid points and the same number of optimizing variables. While the LMA-XP was only tried once for a UV grid of 128×128, the IA-LMA-XP was tried for larger grids. The antenna specifications and starting point for the optimization are the same as the ones described in Section 5.2.5.1 for the optimization of the LMDS pattern with the LMA-XP.

Table 5.1: *Comparison between the LMA-XP and IA-LMA-XP algorithms for the crosspolar optimization of a reflectarray antenna with LMDS pattern using a full-wave analysis based on local periodicity.*

UV grid	# it	CPx (dB)	XPx (dB)	CPy (dB)	XPy (dB)
128×128	1	20.52	−3.44	21.15	−2.94
256×256	1	20.52	−3.41	21.17	−2.89
512×512	1	20.54	−3.41	21.17	−2.89
1024×1024	1	20.54	−3.40	21.17	−2.89
LMA-XP 128	659	20.42	−8.44	20.81	−6.99
IA-LMA-XP 128	177	20.78	−10.59	21.06	−9.82
IA-LMA-XP 256	219	20.76	−10.82	21.04	−10.59
IA-LMA-XP 512	120	20.83	−9.82	21.06	−8.89
IA-LMA-XP 1024	69	20.66	−7.05	21.00	−5.71

Table 5.1 shows the comparison between the two algorithms. The column with the number of iterations correspond to the LMA iterations in the IA-LMA-XP, which was set to perform three iterations per iteration of the IA. This column represents the iteration at which the algorithm was stopped. The values of the copolar and crosspolar patterns for both polarizations represent the maximum value in the whole visible region. As it can be seen, the IA-LMA-XP provides better results in less iterations than the LMA-XP, due to the improved convergence properties. For the heavier optimizations of the IA-LMA-XP, with UV grids of 512×512 and 1024×1024 points, the optimizations were stopped earlier due to the large amounts of time that they were taking. However, for the 512×512 grid the results were already better than those of the LMA-XP, and for the biggest grid, although they still did not reach those of the LMA-XP, they were quite close with a tenth of the iterations performed. If the last optimization would have been left more iterations, it would improve the results of the LMA-XP.

5.4. Conclusions

In this chapter, the crosspolar optimization of reflectarray antennas by directly optimizing the reflectarray element geometry has been addressed. First, the LMA was used, taking advantage of all the improvements introduced in the previous chapter, along with some new to minimize the impact of MoM in the optimization process. The algorithm, known as LMA-XP, was tested with a LMDS pattern, obtaining good results in the crosspolar optimization. However, since the cost function represents a non-convex search space, it presents convergence problems for larger reflectarrays, since the number of local minima grows exponentially with the number of optimizing variables. This was confirmed trying to optimize a large reflectarray comprised of 5180 elements, optimizing more than 30000 variables at the same time. The algorithm always converged to non-desired local minima, obtaining very poor results.

In order to address the convergence issue, it was decided to use a generalization of

the IA, working with the squared field amplitude, which convexifies the set of radiation patterns that comply with the specifications. Although it does not convexify the whole problem, it certainly alleviates the trap issue, as it was demonstrated with the two test cases which are provided. Due to the improved convergence, the algorithm is able to handle thousands of optimizing variables and still obtain good results in crosspolar optimization. An isoflux pattern for global Earth coverage and a European coverage for DBS application were optimized in order to validate the developed algorithm. In both cases good results were obtained, and in the DBS coverage, the crosspolar component was reduced several dB optimizing more than 30 thousand variables, while maintaining the copolar shape within specifications.

The LMA-XP and IA-LMA-XP were compared to assess the improved convergence achieved by the IA-LMA-XP. It was shown that not only is the IA-LMA-XP capable of handling large problems (as demonstrated with the optimization of the large reflectarray for DBS applications), but it also provides better results in less iterations than the LMA-XP, which makes it a more suitable algorithm for the crosspolar optimization of reflectarray antennas.

CHAPTER 6

Conclusions and future research lines

6.1. Final conclusions

This thesis has been devoted to the development of efficient and accurate techniques for the analysis and synthesis of reflectarray antennas for both far field and near field applications. With regard to the improvement of the analysis techniques, the efficient approach to the far field computation of reflectarray antennas is based on the use of the Fast Fourier Transform (FFT) algorithm, since it is able to compute the spectrum functions faster than a direct implementation of the equations. Also, the accuracy was improved by considering each element of the reflectarray a small rectangular aperture, instead of a punctual isotropic source. However, this analysis was only available for periodic reflectarrays in the literature. When aperiodic reflectarrays were considered, there were two options. An accurate analysis considering small apertures as the elements meant a slow computation of the spectrum functions, since there was no efficient technique for their computation. For an efficient analysis using the Non-Uniform FFT (NUFFT), the elements were considered to be punctual isotropic sources, loosing accuracy. For the first time, a new formulation has been developed that allows to efficiently compute the spectrum functions (and thus the far fields) of aperiodic reflectarrays employing the NUFFT algorithm and modeling each reflectarray element as small rectangular apertures. Furthermore, since the NUFFT is a generalization of the FFT algorithm, it can also be applied to the periodic case overcoming one limitation of the FFT use, that is, the impossibility of efficiently computing the far fields in the whole visible region when the periodicity of the reflectarray is larger than half a wavelength.

The reflectarray analysis also assumes a constant incident field on the surface of each element (modeled as a small aperture). This assumption is convenient because it facilitates the analytical operations with the equations. In this thesis, a generalization of this approach has been proposed, considering a continuous incident field on each cell. In the new formulation, the field at each cell is considered to be narrowband since its variation is

smooth in a period of the reflectarray. Thus, it is possible to represent such incident field by means of its Fourier coefficients. Then, following a similar development as when the incident field was constant, the spectrum functions could be computed as a linear combination of FFT for the periodic case, or a linear combination of NUFFT in the aperiodic case. This new analysis technique could improve the characterization of secondary lobes and crosspolar component of the radiated far fields.

When computing the far fields radiated by aperture antennas, three Principles of Equivalence can be used, depending on the knowledge of the field in the aperture. Until recently, it was common to employ the Second Principle of Equivalence, since it only requires knowledge of the tangential electric field. However, the First Principle of Equivalence provides more accurate results in both the copolar and crosspolar components. It requires the tangential magnetic field in the aperture, which can be easily obtained by assuming a locally incident plane wave at each reflectarray element. Furthermore, reflectarrays usually present a dielectric frame to screw the breadboard to the supporting structures. It has been demonstrated the importance of correctly modeling such dielectric frame in the design process since it can alter the radiation patterns, leading to a wrong characterization of the far fields.

Although the new developments in far field analysis techniques previously described were mainly focused for reflectarray antennas, they can be easily employed in the analysis of other planar-like structures, such as array antennas, transmitarrays or Frequency Selective Surfaces (FSS), due to their similarities to reflectarray antennas.

A new model for the near field analysis of reflectarray antennas has been presented. Again, instead of considering each element as a punctual source, it is modeled as a small aperture. Then, the near field of the reflectarray antenna is computed at each point of space as far field contributions of all the elements that comprise the array. The aim of this analysis was the prediction of the quiet zone generated by reflectarrays. Hence, a detailed development to compute the near field in planes perpendicular to the reflectarray pointing direction was presented. The computation of the near field is slower than the far field, since the FFT cannot longer be used. Thus, a strategy to parallelize its computation is presented, speeding up computations taking advantage of modern computers. The near field model presented in this thesis was validated by means of simulations with commercial software as well as measurements.

The rest of the thesis is devoted to the development of efficient synthesis and optimization techniques to improve the crosspolar component of the reflectarray far fields. In addition, some of the developed algorithms were applied to the near field optimization in order to improve the quiet zone generated by reflectarray antennas, with the future goal of using reflectarrays as probes for Compact Antenna Test Ranges (CATR).

First, an efficient implementation of the Intersection Approach (IA) algorithm for Phase-Only Synthesis (POS), and denoted IA-POS, was described. This algorithm has been extensively used in the past for reflectarray synthesis with great success. The POS formulation for the First Principle of Equivalence has been introduced for the first time. Also, the algorithm has been improved by including the dielectric frame in the analysis

as well as a constraint in the backward projector to recover the field at the aperture. It is a very efficient algorithm which can deal with very large reflectarrays. Its efficiency is based on the use of the FFT to compute the far fields and to recover the source field. Large reflectarrays are dealt with by modifying the illumination taper of the feed and performing the synthesis in several steps, in order to reduce in the first steps the number of local minima, minimizing the problem of traps and improving the algorithm convergence. However, as a POS algorithm, it only deals with the copolar pattern, and there is no control over the crosspolar one during the synthesis process. This fact motivated the search for an efficient algorithm to synthesize/optimize the crosspolar component of reflectarray antennas. Using the IA-POS as starting point, its formulation was extended to include crosspolar requirements in the synthesis process, obtaining what is called the IA-XP. In order to do that, instead of working with phase distributions, now the algorithm works with reflection coefficient matrix distributions, since this matrix fully describes the behavior of the element and can accurately account for the crosspolarization contribution of the reflectarray elements to the crosspolar pattern. As the IA-POS, the IA-XP is computationally very efficient, since it still uses the FFT in both projectors, although now four FFT are used in each projector instead of two in the IA-POS. Also, the IA-XP does not perform any electromagnetic analysis of the periodic cell. If the IA-XP is left to run without any constraints imposed to the reflection coefficient matrices, it will converge quickly to the desired solution, although the coefficients will not be feasible for passive reflectarrays since they will not meet the power balance. Hence, a complete formulation was developed in order to obtain the feasibility conditions of lossy two-port networks in order to implement those constraints in the algorithm. This way, the convergence is more difficult, but the obtained reflection coefficients will be feasible for passive networks, including passive reflectarrays. The algorithm was validated with a number of examples, showing good results.

Despite developing an efficient algorithm along with suitable constraints to obtain feasible passive reflection coefficients, it presents a major handicap. This is better understood comparing it with the IA-POS. The output of the IA-POS is two phase distributions, one for each polarization. The reflectarray design is obtained by adjusting the geometry of each element to match the required phase. This is easy to achieve due to the good behavior of the phases (almost linear in the desired variation range), because there are only two parameters to adjust per reflectarray element, and it is easy to do since the orthogonal dimensions of the element can almost adjust independently each required phase. However, for the IA-XP case, instead of two real parameters to adjust with the geometry, there are four complex numbers (equivalent to eight real parameters). Not only that, the reflection crosscoeffients are highly non-linear, so finding a reflectarray layout that is able to match the required reflection coefficient matrices is a really challenging task which was not pursued in this work, although some guidelines were provided. Hence, a difference approach was followed to be able to control the crosspolar component in the synthesis process.

The new approach was to directly optimize the geometry of the reflectarray elements using a full-wave analysis tool based on local periodicity, Method of Moments (MoM)

in this case. Due to this new layer added to the reflectarray analysis in the synthesis process, the IA could no longer be used as implemented in the IA-POS and IA-XP. Now, a general optimizing algorithm is needed. The Levenberg-Marquardt algorithm (LMA) was chosen due to its simplicity and capacity to work with non-linear optimization problems. However, instead of addressing directly the crosspolar optimization with the LMA, a POS version was developed in order to study the algorithm and introduce several computing optimizations to make the algorithm as fast as possible. This implementation is known as LMA-POS. The improvements introduced in the algorithm were the parallelization of the Jacobian matrix evaluation; minimization of the evaluation error of the derivatives which are evaluated by finite difference; appropriate choice of the libraries to perform matrix-vector and matrix multiplications; simplification of the matrix multiplication computing only half the matrix, since the result is symmetric; and optimum choice of the matrix equation solver, based on a Cholesky factorization due to the symmetric nature of the problem. With these improvements, the LMA is greatly sped up. Furthermore, the obtained results improve others in the literature. The implemented algorithm is accurate and scalable.

Then, the LMA-POS was extended to include MoM as analysis tool in order to optimize the crosspolar radiation pattern, obtaining the LMA-XP algorithm. Despite the improvements introduced in the LMA in the previous implementation, the inclusion of MoM in the optimization caused the algorithm to be extremely slow and of no practical use. Then, some strategies to minimize the impact of MoM were devised and implemented. First, with regard to the finite differences, a lateral difference was employed, reducing by half the calls to MoM. Also, for the computation of each column of the Jacobian, only one element is modified. Hence, there is no need to recompute the tangential field processing all elements with MoM, but just one, reusing the tangential field matrix from the first call to the cost function at the beginning of each iteration of the LMA. Since a good starting point is very important in a local optimizer, to test the LMA-XP, first a POS was carried out for a LMDS pattern, and after the reflectarray design was obtained, the crosspolar pattern was reduced several dB with the LMA-XP, verifying the proposed method. However, the LMA-XP presented some convergence issues when dealing with large reflectarrays due to the increasing number of variables and that the LMA cost function represented a non-convex search space. For that reason, it was necessary to improve the convergence of the algorithm following a different path.

In order to improve the convergence of the LMA-XP, it was decided to employ the generalized IA framework, which provided a more powerful and general framework to deal with the synthesis problem. In particular, working with the squared field amplitude instead of the field itself would alleviate the problem of local minima or traps. However, this caused a redefinition of the backward projector, which now implied the minimization of a distance, which needed to be implemented with an optimization algorithm. To take advantage of all the previous work, the LMA was chosen as backward projector, with all of its previous improvements. The resulting algorithm was denoted as IA-LMA-XP. The new algorithm greatly improved the converge of the LMA-XP. Now, the IA-LMA-XP can

handle thousands of optimizing variables and still achieve good results. Two examples were provided to validate the algorithm, one isoflux pattern for global Earth coverage, and a European coverage for DBS applications. In both cases the crosspolar pattern was greatly reduced while preserving the copolar shape, and in the latter case (DBS coverage), there were more than 30 thousand optimizing variables. Still, computing times using MoM in the optimization process were acceptable using a workstation. Also, the LMA-XP and the IA-LMA-XP were compared in order to assess the convergence improvement, showing that better results were obtained with the IA-LMA-XP in less iterations.

6.2. Original contributions

The original contributions of this thesis can be grouped depending on whether they are aimed to far field or near field applications.

6.2.1. Contributions related to reflectarray analysis for far field applications

- Development of an efficient technique for the far field computation of aperiodic arrays based on the Non-Uniform Fast Fourier Transform (NUFFT). The novelty of this approach is that it considers each reflectarray element as a small aperture instead of a punctual source (as in the array factor), increasing the accuracy of the computations. Before this technique was available, the computations of radiated fields of aperiodic reflectarrays only could be computed efficiently by using the NUFFT and the array factor (loosing efficiency), or by a direct implementation of the double summations of the spectrum functions, which is not efficient. *Related papers:* [J1, C4]. *Related projects:* [P2].

- Generalization of the reflectarray analysis considering a continuous incident field. The incident field at each reflectarray element is represented by means of its Fourier coefficients. Then, the spectrum functions are efficiently computed as a linear combination of FFT or NUFFT, for periodic or aperiodic reflectarrays, respectively. *Related papers:* [C4]. *Related projects:* [P3, P4, P5].

6.2.2. Reflectarray synthesis for far field applications

- Design, manufacture, and measurement of a low-cost reflectarray for global Earth coverage. The synthesis and design processes were conveniently adapted in order to obtain a suitable reflectarray geometry based on a single rectangular patch backed by a ground plane. Since this reflectarray element is not able to provide a full 360° phase-shift, the IA-POS was modified in order to impose this phase constrain. Moreover, since the behavior of the unit cell with regard to the patch size is non-linear, the patch dimensions were constrained during the design process in order to ensure a smooth distribution of the patches. This way, the local periodicity assumption of the MoM tool is preserved and the obtained reflectarray design is more reliable. Finally,

simulations and measurements are in good agreement. *Related papers:* [J4]. *Related projects:* [P3, P4, P5].

- Improvement of the phase-only synthesis algorithms by developing a POS formulation of the First Principle of Equivalence to correctly characterize the copolar component of the far field. *Related projects:* [P3, P4, P5].

- Improvement of the synthesis algorithms by including the effect of the dielectric frame in the synthesis process as a constraint, since the field in the frame is not modified during the synthesis process due to the lack of metallizations in that region of the antenna. *Related projects:* [P3, P4, P5].

- Efficient generalization of the Intersection Approach (IA) algorithm applied to dual-linear planar reflectarray antennas including crosspolar requirements during the synthesis process. Previously, the only efficient implementation of the IA algorithm only allowed to perform phase-only synthesis (POS), which only deals with copolar requirements during the synthesis process. The efficiency of the method lies in the use of the FFT in both projectors, to compute the radiated far fields and to recover the source field. The output of this new formulation of the IA is a distribution of reflection coefficient matrices, which fully characterize the behavior of the reflectarray element. *Related papers:* [J2]. *Related projects:* [P3, P4, P5].

- As part of the generalization of the IA algorithm described in the previous point, the feasibility conditions for lossy passive networks were derived from the generalized S matrix which characterize these networks. This development was carried out modeling the reflectarray unit cell as a 2-port network in order to find appropriate feasibility constraints to include during the synthesis process. *Related papers:* [J2]. *Related projects:* [P3, P4, P5].

- Improvement of the Levenberg-Marquardt algorithm (LMA) for the POS of reflectarray antennas, keeping in mind that it will be used later for the direct optimization of the reflectarray geometry. All the building blocks of the algorithm have been conveniently optimized in order to obtain a scalable algorithm. In particular, the reflectarray analysis is efficient since it uses the FFT; the Jacobian matrix evaluation is parallelized, computing one column per available thread; the matrix-vector and matrix multiplications are performed by highly optimized and fully parallelized commercial libraries which have been manually implemented using low-level hardware instructions; and the matrix equation system is efficiently solved by a Cholesky-based solver, which is the fastest solver available for this type of problem. The implementation of the LMA in this thesis outperforms others reported in the literature, allowing to solver larger problems in less time. *Related papers:* [J3]. *Related projects:* [P1].

- Extension of the LMA to directly optimize the reflectarray geometry using a full-wave Method of Moments based on local periodicity as analysis tool during the

optimization process. This way, the crosspolar component can be properly lowered since the crosspolarization introduced by the elements is taken into account. All the optimizations introduced for the POS version are used in this extension, and some new are introduced in order to minimize the impact of MoM in the optimization. The resulting algorithm was tested in a LMDS pattern for the crosspolar optimization, lowering the crosspolar pattern several dB while keeping the copolar specifications. *Related papers:* [C5, C7, N1]. *Related projects:* [P3, P4, P5].

- A generalization of the IA algorithm for the crosspolar optimization of reflectarrays employing MoM as the analysis tool has been implemented with improved convergence. It supersedes the LMA described in the previous point, which presented scalability issues due to the problem trap (local minima). The new developed algorithm is able to handle several thousands of optimizing variables while still having good convergence properties, as it was demonstrated by optimizing a large dual-polarized reflectarray for DBS applications, in which both the XPD and XPI were improved in both polarization, and, in particular, more than 5 dB in the case of the Y polarization, which presented the worst initial values. *Related papers:* [J5]. *Related projects:* [P3, P4, P5].

6.2.3. Contributions related to near field applications

- In the literature, array near-field models usually represent the array element as a punctual isotropic source, computing the near field of the whole array as far field contributions of all the elements. In this thesis, a similar approach has been followed, but considering the element as a small aperture instead of a punctual isotropic source, providing more accuracy in the near field analysis while keeping the simplicity of the model over others which are more accurate. Since this model computes the near field of the reflectarray as far field contributions, it is more accurate the farther the field is computed. This model has been validated by means of the commercial software GRASP and measurements. *Related papers:* [C1, C2, J6]. *Related projects:* [P1, P2].

- Some of the algorithms developed for reflectarray far field synthesis can be easily adapted for near field synthesis by using the new reflectarray near field model. In particular, the LMA-POS and IA-LMA-POS were used to greatly improve the quiet zone generated by a reflectarray antenna, with the aim of using reflectarrays as near field probes in compact antenna test ranges (CATR) at millimeter or higher frequencies. This concept has been proved at different frequencies in the work presented in this thesis, making the reflectarray a potential substitute of parabolic reflectors in CATR systems at high frequencies. *Related papers:* [C3, C6, J6]. *Related projects:* [P4, P5].

6.3. List of publications related to this work

The original contributions of this thesis have motivated the publication of several papers in international journals and conferences. They are listed below.

6.3.1. International journals

[J1] **D. R. Prado**, M. Arrebola, M. R. Pino, F. Las-Heras, "An Efficient Calculation of the Far Field Radiated by Non-Uniformly Sampled Planar Fields complying Nyquist theorem", *IEEE Transactions on Antennas and Propagation*, vol. 63, no. 2, pp. 862-865, Feb. 2015.

[J2] **D. R. Prado**, M. Arrebola, M. R. Pino, F. Las-Heras, "Complex Reflection Coefficients Synthesis applied to Dual-Polarized Reflectarrays with Crosspolar Requirements", *IEEE Transactions on Antennas and Propagation*, vol. 63, no. 9, pp. 3897-3907, Sept. 2015.

[J3] **D. R. Prado**, J. Álvarez, M. Arrebola, M. R. Pino, R. G. Ayestarán, F. Las-Heras, "Efficient, accurate and scalable reflectarray phase-only synthesis based on the Levenberg-Marquardt algorithm", *Applied Computational Electromagnetics Society (ACES) Journal*, vol. 30, no. 12, pp. 1246-1255, Dec. 2015.

[J4] **D. R. Prado**, A. Campa, M. Arrebola, M. R. Pino, J. A. Encinar, F. Las-Heras, "Design, Manufacture and Measurement of a Low-Cost Reflectarray for Global Earth Coverage", *IEEE Antennas Wireless Propagation Letters*, vol. 15, pp. 1418-1421, 2016.

[J5] **D. R. Prado**, M. Arrebola, M. R. Pino, R. Florencio, R. R. Boix, J. A. Encinar, F. Las-Heras, "Crosspolar optimization of dual-polarized reflectarrays based on full-wave characterization of the antenna element", *IEEE Transactions on Antennas and Propagation* (under review).

[J6] **D. R. Prado**, A. F. Vaquero, M. Arrebola, M. R. Pino, F. Las-Heras, "Optimization of the quiet zone generated by a reflectarray antenna", (in preparation).

6.3.2. International conferences

[C1] **D. R. Prado**, M. Arrebola, M. R. Pino, F. Las-Heras, "Evaluation of the quiet zone generated by a reflectarray antenna", *International Conference on Electromagnetics in Advanced Applications (ICEAA)*, Cape Town (South Africa), 2-7/09/2012.

[C2] G. León, M. Arrebola, **D. R. Prado**, E. González, S. Loredo, L. F. Herrán, M. R. Pino, F. Las-Heras, "Planar arrays modelling for near-field applications", *9th Iberian Meeting on Computational Electromagnetics (EIEC)*, Dénia, Alicante (Spain), 14-17/05/2013.

[C3] **D. R. Prado**, A. F. Vaquero, M. Arrebola, M. R. Pino, F. Las-Heras, "Optimization of the reflectarray quiet zone for use in compact antenna test range", *Proc. of the 37th Annual Meeting & Symposium of the Antenna Measurement Techniques Association (AMTA)*, Long Beach, California (USA), 11-16/10/2015.

[C4] **D. R. Prado**, M. Arrebola, M. R. Pino, F. Las-Heras, "Computation of the far field radiated by aperiodic sampled planar fields by means of NUFFT", *Proc. of the 37th Annual Meeting & Symposium of the Antenna Measurement Techniques Association (AMTA)*, Long Beach, California (USA), 11-16/10/2015.
2^{nd} place Student Paper Award.

[C5] **D. R. Prado**, M. Arrebola, M. R. Pino, F. Las-Heras, R. Florencio, R. R. Boix, J. A. Encinar, "Reflectarray antenna with reduced crosspolar radiation pattern", *10th European Conference on Antennas and Propagation (EuCAP)*, Davos (Switzerland), 10-15/04/2016.

[C6] A. F. Vaquero, **D. R. Prado**, M. Arrebola, M. R. Pino, F. Las-Heras, "Reflectarray probe optimization at millimeter frequencies", *10th European Conference on Antennas and Propagation (EuCAP)*, Davos (Switzerland), 10-15/04/2016.

[C7] **D. R. Prado**, M. Arrebola, M. R. Pino, F. Las-Heras, "Techniques for the crosspolar optimization in reflectarray antennas", *11th Iberian Meeting on Computational Electromagnetics (EIEC)*, Las Caldas, Asturias (Spain), 9-11/11/2016 (under review).

[C8] **D. R. Prado**, A. F. Vaquero, M. Arrebola, M. R. Pino and F. Las-Heras, "Near field synthesis of reflectarray antennas based on Intersection Approach", *11^{th} European Conference on Antennas and Propagation (EuCAP)*, Paris, (France), 19-24/03/2017 (convened session).

6.3.3. National conferences

[N1] **D. R. Prado**, M. Arrebola, M. R. Pino, F. Las-Heras, R. Florencio, R. R. Boix, J. A. Encinar, "Reducción de Contrapolar en Antenas Reflectarray", *XXXI Simposium Nacional de la Unión Científica Internacional de Radio (URSI)*, Madrid (Spain), 5-7/09/2016 (accepted).

6.4. Other publications

During the thesis period, and as a result of a short stay at KTH Royal Institute of Technology, Stockholm, Sweden, under the supervision of Dr. Óscar Quevedo-Teruel, two papers were published on the subject of Transformation Optics applied to lenses, one in an international conference and another in an international journal. They are listed below:

[O1] **D. R. Prado**, A. V. Osipov, O. Quevedo-Teruel, "Implementation of transformed lenses in bed of nails reducing refractive index maximum value and sub-unity regions", *Optics Letters*, vol. 40, no. 6, Mar. 2015.

[O2] A. V. Osipov, **D. R. Prado**, O. Quevedo-Teruel, "Flattened Generalized Maxwell Fish-Eye Lens", *9th European Conference on Antennas and Propagation (EuCAP)*, Lisbon (Portugal), 12-17/04/2015.

In addition, as part of an ESA funded project (see next section), the following technical reports were written:

[R1] J. A. Encinar, **D. R. Prado**, M. Arrebola, J. A. Muñiz, "TN-3: Algorithm Description Part II: Techniques and Tools for the Analysis and Design of Reflectarray Antennas", *Reflectarray antennas with improved performances and design techniques (ESTEC ITT AO/1-7064/12/NL/MH)*, 2015.

[R2] J. A. Encinar, **D. R. Prado**, M. Arrebola, R. R. Boix, R. Florencio, "TN-4: Software Tool for Advance Reflectarray Design", *Reflectarray antennas with improved performances and design techniques (ESTEC ITT AO/1-7064/12/NL/MH)*, 2015.

[R3] J. A. Encinar, **D. R. Prado**, M. Arrebola, R. R. Boix, R. Florencio, "Final report", *Reflectarray antennas with improved performances and design techniques (ESTEC ITT AO/1-7064/12/NL/MH)*, Jun. 2016.

6.5. Projects related to this work

Part of the work of the present thesis has contributed to the development of several research projects. The listed main researchers belong to the institution where the thesis work was developed.

[P1] **"Innovative Reconfigurable Systems based on Liquid Crystals"**, Code: 1-6419/10/NL/JK, Funding: Europen Space Agency (ESA), Term: 21/03/2011–20/03/2013. Main researcher: Manuel Arrebola.

[P2] **"Técnicas de imaging mediante problema inverso de dispersión: nuevos algoritmos y técnicas de medida (iScat)"**, Code: TEC2011-24492, Funding: Ministerio de Economía y Competitividad (Spanish Goverment), Term: 01/01/2012 –31/12/2014. Main researcher: Fernando Las-Heras Andrés.

[P3] **"Reflectarray Antennas with Improved Performances And Design Techniques (RAIPAD)"** , Code: 1-7064/12/NL/MH, Funding: European Space Agency (ESA), Term: 01/09/2012–31/03/2014. Main researcher: Manuel Arrebola.

[P4] **"Múltiples fuentes de información para mejorar técnicas de EM inverso para aplicaciones de reflectometría e imaging (MIRIIEM)"**, Code: TEC2014 -54005-P, Funding: Ministerio de Economía y Competitividad (Spanish Goverment), Term: 01/01/2015–31/12/2017. Main researchers: Marcos R. Pino and Luis Fernando H. Ontañón

[P5] **"Teoría de la señal y comunicaciones (TSC-UNIOVI)"**, Code: FC-15-GRUPIN14-114, Funding: Principado de Asturias, Term: 31/12/2014–31/15/2017. Main researcher: Fernando Las-Heras Andrés.

6.6. Future research lines

The work presented in this thesis has opened several research lines of interest that could not be pursued. They are listed below, grouped whether they are aimed to far field or near field applications.

6.6.1. Related to far field applications

- Extension of the synthesis algorithms by including new and improved analysis tools, which include the optimization of aperiodic reflectarrays with the new efficient analysis technique introduced in this thesis, the inclusion of a diffraction model or the optimization of reflectarrays in complex configurations.
    - Optimization of aperiodic reflectarrays using the NUFFT algorithm for the analysis. With the new developed technique for the efficient and accurate analysis of aperiodic reflectarrays, its inclusion in synthesis algorithms will speed up computations since it uses the NUFFT, which is more efficient than a direct computation of the spectrum functions. Also, since it considers the reflectarray element as a small aperture instead of a punctual isotropic source, the analysis is more accurate. However, for the phase-only synthesis it presents the disadvantage, with regard to the periodic case, that the field source cannot be recovered with another NUFFT, and an optimization algorithm needs to be used, for instance, the LMA. There is also the possibility of optimizing the elements positions in order to have extra degrees of freedom in order to obtain better results. Nevertheless, letting all the elements to freely vary their position might cause a tessellation problem, which can be difficult to solve. Also, the extra degrees of freedom cause the problem of traps to worsen. These problems are easily solved by only optimizing the positions moving full columns and rows; and employing algorithms that minimize the problem of traps, such as the IA-LMA.
    - Although the diffraction effects can be minimized by imposing a low illumination level in the edges of the reflectarray, including a diffraction model in the reflectarray analysis would improve the characterization of the radiated field in both far and near fields. Once this model is validated, it can be included in the synthesis process.
    - The optimization algorithms can be extended to include analysis tools in order to optimize the radiated fields of complex configurations that have appeared in recent years, such as dual configurations, having main parabolic reflectors working with reflectarrays as subreflectors, or a dual reflectarray system. For the first case, the subreflectarray can be optimized in order to obtain an optimum illumination of the main parabolic reflector increasing the efficiency of the antenna, or for near field applications. Having a dual reflectarray system, the number of degrees of freedom increases substantially, since both reflectarrays can be optimized at the same time.

- Manufacture of reflectarray prototypes in order to validate with measurements the proposed algorithms for the crosspolar optimization. This point should be subordinated to the improvement in the crosspolar analysis, in order to correctly optimize the crosspolar component that is actually radiated by the reflectarray antenna. Since the crosspolar far field presents really low levels of field with regard to the copolar component, the manufacturing and measurement processes should be tightly controlled in order to avoid undesired effects that would alter the crosspolar radiation pattern.

- Extension of the crosspolar optimization from a single frequency to a frequency band.

  - All the crosspolar optimizations shown were performed at a single frequency. The next step is to extend the algorithm to optimize the reflectarray in a given frequency band. This can be done at the expense of using more memory and computing times, since the reflectarray elements would need to be analyzed at all the required frequencies.

  - A further step would be to optimize the reflectarray at two frequency bands, which is interesting in DBS applications, since one band is used for transmission while the other is used for reception. Since the optimization problem is becoming quite complex by considering one or two frequency bands, a suitable starting point for the optimization will be very important, in order to ease the whole process.

  - One way to obtain a suitable starting point would be to perform a direct optimization of the reflectarray element geometry for copolar only synthesis at two different frequency bands. Since this time only the copolar pattern is synthesized, convergence to a suitable solution should be faster than in a crosspolar optimization.

- Improvements in the algorithm speed to compensate for the slowness due to the extension to several frequencies.

  - With the extension of the crosspolar optimization to one or two frequency bands, the algorithm will become slower and will consume more memory. Nevertheless, it will still scale well with the number of processors due to its efficient implementation. In any case, due to the intensive use of MoM in the optimization, the algorithm will greatly benefit from MoM improvements in computing times, derived from more efficient formulations and implementations. This would affect directly the cost function computation, and specially the Jacobian matrix computation. However, as the Jacobian matrix size increases, the most expensive operation of the algorithm will be the matrix multiplication involving the Jacobian and its transpose. This operation is already optimized by using highly optimized libraries for numerical computations and by computing only half the matrix, since the result is a symmetric matrix. However, its computing times can be further reduced by using more specialized hardware, such as GPU.

- In this thesis, the Jacobian matrix computation was greatly improved by making just one call to the MoM routine per Jacobian column. It can be further sped up by computing the far field with differential contributions. If M is the number of points in which the far field is discretized, by using the FFT, it takes $\mathcal{O}(M \log M)$ to compute them. However, only one reflectarray element is modified when computing one column of the Jacobian. Thus, by reusing the computed far field from the first call to the cost function, a differential contribution of the modified element would reduce the complexity to $\mathcal{O}(M)$, by subtracting the original contribution and adding the new one using the direct formulation of the spectrum function. Moreover, if the optimization is only carried out in a region smaller than the visible region (unit circle), having $M' < M$ points in the UV grid, the complexity is further reduced to $\mathcal{O}(M')$. Since this operation is repeated four times per Jacobian column, significant time could be saved.
- A total different approach to speed up the crosspolar optimization (although complementary with the two previous strategies) would be to substitute the LMA for another algorithm. In particular, the Broyden–Fletcher–Goldfarb–Shanno (BFGS) algorithm might be more suitable for very large optimization problems for several reasons. First, this algorithm substitutes the Jacobian matrix for an approximation of the Hessian matrix, which is smaller, saving memory. Also, there is no big matrix multiplication. Instead, only vector and matrix-vector multiplications are performed, which are substantially faster for large problems. Finally, there is no need to solve a matrix equation system, since the algorithm is able to directly work with the inverse of the Hessian approximation. This way, the IA-BFGS-XP algorithm would be obtained, instead of the IA-LMA-XP. Furthermore, there is a version of the BFGS which consumes a limited amount of memory, known as L-BFGS, which stores only a few vectors that represent the approximation of the Hessian implicitly, further saving memory.

6.6.2. Related to near field applications

- Improvements to the reflectarray near field model, including evanescent modes and a diffraction model.
  - Evanescent modes are negligible in the far field analysis of reflectarray antennas. However, they can play a role in the near field analysis. It is proposed to include the high order evanescent Floquet modes in the near field analysis and characterize their influence in the radiated field. This new formulation could improve the analysis and optimization of the quiet zone generated by the reflectarray and improve other near field applications by better characterizing the near field, which can be specially important when the distance at which the near field is computed is very close to the aperture.

- One of the main disadvantages of using a reflectarray as a probe for compact antenna test range (CATR) applications is the strong amplitude taper that presents the radiated near field due to the illumination taper introduced by the feed. The model presented in this thesis for the near field analysis does not include diffraction effects, so lowering the illumination taper to decrease its effect would cause that the computed near field would not be accurate. By including the diffraction effects, the near field could be conveniently optimized having a lower illumination at the edges of the reflectarray, which would facilitate obtaining a suitable quiet zone.

- Improvements in the near field optimization algorithm by extending the algorithms to a given frequency band, speeding up its computations with the differential contributions, use of continuous functions to improve the smoothness of the phases in POS and optimization of the polarization purity by using MoM in the computation of the near field.

  - All the quiet zone optimizations were carried out at a single frequency. They can be easily extended to a frequency band by following the same approach used in the far field POS of reflectarrays with enhanced bandwidth, by adjusting the reflectarray geometry of each element to match the required phase-shifts at each frequency.

  - The phases obtained with the near field optimization were not as smooth as desired, which lead to unreliable designs. One possibility to obtain smooth phases in near field optimization would be to model the initial phase distribution with smooth functions such as splines. Then, by optimizing the coefficients of the splines, the resulting phases would still be smooth, but radiating the required near field. Other functions can also be used, such as Zernike polynomials, among others.

  - The computation of the near field is slower than the far field since there is no possibility of using the FFT, which was the main reason for the high efficiency of the latter. One possibility to accelerate the computation of the near field during the optimization process, specifically in the Jacobian matrix evaluation, is to only consider differential contributions of each element to the radiated field. The way of proceeding would be as follows. With the initial call to the cost function, the near field is fully computed, as far field contributions of all the elements of the reflectarray. For the Jacobian matrix evaluation, and for each column of the matrix, only one element is modified. Then, one can reuse the near field previously computed and, for the current element being modified, its original contribution to the field is subtracted, and the new contribution of the modified element is added. This differential computation of the near field would greatly speed up the computation of the Jacobian matrix, allowing the optimization process to finish early, saving considerably amounts of time.

  - The POS done to the near field does not allow to directly optimize the crosspolar component of the near field. It is proposed, as for the far field, to compute the near field using MoM as analysis tool in order to be able to improve the polarization purity of the near field. For the optimization of the near field using full-wave analysis based on local periodicity to take affordable computing times, the previous point should also be implemented.

- The algorithms used in the quiet zone optimization can also be used for other near field applications, such as near field focusing/multifocusing, imaging, hyperthermia, etc.; by only modifying the templates, provided a suitable starting point.

References

[1] D. G. Berry, R. G. Malech, and W. A. Kennedy, "The reflectarray antenna," *IEEE Trans. Antennas Propag.*, vol. 11, no. 6, pp. 645–651, Nov. 1963.

[2] J. Huang and J. A. Encinar, *Reflectarray Antennas*. John Wiley & Sons, 2008.

[3] D. Pilz and W. Menzel, "Folded reflectarray antenna," *Electron. Lett.*, vol. 34, no. 9, pp. 832–833, Apr. 1998.

[4] W. Menzel, D. Pilz, and M. Al-Tikriti, "Millimeter-wave folded reflector antennas with high gain, low loss, and low profile," *IEEE Antennas Propag. Mag.*, vol. 44, no. 3, pp. 24–29, Jun. 2002.

[5] J. A. Zornoza, R. Leberer, J. A. Encinar, and W. Menzel, "Folded multilayer microstrip reflectarray with shaped pattern," *IEEE Trans. Antennas Propag.*, vol. 54, no. 2, pp. 510–518, Feb. 2006.

[6] Q. Luo, S. Gao, C. Zhang, D. Zhou, T. Chaloun, W. Menzel, V. Ziegler, and M. Sobhy, "Design and analysis of a reflectarray using slot antenna elements for Ka-band SatCom," *IEEE Trans. Antennas Propag.*, vol. 63, no. 4, pp. 1365–1374, Apr. 2015.

[7] J. Huang, "The development of inflatable array antennas," *IEEE Antennas Propag. Mag.*, vol. 43, no. 4, pp. 44–50, Aug. 2001.

[8] S. Montori, F. Cacciamani, R. V. Gatti, R. Sorrentino, G. Arista, C. Tienda, J. A. Encinar, and G. Toso, "A transportable reflectarray antenna for satellite Ku-band emergency communications," *IEEE Trans. Antennas Propag.*, vol. 63, no. 4, pp. 1393–1407, Apr. 2015.

[9] J. Huang, "Bandwidth study of microstrip reflectarray and a novel phased reflectarray concept," in *Antennas and Propagation Society International Symposium*, vol. 1, Newport Beach, California, USA, Jun. 18–23, 1995, pp. 582–585.

[10] D. M. Pozar, "Bandwidth of reflectarrays," *Electron. Lett.*, vol. 39, no. 21, pp. 1490–1491, Oct. 2003.

[11] J. A. Encinar and J. A. Zornoza, "Broadband design of three-layer printed reflectarrays," *IEEE Trans. Antennas Propag.*, vol. 51, no. 7, pp. 1662–1664, Jul. 2003.

[12] J. H. Yoon, Y. J. Yoon, W. sang Lee, and J. ho So, "Broadband microstrip reflectarray with five parallel dipole elements," *IEEE Antennas Wireless Propag. Lett.*, vol. 14, pp. 1109–1112, 2015.

[13] L. Moustafa, R. Gillard, F. Peris, R. Loison, H. Legay, and E. Girard, "The phoenix cell: A new reflectarray cell with large bandwidth and rebirth capabilities," *IEEE Antennas Wireless Propag. Lett.*, vol. 10, pp. 71–74, 2011.

[14] E. Carrasco, J. A. Encinar, and M. Barba, "Bandwidth improvement in large reflectarrays by using true-time delay," *IEEE Trans. Antennas Propag.*, vol. 56, no. 8, pp. 2496–2503, Aug. 2008.

[15] J. A. Encinar, M. Arrebola, and G. Toso, "A parabolic reflectarray for a bandwidth improved contoured beam coverage," in *The Second European Conference on Antennas and Propagation (EuCAP)*, Edinburgh, Scotland, United Kingdom, Nov. 11–16 2007, pp. 1–5.

[16] M. Zhou, S. B. Sørensen, O. Borries, and E. Jørgensen, "Analysis and optimization of a curved transmit-receive contoured beam reflectarray," in *The 9th European Conference on Antennas and Propagation (EuCAP)*, Lisbon, Portugal, Apr. 13–17, 2015, pp. 1–5.

[17] H. Legay, D. Bresciani, E. Labiole, R. Chiniard, and R. Gillard, "A multi facets composite panel reflectarray antenna for a space contoured beam antenna in ku band," *Progr. Electromagn. Res. B*, vol. 54, pp. 1–26, Aug. 2013.

[18] M. Zhou, S. B. Sørensen, P. Meincke, and E. Jørgensen, "Design and optimization of multi-faceted reflectarrays for satellite applications," in *The 8th European Conference on Antennas and Propagation (EUCAP)*, The Hague, The Netherlands, Apr. 6–11, 2014, pp. 1423–1427.

[19] J. A. Encinar, L. S. Datashvili, J. A. Zornoza, M. Arrebola, M. Sierra-Castaner, J. L. Besada-Sanmartin, H. Baier, and H. Legay, "Dual-polarization dual-coverage reflectarray for space applications," *IEEE Trans. Antennas Propag.*, vol. 54, no. 10, pp. 2827–2837, Oct. 2006.

[20] J. A. Encinar, M. Arrebola, L. F. de la Fuente, and G. Toso, "A transmit-receive reflectarray antenna for direct broadcast satellite applications," *IEEE Trans. Antennas Propag.*, vol. 59, no. 9, pp. 3255–3264, Sep. 2011.

[21] P. Nayeri, F. Yang, and A. Z. Elsherbeni, "Design of single-feed reflectarray antennas with asymmetric multiple beams using the particle swarm optimization method," *IEEE Trans. Antennas Propag.*, vol. 61, no. 9, pp. 4598–4605, Sep. 2013.

[22] D. M. Pozar, S. D. Targonski, and R. Pokuls, "A shaped-beam microstrip patch reflectarray," *IEEE Trans. Antennas Propag.*, vol. 47, no. 7, pp. 1167–1173, Jul. 1999.

[23] A. E. Martynyuk, J. I. M. Lopez, and N. A. Martynyuk, "Spiraphase-type reflectarrays based on loaded ring slot resonators," *IEEE Trans. Antennas Propag.*, vol. 52, no. 1, pp. 142–153, Jan. 2004.

[24] J. Huang, "Microstrip reflectarray," in *Antennas and Propagation Society International Symposium*, vol. 2, London, Ontario, Canada, Jun. 24–28, 1991, pp. 612–615.

[25] D.-C. Chang and M.-C. Huang, "Multiple-polarization microstrip reflectarray antenna with high efficiency and low cross-polarization," *IEEE Trans. Antennas Propag.*, vol. 43, no. 8, pp. 829–834, Aug. 1995.

[26] M. E. Cooley, J. F. Walker, D. G. Gonzalez, and G. E. Pollon, "Novel reflectarray element with variable phase characteristics," *IEE Proc. Microw. Antennas Propag.*, vol. 144, no. 2, pp. 149–151, Apr. 1997.

[27] H. Deguchi, N. Takagi, M. Tsuji, and H. Shigesawa, "Microstrip reflectarray with offset feed for improving effective aperture area," in *IEEE Antennas and Propagation Society International Symposium*, vol. 3, Columbus, Ohio, USA, Jun. 22–27 2003, pp. 290–293.

[28] D. M. Pozar and S. D. Targonski, "A microstrip reflectarray using crossed dipoles," in *IEEE Antennas and Propagation Society International Symposium*, vol. 2, Atlanta, Georgia, USA, Jun. 21–26, 1998, pp. 1008–1011.

[29] D. M. Pozar and T. A. Metzler, "Analysis of a reflectarray antenna using microstrip patches of variable size," *Electron. Lett.*, vol. 29, no. 8, pp. 657–658, Apr. 1993.

[30] D. M. Pozar, S. D. Targonski, and H. D. Syrigos, "Design of millimeter wave microstrip reflectarrays," *IEEE Trans. Antennas Propag.*, vol. 45, no. 2, pp. 287–296, Feb. 1997.

[31] M. R. Chaharmir, J. Shaker, M. Cuhaci, and A.-R. Sebak, "Reflectarray with variable slots on ground plane," *IEE Proc. Microw. Antennas Propag.*, vol. 150, no. 6, pp. 436–439, Dec. 2003.

[32] J. Huang and R. J. Pogorzelski, "A Ka-band microstrip reflectarray with elements having variable rotation angles," *IEEE Trans. Antennas Propag.*, vol. 46, no. 5, pp. 650–656, 1998.

[33] J. A. Encinar, "Design of two-layer printed reflectarrays using patches of variable size," *IEEE Trans. Antennas Propag.*, vol. 49, no. 10, pp. 1403–1410, Oct. 2001.

[34] J. A. Encinar and J. A. Zornoza, "Three-layer printed reflectarrays for contoured beam space applications," *IEEE Trans. Antennas Propag.*, vol. 52, no. 5, pp. 1138–1148, May 2004.

[35] F.-C. E. Tsai and M. E. Bialkowski, "Designing a 161-element Ku-band microstrip reflectarray of variable size patches using an equivalent unit cell waveguide approach," *IEEE Trans. Antennas Propag.*, vol. 51, no. 10, pp. 2953–2962, Oct. 2003.

[36] M. E. Bialkowski and H. J. Song, "Dual linearly polarized reflectarray using aperture coupled microstrip patches," in *IEEE Antennas and Propagation Society International Symposium*, vol. 3, Boston, Massachusetts, USA, Jul. 8–13, 2001, pp. 486–489.

[37] E. Carrasco, M. Barba, and J. A. Encinar, "Aperture-coupled reflectarray element with wide range of phase delay," *Electron. Lett.*, vol. 42, no. 12, pp. 667–668, Jun. 2006.

[38] S. Costanzo, F. Venneri, and G. D. Massa, "Bandwidth enhancement of aperture-coupled reflectarrays," *Electron. Lett.*, vol. 42, no. 23, pp. 1320–1321, Nov. 2006.

[39] B. D. Nguyen, K. T. Pham, V.-S. Tran, L. Mai, and N. Yonemoto, "Reflectarray element using cut-ring patch coupled to delay line," *IEEE Antennas Wireless Propag. Lett.*, vol. 14, pp. 571–574, 2015.

[40] L. Li, Q. Chen, Q. Yuan, K. Sawaya, T. Maruyama, T. Furuno, and S. Uebayashi, "Novel broadband planar reflectarray with parasitic dipoles for wireless communication applications," *IEEE Antennas Wireless Propag. Lett.*, vol. 8, pp. 881–885, 2009.

[41] J. H. Yoon, Y. J. Yoon, W.-S. Lee, and J.-H. So, "Broadband microstrip reflectarray with five parallel dipole elements," *IEEE Antennas Wireless Propag. Lett.*, vol. 14, pp. 1109–1112, 2015.

[42] R. Florencio, J. Encinar, R. R. Boix, and G. Perez-Palomino, "Dual-polarisation reflectarray made of cells with two orthogonal sets of parallel dipoles for bandwidth and cross-polarisation improvement," *IET Microw. Antennas Propag.*, vol. 8, no. 15, pp. 1389–1397, Aug. 2014.

[43] R. Florencio, J. A. Encinar, R. R. Boix, V. Losada, and G. Toso, "Reflectarray antennas for dual polarization and broadband telecom satellite applications," *IEEE Trans. Antennas Propag.*, vol. 63, no. 4, pp. 1234–1246, Apr. 2015.

[44] S. Adel and H. Hammad, "Modified phoenix cell for microstrip reflectarray antennas," in *Middle East Conference on Antennas and Propagation (MECAP)*, Cairo, Egypt, Dec. 29–31, 2012, pp. 1–3.

[45] S. A. Ibrahim and H. F. Hammad, "Modified phoenix cell for microstrip reflectarray antennas," in *IEEE Antennas and Propagation Society International Symposium (APSURSI)*, Orlando, Florida, USA, Jul. 7–13, 2013, pp. 1562–1563.

[46] I. Derafshi, N. Komjani, and M. Mohammadirad, "A single-layer broadband reflectarray antenna by using quasi-spiral phase delay line," *IEEE Antennas Wireless Propag. Lett.*, vol. 14, pp. 84–87, 2015.

[47] M. K. Arshad, F. A. Tahir, and A. Rashid, "Design of a single layer reflectarray unit cells based on hexagonal ring for wideband operation," in *IEEE Antennas and Propagation Society International Symposium (APSURSI)*, Memphis, Tennessee, USA, Jul. 6–11, 2014, pp. 815–816.

[48] M. R. Chaharmir, J. Shaker, M. Cuhaci, and A. Ittipiboon, "A broadband reflectarray antenna with double square rings as the cell elements," in *First European Conference on Antennas and Propagation (EuCAP)*, Nice, France, Nov. 6–10, 2006, pp. 1–4.

[49] R. S. Malfajani and Z. Atlasbaf, "Design and implementation of a broadband single-layer reflectarray antenna with large-range linear phase elements," *IEEE Antennas Wireless Propag. Lett.*, vol. 11, pp. 1442–1445, 2012.

[50] A. K. Bhattacharyya, *Phased Array Antennas: Floquet Analysis, Synthesis, BFNs, and Active Array Systems.* John Wiley & Sons, 2006.

[51] "HFSS," Ansys Inc., Pittsburgh, Pennsylvania, USA.

[52] "FEKO," Altair Engineering, Troy, Michigan, USA.

[53] "CST," Computer Simulation Technology AG, Darmstadt, Germany.

[54] C. Wan and J. A. Encinar, "Efficient computation of generalized scattering matrix for analyzing multilayered periodic structures," *IEEE Trans. Antennas Propag.*, vol. 43, no. 11, pp. 1233–1242, Nov. 1995.

[55] D. Pilz and W. Menzel, "Full wave analysis of a planar reflector antenna," in *Asia-Pacific Microwave Conference Proceedings (APMC)*, vol. 1, Hong Kong, China, Dec. 2–5, 1997, pp. 225–227.

[56] P. De Vita, A. Freni, F. Vipiana, P. Pirinoli, and G. Vecchi, "Fast analysis of large finite arrays with a combined multiresolution–SM/AIM approach," *IEEE Trans. Antennas Propag.*, vol. 54, no. 12, pp. 3827–3832, Dec. 2006.

[57] J. Gómez, A. Tayebi, I. González, and F. Cátedra, "Analysis of a dual-band reflectorarray by using a full wave moment method code," in *International Workshop on Antenna Technology (iWAT)*, Lisbon, Portugal, Mar. 1–3, 2010, pp. 1–4.

[58] I. González, A. Tayebi, J. Gomez, C. Delgado, and F. Cátedra, "Fast analysis of a dual-band reflectarray using two different numerical approaches based on the moment method," *IEEE Trans. Antennas Propag.*, vol. 61, no. 4, pp. 2333–2336, Apr. 2013.

[59] A. Tayebi, J. Gómez, I. González, and F. Cátedra, "Computer tool for designing reflectarray antennas," in *15^{th} International Symposium on Antenna Technology and Applied Electromagnetics (ANTEM)*, Toulouse, France, Jun. 25–28, 2012, pp. 1–4.

[60] Y. Abdallah, C. Menudier, M. Thevenot, and T. Monediere, "Synthesis of reflectarrays with mutual couplings," in *7^{th} European Conference on Antennas and Propagation (EuCAP)*, Gothenburg, Sweden, Apr. 8–12, 2013, pp. 3446–3450.

[61] A. Capozzoli, C. Curcio, A. Liseno, M. Migliorelli, and G. Toso, "Fast analysis and database generation in aperiodic reflectarrays," in *7^{th} European Conference on*

Antennas and Propagation (EuCAP), Gothenburg, Sweden, Apr. 8–12, 2013, pp. 3913–3916.

[62] E. Ercil, L. Alatan, and O. A. Civi, "An efficient numerical solution method for reflectarrays of varying element sizes," *IEEE Trans. Antennas Propag.*, vol. 63, no. 12, pp. 5668–5676, Dec. 2015.

[63] P. R. Bayón, "Estudio y aplicación de redes neuronales artificiales al análisis y diseño de reflectarrays," Ph.D. dissertation, Universidad Politécnica de Madrid, 2013, (in spanish).

[64] D. Caputo, A. Pirisi, M. Mussetta, A. Freni, P. Pirinoli, and R. E. Zich, "Neural network characterization of microstrip patches for reflectarray optimization," in *3rd European Conference on Antennas and Propagation (EuCAP)*, Berlin, Germany, Mar. 23–27, 2009, pp. 2520–2522.

[65] S. Nesil, F. Güneş, and U. Özkaya, "Phase characterization of a reflectarray unit cell with minkowski shape radiating element using multilayer perceptron neural network," in *7th International Conference on Electrical and Electronics Engineering (ELECO)*, vol. 2, Bursa, Turkey, Dec. 1–4, 2011, pp. 219–222.

[66] P. Robustillo, J. Zapata, J. A. Encinar, and J. Rubio, "ANN characterization of multi-layer reflectarray elements for contoured-beam space antennas in the Ku-band," *IEEE Trans. Antennas Propag.*, vol. 60, no. 7, pp. 3205–3214, Jul. 2012.

[67] P. Robustillo, J. Zapata, J. A. Encinar, and M. Arrebola, "Design of a contoured-beam reflectarray for a eutelsat european coverage using a stacked-patch element characterized by an artificial neural network," *IEEE Antennas Wireless Propag. Lett.*, vol. 11, pp. 977–980, 2012.

[68] H. M. Linh, M. Mussetta, P. Pirinoli, and R. E. Zich, "Modeling of reflectarray elements by means of metaPSO-based artificial neural network," in *7th European Conference on Antennas and Propagation (EuCAP)*, Gothenburg, Sweden, Apr. 8–12, 2013, pp. 3450–3451.

[69] P. Robustillo, J. Zapata, J. A. Encinar, R. Florencio, R. R. Boix, and J. R. Mosig, "Accurate characterization of multi-resonant reflectarray cells by artificial neural networks," in *The 8th European Conference on Antennas and Propagation (EUCAP)*, The Hague, The Netherlands, Apr. 6–11, 2014, pp. 2297–2299.

[70] V. Vapnik, *The Nature of Statistical Learning Theory*, 2nd ed. Springer, 1999.

[71] R. G. Ayestarán and F. Las-Heras, "Support vector regression for the design of array antennas," *IEEE Antennas Wireless Propag. Lett.*, vol. 4, pp. 414–416, 2005.

[72] R. G. Ayestarán, M. F. Campillo, and F. Las-Heras, "Multiple support vector regression for antenna array characterization and synthesis," *IEEE Trans. Antennas Propag.*, vol. 55, no. 9, pp. 2495–2501, Sep. 2007.

[73] F. S. Johansson, L. G. Josefsson, and T. Lorentzon, "A novel frequency-scanned reflector antenna," *IEEE Trans. Antennas Propag.*, vol. 37, no. 8, pp. 984–989, Aug. 1989.

[74] R. A. Kipp and C. H. Chan, "A numerically efficient technique for the method of moments solution for planar periodic structures in layered media," *IEEE Trans. Microw. Theory Tech.*, vol. 42, no. 4, pp. 635–643, Apr. 1994.

[75] D. Gonzalez-Ovejero, F. Mesa, and C. Craeye, "Accelerated macro basis functions analysis of finite printed antenna arrays through 2D and 3D multipole expansions," *IEEE Trans. Antennas Propag.*, vol. 61, no. 2, pp. 707–717, Feb. 2013.

[76] R. Florencio, R. R. Boix, and J. A. Encinar, "Enhanced MoM analysis of the scattering by periodic strip gratings in multilayered substrates," *IEEE Trans. Antennas Propag.*, vol. 61, no. 10, pp. 5088–5099, Oct. 2013.

[77] ——, "Fast and accurate MoM analysis of periodic arrays of multilayered stacked rectangular patches with application to the design of reflectarray antennas," *IEEE Trans. Antennas Propag.*, vol. 63, no. 6, pp. 2558–2571, Jun. 2015.

[78] Y.-T. Lo and S.-W. Lee, Eds., *Antenna Handbook Vol. 1.* Van Nostrand Reinhold, 1993, ch. 1, pp. 28–29.

[79] J. A. Z. Ramírez, "Desarrollo de técnicas de diseño para reflectarrays impresos multicapa con haz conformado," Ph.D. dissertation, Universidad Politécnica de Madrid, 2004, (in spanish).

[80] W. Hu, M. Arrebola, R. Cahill, J. A. Encinar, V. Fusco, H. S. Gamble, Y. Álvarez, and F. Las-Heras, "94 GHz dual-reflector antenna with reflectarray subreflector," *IEEE Trans. Antennas Propag.*, vol. 57, no. 10, pp. 3043–3050, Oct. 2009.

[81] M. Arrebola, J. A. Encinar, and M. Barba, "Multifed printed reflectarray with three simultaneous shaped beams for LMDS central station antenna," *IEEE Trans. Antennas Propag.*, vol. 56, no. 6, pp. 1518–1527, Jun. 2008.

[82] M. Arrebola, Y. Álvarez, J. A. Encinar, and F. Las-Heras, "Accurate analysis of printed reflectarrays considering the near field of the primary feed," *IET Microw. Antennas Propag.*, vol. 3, no. 2, pp. 187–194, Mar. 2009.

[83] M. A. Moharram and A. A. Kishk, "Optimum feeds for reflectarray antenna: Synthesis and design," *IEEE Trans. Antennas Propag.*, vol. 64, no. 2, pp. 469–483, Feb. 2016.

[84] G. Perez-Palomino, J. A. Encinar, and M. Barba, "Method for accurately solving the scattering in planar reflectarrays under an arbitrary excitation," in *6^{th} European Conference on Antennas and Propagation (EUCAP)*, Prague, Czech Republic, Mar. 26–30, 2012, pp. 1081–1085.

[85] Y.-T. Lo and S.-W. Lee, Eds., *Antenna Handbook Vol. 2.* Van Nostrand Reinhold, 1993.

[86] A. Capozzoli, C. Curcio, E. Iavazzo, A. Liseno, M. Migliorelli, and G. Toso, "Phase-only synthesis of a-periodic reflectarrays," in *Proceedings of the 5th European Conference on Antennas and Propagation (EUCAP)*, Rome, Italy, Apr. 11–15, 2011, pp. 987–991.

[87] A. Capozzoli, C. Curcio, A. Liseno, M. Migliorelli, and G. Toso, "Phase-only synthesis of conformal aperiodic reflectarrays with multi-frequency specifications," in *6th European Conference on Antennas and Propagation (EUCAP)*, Prague, Czech Republic, Mar. 26–30, 2012, pp. 2220–2224.

[88] M. Zhou, S. B. Sørensen, E. Jørgensen, P. Meincke, O. S. Kim, and O. Breinbjerg, "An accurate technique for calculation of radiation from printed reflectarrays," *IEEE Antennas Wireless Propag. Lett.*, vol. 10, pp. 1081–1084, 2011.

[89] O. M. Bucci, G. D'Elia, G. Mazzarella, and G. Panariello, "Antenna pattern synthesis: a new general approach," *Proc. IEEE*, vol. 82, no. 3, pp. 358–371, Mar. 1994.

[90] P. M. Woodward, "A method of calculating the field over a plane aperture required to produce a given polar diagram," *J. Inst. Elec. Eng.*, vol. 93, pt. III, no. 10, pp. 1554–1558, 1946.

[91] A. Chakraborty, B. N. Das, and G. S. Sanyal, "Beam shaping using nonlinear phase distribution in a uniformly spaced array," *IEEE Trans. Antennas Propag.*, vol. 30, no. 5, pp. 1031–1034, Sep. 1982.

[92] J. Perini and M. Idselis, "Note on antenna pattern synthesis using numerical iterative methods," *IEEE Trans. Antennas Propag.*, vol. 19, no. 2, pp. 284–286, Mar. 1971.

[93] T. S. Fong and R. A. Birgenheier, "Method of conjugate gradients for antenna pattern synthesis," *Radio Sci.*, vol. 6, no. 12, pp. 1123–1130, Dec. 1971.

[94] O. M. Bucci, G. Franceschetti, G. Mazzarella, and G. Panariello, "Intersection approach to array pattern synthesis," *IEE Proc. Microw. Antennas Propag.*, vol. 137, no. 6, pp. 349–357, Dec. 1990.

[95] J. A. Zornoza and J. A. Encinar, "Efficient phase-only synthesis of contoured-beam patterns for very large reflectarrays," *Int. J. RF Microw. Comput. Eng.*, vol. 14, no. 5, pp. 415–423, Sep. 2004.

[96] T. H. Ismail, D. I. Abu-Al-Nadi, and M. J. Mismar, "Phase-only control for antenna pattern synthesis of linear arrays using the Levenberg-Marquardt algorithm," *Electromagnetics*, vol. 24, no. 7, pp. 555–564, 2004.

[97] J. Álvarez, M. Arrebola, R. G. Ayestarán, and F. Las-Heras, "Systematic framework for reflectarray synthesis based on phase optimization," *Int. J. Antennas Propag.*, vol. 2012, pp. 1–9, Jun. 2012.

[98] J. M. Johnson and Y. Rahmat-Samii, "Genetic algorithm optimization and its application to antenna design," in *Antennas and Propagation Society International Symposium*, vol. 1, Seattle, Washington, USA, Jun. 20–24, 1994, pp. 326–329.

[99] I. López, J. R. Pérez, and J. Basterrechea, "An approach for the design of reflectarrays using CG-FFT and PSO," in *Proceedings of the Fourth European Conference on Antennas and Propagation (EuCAP)*, Barcelona, Spain, Apr. 12–16, 2010, pp. 1–5.

[100] J. Nocedal and S. J. Wright, *Numerical Optimization*, 2nd ed. Springer, 2006.

[101] G. A. F. Seber and C. J. Wild, *Nonlinear Regression*. John Wiley & Sons, 2003.

[102] O. M. Bucci, G. D'Elia, and G. Romito, "Power synthesis of conformal arrays by a generalised projection method," *IEE Proc. Microw. Antennas Propag.*, vol. 142, no. 6, pp. 467–471, Dec. 1995.

[103] D. W. Boeringer and D. H. Werner, "Particle swarm optimization versus genetic algorithms for phased array synthesis," *IEEE Trans. Antennas Propag.*, vol. 52, no. 3, pp. 771–779, Mar. 2004.

[104] J.-L. Guo and J.-Y. Li, "Pattern synthesis of conformal array antenna in the presence of platform using differential evolution algorithm," *IEEE Trans. Antennas Propag.*, vol. 57, no. 9, pp. 2615–2621, Sep. 2009.

[105] F. Zhang, W. Jia, and M. Yao, "Linear aperiodic array synthesis using differential evolution algorithm," *IEEE Antennas Wireless Propag. Lett.*, vol. 12, pp. 797–800, 2013.

[106] O. Quevedo-Teruel and E. Rajo-Iglesias, "Ant colony optimization in thinned array synthesis with minimum sidelobe level," *IEEE Antennas Wireless Propag. Lett.*, vol. 5, no. 1, pp. 349–352, Dec. 2006.

[107] E. Rajo-Iglesias and O. Quevedo-Teruel, "Linear array synthesis using an ant-colony-optimization-based algorithm," *IEEE Antennas Propag. Mag.*, vol. 49, no. 2, pp. 70–79, Apr. 2007.

[108] U. Singh and M. Rattan, "Design of thinned concentric circular antenna arrays using firefly algorithm," *IET Microw. Antennas Propag.*, vol. 8, no. 12, pp. 894–900, Sep. 2014.

[109] R. M. Shiju and N. Venkateswaran, "Optimization of linear array antenna pattern synthesis using bacterial foraging algorithm," in *International Conference on Recent Advances in Computing and Software Systems (RACSS)*, Chennai, India, Apr. 25–27, 2012, pp. 130–134.

[110] S. Mishra, S. Chattopadyay, and M. Gangopadhyaya, "A comparative study of DE, PSO and BFO for optimisation of rectangular microstrip patch antenna with inset feed parameter," in *International Conference and Workshop on Computing and Communication (IEMCON)*, Vancouver, British Columbia, Canada, Oct. 15–17, 2015, pp. 1–7.

[111] U. Singh and T. S. Kama, "Synthesis of thinned planar concentric circular antenna arrays using biogeography-based optimisation," *IET Microw. Antennas Propag.*, vol. 6, no. 7, pp. 822–829, May 2012.

[112] W.-C. Weng, F. Yang, and A. Z. Elsherbeni, "Linear antenna array synthesis using Taguchi's method: A novel optimization technique in electromagnetics," *IEEE Trans. Antennas Propag.*, vol. 55, no. 3, pp. 723–730, Mar. 2007.

[113] H. Hasani, M. Kamyab, and M. Ali, "Low cross-polarization reflectarray antenna," *IEEE Trans. Antennas Propag.*, vol. 59, no. 5, pp. 1752–1756, May 2011.

[114] J. A. Encinar and M. Arrebola, "Reduction of cross-polarization in contoured beam reflectarrays using a three-layer configuration," in *IEEE Antennas and Propagation Society International Symposium*, Honolulu, Hawaii, USA, Jun. 9–15, 2007, pp. 5303–5306.

[115] C. Tienda, J. A. Encinar, M. Arrebola, M. Barba, and E. Carrasco, "Design, manufacturing and test of a dual-reflectarray antenna with improved bandwidth and reduced cross-polarization," *IEEE Trans. Antennas Propag.*, vol. 61, no. 3, pp. 1180–1190, Mar. 2013.

[116] O. M. Bucci, A. Capozzoli, G. D'Elia, and S. Musto, "A new approach to the power pattern synthesis of reflectarrays," in *Proc. URSI International Symposium on Electromagnetic Theory (EMTS'04)*, Pisa, Italy, May 23–27, 2004, pp. 1053–1055.

[117] O. M. Bucci, A. Capozzoli, G. D'Elia, and S. Russo, "Power pattern synthesis of reflectarrays: comparison between two approaches," in *Proc. of the XV Riunione Nazionale di Elettromagnetismo (CD-ROM)*, Cagliari, Italy, Sep. 13–16, 2004, pp. 1–4.

[118] ——, "An advanced technique for reflectarray power pattern synthesis and its experimental validation," in *Proc. of the International Symposium on Antennas and Propagation (ISAP)*, Seoul, South Korea, Aug. 3–5, 2005, pp. 561–564.

[119] M. Zhou, S. B. Sørensen, O. S. Kim, E. Jørgensen, P. Meincke, and O. Breinbjerg, "Direct optimization of printed reflectarrays for contoured beam satellite antenna applications," *IEEE Trans. Antennas Propag.*, vol. 61, no. 4, pp. 1995–2004, Apr. 2013.

[120] M. Zhou, S. B. Sørensen, O. S. Kim, E. Jørgensen, P. Meincke, O. Breinbjerg, and G. Toso, "The generalized direct optimization technique for printed reflectarrays," *IEEE Trans. Antennas Propag.*, vol. 62, no. 4, pp. 1690–1700, Apr. 2014.

[121] M. Zhou, O. Borries, and E. Jørgensen, "Design and optimization of a single-layer planar transmit-receive contoured beam reflectarray with enhanced performance," *IEEE Trans. Antennas Propag.*, vol. 63, no. 4, pp. 1247–1254, Apr. 2015.

[122] M. Arrebola, L. De Haro, and J. A. Encinar, "Analysis of dual-reflector antennas with a reflectarray as subreflector," *IEEE Antennas Propag. Mag.*, vol. 50, no. 6, pp. 39–51, Dec. 2008.

[123] C. Tienda, M. Arrebola, J. A. Encinar, and G. Toso, "Analysis of a dual-reflect array antenna," *IET Microw. Antennas Propag.*, vol. 5, no. 13, pp. 1636–1645, Oct. 2011.

[124] S. D. Targonski and D. M. Pozar, "Minimization of beam squint in microstrip reflectarrays using an offset feed," in *Antennas and Propagation Society International Symposium*, vol. 2, Baltimore, Maryland, USA, Jul. 21–26, 1996, pp. 1326–1329.

[125] M. Arrebola, "Contribution to the analysis and design of shaped-beam printed reflectarrays in complex configurations," Ph.D. dissertation, Universidad Politécnica de Madrid, 2008.

[126] Y. Rahmat-Samii, "Useful coordinate transformations for antenna applications," *IEEE Trans. Antennas Propag.*, vol. 27, no. 4, pp. 571–574, Jul. 1979.

[127] R. F. Díaz, "Contribución al análisis eficiente y a la mejora de prestaciones de antenas reflectarray," Ph.D. dissertation, Universidad Politécnica de Madrid, 2015, (in spanish).

[128] J. A. Encinar and M. Barba, "Design manufacture and test of Ka-band reflectarray antenna for trasmitting and receiving in orthogonal polarization," in *14^{th} International Symposium on Antenna Technology and Applied Electromagnetics (ANTEM) and the American Electromagnetics Conference (AMEREM)*, Ottawa, Canada, Jul. 5–8, 2010, pp. 1–4.

[129] C. A. Balanis, Ed., *Modern antenna handbook*. John Wiley & Sons, 2008.

[130] W. L. Stutzman and G. A. Thiele, *Antenna Theory and Design*, 3rd ed. John Wiley & Sons, 2012.

[131] A. C. Ludwig, "The definition of cross polarization," *IEEE Trans. Antennas Propag.*, vol. 21, no. 1, pp. 116–119, Jan. 1973.

[132] *Intel® Math Kernel Library for the Linux OS. User's Guide*, Intel Corporation, Aug. 2008.

[133] L. Greengard and J.-Y. Lee, "Accelerating the nonuniform Fast Fourier Transform," *SIAM Rev.*, vol. 46, no. 3, pp. 443–454, Jul. 2004.

[134] J.-Y. Lee and L. Greengard, "The type 3 nonuniform FFT and its applications," *J. Comput. Phys.*, vol. 206, no. 1, pp. 1–5, Jun. 2005.

[135] A. Dutt and V. Rokhlin, "Fast Fourier transforms for nonequispaced data," *SIAM J. Sci. Comput.*, vol. 14, no. 6, pp. 1368–1393, Nov. 1993.

[136] H.-T. Chou, T.-M. Hung, N.-N. Wang, H.-H. Chou, C. Tung, and P. Nepa, "Design of a near-field focused reflectarray antenna for 2.4 GHz RFID reader applications," *IEEE Trans. Antennas Propag.*, vol. 59, no. 3, pp. 1013–1018, Mar. 2011.

[137] H. Kamoda, T. Iwasaki, J. Tsumochi, T. Kuki, and O. Hashimoto, "60-GHz electronically reconfigurable large reflectarray using single-bit phase shifters," *IEEE Trans. Antennas Propag.*, vol. 59, no. 7, pp. 2524–2531, Jul. 2011.

[138] W.-T. Hung, J.-J. Tung, and S.-Y. Chen, "A focusing reflectarray and its application in microwave virus sanitizer," *Radio Sci.*, vol. 49, no. 10, p. 890–898, Oct. 2014.

[139] J. Lanteri, C. Migliaccio, J.-Y. Dauvignac, and C. Pichot, "Reflectarray using an offset prolate feed at 94 GHz," in *IEEE Antennas and Propagation Society International Symposium*, San Diego, California, USA, Jul. 5–11, 2008, pp. 1–4.

[140] Y. Rahmat-Samii, L. I. Williams, and R. G. Yaccarino, "The UCLA bi-polar planar-near-field antenna-measurement and diagnostics range," *IEEE Antennas Propag. Mag.*, vol. 37, no. 6, pp. 16–35, Dec. 1995.

[141] K. Pontoppidan, *GRASP9 Technical description*, TICRA, Jun. 2008.

[142] M. Sato, "OpenMP: parallel programming API for shared memory multiprocessors and on-chip multiprocessors," in *15th International Symposium on System Synthesis*, Kyoto, Japan, Oct. 2–4, 2002, pp. 109–111.

[143] "Grasp v9," TICRA, Copenhagen, Denmark.

[144] A. Arboleya, Y. Alvarez, and F. Las-Heras, "Millimeter and submillimeter planar measurement setup," in *IEEE Antennas and Propagation Society International Symposium (APSURSI)*, Orlando, Florida, USA, Jul. 7–13, 2013, pp. 1–2.

[145] O. M. Bucci, G. Mazzarella, and G. Panariello, "Reconfigurable arrays by phase-only control," *IEEE Trans. Antennas Propag.*, vol. 39, no. 7, pp. 919–925, Jul. 1991.

[146] P. Nayeri, A. Z. Elsherbeni, and F. Yang, "Design, full-wave analysis, and near-field diagnostics of reflectarray antennas," *Appl. Comp. Electro. Society (ACES) Journal*, vol. 28, no. 4, pp. 284–292, Apr. 2013.

[147] S. D. Targonski and D. M. Pozar, "Analysis and design of a microstrip reflectarray using patches of variable size," in *Antennas and Propagation Society International Symposium*, vol. 3, Seattle, Washington, USA, Jun. 20–24, 1994, pp. 1820–1823.

[148] D. M. Pozar, *Microwave Engineering*, 3rd ed. John Wiley & Sons, 2005.

[149] Agilent Technologies, "S-parameter design," Application Note AN 154, p. 7.

[150] R. A. Horn and C. R. Johnson, *Matrix analysis*, 2nd ed. Cambridge University Press, 2013.

[151] J. A. Encinar, M. Arrebola, M. Dejus, and C. Jouve, "Design of a 1-metre reflectarray for DBS application with 15% bandwidth," in *First European Conference on Antennas and Propagation (EuCAP)*, Nice, France, Nov. 6–10, 2006, pp. 1–5.

[152] J. Álvarez, R. G. Ayestarán, G. León, L. F. Herrán, A. Arboleya, J. A. López-Fernández, and F. Las-Heras, "Near field multifocusing on antenna arrays via non-convex optimisation," *IET Microw. Antennas Propag.*, vol. 8, no. 10, pp. 754–764, Jul. 2014.

[153] S. E. Nai, W. Ser, Z.-L. Yu, and H. Chen, "Beampattern synthesis for linear and planar arrays with antenna selection by convex optimization," *IEEE Trans. Antennas Propag.*, vol. 58, no. 12, pp. 3923–3930, Dec. 2010.

[154] Z. Xianyi, W. Qian, and Z. Yunquan, "Model-driven level 3 BLAS performance optimization on Loongson 3A processor," in *IEEE 18th International Conference on Parallel and Distributed Systems (ICPADS)*, Singapore, Dec. 17–19, 2012, pp. 684–691.

[155] *Intel® Math Kernel Library Reference Manual*, Intel Corporation, Aug. 2008.

[156] G. H. Golub and C. F. V. Loan, *Matrix computations*, 4th ed. The Johns Hopkins University Press, 2013.

[157] O. M. Bucci, G. Franceschetti, G. Mazzarella, and G. Panariello, "A general projection approach to array synthesis," in *Proc. Antennas and Propagation Society International Symposium*, San Jose, California, USA, Jun. 26–30 1989, pp. 146–149.